

Diss. ETH No. 24719

Transcutaneous Energy and Information Transfer for Left Ventricular Assist Devices

A thesis submitted to attain the degree of

DOCTOR OF SCIENCES of ETH ZURICH
(Dr. sc. ETH Zurich)

presented by

OLIVER MARCO KNECHT

MSc ETH

born on 09.07.1986

citizen of Uster, Switzerland

accepted on the recommendation of

Prof. Dr. Johann W. Kolar, examiner

Prof. Dr. Juan Rivas-Davila, co-examiner

2017

ETH Zurich
Power Electronic Systems Laboratory
Physikstrasse 3
8092 Zurich
Switzerland

<http://www.pes.ee.ethz.ch>

© 2017 by Oliver Knecht

*dedicated to
Stefan, Gabriella, Anina
and Leoni*

Acknowledgments

Power Electronic Systems Laboratory

FIRST of all, I would like to thank Prof. Dr. Johann W. Kolar, who invited me four years ago to join the Power Electronic Systems Laboratory (PES) and who gave me this unique opportunity to make a contribution in the field of power electronics research. And in particular I would like to thank him for sharing his extensive expertise, his valuable advice and for the great amount of confidence in my work. I particularly enjoyed the large freedom of research and I was able to benefit from the extensive know-how and technical expertise of the scientific staff at PES, be it the professor, the senior researchers or the PhD students. The education in the field of power electronics could hardly have been better.

Further, I want to express my sincere gratitude for the financial funding of my PhD project by the Baugarten Zurich foundation and the Power Electronic Systems Laboratory.

I specifically thank Prof. Dr. Juan Rivas-Davila for his interest in my work and for taking the time to evaluate my thesis. Further, I would like to thank him for travelling the long way from Stanford to Zurich to attend my PhD defense as the co-examiner of my work.

Since the beginning of my work at PES I had the privilege to share the office with Daniel Rothmund, Thomas Guillod, and recently with Panteleimon Papamanolis. I am very grateful for all the interesting technical discussions and for the fun we had in our office. A special thank goes to Thomas Guillod who helped me with his experience and knowledge in numerical computing and finite element simulations, and equally important, who provided an almost inexhaustible source of excellent chocolate cookies in the office.

Particularly, I would like to thank Dr. Roman Bosshard for his valuable technical advice and his support throughout my thesis. I can proudly admit that, in fact, he is the origin and motivation of my ever-increasing Adobe Illustrator skills. Further thanks go to Dr. Ralph Burkart, who allowed me to use his comprehensive inductor modeling and optimization scripts. Halfway through my time as a PhD student, I had the opportunity to be part of the PES team participating in the Google Little-Box challenge. It was an exciting experience and I really enjoyed the challenging tasks and the nightly work with

Dr. Dominik Bortis, Dr. Florian Krismer, Dominik Neumayr and Prof. Kolar. The inspiring working atmosphere at PES is due to the constant exchange of experience and knowledge within the PES team. I am very grateful for the good times we had at work, at conferences or at the ski-weekends, and after work in bQm. Thanks to everyone in the team: Dr. Arda Tüysüz, Christoph Gammeter, Dr. David Boillat, Jannik Schäfer, Jon Azurza Anderson, Julian Böhler, Lukas Schrittwieser, Mario Maurerer, Dr. Matthias Kasper, Mattia Guacci, Michael Antivachis, Michael Flankl, Michael Leibl, Dr. Gabriel Ortiz, Pedro Bezerra, Dr. Toke Andersen, and Dr. Yanick Lobsiger.

The PES is incredibly well organized, which is mainly attributed to the permanent staff at PES, in particular Monica Kohn, Roswitha Coccia, Prisca Maurantonio, Damaris Egger, Yvonne Schnyder-Lieberherr, Dr. Beat Seiler, Peter Seitz, Peter Albrecht and Claudia Stucki. I would like to thank all of them for their help and support.

I was lucky to supervise several very good MSc students and I am grateful for all the efforts they put into their projects. Specifically, I would like to thank Yves Jundt for his great work with the implantable antenna. Furthermore, I want to thank the team of the D-ITET workshop, specifically Martin Vogt, Daniel Wegmann and Stephan Siegrist, who manufactured the mechanical parts for the implant prototype with highest precision and quality. Additionally, I thank Hansruedi Benedikter and Martin Lanz from the Millimeter-Wave Electronics Laboratory for their help with the fabrication and the performance measurement of the implant antenna. Finally, I thank Dr. Peter Neukomm for sharing his great knowledge and experience on passive biotelemetry and body-mounted antennas.

Zurich Heart

This work is part of the Zurich Heart project, which was initiated by Prof. Dr. Volkmar Falk in 2012 in response to the existing problems with implantable mechanical circulatory support devices. I would like to thank him for the support and for the encouraging and motivating manner he supervises the project. And I thank Dr. Corina Schütt from University Medicine Zurich for her help and for the excellent organization of the annual workshops and meetings.

As a part of the Zurich Heart project, I had the opportunity to work with several outstanding researchers from different fields in engineering,

material science and medicine. A special thank goes to Dr. Marianne Schmid Daners for her support and for offering me the opportunity to take part in the animal experiments. In this context, I would like to thank Prof. Dr. Markus Wilhelm, Dr. Nikola Cesarovic and the perfusionist team of the department of cardiovascular surgery at the University Hospital Zurich, who carried out the experiments. In addition I would like to thank Prof. Dr. Christoph Starck for his valuable inputs and for his help with my questions in the medical field.

In particular, I would like to thank the members of the OctoVAD team, namely Dr. Gregor Ochsner, Dr. Raffael Amacher, Dr. Bente Thamsen, Anastasios Petrou, Georgios Stefopoulos, Seraina Dual, Lena Wiegmann, Stefan Boës, Silvan Staufert and Martina Cihova for the good collaboration and the familiar atmosphere either at or outside work. In this regard, I would like to thank Seraina Dual and Lena Wiegmann for the organization of the many social events, such as the OctoVAD retreats, ski-weekends and hiking tours.

Finally, I thank all my friends who are still standing by me, despite my constant absence. And in particular I thank my parents Gabriella and Stefan, and my sister Anina for the motivating words and the unlimited support during this intense period of time. And I thank Leoni for her love and her infinite patience during all the ups and downs of the past. Without all of you, this work would not have been possible.

Zurich, August 2017

Oliver Knecht

Abstract

CONCURRENTLY to the growth of the ageing population in the industrialized countries, an increasing number of people is suffering from severe heart failures. In the end stage, a heart transplantation is often the only curative treatment option. However, the availability of suitable donor hearts is limited and the number of patients awaiting a heart transplantation has increased significantly. This trend promoted the development of implantable mechanical circulatory support systems, such as Left Ventricular Assist Devices (LVADs), which help the weakened heart to provide the pump capacity, which is needed to maintain the regular blood circulation in the body. The technological advances of the recent years with continuous flow LVADs have resulted in more effective designs, which allow for higher power conversion efficiency, improved reliability and reduced overall volume. Hence, the LVAD became a feasible solution to treat end-stage heart failures and is being used today not only as a bridge to transplant, but it became also an option for a treatment, known as *destination therapy*, which is intended for people suffering from end-stage heart failure, but which do not meet the medical criteria for a heart transplantation.

Due to the continuous high power consumption of an LVAD, a percutaneous driveline is used today to ensure the energy supply of the implanted mechanical blood pump. The permanent penetration of the skin affects the quality of life of the patient and poses a high risk of severe infections, which are a common cause of death. In clinical trials it was observed, that such a driveline infection has developed in approximately 19 % of all patients in the first year after the LVAD implantation. Therefore, wireless power transfer technology, such as Inductive Power Transfer (IPT) is a promising solution to overcome this problem and to power the LVAD without the need for a galvanic contact.

The main topic of this thesis is the realization and the optimization of a Transcutaneous Energy Transfer (TET) system, based on inductive power transfer, and which is capable of delivering up to 30 W of electrical power across the skin. A main objective is the maximization of the energy transfer efficiency of the IPT system, which in turn allows to prolong the battery runtime and to reduce the heating of the tissue, which surrounds the implant. Several IPT circuit topologies are analyzed, using both analytical and numerical modeling of the power electronic circuit and a comparative evaluation has revealed, that for the power levels at hand, the series-series compensated IPT resonant

circuit topology is of particular interest. Therefore, this work provides an in-depth analysis of this particular IPT topology and discusses the advantages and disadvantages of two different operating modes, i.e. the operation at resonance and above resonance of the IPT circuit. A hardware prototype of the IPT system is then used to experimentally verify the performance of the converter, and as a result, a DC-DC efficiency of up to 97 % is achieved for the IPT converter stage for a transmission of 30 W across an air gap of 10 mm with 70 mm diameter energy transfer coils.

Equally important as the electrical performance is the operational safety of the TET system, in particular concerning the heating of the tissue and the compliance to regulations regarding the electro-magnetic field exposure of the human body. Accordingly, numerical simulation models are developed which allow for the safety assessment of the IPT system, and which are then used to disclose the physical performance limits and the design limitations for the TET system application at hand.

Additional DC-DC converter stages are required on the primary and secondary side to control the IPT system. The converter stages are optimized by means of a multi-objective optimization, in order to find the best trade-off between the converter efficiency and power density. In addition, a comparative evaluation of two soft-switched DC-DC converter topologies and the conventional hard-switched solution was carried out and as a result, it was shown that the latter provides a superior performance, unless the constant control power losses of the soft-switched solutions can be reduced substantially. The findings are then verified using a hardware prototype.

Finally, a hardware prototype of the TET implant is realized, which integrates the electronics for the IPT energy receiver, the control, the backup battery, including the charging converter, as well as the communication electronics and the antenna, which was specifically designed for the operation inside the human body. Depending on the operating mode of the IPT system, an overall TET system DC-DC efficiency of up to 90 % is achieved for the maximum output power and minimum coil separation distance of 10 mm. The thermal measurements at the energy transfer coils and the numerical simulations for the electro-magnetic field exposure have shown, that the realized TET system allows for a safe operation, even at power transfer levels of up to 30 W.

The thesis is concluded with an in-depth discussion of the limitations

and the capabilities of the two considered operating modes of the series-series compensated IPT system design and recommendations for future research areas are provided.

Kurzfassung

AUFGRUND der alternden der Gesellschaft, leidet in den industrialisierten Ländern eine wachsende Anzahl Menschen an einer schweren Herzinsuffizienz. Im Endstadium ist eine Herztransplantation oft die letztmögliche Behandlungsoption. In den vergangenen 15 Jahren ist jedoch die Zahl verfügbarer Spenderorgane um einen Drittel gesunken, während sich die Anzahl der Patienten, die auf eine Herztransplantation warten, beinahe verdoppelt hat. Dieser Trend förderte die Entwicklung von implantierbaren, mechanischen Kreislauf-Unterstützungssystemen, den sogenannten Left Ventricular Assist Devices (LVADs). Diese elektromechanischen Blutpumpen unterstützen das geschwächte Herz, um die benötigte Pumpleistung zur Verfügung zu stellen, damit eine reguläre Blutzirkulation im Körper aufrechterhalten werden kann. Der technologische Fortschritt der letzten Jahre hat bei LVADs mit kontinuierlichem Blutstrom zu immer effektiveren Konstruktionen geführt, sodass eine höhere Energieeffizienz, eine verbesserte Zuverlässigkeit und ein geringeres Bauvolumen erreicht werden konnten. Daher werden diese Herzunterstützungssysteme heutzutage nicht nur zur zeitlichen Überbrückung bis hin zur Transplantation verwendet, sondern die LVADs werden auch vermehrt für die sogenannte ‚Destination Therapy‘ eingesetzt. Diese entgültige Form der Behandlung wird bei Patienten mit Herzinsuffizienz im Endstadium angewandt, welche die anspruchsvollen medizinischen Kriterien für eine Herztransplantation nicht erfüllen.

Aufgrund des hohen, kontinuierlichen Leistungsverbrauchs eines LVADs wird gegenwärtig ein perkutanes Kabel verwendet, welches die Energieversorgung der implantierbaren Blutpumpe gewährleistet. Diese Kabelverbindung reduziert einerseits die Lebensqualität des Patienten und andererseits hat die dauerhafte Penetration der Haut oftmals schwere Infektionen zur Folge. Diese sind eine häufige Todesursache und klinische Studien haben gezeigt, dass etwa 19% aller Patienten im ersten Jahr nach der LVAD-Implantierung eine Infektion entwickelt haben. Technologien zur drahtlosen Energieversorgung, wie z.B. die induktive Energieübertragung (IPT), bieten daher einen vielversprechenden Lösungsansatz, um das LVAD ohne galvanischen Kontakt durch die Haut hindurch mit Energie zu versorgen.

Das Hauptthema dieser Arbeit ist die Realisierung und die Optimierung eines Systems zur transkutanen Energieübertragung (TET), basierend auf dem Prinzip der elektromagnetischen Induktion, welches in der Lage ist, eine Leistung von bis zu 30 W drahtlos zu übertragen. Der

Fokus liegt dabei auf der Maximierung der Energieübertragungseffizienz des IPT Systems, was schlussendlich die Laufzeit der Batterie verlängert und die Erwärmung des Gewebes auf ein Minimum reduziert. Dazu werden mit Hilfe analytischer und numerischer Modellierung des leistungselektronischen Systems mehrere verschiedene Schaltungstopologien miteinander verglichen. Dabei zeigt sich, dass sich ein serienkompensierter IPT Resonanzkonverter besonders gut für die Energieübertragung eignet. Demnach bietet diese Arbeit eine vertiefte Analyse dieser Topologie und diskutiert die verschiedenen Betriebsarten, sowie die verschiedenen Vor- und Nachteile, die im Zusammenhang mit dem Betrieb der Schaltung einhergehen. Ein Prototyp der drahtlosen Energieübertragungsstrecke wird anschliessend verwendet, um die Leistungsfähigkeit des Systems zu zeigen und um die theoretische Analyse des Konverters experimentell zu verifizieren. Die Messungen zeigen, dass für die Energieübertragungsstrecke eine maximale DC-DC-Effizienz von bis zu 97 % erreicht werden kann. Dies bei einem Spulendurchmesser von 70 mm, einem Luftspalt von 10 mm und einer Übertragungsleistung von 30 W.

Ebenso wichtig wie die elektrische Leistungsfähigkeit des Systems ist die Betriebssicherheit des TET Systems. Dies betrifft vor allem die zulässige Erwärmung des Gewebes und die Einhaltung von Grenzwerten bezüglich der erzeugten elektromagnetischen Felder. Zur Beurteilung der Betriebssicherheit werden numerische Simulationsmodelle entwickelt, welche zudem ermöglichen, die physikalischen Leistungsgrenzen und die Designbeschränkungen der Energieübertragungsstrecke aufzuzeigen.

Um den Leistungsfluss zu steuern, werden auf der Primär- und Sekundärseite des IPT Systems zusätzliche DC-DC Konverter benötigt. Die Auslegung dieser Konverter basiert auf einer Mehrkriterien-Optimierung, die es erlaubt, den besten Kompromiss zwischen Energieeffizienz und der Leistungsdichte zu finden. Zusätzlich werden zwei weich geschaltete DC-DC Konverter-Topologien mit der konventionellen, hart geschalteten Topologie verglichen, wobei sich zeigt, dass letztere im Vergleich am besten abschneidet, es sei denn, die konstanten Verluste der Steuerung der weich geschalteten Konverter können wesentlich reduziert werden. Die theoretischen Erkenntnisse werden mit Hilfe eines Prototypen experimentell nachgewiesen.

Abschliessend wird ein Prototyp des gesamten TET Implantats realisiert, welcher die sekundärseitigen elektronischen Baugruppen des IPT

Systems enthält, sowie die Steuereinheit, die Backup-Batterie, deren Laderegler und die Kommunikationselektronik, mitsamt der Antenne. Die Antenne wird daher speziell für den Betrieb innerhalb des menschlichen Körpers optimiert. Je nach Betriebsmodus des TET Systems werden DC-DC Effizienzen von bis zu 90% erreicht. Dies bei der maximalen Übertragungsleistung von 30 W und dem minimalen Spulenabstand von 10 mm. Zusätzlich zeigen thermische Messungen an den Energieübertragungsspulen und numerische Simulationen zur elektromagnetischen Verträglichkeit, dass diesbezüglich auch bei einer hohen Leistungsübertragung von bis zu 30 W ein sicherer Betrieb des entwickelten TET Systems gewährleistet werden kann.

Abgerundet wird die Arbeit mit einer vertieften Diskussion über die Limitierungen und die Leistungsfähigkeit der betrachteten IPT Systeme. Abschliessend werden weiterführende Forschungsarbeiten für mögliche weitere Verbesserungen des TET Systems aufgezeigt.

Abbreviations

AC	Alternating Current
ADC	Analog-to-Digital Converter
ASIC	Application Specific Integrated Circuit
ASK	Amplitude Shift Keying
BTT	Bridge to Transplant
BTR	Bridge to Recovery
CAD	Computer Aided Design
CC	Constant Current
CL-TCM	Clamp-Switch Triangular Current Mode
CM	Common-Mode
CPU	Central Processing Unit
CPLD	Complex Programmable Logic Device
CV	Constant Voltage
DC	Direct Current
DM	Differential Mode
DoD	Depth-of-Discharge
DOI	Digital Object Identifier
DSP	Digital Signal Processor
DT	Destination Therapy
DUT	Device Under Test
EIRP	Equivalent Isotropically Radiated Power
EMF	Electro-Magnetic Field
EMI	Electro-Magnetic Interference
ESR	Equivalent Series Resistance
FCC	Federal Communications Commission
FEM	Finite Element Method
FET	Field Effect Transistor
FPGA	Field Programmable Gate Array
FSK	Frequency Shift Keying
FSM	Finite State Machine
GaN	Gallium-Nitride
GND	Circuit Ground
GSE	Generalized Steinmetz Equation
HFSS	High Frequency Structure Simulator
IC	Integrated Circuit
ICD	Implantable Cardioverter-Defibrillator
ICNIRP	International Commission on Non-Ionizing

Abbreviations

	Radiation Protection
IEEE	Institute of Electrical and Electronics Engineers
INTERMACS	Interagency Registry for Mechanically Assisted Circulatory Support
IPT	Inductive Power Transfer
ISM	Industrial, Scientific and Medical
ITIS	Foundation for Research on Information Technologies in Society
LNA	Low Noise Amplifier
LSK	Load Shift Keying
LVAD	Left Ventricular Assist Device
MCS	Mechanical Circulatory Support
MCU	Microcontroller Unit
MICS	Medical Implant Communication Service
MOSFET	Metal-Oxide Semiconductor Field Effect Transistor
NFC	Near Field Communication
OOK	On-Off Keying
PCB	Printed Circuit Board
PA	Power Amplifier
PEEK	Polyetheretherketone
PI	Proportional-Integral
PIFA	Planar Inverted-F Antenna
PSU	Power Supply Unit
PTFE	Polytetrafluoroethylene
PWM	Pulse-Width Modulation
RF	Radio Frequency
RSSI	Received Signal Strength Indicator
SAR	Specific Absorption Rate
SCM	Synchronous Conduction Mode
SPICE	Simulation Program with Integrated Circuit Emphasis
SRF	Self-Resonance Frequency
SSP	Series-Series-Parallel
SSR	Series-Series-Resonant
SSU	Series-Series-Unity-Gain
SP	Series-Parallel
TCM	Triangular Current Mode
TET	Transcutaneous Energy Transfer

USB	Universal Serial Bus
VAD	Ventricular Assist Device
VNA	Vector Network Analyzer
WPT	Wireless Power Transfer
ZVS	Zero Voltage Switching

Contents

Abstract	ix
Kurzfassung	xiii
Abbreviations	xvii
1 Introduction	1
1.1 Mechanical Circulatory Support	3
1.1.1 Driveline Infections	6
1.2 Transcutaneous Energy Transfer for Mechanical Circulatory Support	7
1.2.1 TET System Overview	9
1.2.2 Design Challenges	10
1.2.3 Previous Work	13
1.3 Goals and Contributions of the Thesis	15
1.4 Outline of the Thesis	16
1.5 List of Publications	18
2 Inductive Power Transfer System	21
2.1 IPT Fundamentals	22
2.1.1 Capacitive Compensation	24
2.1.2 Maximum Energy Transfer Efficiency	29
2.1.3 Equivalent Load Modeling	33
2.1.4 Series-Series Compensation - Operation above Resonance	36
2.1.5 IPT Coil Design and Power Loss Modeling	40
2.2 IPT Topology Comparison	49
2.2.1 IPT System Design	49
2.2.2 Topology Comparison Results	55
2.3 IPT System Power Loss Modeling	58
2.3.1 Extended Load Model	58
2.3.2 Diode Rectifier Losses	62
2.3.3 Resonant Circuit Power Loss	63
2.3.4 Inverter Losses	63
2.4 Experimental Verification	68
2.4.1 IPT System Prototype	69
2.4.2 Measurement Results	72

2.5	Synchronous Rectification	74
2.5.1	Hardware Prototype	75
2.5.2	Power Loss Modeling	78
2.5.3	Measurement Results	79
2.6	IPT System Operation and Control	83
2.6.1	SSR IPT System	84
2.6.2	SSU IPT System	88
2.6.3	Discussion	91
2.7	Summary of the Chapter	94
3	Thermal Model	97
3.1	Heat Transfer in the Living Tissue	97
3.1.1	Bioheat Transfer Model	98
3.1.2	Thermal Tissue Damage	100
3.2	Numerical Thermal Model	101
3.3	In-Vivo Experiment	105
3.3.1	Comparison with the Numerical Model	110
3.4	Thermal Exposure Assessment	113
3.5	Summary of the Chapter	115
4	Dielectric Model	119
4.1	Electrical Properties of Human Tissue	120
4.2	Regulations on EMF Exposure	123
4.3	Simulation Model	126
4.4	Influence of Common-Mode Voltage	129
4.4.1	Equivalent Circuit Model	129
4.4.2	EMF Exposure Assessment	134
4.4.3	Common-Mode Voltage Suppression	137
4.5	Electrical Shielding	140
4.6	Summary of the Chapter	144
5	IPT System Design Limitations	147
5.1	IPT System Modeling	148
5.2	EMF Exposure Simulation	149
5.3	Simulation Results	152
5.4	Summary of the Chapter	156

6	DC-DC Converter	159
6.1	Topology Overview	160
6.2	CL-TCM Boost Converter Operation	164
6.2.1	ZVS Modulation Scheme	164
6.2.2	ZVS Conditions	168
6.2.3	CL-TCM Control	172
6.3	Experimental Verification	177
6.3.1	Hardware Prototype	177
6.3.2	Performance Measurement	179
6.4	Hard-Switched Boost Converter	184
6.4.1	Multi-Objective Optimization	185
6.4.2	Performance Measurement	191
6.5	DC-DC Converter Comparison	193
6.6	Summary of the Chapter	196
7	Wireless Communication	199
7.1	Medical Device Radiocommunications Service	201
7.2	MICS Band Transceiver	202
7.3	Implant Antenna Design	205
7.3.1	Antenna Patch Design	206
7.3.2	Substrate Material	209
7.3.3	Superstrate Material	210
7.3.4	Influence of the Human Tissue	211
7.3.5	Hardware Prototype	212
7.4	Experimental Verification	212
7.5	Exposure Assessment	216
7.6	Summary of the Chapter	217
8	Hardware Prototype	219
8.1	TET Implant Design	219
8.1.1	Rechargeable Battery	221
8.1.2	Hardware Realization	224
8.2	Performance Measurement	229
8.2.1	Battery Charging Converter	229
8.2.2	SSU TET System	233
8.2.3	SSR TET System	241
8.3	Summary of the Chapter	245

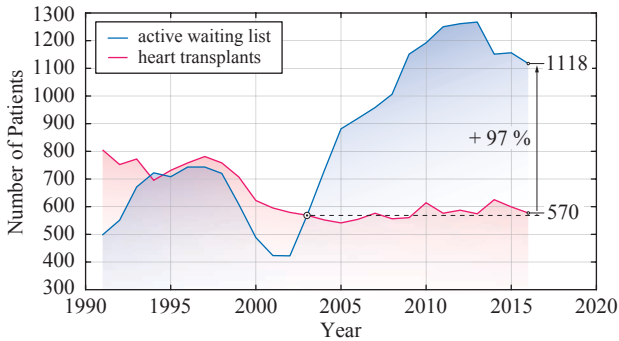
9	TET System Optimization	247
9.1	Optimization Procedure	249
9.2	Optimization Results	254
9.3	Summary of the Chapter	262
10	Conclusion & Outlook	265
10.1	Results & Conclusions	266
10.2	Future Research Areas	271
	Appendices	275
A	IPT Efficiency Calculation	277
A.1	Series-Series Compensation	278
A.1.1	Operation at Resonance	278
A.1.2	Operation above Resonance	279
A.2	Series-Parallel Compensation	280
A.3	Series-Series-Parallel Compensation	281
B	CL-TCM Boost Converter with Reduced Hardware Complexity	283
B.1	Modulation Scheme	285
B.1.1	3-Switch CL-TCM Operation	287
B.1.2	2-Switch CL-TCM Operation	292
B.2	Operating Modes	294
B.2.1	Variable Switching Frequency Operation	294
B.2.2	Constant Switching Frequency Operation	297
B.3	Controller Implementation	299
B.3.1	3-Switch CL-TCM Control	299
B.3.2	2-Switch CL-TCM Control	301
B.4	Experimental Verification	303
B.5	Filter Design	308
B.6	Summary of the Chapter	312
	Bibliography	315
	Curriculum Vitae	339

1

Introduction

CONCURRENTLY to the ageing population in the industrialized nations, the number of people with severe heart failures has increased. The recently published Eurotransplant Annual Report 2016 [1] confirms the trend of a dramatically increasing number of patients on the active waiting list for a heart transplantation. As shown in **Fig. 1.1**, since 2003 when the number of patients on the active waiting list was equal to the heart transplants for the last time, the number of patients awaiting a donor heart has almost doubled. The situation is further aggravated by the lack of available donor organs, which is reflected by the stagnating number of heart transplants since then. Consequently, as reported in [1], the median waiting time for patients on the active waiting lists has increased to approximately 15 months at the end of 2016. At the end of 2002, the median waiting time was about 5.2 months and has now almost tripled. This trend promoted the ongoing development of implantable Mechanical Circulatory Support (MCS) systems, such as Total Artificial Hearts (TAHs) and Left Ventricular Assist Devices (LVADs). Whereas TAHs are developed to fully replace the human heart, LVADs are designed to support the weakened heart in order to provide the pump capacity that is needed to maintain a regular blood circulation in the body. The LVAD is connected with its inflow cannula to the apex of the left ventricle and the outflow graft is connected to the aorta, as it is schematically shown in **Fig. 1.2(a)**. Hence, a part of the blood entering the ventricle is pumped directly into the aorta, which reduces the load of the heart significantly.

Due to the significant technological improvements, these implantable mechanical blood pumps became a widely accepted treatment option for severe end-stage heart failures. Today, MCS systems are used



Source: Eurotransplant - Annual Report 2016 [2] (Fig. 6.9, pp. 103)

Fig. 1.1: Dynamics of the Eurotransplant donor heart waiting list and heart transplants between 1991 and 2016 [1].

for several different treatment options, such as bridge-to-transplantation (BTT), as bridge-to-candidacy (BTC), as bridge-to-recovery (BTR) and for destination therapy (DT), which denotes the treatment for patients with severe heart failures, who do not qualify as candidates for transplantation [2].

Nevertheless, the implantation of a LVAD is a serious surgical intervention and there is a large number of adverse events associated with the LVAD implantation, such as ventricular arrhythmias, infections, bleeding, thromboembolic events and strokes, as well as pump thrombosis and device failures [2], which limit the life expectancy of the patients.

In response to these unresolved problems, the Zurich Heart project was initiated in 2012 as a collaboration of the ETH Zurich, the University of Zurich and the University Hospital of Zurich, under the umbrella of University Medicine Zurich/Hochschulmedizin Zürich. The aim of the ongoing project is to improve the critical components of the state-of-the-art MCS systems, and includes optimized control and sensor concepts, power supply management, novel surface materials and optimized pump design. On a second track, the project focuses on research for novel circulatory support devices.

A major problem of the LVAD therapy is the risk of severe infections associated with the percutaneous driveline, which is used today to power the implanted LVAD (cf. **Fig. 1.2(a)**). Hence, as a part of the Zurich Heart project, the focus of this work is on the development and the opti-

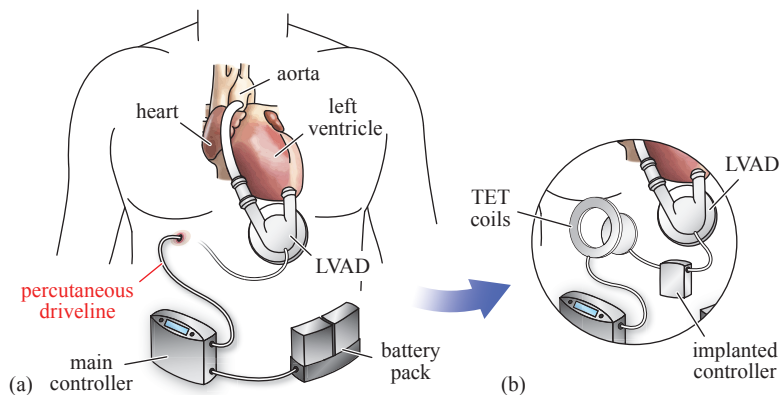


Fig. 1.2: (a) Mechanical Circulatory Support(MCS) system with an LVAD and percutaneous driveline [3], as it is clinically used today. (b) Fully implantable MCS system, incorporating a Transcutaneous Energy Transfer (TET) system for the wireless power transfer.

mization of a wireless Transcutaneous Energy Transfer (TET) system, which allows to eliminate the percutaneous driveline and to progress towards a fully implantable MCS system, as illustrated in **Fig. 1.2(b)**.

1.1 Mechanical Circulatory Support

A comprehensive review of the current state-of-the-art, the perspectives and the history of LVAD technology is given in [4–6], and is summarized in the following.

In 1963, DeBakey and his colleagues used an early development of their LVAD for the first time in a patient [7]. Later in 1966, an improved version was applied in a small number of patients, one year before the first human-to-human heart transplantation. The LVAD was a pneumatically driven pulsatile pump and was located completely outside of the human body. The first Total Artificial Heart (TAH) was implanted in 1982, but due to the high rate of complications, the concept could never establish as a permanent replacement for the human heart, and hence, the focus was more on ventricular support [6].

The first generation of VADs were exclusively pulsatile pumps, i.e.

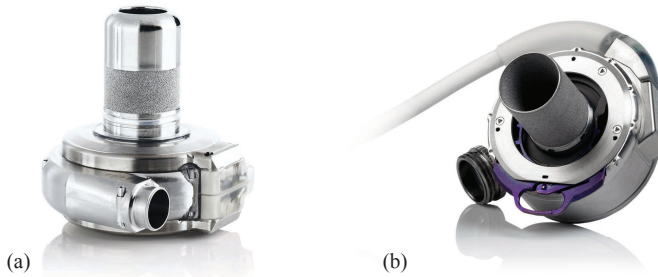


Fig. 1.3: (a) HeartWare™ HVAD™, reprinted with friendly permission of [8]. (b) Thoratec HeartMate 3™ LVAD [9], image provided courtesy of St. Jude Medical, Inc.

volume displacement pumps without continuous blood flow, and were driven either electrically or pneumatically. The main disadvantages of these pumps were the large volume, the material wear-out, noise emissions and the increased risk of infections of the cannulas [6].

The second generation included the continuous-flow centrifugal blood pumps, which are smaller in volume and which could be fully implanted into the body. The most widely used second generation LVAD was the Thoratec HeartMate II and was the first continuous-flow LVAD approved for BTT therapy by the US Food and Drug Administration (FDA) in 2008, and has been widely used worldwide. These devices allowed for single ventricular support only and a bi-ventricular support was not feasible, due of the size of the pumps. However, the risk of infections and device failures was reduced and the survival rate was significantly improved when compared to the pulsatile pumps [4, 6].

The third generation LVADs, with its further reduced size, allows for bi-ventricular support, using two identical fully implanted pumps. Leading examples of these devices are the HeartWare HVAD and the Thoratec HeartMate 3 shown in **Figs. 1.3(a)** and **(b)**, respectively. Both pumps are radial pumps with an impeller that is fully suspended in the blood stream. The HVAD uses a combination of a passive magnetic and hydrodynamic bearing to position the impeller in the blood flow. The maximum flow rate is up to 10l/min and is operated at a fixed rotor speed [4, 5]. In the HeartMate 3 LVAD, the impeller is magnetically suspended, using a passive and an active magnetic bearing, which allows for larger gaps between the pump housing and the rotor, and hence, has

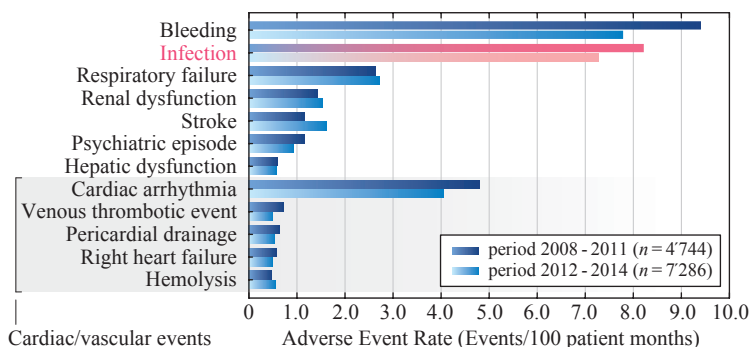


Fig. 1.4: Seventh INTERMACS report: Adverse event rates in the first 12 months after implantation, for continuous-flow left- and bi-ventricular assist device support [10].

the potential to reduce the shear stress on the blood cells and to mitigate haemolysis. The pump is able to provide a flow-rate of 2.5-10l/min and allows for artificial pulsatility [9].

The latest generation of LVADs are small enough to allow for an implantation without full sternotomy and are placed intrapericardial, i.e. the abdominal pump pocket which was required for the HeartMate II LVAD is eliminated [4, 6]. Hence, the pumps can be used in patients with smaller body size. As another main advantage, they offer a high durability with almost eliminated wear-out, and are thus suited for BTT and also for DT. The application of the third generation LVADs further increased the rates of survival and reduced the number of adverse events [6], i.e. with the HeartMate 3, a 6-month survival rate of 92% is reported in [9].

The seventh annual report of the Interagency Registry for Mechanically Assisted Circulatory Support (INTERMACS) [10] summarizes the experience with continuous-flow MCS devices of more than 15000 patients in the period from 2006 to 2014. From the 15745 enrolled patients, the large majority of 12030 patients received a continuous-flow LVAD. From 2008 to 2011, 70.3% of totally 4744 VADs were used as a bridge to transplantation and 28.6% of the implanted devices were designated for destination therapy. However, in 2014, the amount of devices used for DT has increased to almost 46%, meaning that an increasing number of patients will rely on the MCS for the rest of their life

expectancy. As stated in [10], about 30 % of the patients that were listed for heart transplantation at the time of implant, i.e. with the bridge-to-transplant strategy, have received a heart transplantation within one year. For patients who received the MCS as a bridge-to-candidacy, the likelihood for a heart transplantation within the first year after MCS implantation is considerably lower and attains only 20 %. As it is reported in [10], the overall 1-year survival rate for patients with continuous-flow VADs reaches 80 % and drops to about 70 % at 2 years after implantation. The survival rate for patients listed for transplantation is about 85 % at 1 year after VAD implantation and is generally higher than the survival rate among DT patients, which drops to about 76 % at 1 year and to 57 % at 3 years after VAD implantation. As shown in [10], the main causes or modes of death are neurological events, right heart failure and multisystem organ failure, which occur particularly in the first few month after VAD implantation. The risk of death caused by malfunctions of the VAD itself appears to be unlikely and constant over time.

The INTERMACS report [10] also lists the adverse events and the rates of occurrence during the first year after VAD implantation, as shown in **Fig. 1.4**. Bleeding and infection are by far the most likely causes with 7.8 and 7.3 events per 100 patient months, respectively, during the time period between 2012 and 2014. Other major adverse events are cardiac arrhythmia, respiratory failure and stroke.

1.1.1 Driveline Infections

Despite the impressive developments made in LVAD technology, at the present time, all implantable MCS systems are powered by means of a percutaneous driveline. The experience with 73 patients, who received an implantable first generation LVAD between 1996 and 2005 showed that the risk of driveline infection increases dramatically with the duration of support and the cumulative hazard of developing a driveline infection reached 94 % after one year of therapy [11]. In the majority of the cases, the driveline infection is initiated by a mechanical trauma due to tension and/or torque at the driveline exit site, resulting in an opportunity for bacterial overgrowth at the location of injury [11, 12]. As the infections likely develop on the surface at the barrier between the skin and the driveline, it may spread deeper along the driveline path and can cause severe complications. Today, there is a variety of

preventive strategies that are applied, which allow to reduce the risk of an infection at the driveline exit site, such as perioperative antibiotics, various anchoring devices that help to minimize the mechanical stress and tension at the exit site, and the patients are educated in routine driveline site care [13].

Generally, since the replacement of the bulky pulsatile pumps, which required more surgical dissection for implantation, with the more compact second generation continuous-flow LVADs such as the HeartMate II, the rate of device-related infections was significantly reduced by up to 50 % [13, 14]. Nevertheless, the evaluation of the INTERMACS registry data in the years from 2006 to 2010 by Goldstein et al. [12] has shown, that after one year still 19 % of the 2006 patients who received the HeartMate II LVAD have suffered from a driveline infection. After two years of treatment, the number increased to more than 25 % of the patients, and the mean time to develop a percutaneous site infection was 6.6 months.

Hence, a major problem associated with the LVAD therapy remains the high risk of infections, specifically at the driveline exit site, and is an increasing cause of morbidity and together with multisystem organ failure, infections are the second most common cause of death after the first six month from the implantation of the LVAD [10, 13]. Specifically for the long term LVAD therapy, such as for the destination therapy, the high risk of driveline infection remains a serious problem and substantially diminishes the quality of life of the patient. Hence, an important step towards the prevention of device-related infections is the elimination of the percutaneous driveline [2].

1.2 Transcutaneous Energy Transfer for Mechanical Circulatory Support

The choice of the most suitable energy source for an implantable medical device depends on several factors, such as the available volume, the amount and time profile of the power consumption and on the targeted lifetime of the implant [15]. The requirements on the energy source are exceptionally high for medical implants, since a failure or malfunction could have fatal consequences for the patient. Hence, the most important criteria is a reliable and safe operation of the implant and its energy source.

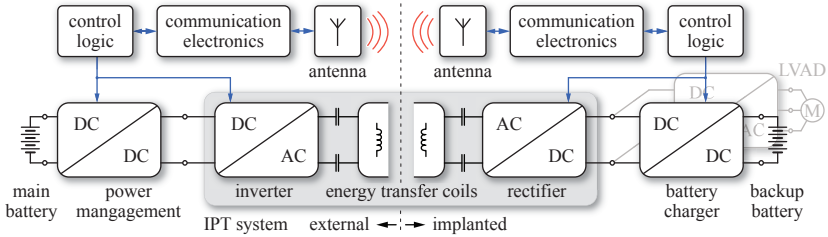


Fig. 1.5: TET system concept for a fully implantable MCS system.

Today's implantable medical devices, such as pacemakers, cochlear implants, retinal implants, neural recorder/stimulators, biomonitoring systems as well as Implantable Cardioverter-Defibrillators (ICDs) have a continuous power consumption of less than $1/4\text{ W}$, and are mainly powered by electrochemical batteries, i.e. specifically lithium-ion batteries, or by means of low-power inductive power transfer [15]. In contrast, the typical continuous average power consumption of current state-of-the-art LVADs is in a range of $4\text{--}7\text{ W}$ with peak power consumption of up to 12 W [16, 17]. For bi-ventricular support or total artificial hearts, the power demand is even higher. For the recently developed ReinHeart TAH, the reported average power consumption is 20 W [18]. In addition, in case of destination therapy, the targeted runtime of the LVAD is several years.

Hence, a fully implantable mechanical circulatory support system cannot solely rely on an implanted energy storage, but must be continuously powered across the skin by means of a transcutaneous energy transfer system. Nevertheless, an additional backup battery storage must be included in a fully implantable MCS, since an interruption of operation is immediately life threatening. Beside the safety considerations, it allows for a completely untethered operation of the LVAD for durations ranging from 30 minutes to 1.5 hours, and hence increases the quality of life of the patient [17]. The power transfer capability requirement of the TET system is increased by the recharging of the internal backup battery, and is therefore expected to be in a range of $25\text{--}30\text{ W}$, depending on the LVAD power consumption and the maximum feasible battery charging power.

Wireless power transfer systems for medical implants include a wide range of technologies, such as radiative energy transmission in the mega-

hertz and gigahertz frequency range, capacitive coupling, ultrasonic or optical energy transfer, and inductive coupling of an energy transmitting and receiving coil [15]. Due to the high power transfer requirement of the MCS system, only the inductively coupled energy transfer is an appropriate solution. The idea of powering an artificial heart via an inductive link goes back to the 1960s [19] and the following section provides an overview of the important components and the basic functionality of an inductively coupled TET system.

1.2.1 TET System Overview

A fully implantable MCS system employs mainly four key parts, the Inductive Power Transfer (IPT) system, the control and communication electronics, the internal battery backup with its charging power converter and the LVAD and its motor driver, which can be connected either directly in parallel to the output of the IPT system or in parallel to the internal backup battery. An illustration of the general TET system concept is provided in **Fig. 1.5**. An external battery pack provides the main power supply to operate the LVAD. The inverter circuit as part of the IPT system supplies an AC current to the energy transmitting coil, which is placed in close proximity above the implanted energy receiving coil. The energy between the two coils is transferred by means of electromagnetic induction and on the secondary side, the induced AC voltage is rectified back to a DC voltage. The transferred electrical power is then supplied to the motor inverter, which is driving the LVAD and to the battery charging converter, which allows to recharge the implanted backup battery.

As mentioned earlier, the internal backup battery allows for an uninterrupted operation of the LVAD and permits a fully untethered operation of the LVAD and hence, facilitates activities that demand increased mobility of the patient. The runtime of the standalone implant is mainly limited by the available battery volume and by the energy density that current battery technologies can provide. Today's medical grade rechargeable lithium-ion batteries reach volumetric energy densities of up to 255 Wh/l, i.e. such as the Greatbatch Xcellion R220 rechargeable battery [20]. Accordingly, with a battery volume of 5 cl (50 cm³), a total capacity of 12.75 Wh is available for the LVAD operation. Assuming an average LVAD power consumption of 7 W, a battery runtime of up to 55 minutes can be achieved at an allowed Depth-of-

Discharge (DoD) of 50 %.

In addition to the wireless power transfer system, a wireless communication channel is needed to allow for a closed-loop control of the IPT system and for transmission of sensor data and for the high level control of the LVAD. For low power TET systems, the data is often transmitted using the IPT coils, by means of an amplitude modulation of the power signal [21, 22]. For higher power transmission it is often advantageous to separate the power transfer and the data transmission path. In this case, additional data transmission coils can be embedded in the energy transfer coils to implement a Near Field Communication (NFC) link [23, 24]. For long-range and high data rate communication channels, Radio Frequency (RF) transceivers are used with dedicated RF antennas [25]. For the TET system application at hand, it is advantageous to use a dedicated short-range data transmission channel for the real-time control of the power transmission and a separate long-range communication channel, which is used for high-level implant control and monitoring tasks.

1.2.2 Design Challenges

A TET system that is capable of delivering up to 30 W across the human skin to power a fully implantable MCS is a complex system and has to meet highly demanding requirements. Hence, as outlined in [3], several design challenges are associated with the practical design and implementation of the TET system, and are summarized in the following:

- **Energy efficiency** is a major performance characteristic of any battery powered TET system. But specifically for the power levels at hand, high power losses within the implant or the energy transfer coil can cause discomfort to the patient or may even cause permanent tissue damage in case of excessive heating of the tissue surrounding the implanted TET system components. Therefore, the TET system must be optimized for highest energy transfer efficiency in order to minimize the power losses and in order to prolong the battery runtime. Specifically the minimization of the implant power loss is therefore one of the main objectives in the optimization process of the TET system. A highly efficient system also requires less cooling and allows for a more compact design of the implant.

- ▶ **Coil misalignment** has a big impact on the IPT system performance, since the magnetic coupling of the energy transfer coils is directly related to the physical size and geometric arrangement of the two coils. If the coil separation distance or the lateral coil misalignment is increased, the magnetic coupling is decreased and as a result, the achievable energy transfer efficiency and the power transfer capability of the TET system is reduced. For the application at hand, the coil separation distance is mainly defined by the thickness of the skin and subcutaneous tissue between the two coils and their lateral alignment. It is expected that the nominal distance between the perfect axially aligned coils is 10 mm, but the system must be designed to maintain good performance at coil separation distances of 20 mm or even 30 mm. With varying coil coupling, the electrical transfer characteristics of the IPT system are altered as well. Consequently, the IPT system requires a robust control, in order to stabilize the output voltage.
- ▶ **System volume** is a particularly critical parameter for implantable medical devices. The interior of the human body is rather volume optimized and does not provide intermediate space for additional equipment. But considering **Fig. 1.5**, the amount of electronic components that must fit into the MCS implant is high. Even with the latest available technology for system integration, the TET implant volume will be considerably larger than modern implantable pacemakers or ICDs, and is mainly determined by the installed capacity of the backup battery. Similar considerations apply to the implanted TET coil. A small TET coil simplifies the implantation, but the magnetic coupling with the extracorporeal coil is reduced and diminishes the overall IPT system performance. Furthermore, a smaller TET coil aggravates the heating of the surrounding tissue due to the increased power loss density.
- ▶ **Implant weight** is difficult to control and may be only reduced considerably by reducing the size of the internal backup battery. With typical gravimetric energy densities of lithium-ion battery technologies of 90-185 Wh/kg [26], an installed battery capacity of 10 Wh already weighs between 55 g and more than 100 g. A heavy implant is more difficult to fixate inside the body and may cause pressure marks on the surrounding tissue.

- ▶ **System reliability** is naturally a priority criteria, which applies to all kinds of active medical implants. Specifically in the case at hand, the implant has to continuously deliver a comparably large amount of electrical power and the failure of the implanted electronic system is immediately life-threatening and provokes a surgical intervention. The implant is intended to operate for several years inside the human body, and hence, the implant must be hermetically sealed and only long-life components must be used for its implementation. Redundancy may be required for particularly critical electronic sub-assemblies which experience the highest electrical stress, such as the power electronic stages in the TET system. However, any requirement for redundant circuits also increases the implant volume and adds more complexity to the system.

- ▶ **Operational safety** is particularly important and is closely related to the system reliability. The implant and TET coil enclosure must be biocompatible and potentially toxic materials, e.g. inside the backup batteries, must be hermetically separated from the human body. Due to the high power transfer capability, there are several safety risks associated with the TET system operation, such as high operating voltages related to the IPT system, excessive heating of the tissue or the exposure of the human body to strong electromagnetic fields, which must remain within safe limits. An increased safety risk is the backup battery, as it stores a large amount of energy. The batteries must be monitored continuously and safety measures must be applied in order to prevent mechanical or electrical damage to the battery. Furthermore, in the case of a temporary loss of communication, the energy transfer system must not fail and the long-range wireless communication must not interfere with other medical equipment or other wireless devices and must be protected from unauthorized access.

The following section briefly summarizes the previous work on TET systems used for fully implantable MCS systems and provides the basic benchmark data for several TET system developments reported in the literature.

1.2.3 Previous Work

In the past 15 years, LVAD technology underwent tremendous improvements, but up to this date, only two TET systems were clinically used in conjunction with LVADs or artificial hearts:

- ▶ **Lionheart LVD-2000:** This LVAD was designed specifically for DT and was first implanted in 1999. The pump is a pulsatile type and requires a compliance chamber for pump volume compensation. The pump provides a maximum outflow of approximately 8 l/min and is operated by a TET system, with the implanted energy receiving coil having a diameter of 73 mm and a thickness of 16 mm. The implanted backup battery allowed for a standalone operation of about 20-30 minutes without recharging [27,28]. The LionHeart LVAD was implanted in 23 patients and the overall survival rates for one and two years were 39 % and 22 %, respectively. The number of device-related infections was lower, which was likely due to the use of the TET system [17].
- ▶ **AbioCor TAH:** The TAH includes two artificial ventricles and replaces the entire human heart. The pulsation pump uses an electrical motor to drive a hydraulic pumping system. The ventricular membranes are durable enough to withstand at least 180 million beats, which corresponds to a lifetime of 5 years. The total device weighs about 1 kg and has the size of a grapefruit. The TET system used for the power supply has achieved power transfer efficiencies in the range of 68-72 % for coil separation distances of 3-10 mm [29]. The internal backup battery allows for an untethered operation of the system of about 30 minutes without recharging [17]. A main problem with the AbioCor TAH is its large size, which precludes a large number of patients due to their small posture. Another reported drawback of the long-term operation is the thermal stress of the human tissue due to the power losses in the TET coils [29].

Today, both devices are outdated and are no longer in the market, but the studies with both devices indicated a decrease of the device-related infections and the TET system showed reliable operation for at least one or two years [17]. With the second and third generation LVADs many of the technological problems of the early pumps have been solved, and consequently, the duration of the LVAD therapy could be increased

Year of publication	Prim. coil diameter (mm)	Sec. coil diameter (mm)	Core material	Coil distance (mm) [†]	Operating frequency (kHz)	Output power (W)	DC-DC efficiency (%)
1993 [30,31]	90	66	none	15	437	18	76
2000 [32]	90	60	none	14	430	36	61
2006 [33]	90	72	ferrite	20	160	27	86
2009 [34]	64	64	ferrite	20	285	24	89
2009 [35]	92	53	ferrite	15	163	20	85
2010 [36]	50	50	none	20	200	15	84
2012 [37]	65	50	none	20	386 ^{††}	15	79
2014 [38]	95	55	none	20	790	16	82
2015 [39]	88	66	none	15	600	29	84

[†]coil separation distance at perfect axial alignment.

^{††}presumed from the system specifications given in [37].

Tab. 1.1: Specifications and performance overview of previously developed TET systems [30–39] for the use with LVADs and/or artificial hearts [3]. Note that the TET systems of the LionHeart VAD and the AbioCor TAH are not listed in the table, which is due to the limited availability of information on the implementation and operation of the TET systems.

and the patient outcome was improved. Therefore, in recent years the driveline-related infections became a major problem and the need for a fully implantable solution has increased again.

Several prototype TET systems have been designed and were tested at different stages of development *in-vitro* or even in long-term animal trials. **Tab. 1.1**, given in [3], provides an overview of the main characteristic parameters of several promising TET system developments of the past [30–39]. The main parameters that characterize the performance of a TET system is the achievable energy transfer efficiency of the IPT system at a given output power and geometrical arrangement of the energy transfer coils, i.e. the coil diameters and separation distance of the coils at which the indicated efficiency was achieved. Additionally, **Tab. 1.1** specifies whether a magnetic core material was used to enhance the magnetic coupling of the coils and at which frequency the IPT system was operated. The coil separation distance has a significant impact on the energy transmission efficiency and for small coil distances it is fairly simple to achieve high efficiencies. Hence, it was decided to summarize the efficiencies for the largest reported coil separation distance up to 20 mm, which allows for a more meaningful judgement of the system performance. However, it is important to note

that without additional information on the topology or the input and output voltages and on the coverage of the power loss measurement, a direct comparison of the individual systems is unfair in most of the cases. Unfortunately, in some cases the required information is not reported. Therefore, **Tab. 1.1** is intended to give the reader a general impression for the range of the key design and performance parameters achieved in the past [3].

In summary, even though TET systems have been successfully tested in animal studies and in a small number of patients, there are open questions and specifically at power transfer levels beyond 15 W further technological improvements are needed to enhance the energy transfer efficiency and safety of this technology. In addition, according to the knowledge of the author, there exists no publication on the implementation of an overall TET system, which is designed for high power transmission, considering multiple aspects, such as the energy transfer efficiency, the heating of the tissue and the electromagnetic field exposure of the human body.

1.3 Goals and Contributions of the Thesis

The main objective of the thesis is the optimization and realization of a TET system with increased power transfer capability, that provides highest energy efficiency of the wireless power transmission and the implant electronics. Furthermore, the TET system must comply to safety regulations concerning the heating of the tissue and the exposure of the human body to electromagnetic fields.

Despite the many TET system developments of the past, a direct comparison of the performance of different IPT system topologies is missing and the global design limitations are not shown. Hence, in this thesis, multiple wireless power transfer circuit topologies are investigated. The development of comprehensive analytical and numerical models of the wireless power transfer link and the power electronic converter stages allow for a comparative evaluation of suitable IPT system topologies, revealing the advantages and disadvantages of each system topology. In addition, the design limitations due to the heating of the human tissue and due to regulations on electromagnetic fields are investigated. Consequently, the mutual dependencies of different design parameters and the design trade-offs are revealed and hence, allow for a more complete picture of the TET system design.

In order to verify the analytical and numerical models, converter prototypes of the wireless power transfer link and the DC-DC converter stages are designed and realized in hardware, using the latest Gallium-Nitride (GaN) semiconductor technology. In addition to the power electronic circuit of the TET system, the wireless communication channel, which is needed for the implant monitoring and the control of the wireless power transfer link, is designed in a form suitable for implantation.

Finally, the individual components are integrated into a fully functional, volume optimized hardware prototype of the TET system implant, which sets the basis for future animal trials. The overall TET system performance is then verified using the hardware prototypes.

1.4 Outline of the Thesis

As outlined above, the design of a TET system with increased power transfer capability is associated with several engineering problems and design challenges. The thesis is organized in eight main chapters, each addressing a specific problem or aspect of the TET system implementation. A short outline of each chapter is given in the following:

- ▶ **Chapter 2** provides an introduction into the basic concept and theory of wireless power transmission and forms the basis of this work. Different IPT topologies are analyzed and compared regarding the electrical characteristics and performance measures. The most suitable IPT circuit topology for the application at hand is identified and a power loss model is developed, which allows for the further optimization steps, and is verified using a hardware prototype of the IPT system.
- ▶ **Chapter 3** addresses the thermal safety assessment of the energy transfer coils. First, a brief introduction into the numerical thermal modeling of the living tissue is given and a finite element model is presented, that is used throughout the thesis for the tissue temperature estimation.
- ▶ **Chapter 4** analyzes the impact of the exposure of the human tissue to the electromagnetic fields in close proximity to the TET coils. The additional power loss in the tissue due the absorbed energy is moderate and does not contribute significantly to the

heating of the tissue. However, the electric field strength in the vicinity of the implanted TET coil can attain values, which are exceeding the applicable regulations. Therefore, the IPT topology and the grounding scheme of the implanted power electronic converter are reviewed and measures are presented, which allow to significantly reduce the electric field strength.

- ▶ Using the numerical models for the IPT system power losses, the TET coil temperature and EMF exposure estimation, the design and performance limitations are shown in **Chapter 5** for a large number of electrically feasible IPT system designs, regarding the energy conversion efficiency, the tissue heating and the EMF exposure.
- ▶ Due to the large variation of the IPT system operating conditions, i.e. the magnetic coupling variations of the energy transfer coils and/or changes of the load conditions, additional DC-DC conversion stages are needed in order to control the IPT system. Hence, in **Chapter 6** different hard- and soft-switched DC-DC converter topologies are optimized and compared, in order to find the most suitable converter topology for the application at hand.
- ▶ The TET system requires a wireless communication system as well, in order to implement a closed-loop control of the contactless energy transfer system and to allow for high level control of the LVAD and the transmission of sensor data. Hence, **Chapter 7** shows the implementation of a wireless communication link operating in the Medical Implant Communication Service (MICS) band at 403.5 MHz. The main focus is on the design of the implantable antenna, as it is the most critical component in the communication system.
- ▶ **Chapter 8** shows the realization of a TET system implant prototype, which brings together the findings from the previous analyses. The hardware prototype is then used for the final system performance assessment, which is carried out for two different IPT system operating schemes.
- ▶ **Chapter 9** provides a comprehensive multi-objective optimization of the total TET system, i.e. including each power electronic converter stage between the main external battery supply and

the implanted backup battery. The optimization is based on the power loss estimation of each converter stage, using the numerical models, which were developed in the course of this work. The optimization further accounts for the varying operating conditions of the TET system by means of a weighted system efficiency, considering partial load operation and variable coil alignment.

At the end of each chapter, a short summary is provided, which highlights the essential findings and results. Final conclusions of the thesis and ideas or proposals for future research projects in the field are given in **Chapter 10**.

In the course of the project, several scientific papers have been published in the form of journal articles or were presented at international conferences and many of the chapters are based on these publications. Hence, the papers are cited at the beginning of the associated chapter or where appropriate within the text. A complete list of the publications that originated in connection with this work is provided in the following.

1.5 List of Publications

Various content and findings presented in this thesis have already been published in scientific journals and proceedings of international conferences, or are protected by patents. The publications and patents developed in the course of this thesis, or in other projects carried out in parallel to this work, are listed below.

Journal Papers

- ▶ O. Knecht, and J. W. Kolar, "Performance evaluation of series-compensated IPT systems for transcutaneous energy transfer," *IEEE Trans. Power Electron.*, pp. 1–14, published, April 2018. DOI: [10.1109/TPEL.2018.2822722](https://doi.org/10.1109/TPEL.2018.2822722)
- ▶ O. Knecht, D. Bortis, and J. W. Kolar, "ZVS modulation scheme for reduced complexity clamp-switch TCM DC-DC boost converter," *IEEE Trans. Power Electron.*, vol. 33, no. 5, pp. 4204–4214, May 2018. DOI: [10.1109/TPEL.2017.2720729](https://doi.org/10.1109/TPEL.2017.2720729)

- ▶ O. Knecht, R. Bosshard, and J. W. Kolar, "High efficiency transcutaneous energy transfer for implantable mechanical heart support systems," *IEEE Trans. Power Electron.*, vol. 30, no. 11, pp. 6221–6236, November 2015. DOI: [10.1109/TPEL.2015.2396194](https://doi.org/10.1109/TPEL.2015.2396194)
IEEE Power Electronics Transactions First Prize Paper Award
- ▶ M. Leibl, O. Knecht, and J. W. Kolar, "Inductive power transfer efficiency limit of a flat half-filled disc coil pair," *IEEE Trans. Power Electron.*, vol. 33, no. 11, pp. 9154–9162, November 2018. DOI: [10.1109/TPEL.2018.2797366](https://doi.org/10.1109/TPEL.2018.2797366)

Conference Papers

- ▶ O. Knecht, and J. W. Kolar, "Comparative evaluation of IPT resonant circuit topologies for wireless power supplies of implantable mechanical circulatory support systems," in *Proc. of the 32nd Applied Power Electronics Conf. and Expo. (APEC)*, Tampa (FL), USA, March 2017, pp. 3271–3278. DOI: [10.1109/APEC.2017.7931166](https://doi.org/10.1109/APEC.2017.7931166)
- ▶ O. Knecht, Y. Jundt, and J. W. Kolar, "Planar inverted-F antenna design for a fully implantable mechanical circulatory support system," in *Proc. of the 18th IEEE Int. Conf. on Industrial Technology (ICIT)*, Toronto, Canada, March 2017, pp. 1366–1371. DOI: [10.1109/ICIT.2017.7915563](https://doi.org/10.1109/ICIT.2017.7915563)
- ▶ O. Knecht, D. Bortis, and J. W. Kolar, "Comparative evaluation of a triangular current mode (TCM) and clamp-switch TCM DC-DC boost converter," in *Proc. of the IEEE Energy Conversion Congr. & Expo. (ECCE USA)*, Milwaukee (WI), USA, September 2016, pp. 1–8. DOI: [10.1109/ECCE.2016.7854934](https://doi.org/10.1109/ECCE.2016.7854934)
Best Paper Award
- ▶ O. Knecht, and J. W. Kolar, "Impact of transcutaneous energy transfer on the electric field and specific absorption rate in the human tissue," in *Proc. of the 41th Annu. Conf. of the IEEE Industrial Electronics Society (IECON)*, Yokohama, Japan, November 2015, pp. 4977–4983. DOI: [10.1109/IECON.2015.7392881](https://doi.org/10.1109/IECON.2015.7392881)
- ▶ O. Knecht, R. Bosshard, J. W. Kolar, and C. T. Starck, "Optimization of transcutaneous energy transfer coils for high power

medical applications,” in *Proc. of the 15th IEEE Workshop on Control and Modeling for Power Electronics (COMPEL)*, Santander, Spain, June 2014, pp. 1–10.

DOI: [10.1109/COMPEL.2014.6877190](https://doi.org/10.1109/COMPEL.2014.6877190)

- ▶ D. Bortis, O. Knecht, D. Neumayr, and J. W. Kolar, ”Comprehensive evaluation of GaN GIT in low- and high-frequency bridge leg applications,” in *Proc. of the 8th Int. Power Electronics and Motion Control Conf. (IPEMC-ECCE Asia)*, Hefei, China, May 2016, pp. 21–30. DOI: [10.1109/IPEMC.2016.7512256](https://doi.org/10.1109/IPEMC.2016.7512256)

Patents

- ▶ O. Knecht, ”Implantierbare Spule mit elektrischer Schirmung (in German),”
 - Swiss Patent Application No. CH711433 (A2), filed Aug. 18, 2015, published Feb. 28, 2017.
- ▶ J. W. Kolar, D. Bortis, O. Knecht, F. Krismer, and D. Neumayr, ”Inverter zum Austausch elektrischer Energie zwischen einem DC-System und einem AC-System (in German),”
 - Swiss Patent Application No. CH711566 (A2), filed Sept. 24, 2015, published Mar. 31, 2017.
- ▶ D. Bortis, O. Knecht, and J. W. Kolar, ”Vorrichtung zur pulsdauerunabhängigen sicheren Ansteuerung von Leistungstransistoren (in German),”
 - Swiss Patent Application No. CH711455 (A2), filed Aug. 28, 2015, published Feb. 28, 2017.

2

Inductive Power Transfer System

THE basic technological concept of Inductive Power Transfer (IPT), which is also often referred to as Wireless Power Transfer (WPT), has its origin in the pioneering work of Nikola Tesla, which dates back to 1891 [40]. Recently, IPT has gained wide attention in a variety of applications such as battery charging systems for consumer electronics or electrical vehicles and biomedical implants, such as the TET system application presented in this work.

In the first part of this chapter a summary of the fundamental theoretical background of IPT systems is provided and is based mainly on the comprehensive introductions into the subject given in [41] and [42], which cover theoretical aspects as well as practical designs. Another more intuitive understanding of the fundamental concepts of IPT systems is given in [43, 44].

In the course of this chapter, several different IPT circuit topologies are compared regarding the power transfer efficiency and the most suitable IPT topology is identified for the application at hand. The power loss model is then refined for this specific IPT system topology and a hardware prototype is realized in order to verify the performance and the power loss models. Finally, two promising operating modes of the IPT system are compared regarding the achievable power transfer efficiency, tolerance to coil misalignment and possible adverse effects on the human body. Note that this chapter is to a large part based on the results published in [3, 45–47].

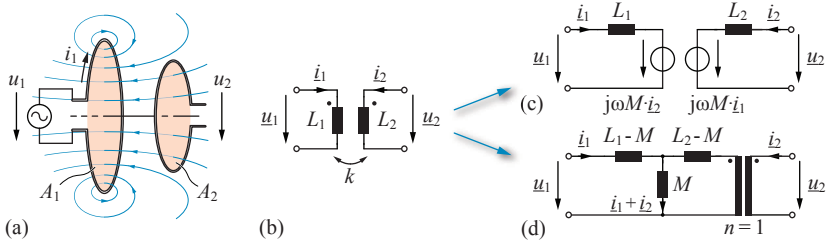


Fig. 2.1: (a) Schematic drawing of two magnetically loosely coupled coils and (b) its electrical circuit symbol. (c) General two-port transformer equivalent circuit and (d) T-type transformer equivalent circuit, neglecting the series resistance of the coils.

2.1 IPT Fundamentals

In order to understand the IPT operation, it is beneficial to start with the simple transformer and its equivalent circuit. The term *inductive power transfer* might be misleading, since the operation principle of a traditional transformer using a magnetic core provides an inductive power transfer by definition. But in this context, inductive power transfer denotes the power transfer between two (or more) magnetically *loosely coupled* coils, i.e. without the use of a magnetic core material.

Fig. 2.1(a) illustrates two magnetically coupled coils with a single winding each. The alternating current i_1 in the primary winding generates an alternating magnetic field, as described by Ampère's law. The total magnetic flux that is generated by the primary-side current loop is calculated according to

$$\Phi_1 = \iint_{A_1} \vec{B} \cdot d\vec{A}_1, \quad (2.1)$$

where A_1 denotes the area enclosed by the coil winding and \vec{B} is the generated magnetic flux density. As stated by Faraday's law, the alternating magnetic flux induces an electric field along the primary winding, which in turn causes a current in the winding that is counteracting the current that generated the alternating magnetic flux in the first place. The proportionality factor that links the time-derivative of the resulting total coil current and the coil terminal voltage is called self-inductance L_1 .

If a second (secondary-side) winding with the self-inductance L_2 is put in close proximity to the primary-side coil, a part of the magnetic flux Φ_1 passes through the secondary-side coil, as illustrated in **Fig. 2.1(a)**. As a result, an electric field is induced in the secondary-side coil as well, which is proportional to the time-derivative of the magnetic flux passing through the coil; the magnetic flux is linear proportional to the current in the primary-side coil. The proportionally factor that links the time-derivative of the primary-side coil current to the induced secondary-side coil terminal voltage, is called *mutual inductance*. The mutual inductance M is dependent on the geometrical arrangement and the size of the two coils and can be significantly influenced by adding materials with high permeability or electrical conductivity to the coil arrangement. Obviously, the described two-coil circuit is reciprocal, i.e. the mutual inductance that links an alternating secondary-side coil current to the induced voltage in the primary-side coil, is the same.

The circuit symbol of the loosely coupled transformer is shown in **Fig. 2.1(b)**. Since for mutually coupled coils, the self- and the mutual inductance act always simultaneously, the circuit in **Fig. 2.1(b)** is mathematically described with

$$\begin{bmatrix} \underline{u}_1 \\ \underline{u}_2 \end{bmatrix} = j\omega \cdot \begin{bmatrix} L_1 & M \\ M & L_2 \end{bmatrix} \cdot \begin{bmatrix} \underline{i}_1 \\ \underline{i}_2 \end{bmatrix}, \quad (2.2)$$

neglecting any resistive elements in the circuit and considering sinusoidal coil voltages \underline{u} and sinusoidal coil currents \underline{i} only, and using the phasor notation $u(t) = \hat{U} \cos(\omega t + \varphi) = \Re \left\{ \hat{U} e^{j\varphi} e^{j\omega t} \right\} = \Re \{ \underline{u} \cdot e^{j\omega t} \}$.

The parameter k in **Fig. 2.1(b)** denotes the magnetic coupling coefficient or *coupling factor*, which is defined as

$$k = \frac{M}{\sqrt{L_1 L_2}} \in [0, 1], \quad (2.3)$$

and which is equal to the fraction of the total flux generated by one of the coils that passes through the other coil [41], and is decreasing with increasing coil separation distance. The coupling factor is of particular importance for wireless power transfer systems, as it has a direct influence on the maximum power transfer capability and the maximum achievable energy transmission efficiency, as it will be shown later in this chapter.

For the circuit analysis it is convenient to use an equivalent circuit model which exactly represents the electrical behaviour of the magnetically coupled coils. The transformer equivalent circuit shown in **Fig. 2.1(c)** can be deduced directly from (2.2), using two current controlled voltage sources to model the mutual coupling of the coils. This equivalent circuit is particularly useful for the analysis of the IPT circuit topologies. Another useful equivalent circuit is depicted in **Fig. 2.1(d)**, which separates the non-coupled part of the inductances from the mutual inductance [41]. The ideal transformer in **Fig. 2.1(d)** has no particular function and represents the galvanic isolation only.

Fig. 2.1(d) already reveals the main limitation of wireless power transfer by means of two loosely coupled coils. If the mutual inductance of the two coils is small, the impedances of the leakage-inductances $L_1 - M$ and $L_2 - M$ in the series paths get large and the shunt impedance is small. Hence, in this case, and considering the winding resistance of the coils, it can be inferred that a power transmission from the primary-side to the secondary-side coil is highly inefficient, which is due to the large reactive power that must be supplied at the input of the primary-side coil in order to provide the required power transmission. As a solution, additional capacitors can be inserted on the primary and secondary side of the circuit in order to partly or fully eliminate the inductive series impedance. Accordingly, reasonable energy transmission efficiencies can be achieved, even at low coil coupling factors. The concept of the capacitive compensation is explained in detail in the following section.

2.1.1 Capacitive Compensation

As stated above, the main challenge of the design of an IPT system is the low magnetic coupling of the energy transfer coils at large coil separation distances which limits the power transfer capability. As a solution, compensation capacitances can be introduced on both sides which provide the reactive power that is 'consumed' by the stray-inductances, and hence, which allows to reduce the series impedance of the loosely coupled transformer. The type of capacitive compensation, i.e. series or parallel compensation, has a significant influence on the IPT circuit behaviour, and has also implications on the design of the energy transfer coils. Furthermore, it influences the power loss distribution within the IPT system itself.

In the following, the primary-side and secondary-side series compen-

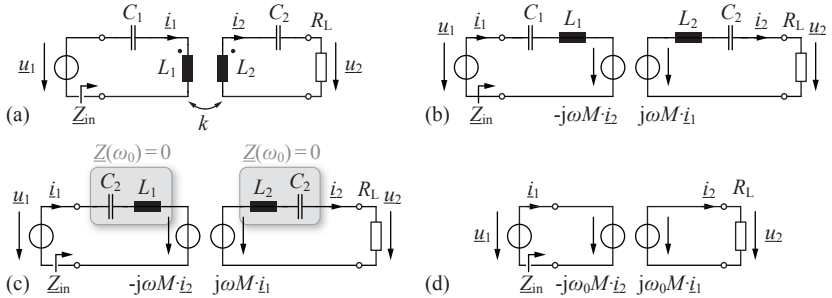


Fig. 2.2: (a)-(b) Series-series compensated IPT topology and its equivalent circuit. (c)-(d) Equivalent circuit for the operation at the resonance frequency.

sation as well as the secondary-side parallel compensation are analyzed in more detail.

Series-Series Compensation

The most intuitive understanding of the properties and the operation of an IPT system can be obtained at the example of the series-series compensated IPT topology shown in **Fig. 2.2(a)**, and is explained in detail in [43]. Note that in the first place, a lossless operation of the circuit is assumed.

Using the equivalent circuit in **Fig. 2.1(c)**, the series-series IPT circuit topology can be redrawn as illustrated in **Fig. 2.2(b)**. In this case, the compensation capacitors are designed to fully consume the reactive power of the self-inductance of the primary-side and secondary-side coil, i.e. with

$$C_i = \frac{1}{\omega_0^2 L_i}, \quad i \in [1, 2], \quad (2.4)$$

where $\omega_0 = 2\pi f_0$ is the operating frequency of the IPT system. As a result, the total impedance of the series resonant circuits is fully cancelled at the operating frequency (cf. **Fig. 2.2(c)**). Hence, the equivalent circuit is simplified significantly as shown in **Fig. 2.2(d)**.

Since the primary voltage u_1 is directly connected in parallel to the primary-side current controlled voltage source, the load current is given by

$$i_2 = j \frac{u_1}{\omega_0 M}, \quad (2.5)$$

which reveals the current source behaviour of the IPT circuit [43], i.e. at a fixed coil coupling, the load current is independent of the load resistance and can be controlled directly by adjusting the input voltage. The voltage gain follows directly from (2.5) and $i_2 = u_2/R_L$

$$|\underline{G}_v| = \left| \frac{u_2}{u_1} \right| = \frac{R_L}{\omega_0 M}. \quad (2.6)$$

The input impedance $\underline{Z}_{\text{in}}$ at the operating frequency can be calculated according to

$$\underline{Z}_{\text{in}} = \frac{(\omega_0 M)^2}{R_L}, \quad (2.7)$$

which depends on the load resistance and on the coil coupling only. However, it is important to note that the input impedance is purely resistive, i.e. the input voltage u_1 and the input current i_1 are in phase, independent of the operating conditions. Hence, as a main result, by using the primary-side and secondary-side compensation capacitors, it is possible to reduce the reactive power demand at the input of the IPT circuit to zero. However, the reactive power which is oscillating within the resonant circuits can be substantial.

In the following, the previously described series-series compensated IPT topology, operated at the resonance frequency, is referred to as SSR IPT topology.

Series-Parallel Compensation

Instead of a series compensation, it is possible to use a parallel compensation as well on either side of the loosely coupled transformer. In contrast to the series-series compensated IPT system operated at resonance, the primary series and secondary-side parallel (SP) compensation shown in **Fig. 2.3(a)**, allows for an operation with load independent voltage gain [48–50], and is explained in the following. In this case, the compensation capacitors are chosen according to

$$C_1 = \frac{1}{\omega_0^2 L_1 (1 - k_0^2)} \quad \text{and} \quad C_2 = \frac{1}{\omega_0^2 L_2}. \quad (2.8)$$

The factor k_0 is a design parameter and must not be confused with the coil coupling factor k . The choice of the parameter k_0 will become more clear in the following.

In order to analyze the circuit behaviour, it is advantageous to apply some circuit transformations to the basic equivalent circuit, as shown

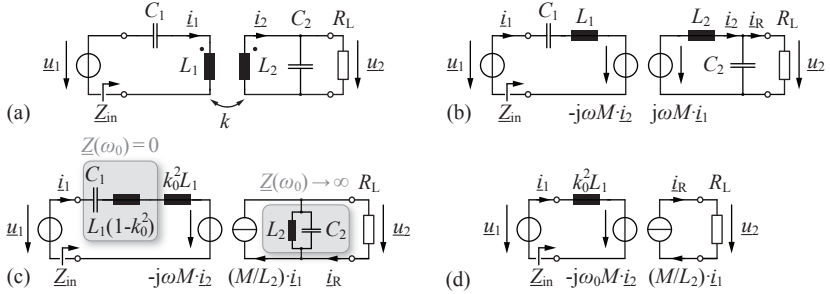


Fig. 2.3: (a) Series-parallel compensation IPT topology and the derivation of the simplified equivalent circuit (b)-(d).

in **Fig. 2.3(b)** and **(c)**. First, the primary-side self-inductance can be split into a part that is fully compensated at the operating frequency by the series compensation capacitance, and a remaining part. On the secondary side, the current controlled voltage source and the LC-network is replaced by its Thévenin equivalent circuit and the voltage source is transformed to a current controlled current source. As a result of the transformations, the secondary-side self-inductance is connected in parallel to the compensation capacitance. The parallel resonant circuit can be eliminated, because its conductance tends to zero at the resonance frequency. The resulting equivalent circuit is shown in **Fig. 2.3(d)** and simplifies the circuit analysis significantly.

Note that the secondary-side coil current i_2 is hidden in **Fig. 2.3(d)**, but is used to determine the voltage of the primary-side current controlled voltage source. The current i_2 can be derived from **Fig. 2.3(b)** and is given by

$$i_2 = u_2 \left(\frac{j}{\omega_0 L_2} + \frac{1}{R_L} \right). \quad (2.9)$$

The voltage gain of the IPT resonant circuit at the operating frequency is calculated according to

$$\underline{u}_1 = \frac{M}{L_2} \underline{u}_2 + j\omega_0 \frac{\underline{u}_2}{R_L} \left(\frac{M_0^2}{M} - M \right), \quad (2.10)$$

using $M_0 = k_0 \sqrt{L_1 L_2}$. (2.10) reveals the voltage source behaviour of the SP resonant circuit, which is obtained at $k = k_0$. In this case, the

voltage gain is given by

$$|\underline{G}_v| = \left| \frac{u_2}{u_1} \right| = \frac{1}{k_0} \sqrt{\frac{L_2}{L_1}}, \quad (2.11)$$

and is independent of the load resistance. In order to achieve unity voltage gain, the secondary-side coil inductance must be chosen such that $L_2 = k_0^2 L_1$, which implicates that the secondary-side coil has a much smaller inductance value than the primary-side coil, since $k_0 = k$ and $k < 1$, i.e. typically in a range of 0.1 to 0.5.

The input impedance can be determined using **Fig. 2.3(d)** and (2.9), and is given in general by

$$\underline{Z}_{\text{in}} = k^2 R_L \sqrt{\frac{L_2}{L_1}} + j\omega_0 L_1 (k_0^2 - k^2). \quad (2.12)$$

From (2.12) it is obvious, that the imaginary part of the input impedance is cancelled, if $k = k_0$. Hence at this specific operating point, the SP compensated IPT topology represents a voltage source at the output and has a purely resistive input impedance. However, in contrast to the SSR topology, in case of the SP compensated circuit, the phase angle of the input impedance is zero only if the coil coupling factor is equal to the design parameter k_0 , which is used to determine the primary-side compensation capacitor.

The simple analysis of the SSR and the SP topology has shown that with the use of capacitive compensation on the primary and secondary side of the loosely coupled energy transfer coils, either a current or voltage source behaviour is achieved at the output of the resonant circuit. Furthermore, it allows to achieve a purely resistive impedance at the input of the circuit, which is the basis for an energy efficient operation of the IPT system. However, there is a substantial amount of reactive power circulating within the resonant circuits itself, which causes additional power losses in the parasitic series resistances of the coil windings and the compensation capacitors.

As shown at the example of the SSR topology, the input impedance given by (2.7) is purely resistive and is dependent on the coil coupling factor and on the load resistance only. It is shown in [41, 43, 51] that for maximum energy transfer efficiency, the load resistance must be chosen such that the reactive power in the resonant circuit is minimized. This concept of *load matching* in order to achieve maximum energy transmission efficiency will be explained in the following.

2.1.2 Maximum Energy Transfer Efficiency

For any IPT circuit topology, the energy transmission efficiency can be maximized by partly matching the load to the impedance of the secondary-side coil, as it will be shown in the following at the example of the SSR topology. The derivations of the maximum energy transmission efficiency of the IPT resonant circuit topologies considered in this work are given in **Appendix A**.

It was previously shown in **Section 2.1** that the input impedance of the SSR topology is purely resistive at the resonance frequency. Hence, the total reactive power provided by the compensation capacitors is given by

$$q_{\text{tot}} = q_{C1} + q_{C2} = \underbrace{\frac{\hat{U}_2^2}{2R_L}}_{P_2} \left(\frac{\gamma}{k^2} + \frac{1}{\gamma} \right), \quad (2.13)$$

where P_2 is the output power of the circuit and \hat{U}_2 is the amplitude of the output voltage. The factor γ in (2.13) is referred to as *load factor* and is defined in [51] with

$$\gamma = \frac{R_L}{\omega_0 L_2}. \quad (2.14)$$

The power transfer efficiency of the IPT system is maximized, if the total reactive power in (2.13) is minimized, which hence, minimizes the primary-side and secondary-side coil RMS currents [44]. This can be achieved for the optimal load factor given by

$$\gamma_{\text{opt,SSR}} = k. \quad (2.15)$$

In this case, the minimum total reactive power in the IPT resonant circuit is given by

$$q_{\text{tot}}|_{\gamma=k} = \frac{2P_2}{k}, \quad (2.16)$$

which is obviously increasing with increasing output power, but also with decreasing coil coupling factor, and therefore limits the maximum feasible coil separation distance.

According to (2.15) and (2.14), the maximum energy transfer efficiency of the SSR topology is obtained, if the load resistance is equal to

$$R_{L,\text{opt,SSR}} = k\omega_0 L_2. \quad (2.17)$$

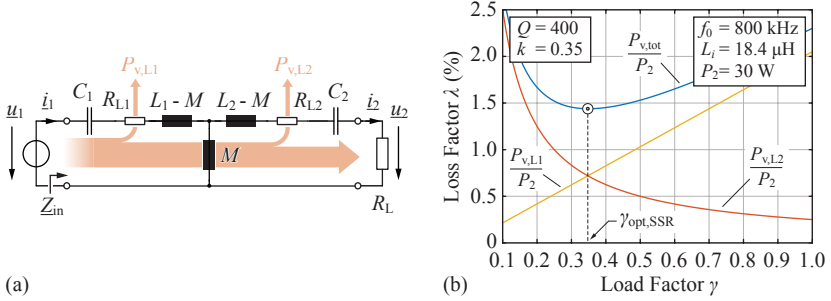


Fig. 2.4: (a) Power losses within the series-series compensated IPT circuit topology. (b) Optimum load factor for achieving the maximum energy transmission efficiency in case of the SSR IPT topology.

In order to actually calculate the maximum energy transfer efficiency of the IPT system, the coil winding resistance and the Equivalent Series Resistance (ESR) of the compensation capacitors must be taken into account. However, when using high quality capacitors, the ESR is usually much smaller than the parasitic coil winding resistance and is therefore often neglected.

The energy transfer efficiency of the IPT resonant circuit can be expressed using the quality factors of the primary-side and secondary-side energy transfer coils given by

$$Q_i = 2\pi \frac{E_{L_i} f_0}{P_{v,L_i}} = \frac{\omega_0 L_i}{R_{L_i}}, \quad i \in [0, 1], \quad (2.18)$$

which describe the ratio of the peak energy stored in the inductor, E_{L_i} , to the energy dissipated per cycle of the oscillation [52]. R_{L_i} describes the frequency dependent parasitic coil resistances and are modeled as a lumped series resistances as shown in **Fig. 2.4(a)**. $P_{v,L1}$ and $P_{v,L2}$ denote the primary-side and secondary-side coil power losses, respectively.

As shown in [48, 51] for the SSR topology, the primary-side and secondary-side coil power loss factor γ_i , $i \in [1, 2]$ can be described with

$$\lambda_1 = \frac{P_{v,L1}}{P_2} = \frac{1}{\gamma Q_1 k^2} \left(\gamma + \frac{1}{Q_2} \right)^2 \quad (2.19)$$

and

$$\lambda_2 = \frac{P_{v,L2}}{P_2} = \frac{1}{\gamma Q_2}. \quad (2.20)$$

The primary and secondary power loss factor as well as the total power loss factor, i.e. $\lambda_{\text{tot}} = \lambda_1 + \lambda_2$, with respect to a varying load factor are depicted in **Fig. 2.4(b)**. As it is also shown in [48], the energy transfer efficiency is maximized if the primary-side power loss factor is equal to the secondary-side power loss factor, i.e. where the total IPT circuit power loss has a minimum (cf. **Fig. 2.4(b)**). The minimization of the total power loss factor yields the optimal load factor, which is given by [51]

$$\gamma_{\text{opt,SSR}} = \frac{1}{Q_2} \sqrt{1 + k^2 Q_1 Q_2} \Big|_{Q_1=Q_2>100} \approx k. \quad (2.21)$$

Note that as indicated in (2.21), for equal and large coil quality factors, i.e. for $Q_1 = Q_2 > 100$, the optimum load factor is simplified to $\gamma_{\text{opt,SSR}} \approx k$, which is the same result as in (2.15).

Inserting (2.21) into (2.19) and (2.20) yields the total energy transfer efficiency given in [41–43]

$$\eta_{\text{max}} = \frac{1}{1 + \lambda_{\text{tot}}} \Big|_{\gamma=\gamma_{\text{opt}}} = \frac{(kQ)^2}{\left(1 + \sqrt{1 + (kQ)^2}\right)^2} \approx 1 - \frac{2}{kQ}, \quad (2.22)$$

and is only dependent on the coil coupling factor and the coil quality factors. It was shown in [41], that the same maximum energy transfer efficiency is achieved for the SP compensated IPT topology discussed in the previous section. Hence, as stated in [19, 51], the product kQ , with $Q = \sqrt{Q_1 Q_2}$, can be used as a Figure-of-Merit (FOM) for the optimization of inductive power transfer systems. Alternatively, the FOM can be rearranged to [42]

$$\text{FOM} = \frac{\omega M}{\sqrt{R_{L1} R_{L2}}}, \quad (2.23)$$

which can be interpreted as the ratio of the peak energy stored in the magnetizing inductance to the energy dissipated in the geometric mean of the primary-side and secondary-side coil resistances per oscillation cycle, and hence, can be viewed as the quality factor of the overall IPT resonant circuit. The result is not surprising and it is already obvious from **Fig. 2.4(a)**, that the energy transfer efficiency is increased in general, if the series resistances tend to zero and the reactance of the mutual inductance is maximized.

As a conclusion, it is important to highlight the following points regarding the efficiency optimization:

- ▶ The coil coupling factor mainly limits the power transfer capability. Even if the power loss in each resonant circuit component is very small and therefore, the circuit is not thermally limited, the reactive power in the energy transfer coils is increasing with decreasing coil coupling and constant output power (cf. (2.16)). Hence, in this case, the power transfer capability is limited by the voltage blocking capability of the resonant circuit components.
- ▶ The magnetic flux linkage between the energy transfer coils and hence, the coil coupling factor, is mainly determined by the ratio of the coil area to the coil separation distance. Accordingly, the larger the coil area and the smaller the separation distance, the larger is the coil coupling factor and the higher is the achievable energy transfer efficiency.
- ▶ According to (2.22), large coil quality factors can compensate for a low coil coupling, i.e. for large coil separation distances, and allow to enhance the energy transmission efficiency in these cases.
- ▶ From (2.23) it is tempting to conclude, that increasing the operating frequency will also increase the energy transfer efficiency. This is only partly true, since the parasitic coil series resistances are increasing with increasing operating frequency as well, which is due to the increasing impact of the skin- and proximity effect losses in the coil winding.
- ▶ The maximum energy transfer efficiency of an IPT resonant circuit is achieved only if the load resistance is matched to the impedance of the secondary-side coil, using its optimal load factor [42].

In the previous analysis, a perfectly sinusoidal AC source was assumed as an excitation for the IPT circuit and an AC load is considered. However, for the application at hand, the IPT system is designed as a DC-DC converter with an inverter at the input and a rectifier stage at the output of the IPT resonant circuit. Hence, in order to accurately calculate the maximum power loss in each IPT coil, the rectifier circuit must be considered to accurately calculate the coil currents i_1 and i_2 . Therefore, the rectifier load model and the fundamental frequency approximation is described in the following.

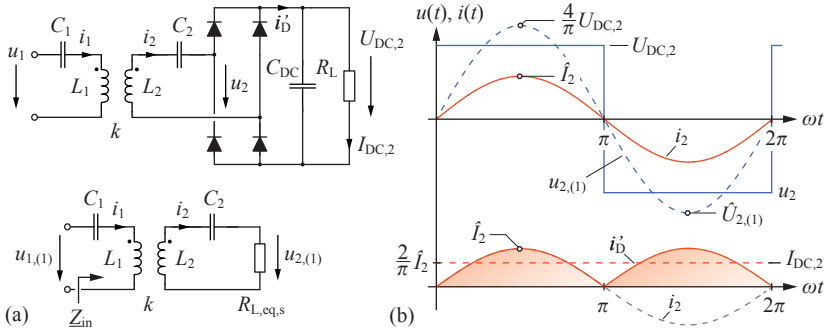


Fig. 2.5: (a) Series-series compensated IPT circuit topology with full-wave rectification and corresponding equivalent circuit model. (b) Associated secondary-side current and voltage waveforms.

2.1.3 Equivalent Load Modeling

At low coil coupling factors, the IPT resonant circuit acts as a band-pass filter with load dependent bandwidth (note that for strong coupling, *pole splitting* occurs [53, 54]). The input impedance of the resonant circuit rises asymptotically with 20 dB/dec above the resonance frequency. In addition, the high frequency harmonic content of the rectangular voltage excitation of a class-D full-bridge inverter drops with -20 dB/dec. Therefore, as outlined in [43], the high frequency harmonic content of the primary-side coil current is damped substantially and drops with -40 dB/dec. Accordingly, the primary-side and secondary-side coil currents i_1 and i_2 are almost perfectly sinusoidal in shape, which justifies the fundamental frequency approximation used in the previous analysis.

In case of the series-series compensated system, a very simple equivalent load model [55] can be used to model the load together with the full-wave rectifier, as it is shown in **Fig. 2.5(a)**. For the model derivation, a purely sinusoidal secondary-side coil current, an ideal full-wave rectifier and a constant output voltage $U_{DC,2}$ is assumed. Using the relations of the current and voltage waveforms depicted in **Fig. 2.5(b)**, the equivalent load resistance can be derived as

$$R_{L,eq,s} = \frac{8}{\pi^2} \frac{U_{DC,2}^2}{P_2}. \quad (2.24)$$

The simple load model in (2.24) is only valid for the special case of a

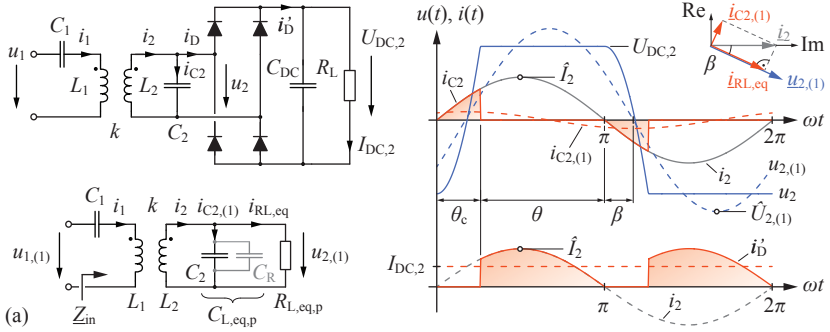


Fig. 2.6: (a) Series-parallel compensated IPT circuit topology with full-wave rectification and corresponding equivalent circuit model. (b) Associated secondary-side current and voltage waveforms.

continuous sinusoidal current at the input of the rectifier and does not apply to the secondary-side parallel compensated IPT circuit topology shown in **Fig. 2.6(a)**. In this case, following the modeling approach presented in [56], a first harmonic model is used, where the rectifier circuit is replaced by an equivalent capacitance and an equivalent load resistance, based on the load dependent conduction time of the diode rectifier. As shown in **Fig. 2.6(b)**, assuming a sinusoidal secondary-side coil current i_2 , the parallel capacitance C_2 must be charged to the output voltage $U_{DC,2}$ at each zero crossing of i_2 in order to deliver the current i'_D to the load. Hence, the first harmonic of the rectifier's input voltage $u_{2,(1)}$ lags i_2 by a phase angle β , which represents a capacitive behaviour of the circuit. Starting with the calculation of the conduction angle θ of the bridge rectifier, which is given by

$$\theta = \arccos \left(\frac{2\omega_0 C_2 U_{DC,2}^2 - \pi P_2}{2\omega_0 C_2 U_{DC,2}^2 + \pi P_2} \right), \quad (2.25)$$

the peak secondary-side coil current \hat{I}_2 can be calculated with

$$\hat{I}_2 = \frac{\pi P_2}{U_{DC,2} (1 - \cos(\theta))}. \quad (2.26)$$

Using the calculation of the first harmonic of the capacitor current $i_{C2,(1)}$, the first harmonic of the rectifier input voltage $u_{2,(1)}$ can be

obtained with

$$u_{2,(1)}(t) = \frac{1}{C_2} \int_0^t i_{C_2,(1)}(\tau) d\tau + c = \frac{\sqrt{a_1^2 + b_1^2}}{\omega_0 C_2} \sin(\omega_0 t - \beta), \quad (2.27)$$

and

$$\begin{aligned} a_1 &= \frac{\hat{i}_2}{\pi} \sin^2(\theta_c) \\ b_1 &= \frac{\hat{i}_2}{\pi} \left(\theta_c - \frac{1}{2} \sin(2\theta_c) \right), \\ \beta &= \arctan\left(\frac{b_1}{a_1}\right) \end{aligned}, \quad (2.28)$$

where $\theta_c = \pi - \theta$ denotes the conduction angle of the parallel capacitor C_2 (cf. **Fig. 2.6(b)**). The angle β describes the phase relation between the secondary-side coil current \hat{i}_2 and the first harmonic of the rectifier input voltage $u_{2,(1)}$.

In the fundamental frequency equivalent model, the same power must be dissipated in the equivalent load resistance $R_{L,\text{eq,p}}$ as in the actual load resistance R_L . Hence, an equivalent resistive-capacitive load model can be obtained using the relations of the secondary-side fundamental voltage and current components depicted in the phasor diagram in **Fig. 2.6(b)**. Accordingly, the resulting equivalent load model is given by

$$R_{L,\text{eq,p}} = \frac{a_1^2 + b_1^2}{(\omega_0 C_2)^2 2P_2} \quad \text{and} \quad C_{L,\text{eq,p}} = \frac{\tan(|\beta|)}{\omega_0 R_{L,\text{eq,p}}}. \quad (2.29)$$

As illustrated in **Fig. 2.6(a)**, the equivalent capacitance $C_{L,\text{eq,p}}$ is actually equal to the parallel connection of the secondary-side resonant tank capacitance C_2 and an additional load dependent capacitance C_R , which is due to the operation of the rectifier circuit.

If the secondary-side capacitance C_2 is decreased, the equivalent load resistance $R_{L,\text{eq,p}}$ converges to the simple load model given in (2.24). However, even a small parallel capacitance at the input of the rectifier, results in a much higher equivalent parallel capacitance, and hence, the peak secondary-side coil current is underestimated with the simple model given in (2.24). Therefore, even for the modeling of a series-series compensated IPT system, the enhanced resistive-capacitive load model can be used, in order to account for the parasitic capacitances of the rectifier diodes, as it was done in [46] for the power loss modeling of the prototype system and is discussed in detail in **Section 2.3**.

2.1.4 Series-Series Compensation - Operation above Resonance

In the previous sections, it was shown that the series-series compensated IPT topology operated at the natural resonance frequency shows a current source behaviour. However, there exists a second mode of operation above the resonance frequency, which allows for a voltage source behaviour and thus allows for a highly reduced voltage gain variation, as it will be shown in the following.

Typical voltage transfer characteristics of the series-series compensated IPT circuit topology are shown in **Figs. 2.7(a)** and **(b)**, calculated for different coil coupling factors and the IPT system specifications shown in **Fig. 2.7(c)**, given a variable load resistance and a constant IPT system output voltage. The previously derived transfer characteristics of the SSR-operation are clearly visible in **Fig. 2.7(a)**, such as the purely resistive input impedance at the operating frequency $f_{0,\text{SSR}}$, denoted with (A), and the large voltage gain variation (B), which is due to the current source behaviour of the system.

As already indicated, a special case of the series-series compensated IPT topology is the operation above resonance at the operating frequency $f_{0,\text{SSU}}$, which allows for an operation with load independent voltage gain, reported in [34, 50, 57, 58], and is indicated in **Fig. 2.7(a)** with (C). The relation between the operating frequencies is given by

$$f_{0,\text{SSU}} = f_{0,\text{SSR}} \frac{1}{\sqrt{1 - k_0}}. \quad (2.30)$$

In order to operate the system at this specific operating point, the compensation capacitors are designed according to

$$C_i = \frac{1}{\omega_0^2 L_i (1 - k_0)}, \quad i \in [1, 2]. \quad (2.31)$$

Again, the factor k_0 is a design parameter that will become more clear in the following analysis. In order to derive the basic electrical properties of this mode of operation, the equivalent circuit of the series-series compensated IPT topology shown in **Figs. 2.8(a)** and **(b)** is used again as a starting point. In this case, with the compensation capacitances given in (2.31), only a part of the impedance of the primary-side and secondary-side coil self-inductances are compensated at the operating frequency, as shown in **Fig. 2.8(c)**. Accordingly, the

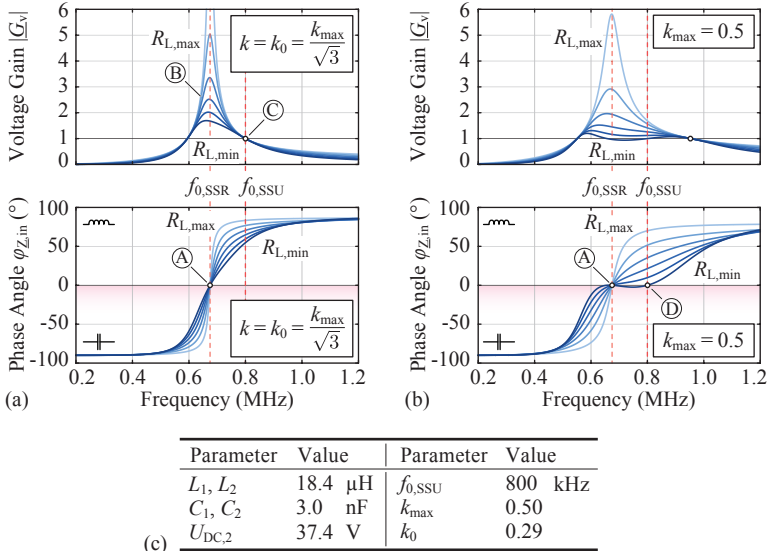


Fig. 2.7: (a)-(b) Typical voltage transfer characteristics and phase angle of the input impedance of the series-series compensated IPT circuit topology, calculated for different coil coupling factors and the IPT system specifications shown in (c), given an output power range of 5-30W and a constant output voltage of $U_{\text{DC},2} = 37.4 \text{ V}$.

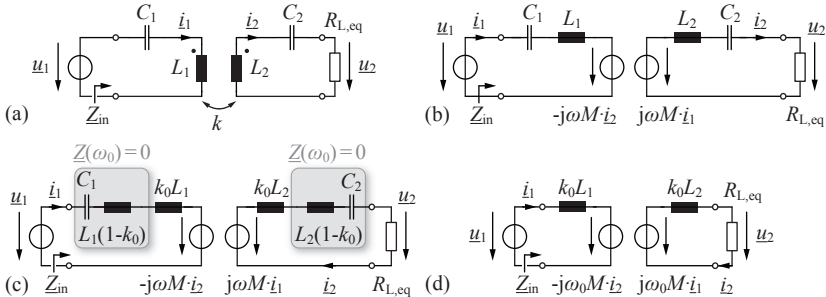


Fig. 2.8: (a)-(b) Series-series compensated IPT topology and its equivalent circuit. (c)-(d) Derivation of the simplified equivalent circuit for the operation above the resonance frequency, i.e. at the frequency for load independent voltage gain.

simplified equivalent circuit is derived as depicted in **Fig. 2.2(d)** and the relationship between the input and output voltage is given by

$$\underline{u}_1 = j\omega_0 \left(k_0 L_1 - \frac{k^2}{k_0} L_1 \right) \cdot \dot{i}_1 + \frac{k}{k_0} \sqrt{\frac{L_1}{L_2}} \cdot \underline{u}_2. \quad (2.32)$$

The first term in (2.32) is cancelled if $k = k_0$. In this case, the voltage gain of the resonant circuit becomes

$$|\underline{G}_v| = \left| \frac{\underline{u}_2}{\underline{u}_1} \right|_{k=k_0} = \sqrt{\frac{L_2}{L_1}}, \quad (2.33)$$

and is synonymous with the operation for load independent voltage gain. Furthermore, unity gain is achieved if the primary-side and secondary-side coils have equal inductance, which is referred to as SSU-operation. Note that in the following, the operation of the series-series compensated IPT system operated above the resonance frequency around the frequency for load independent voltage gain is always referred to as SSU IPT system operation, regardless of the actual gain of the resonant circuit. Further note, that with a fixed operating frequency $f_{0,SSU}$, the load independent voltage gain can be achieved only for $k = k_0$, as shown in **Fig. 2.7(a)**. If the coil coupling factor k increases, the point of load independent voltage gain will move towards higher frequencies, as shown in **Fig. 2.7(b)**. In addition, unlike for the SP compensated topology, the phase angle of the input impedance is greater than zero at the operating point for load-independent voltage gain.

The energy transfer efficiency of the SSU resonant circuit at the operating frequency ω_0 can be derived similar to the analysis presented in **Section 2.1.2** and is summarized in **Appendix A**. Accordingly, the energy transfer efficiency is given by

$$\eta = \frac{\gamma k^2 Q_1 Q_2^2}{1 + Q_2 (2\gamma + k^2 Q_1 + (\gamma^2 + k_0^2 + \gamma k^2 Q_1) Q_2)}, \quad (2.34)$$

where γ denotes the load factor defined in (2.14) and Q_1 and Q_2 are the quality factors of the primary-side and secondary-side coils, respectively. Maximizing (2.34) yields the optimum load factor $\gamma_{\text{opt,SSU}}$, which is given by

$$\gamma_{\text{opt,SSU}} = \frac{1}{Q_2} \sqrt{1 + k^2 Q_1 Q_2 + (k_0 Q_2)^2}. \quad (2.35)$$

For equal and large coil quality factors, i.e. $Q_1 = Q_2 > 100$, the optimal load factor can be approximated with

$$\gamma_{\text{opt,SSU}} = \frac{R_{\text{L,eq,opt}}}{\omega_0 L_2} \approx \sqrt{k^2 + k_0^2}. \quad (2.36)$$

For the application at hand, a full-bridge rectifier stage is used on the secondary side of the IPT resonant circuit to generate the load voltage $U_{\text{DC},2}$. Hence, using the simple equivalent load model for $R_{\text{L,eq}}$ given in (2.24) and combining it with (2.36) yields the optimal secondary-side inductance, which is given by

$$L_{2,\text{opt}} = \frac{8}{\pi^2} \cdot \frac{U_{\text{DC},2}^2}{\sqrt{2}\omega_0 k_0 P_{2,\text{max}}}, \quad (2.37)$$

at maximum output power $P_{2,\text{max}}$ and at the coupling $k = k_0$, and is referred to as load matching condition.

Since the resonant circuit is supplied by a class-D full-bridge inverter using Field Effect Transistors (FETs) for the switches, which have a finite output capacitance, the input impedance and/or the current phase angle of the resonant network has a significant influence on the losses that are generated within the inverter itself. In order to achieve soft-switching, i.e. Zero Voltage Switching (ZVS) of the inverter switches, and thereby reducing the switching loss, the input impedance of the resonant circuit must have an inductive behaviour, i.e. a positive phase angle. Using the simplified equivalent circuit shown in **Fig. 2.8(d)**, the phase angle of the input impedance $\varphi_{\underline{Z},\text{in}}$ can be derived at the operating frequency ω_0 using

$$\varphi_{\underline{Z},\text{in}} = \arctan \left(\frac{k_0 \left(R_{\text{L,eq}}^2 + (k_0^2 - k^2) \omega_0^2 L_2^2 \right)}{k^2 \omega_0 L_2 R_{\text{L,eq}}} \right), \quad (2.38)$$

which is independent of the primary-side coil inductance L_1 [47]. At a coil coupling factor of $k = k_0$, the phase angle of the input impedance is given by

$$\varphi_{\underline{Z},\text{in}} \Big|_{k=k_0} = \arctan \left(\frac{R_{\text{L,eq}}}{k_0 \omega_0 L_2} \right). \quad (2.39)$$

When the load is matched to the secondary-side coil inductance according to (2.37), the phase angle of the input impedance is reduced to

$$\varphi_{\underline{Z},\text{in}} \Big|_{k=k_0, \gamma=\gamma_{\text{opt,SSU}}} = \arctan(\sqrt{2}) = 54.7^\circ. \quad (2.40)$$

This means, that unlike for the SP topology, an operation with load independent voltage gain and maximum energy transfer efficiency cannot be achieved at the same time [58], since in this case, the phase angle of the input impedance $\varphi_{\underline{Z},\text{in}}$ given in (2.38) is only zero if

$$R_{L,\text{eq}} = \omega_0 L_2 \sqrt{k^2 - k_0^2}, \quad (2.41)$$

which is in contradiction with equation (2.36), unless $k_0 = 0$, which is again equal to the SSR-operation.

The characteristic of the phase angle of the input impedance at the constant operating frequency $f_{0,\text{SSU}}$ is shown in **Figs. 2.7(a)** and **(b)**. The phase angle of the input impedance is increasing with decreasing coil coupling factor and with increasing load resistance. Hence, in order to ensure that the phase angle of the input impedance is still positive at maximum output power and at the maximum achievable coupling factor k_{max} , the design parameter k_0 must be chosen according to [47] as

$$k_0 \geq \frac{k_{\text{max}}}{\sqrt{3}}, \quad (2.42)$$

which allows to design the compensation capacitances according to (2.31). (2.42) follows directly from (2.41) with k_{max} and (2.36), in which load matching is considered at maximum output power and coil coupling $k = k_0$. As a result, at maximum output power and maximum coil coupling factor, the phase angle of the input impedance is exactly zero at the operating frequency, as it is shown in **Fig. 2.7(b)**, denoted with (D). At $k = k_0 = k_{\text{max}}/\sqrt{3}$, the operation for load independent voltage gain and load matching is achieved. Accordingly, the voltage gain variation is kept low for a wide load range and coupling factor variation, and a high energy transfer efficiency can be achieved at the maximum coil coupling factor. A main drawback of the SSU-operation is the increasing reactive power demand at the input of the resonant circuit, which is increasing with decreasing coil coupling factor. However, the power losses on the secondary side of the resonant circuit, which are particularly critical for the application at hand, can be even lower as with the SSR-operation, as it will be shown later in this chapter.

2.1.5 IPT Coil Design and Power Loss Modeling

It was shown in **Section 2.1.2** that the theoretical maximum achievable efficiency of the IPT resonant circuit topologies is determined by

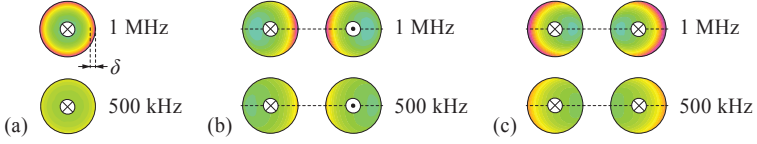


Fig. 2.9: (a) Current density distribution in a solid round conductor with a diameter of 1 mm at different operating frequencies. (b)-(c) Visualization of the proximity effect in two current carrying solid round conductors operated at 500 kHz and 1 MHz.

the coupling factor and the quality factors of the inductors, and that the product $k\sqrt{Q_1Q_2}$ is a FOM for the achievable energy transmission efficiency.

In order to compute the coil quality factor, the AC resistances of the IPT coils must be determined. Since the operating frequency of the IPT system for the application at hand is in a range between 100 kHz and 2.5 MHz, high-frequency effects such as skin-effect and proximity-effect must be considered. The reason being that the high-frequency current generates a magnetic field within the conductor, which in turn induces eddy-currents that are cancelling the current towards the center of the conductor. Hence, the effective conductor cross-section is decreased, and the electrical resistance is increased. This self-induced current displacement is known as the skin-effect and is increasing with increasing frequency. **Fig. 2.9(a)** visualizes the skin-effect for a solid round conductor with a diameter of 1 mm at different operating frequencies. At 1 MHz, the current density at the outer edge of the conductor is much larger than at the center of the conductor, and therefore occupies a lower copper cross-section and experiences a larger electrical resistance when compared to the lower frequency operation, where the current density distribution is more homogeneous.

The proximity-effect arises from the induction of eddy currents in a conductor due to an alternating magnetic field, which has its source outside of the conductor. This effect is visualized in **Figs. 2.9(b)** and **(c)** by the current density distribution of two current carrying parallel conductors, operated at different operating frequencies and different current flow directions. Similar to the skin-effect, the proximity-effect results as well in a reduction of the useful conductor cross-section, which is more decreased at higher frequencies.

In order to decrease the AC resistance of the IPT coil windings,

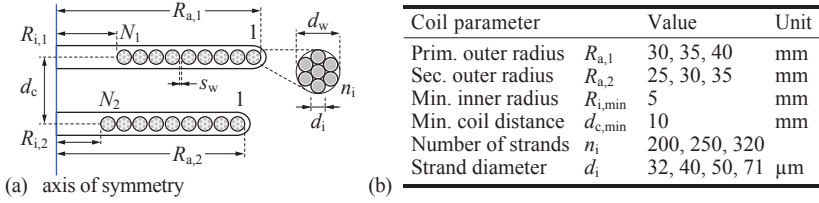


Fig. 2.10: (a) Axis-symmetric model of the IPT coil set and designations of the coil parameters. (b) Ranges of IPT coil parameters used for the TET system optimization.

high-frequency litz-wires are used, which are composed of multiple electrically insulated twisted strands. Ideally, a strand diameter is selected which minimizes the combined skin- and proximity-effect losses on the strand level at a given operating frequency. In order to maintain the required conductor cross section area, multiple strands are used in parallel, which are then twisted in such a way that each strand occupies each position in the litz-wire within a lay length. This ensures that the induced voltage in the current loop that is formed by any two strands in the litz-wire is cancelled and hence allows to reduce the skin- and proximity-effect losses on the bundle level significantly, which is a result of the more homogeneous distribution of the current within the litz-wire [59]. However, experience has demonstrated that the structure of commercially available litz-wires may deviate from the ideal twisting pattern. As a result, the AC resistance of the litz-wire can be substantially larger than expected from theory [60, 61].

For the geometrical design of the IPT coils it was shown in [48] that a flat and circular coil geometry allows for the highest coil coupling factor, compared to other coil geometries such as rectangular or square shaped coils with the same occupied area. Therefore, in this work, flat and circular shaped coils with only one layer of litz-wire winding are used in order to achieve a low profile of the energy transfer coils as well as a high mechanical flexibility, which is in particular needed for the implanted TET coil. In this case, an overall thickness of the implantable coil of 3 mm is targeted, including the silicone encapsulation of the coil. An axis-symmetric schematic drawing of the IPT coil set and the designations of the coil parameters are shown in **Fig. 2.10(a)**. In discussion with medical experts, a maximum feasible implant TET coil diameter of about 70 mm was identified and the expected coil separation

distance is in a range of 10 mm to 25 mm. A smaller secondary-side coil diameter simplifies the implantation and increases the comfort for the patient. However, a reduction of the receiver coil size is only of partial advantage, since a larger coil geometry allows for higher inductances and higher quality factors [45]. As a result, the losses within the coils are reduced and are spread over a larger surface, which in turn simplifies the cooling. Additionally, higher coupling factors between primary-side and secondary-side coil can be achieved with an increased tolerance to misalignment.

Even though additional magnetic material could be used in the coil design in order to increase the self-inductance of the coils and to improve the coil coupling factor [33–35], its contribution to the total coil power loss can be significant. Furthermore, the mechanical flexibility of the coils would be reduced and the thickness of the TET coils would be increased. It was therefore decided to omit any additional magnetic material in the coil design.

The calculation of the power losses in litz-wire windings, due to skin- and proximity-effect, is explained in detail in [59] and is taken as basis for the following coil power loss calculation. For the coil geometry shown in **Fig. 2.10(a)**, the skin-effect based electrical resistance of the coil, including the DC resistance, can be calculated according to

$$R_{\text{skin}} = \frac{2}{n_i} R'_{\text{DC}} F_r(f) l_w, \quad (2.43)$$

using the DC resistance R'_{DC} of a single strand per unit length and the total wire length l_w of the spiral coil, given by

$$R'_{\text{DC}} = \frac{4}{\sigma_{\text{Cu}} \pi d_i^2} \quad (2.44)$$

and

$$l_w = \sum_{i=1}^N 2\pi \left[\left(R_a - \frac{d_w}{2} \right) - (i-1)(d_w + s_w) \right]. \quad (2.45)$$

The factor $F_r(f)$ in (2.43) models the frequency dependent skin-effect in a round solid conductor and is given in [59] by

$$F_r(f) = \frac{\chi}{4\sqrt{2}} \left[\frac{\text{ber}_0(\chi)\text{bei}_1(\chi) - \text{ber}_0(\chi)\text{ber}_1(\chi)}{\text{ber}_1(\chi)^2 + \text{bei}_1(\chi)^2} - \frac{\text{bei}_0(\chi)\text{ber}_1(\chi) + \text{bei}_0(\chi)\text{bei}_1(\chi)}{\text{ber}_1(\chi)^2 + \text{bei}_1(\chi)^2} \right], \quad (2.46)$$

with

$$\chi = \frac{d_i}{\delta\sqrt{2}} \quad \text{and} \quad \delta = \frac{1}{\sqrt{\pi\mu_0\sigma_{\text{Cu}}f}}, \quad (2.47)$$

where δ denotes the skin depth, i.e. the average penetration depth of the current in the conductor at the operating frequency f . $\text{ber}_n(x)$ and $\text{bei}_n(x)$ are the real and the imaginary part of the n^{th} -order Bessel function of the first kind and are commonly known as *Kelvin functions* [59].

As it is further explained in [59], in case of litz-wire, the proximity-effect losses can be divided into *internal* and *external* proximity-effect losses. The internal proximity-effect losses are caused by the magnetic field that is generated by the current in the strands within the litz-wire. Whereas the external proximity-effect losses arise from a magnetic field generated by the current in a neighbouring wire, such as a neighbouring turn of the coil winding. The internal proximity-effect losses and the associated part of the total AC resistance can be calculated easily according to [59] as

$$R_{\text{prox,int}} = n_i R'_{\text{DC}} G_r(f) \frac{l_w}{\pi^2 d_w^2}. \quad (2.48)$$

Similar to $F_r(f)$, the factor $G_r(f)$ models the frequency dependency of the proximity-effect, and is given by

$$G_r(f) = -\frac{\chi\pi^2 d_i^2}{2\sqrt{2}} \left[\frac{\text{ber}_2(\chi)\text{ber}_1(\chi) + \text{ber}_2(\chi)\text{bei}_1(\chi)}{\text{ber}_0(\chi)^2 + \text{bei}_0(\chi)^2} + \frac{\text{bei}_2(\chi)\text{bei}_1(\chi) - \text{bei}_2(\chi)\text{ber}_1(\chi)}{\text{ber}_0(\chi)^2 + \text{bei}_0(\chi)^2} \right]. \quad (2.49)$$

In order to calculate the power loss which is due to the external proximity-effect, the external magnetic field must be determined within each conductor, and depending on the winding arrangement and the magnetic properties of the surrounding materials, this can be difficult and may have to be solved by means of a Finite Element (FE) simulation. In this case however, for circular coils in air (or in any other non-magnetic medium such as the human tissue), each turn can be modeled as a current loop, carrying a sinusoidal current with a peak value \hat{I}_0 and with frequency f , that causes a magnetic field surrounding the current loop. For the single loop shown in **Fig. 2.11**, the non-zero magnetic field vector components in cylindrical coordinates can be calculated at

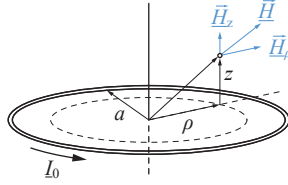


Fig. 2.11: Calculation of the off-axis magnetic field of a single circular current loop.

any point in space according to [62] as

$$\begin{cases} \hat{H}_z(\rho, z) = \frac{I_0}{2\pi\sqrt{Q}} \left[\frac{(a^2 - \rho^2 - z^2)}{Q} \frac{E(q)}{1 - q^2} + K(q) \right] \cdot \vec{e}_z \\ \hat{H}_\rho(\rho, z) = \frac{I_0 z}{2\pi\rho\sqrt{Q}} \left[\frac{(a^2 + \rho^2 + z^2)}{Q} \frac{E(q)}{1 - q^2} - K(q) \right] \cdot \vec{e}_\rho \end{cases}, \quad (2.50)$$

with

$$q = \left(\frac{4a\rho}{z^2 + (a + \rho)^2} \right)^{\frac{1}{2}} \quad \text{and} \quad Q = (a + \rho)^2 + z^2. \quad (2.51)$$

\vec{e}_z and \vec{e}_ρ are the unit vectors of the cylindrical coordinate system and $K(q)$ and $E(q)$ denote the complete elliptic integrals of the first and the second kind, respectively, and are given by

$$K(q) = \int_0^{\frac{\pi}{2}} \frac{d\vartheta}{\sqrt{1 - q^2 \sin^2(\vartheta)}} = \frac{\pi}{2} \sum_{n=0}^{\infty} \left(\frac{(2n)!}{2^{2n} (n!)^2} \right)^2 q^{2n} \quad (2.52)$$

$$E(q) = \int_0^{\frac{\pi}{2}} \sqrt{1 - q^2 \sin^2(\vartheta)} d\vartheta = \frac{\pi}{2} \sum_{n=0}^{\infty} \left(\frac{(2n)!}{2^{2n} (n!)^2} \right)^2 \frac{q^{2n}}{1 - 2n}, \quad (2.53)$$

which must be evaluated numerically. A comprehensive derivation of (2.50) is given in [63].

Each turn of the two IPT coils generates a magnetic field strength vector in each of the other turns, which can be calculated according to (2.50). Accordingly, the total magnetic field strength in a particular turn is then obtained by the superposition of the magnetic field vectors caused by all the other turns in the coil arrangement, including the turns of the opposite TET coil. In order to simplify the calculation of the external proximity-effect losses, the total magnetic field strength is evaluated in the center of each turn in the coil winding and it is

assumed that the magnetic field strength is homogeneous within the cross-section of each turn. Hence, the magnitude of the total magnetic field strength in the center of the i -th turn of the coil winding at the location (ρ_i, z_i) is then obtained with

$$\hat{H}_i = \sqrt{|\hat{H}_{z,\text{tot}}(\rho_i, z_i)|^2 + |\hat{H}_{\rho,\text{tot}}(\rho_i, z_i)|^2}, \quad (2.54)$$

where $\hat{H}_{z,\text{tot}}$ and $\hat{H}_{\rho,\text{tot}}$ denote the sum of the peak magnetic field strength components in z - and ρ -direction, caused by all other turns in the coil winding arrangement.

The total AC resistance due to the external proximity-effect can then be calculated with [59]

$$R_{\text{prox,ext}} = 2n_i R'_{\text{DC}} G_r(f) \sum_{i=1}^N \left[2\pi \left(\left(R_a - \frac{d_w}{2} \right) - (i-1)(d_w + s_w) \right) \frac{\hat{H}_i^2}{|\hat{\underline{L}}_0|^2} \right]. \quad (2.55)$$

The total AC resistance of the coil at the operating frequency f is then given by the sum of each AC resistance component and the total power loss in the IPT coil is calculated according to

$$P_{\text{v,coil}} = \frac{|\hat{\underline{L}}_0|^2}{2} (R_{\text{skin}} + R_{\text{prox,int}} + R_{\text{prox,ext}}) = \frac{|\hat{\underline{L}}_0|^2}{2} R_{\text{ac,tot}}. \quad (2.56)$$

It is important to note that the magnetic field used in (2.55) must be recalculated for each coil winding if either the coil currents or the geometric coil arrangement changes.

In order to validate the power loss modeling of the IPT coils, the calculations are compared to a FE-simulation and to measurements of the AC resistance of one of the two identical TET coil prototypes presented in **Section 2.4.1**. The FE-simulation is carried out using FEMM, which is a FE software that allows to solve low-frequency electromagnetic problems on two-dimensional planar and axis-symmetric domains [64]. **Fig. 2.12(a)** shows the verification of the analytically calculated magnetic field strength amplitude along the radius of the TET coil and in particular in the center of each turn of the coil winding. **Fig. 2.12(b)** shows the magnetic field distribution in the cross-section of the coil winding. As it is expected for the air-core coils, **Fig. 2.12(a)** confirms the high accuracy of the magnetic field strength calculation using the analytic model.

Fig. 2.12(b) shows the comparison of the AC resistance measurement of the TET coil prototype with the results obtained from the

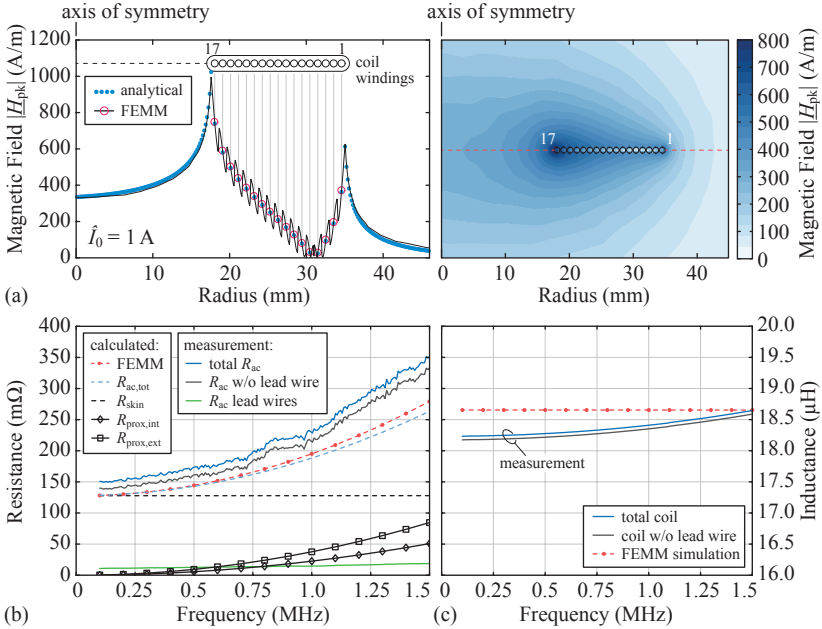


Fig. 2.12: (a) FE-simulation of the peak magnetic field strength along the coil radius and verification of the analytic calculation. (b) Measurement of the AC resistance of one of the two identical TET coil prototypes presented in **Section 2.4.1** and verification of the analytic calculation. (c) Measured and calculated inductance of the prototype TET coil.

FE-simulation and the analytical model. The measurements are performed using the Agilent 4294A precision impedance analyzer [65], and since the AC resistance calculation considers the coil only, the resistance of the lead wires is measured separately and is subtracted from the total coil resistance measurement. The AC resistance obtained from the FE-simulations matches the resistance calculation with good accuracy. However, the measured AC resistance is larger than the predicted values and for frequencies above 1 MHz, the measured resistance increases at a higher rate compared to the calculated values. The discrepancy between the measured and the calculated resistance value is most likely due to imperfect twisting of the top-level bundles of the litz-wire, as explained in detail in [61].

The self-inductance of the TET coil prototype is calculated based

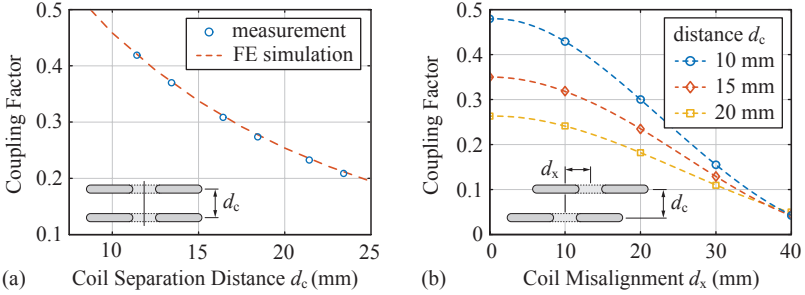


Fig. 2.13: (a) Measured and simulated values of the coil coupling factor at variable coil separation distance d_c and perfect axial alignment. (b) Measurement of the coupling factor with variable axial coil misalignment at different coil separation distances.

on the FE-simulation result for the magnetic flux linkage and is in good agreement with the measured inductance value, shown in **Fig. 2.12(c)**. The coupling factor for the two identical TET coil prototypes was measured for a variable coil separation distance d_c and perfect axial alignment, i.e. $d_x = 0$, which matches the FE-simulation with high accuracy, as it is shown in **Fig. 2.13(a)**. The coupling factor varies over a wide range and decreases rapidly with increasing coil separation distance, and hence limits the power transfer capability and the energy transfer efficiency at large coil separation distances. The influence of the living tissue on the coil coupling factor can be neglected since the magnetic field distribution is barely disturbed by the tissue, which is due to its low electrical conductivity [66] and its relative permeability of one.

In a second measurement, shown in **Fig. 2.13(b)**, the coupling factor was determined with respect to variable axial coil misalignment and fixed coil separation distance. Again, the coupling factor decreases significantly with increased axial misalignment, which could be caused mainly by the movements of the patient.

This section concludes the theoretical introduction into the design, the operation and the modeling of IPT resonant circuit topologies. In the following, different IPT systems are compared regarding several performance metrics, such as the energy transfer efficiency and the heating of the human tissue, and in the course of the analysis, the most suitable IPT system topology for the application at hand is identified.

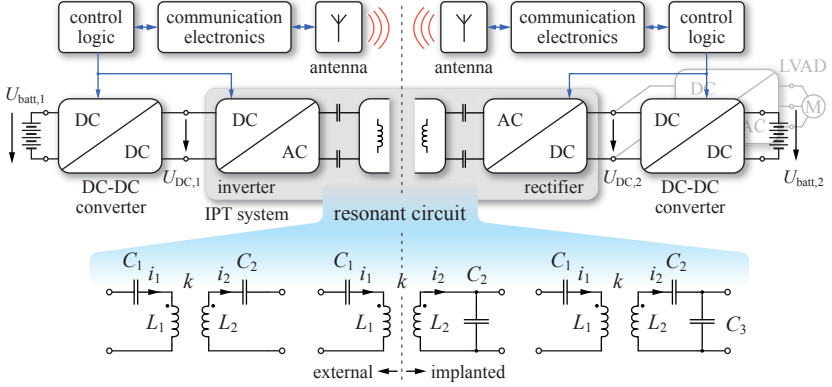


Fig. 2.14: Schematic concept of a fully implantable MCS system and different suitable IPT resonant circuit topologies.

2.2 IPT Topology Comparison

In this section, three commonly used IPT resonant circuit topologies, such as the series-series (SS), the series-parallel (SP) and the series-series-parallel (SSP) compensated IPT topology (cf. **Fig. 2.14**) are compared regarding the power transfer efficiency, the secondary-side coil peak voltage and regarding the thermal limitation due to the heating of the tissue. As explained in the previous section for the series-series IPT circuit topology, it is distinguished between the operation at the resonance frequency (referred to as SSR-compensation) and the operation above resonance near the frequency for load-independent voltage gain, which is referred to as SSU-compensation. In this case, only the primary-side series-compensated IPT resonant circuit topologies are considered, which is due to the employed class-D inverter on the primary side that acts as a voltage source. Primary-side parallel compensated IPT circuit topologies require a current driven inverter, such as the current-fed push-pull inverter, which is used for the parallel-parallel compensated IPT topology presented in [36].

2.2.1 IPT System Design

The evaluation of the performance of each considered IPT resonant circuit topology is based on the power loss modeling of the primary-side

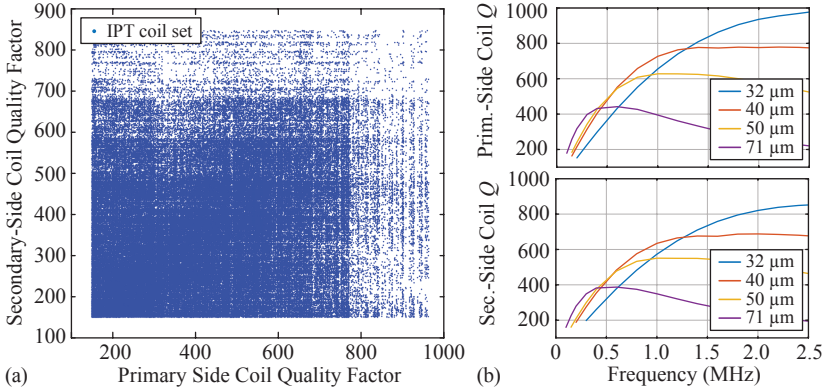


Fig. 2.15: (a) Calculated primary-side and secondary-side coil quality factors of the numerically generated coil sets. (b) Maximum realized quality factors for the primary-side and secondary-side coil with respect to the operating frequency range and variable strand diameter.

and secondary-side energy transfer coils. In order to provide a fair comparison, the operating conditions, i.e. the coil separation distance, the output power and the operating frequency are equal for each topology.

In order to evaluate a large number of possible IPT system designs, a vast number of feasible IPT coil sets is generated in a numerical simulation. As described in the previous section, the coupling factor and the self-inductances of the IPT coils is obtained with an FE-simulation and the AC resistance is calculated for each coil as described in **Section 2.1.5**. The range and the designation of the design parameters, used for the coil set generation, are given in **Fig. 2.10(b)**. For the primary-side IPT coil, an overall diameter of up to 80 mm is allowed and for the secondary-side coil, the maximum outside diameter is limited to 70 mm. The minimum inside diameter of each coil is specified with 10 mm. The maximum coil coupling factor is evaluated for a minimum coil separation distance of $d_{c,\min} = 10$ mm and perfect axial alignment. For both coils, a single layer litz-wire winding is considered, using commercially available litz-wires with strand diameters ranging from 32 μm to 71 μm and with a number of strands in a range of 200 to 320. Accordingly, the overall litz-wire diameter is in a range of 0.74-1.88 mm.

Fig. 2.15(a) shows the achieved primary-side and secondary-side

coil quality factors for each IPT coil set. The coil sets with quality factors below 150 are discarded for the further simulation. **Fig. 2.15(b)** shows the maximum realized primary-side and secondary-side coil quality factors for the different litz-wire strand diameters, with respect to the operating frequency. As expected, the coil quality factors increase with increasing frequency and decreasing strand diameter. However, for each strand diameter there is an optimum operating frequency range. On the primary side, higher quality factors can be achieved because of the larger feasible coil diameter compared to the maximum secondary-side coil diameter, which allows for larger coil inductance values.

In the next step, an IPT system is designed numerically for each coil set and for each of the three considered circuit topologies at various operating frequencies in the specified frequency range. Hence, a vast number of IPT system designs is generated and each resonant circuit is designed for maximum energy transfer efficiency at a maximum output power of $P_{2,\max} = 30 \text{ W}$ and a minimum coil separation distance of $d_{c,\min} = 10 \text{ mm}$.

The design equations for the SSR, SSU and the SP circuit topology are already provided in the previous sections. Similarly, the design equations can be derived for the SSP resonant circuit topology and a summary of the design equations for each IPT topology is given in **Tab. 2.1**. The derivation of the equations for the optimal load factor and the energy transfer efficiency of each considered IPT resonant circuit topology is provided in **Appendix A**.

As explained in **Section 2.1.2**, the maximum energy transfer efficiency is achieved, if the reactive power in the resonant circuit is minimized at the specific operating point. For equal and large coil quality factors, i.e. for $Q_1 = Q_2 > 100$, the equation for the optimal load factor γ_{opt} can be simplified and a simple equation for the optimal equivalent AC load resistance $R_{L,\text{eq,opt}}$ can be found for each IPT system topology, as shown in **Tab. 2.1**.

It is important to note that in the numerical simulation, the IPT systems are designed using this approximation despite the large variation of coil quality factors shown in **Fig. 2.15(a)**, i.e. the approximation is applied also to designs with small and unequal primary-side and secondary-side coil quality factors, and has therefore only limited validity for these specific coil set designs. Nevertheless, the approximation allows for the derivation of meaningful design equations and simplified calculations. Furthermore, in order to achieve a high energy transfer

IPT topology	SSR compensation	SSU compensation
Compensation capacitors	$C_1 = \frac{1}{\omega_0^2 L_1}$ $C_2 = \frac{1}{\omega_0^2 L_2}$	$C_1 = \frac{1}{\omega_0^2 L_1 (1 - k_0)}$ $C_2 = \frac{1}{\omega_0^2 L_2 (1 - k_0)}$
Optimal load factor $\gamma_{\text{opt}} = R_{L,\text{eq}} / (\omega_0 L_2)$	$\frac{1}{Q_2} \sqrt{1 + k^2 Q_1 Q_2}$	$\frac{1}{Q_2} \sqrt{1 + k^2 Q_1 Q_2 + (k_0 Q_2)^2}$
Optimal AC load resistance $R_{L,\text{eq,opt}}^{1)}$	$\omega_0 L_2 k$	$\omega_0 L_2 \sqrt{k^2 + k_0^2}$
Design coupling factor $k_d^{2)}$	$k_d = k_{\text{max}}$	$k_d = k_0 = \frac{k_{\text{max}}}{\sqrt{3}}$

IPT topology	SP compensation	SSP compensation
Compensation capacitors	$C_1 = \frac{1}{\omega_0^2 L_1 (1 - k_0^2)}$ $C_2 = \frac{1}{\omega_0^2 L_2}$	$C_1 = \frac{1}{\omega_0^2 L_1 (1 - k_0)} \quad C_3 = \frac{1}{\omega_0^2 L_2 k_0}$ $C_2 = \frac{1}{\omega_0^2 L_2 (1 - k_0)}$
Optimal load factor $\gamma_{\text{opt}} = R_{L,\text{eq}} / (\omega_0 L_2)$	$\sqrt{\frac{1 + k^2 Q_1 Q_2 + Q_2^2}{1 + k^2 Q_1 Q_2}}$	$k_0 \sqrt{\frac{1 + k^2 Q_1 Q_2 + (k_0 Q_2)^2}{1 + k^2 Q_1 Q_2}}$
Optimal AC load resistance $R_{L,\text{eq,opt}}^{1)}$	$\omega_0 L_2 \frac{1}{k} \sqrt{1 + k^2}$	$\omega_0 L_2 k_0 \sqrt{\frac{k^2 + k_0^2}{k^2}}$
Design coupling factor $k_d^{2)}$	$k_d = k_0 = k_{\text{max}}$	$k_d = k_0 = k_{\text{max}}$

1) valid for $Q_1 = Q_2 > 100$

2) the system is designed for $k = k_d$, $P_2 = P_{2,\text{max}}$ and $\omega_0 = 2\pi f_0$

Tab. 2.1: Design equations for the series-series, the series-parallel and the series-series-parallel compensated IPT resonant circuit topology.

efficiency, the main objective is to increase both the primary and the secondary-side coil quality factor simultaneously, and coil pairs with low primary-side and/or secondary-side coil quality factors are unattractive in any case because of the limited performance.

Each of the IPT resonant circuits is designed using the equations in **Tab. 2.1** for the specified design coupling factor k_d , the maximum output power $P_{2,\text{max}}$ and the operating frequency $\omega_0 = 2\pi f_0$. Accordingly, at maximum output power and at the minimum coil separation distance, i.e. at the maximum coil coupling factor, the input impedance Z_{in} of each IPT resonant circuit topology is purely resistive. With this design methodology, it is guaranteed that the input impedance of each

IPT resonant circuit remains resistive/inductive, i.e. the phase angle of the input impedance $\varphi_{Z,\text{in}}$ is equal to or larger than zero when $k < k_{\text{max}}$ and/or $P_2 < P_{2,\text{max}}$ applies. A positive phase angle of the input impedance is a requirement to avoid hard-switching of the primary-side class-D inverter stage. Except for the SSU-compensation, the design coupling factor corresponds to the coil coupling factor at the considered operating point, i.e. at the maximum achievable coupling factor k_{max} , which is given by the geometric limitations of the coil arrangement for the application at hand (e.g. the minimum feasible coil separation distance at perfect axial alignment of the coils).

Figs. 2.16(a)-(d) show the voltage gain $G_v(\text{dB}) = 20 \log_{10} (|u_2/u_1|)$ and phase angle of the input impedance $\varphi_{Z,\text{in}}$ as an example for each IPT system topology, designed according to the equations provided in **Tab. 2.1**. In **Fig. 2.16**, the primary-side inductance is chosen such that the voltage gain is unity for each circuit topology at the maximum output power and the maximum coil coupling factor.

ZVS operation of the inverter switches requires an inductive behaviour of the input impedance. Hence, as illustrated in **Figs. 2.16(a)** and **(b)**, in a practical realization, the SSR and SSU system must be operated at a frequency which is slightly higher than the nominal operating frequency f_0 , in order to achieve ZVS operation at the maximum output power and maximum coil coupling factor. In contrast, the SP and SSP systems must be operated at a slightly lower operating frequency in order to achieve the same objective.

The optimal secondary-side DC-link voltage $U_{\text{DC},2}$ can be calculated using the equation for the optimal AC load resistance at the operating point and the rectifier load models for the secondary-side series and parallel compensated IPT resonant circuit topologies, as explained in **Section 2.1.3**. Consequently, the primary-side and secondary-side coil peak currents \hat{I}_1 and \hat{I}_2 can be calculated. It is important to note, that in case of the secondary-side parallel compensated IPT systems, the optimal output voltage and the secondary-side compensation capacitance must be calculated iteratively, such that the equivalent load resistance $R_{L,\text{eq,p}}$ and the equivalent parallel capacitance $C_{L,\text{eq,p}}$ match the optimal values calculated with the design equations from **Tab. 2.1**.

In a next step, the power loss in the IPT coils is calculated according to model provided in **Section 2.1.5**. In this case, the calculated AC resistances of the coils are increased by 15 %, in order account for lead wires and for the potential twisting imperfections of off-the-shelf litz-

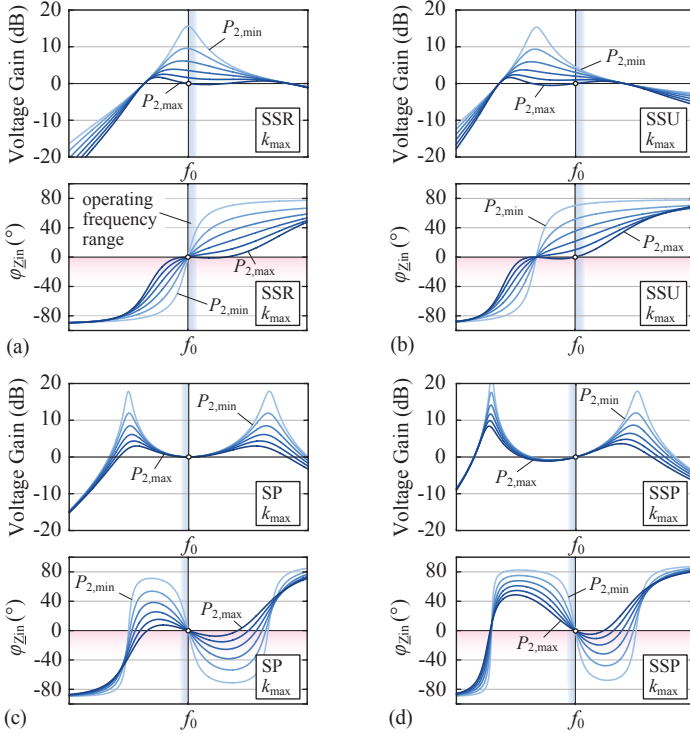


Fig. 2.16: (a)-(d) Calculated voltage gain $G_v(\text{dB}) = 20 \log_{10}(|u_2/u_1|)$ and phase angle of the input impedance $\varphi_{Z_{in}}$ of the series-series (SSR, SSU), the series-parallel (SP) and the series-series-parallel (SSP) compensated IPT circuit topology for variable output power, maximum coil coupling factor and constant output voltage, designed according to the equations provided in **Tab. 2.1**.

wires. In a next step, the thermal model presented later in **Chapter 3** is used to estimate the temperature of the human tissue surrounding the implanted IPT coil.

The power losses caused within the compensation capacitors are estimated with

$$P_{v,C} = \frac{\tan(\delta)}{\omega_0 C} I_{C,RMS}^2, \quad (2.57)$$

assuming high quality class-1 NP0/C0G ceramic capacitors and a dissipation factor of $\tan(\delta) = 0.0005$. In this case, only the power losses of

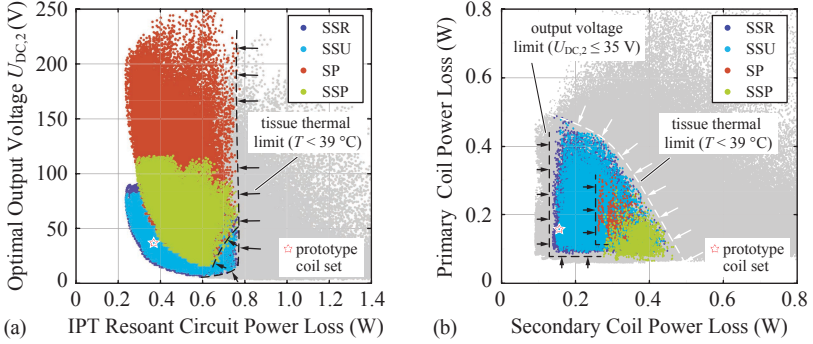


Fig. 2.17: Performance comparison of the considered IPT resonant circuit topologies at maximum power transfer and maximum coil coupling factor, including the indicated IPT coil set prototype (cf. **Section 2.4**) with the specifications given in **Tab. 2.2**. (a) Calculated optimal IPT system output voltage with respect to the total resonant circuit power loss. (b) Calculated primary-side and secondary-side coil power losses, when the IPT system output voltage limit is set to 35 V.

the resonant circuits are of interest and the power losses of the rectifier circuit are neglected. The results of the comparative evaluation of the considered IPT circuit topologies are presented in the following.

2.2.2 Topology Comparison Results

Fig. 2.17(a) shows the optimal output voltage $U_{DC,2}$ for each IPT system design with respect to the total IPT resonant circuit power loss, which includes the power loss of the primary-side and secondary-side coil and the compensation capacitances. The SSR and the SSU IPT systems achieve almost the same energy transmission efficiency, but as shown in **Section 2.1.1**, the SSR system suffers from large voltage gain variations if the coil coupling and/or the load is changed. However, as it is shown in [43], the highest energy transmission efficiency can be achieved with the SSR-compensation in the entire load and coupling factor range, when an increased control effort is feasible, i.e. when the primary-side and secondary-side DC-link voltages $U_{DC,1}$ and $U_{DC,2}$ are adjusted simultaneously in order to operate the resonant circuit always with the optimal equivalent load resistance. The SSU-compensation offers similar high energy transfer efficiency at maximum output power

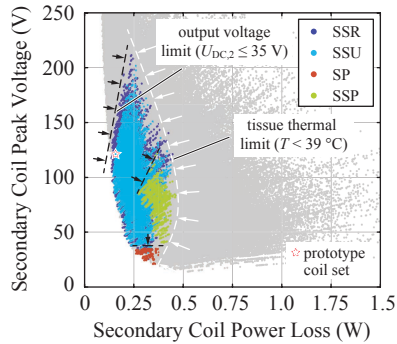


Fig. 2.18: (c) Calculated secondary-side coil peak voltage with respect to the secondary-side coil power loss, when the IPT system output voltage limit is set to 35 V.

and minimum coil separation distance, and achieves a high secondary-side efficiency in the entire range of operation and shows only moderate voltage gain variations.

The SP system can achieve the same performance as the series-series compensated systems, but at much higher output voltages exceeding 100 V, which is not feasible for the application at hand. At an output voltage below 40 V, the series-series compensated system clearly outperforms the secondary-side parallel compensated systems. As it was shown in [46], by allowing for a higher output voltage, it is possible to use coil designs with a much higher FOM than it would be the case at an output voltage equal to the implanted backup battery terminal voltage of 14.8 V. This is because the optimal AC load resistance, and hence also the optimal output voltage at a given output power, is proportional to the operating frequency, the secondary-side coil inductance and the coil coupling factor. Accordingly, considering single-layered IPT coils, a large coil diameter allows for larger inductance values and a higher coil coupling factor at a given coil separation distance. In conjunction with a high operating frequency, the quality factor is increased as shown in **Fig. 2.15(b)** and hence, a coil set with higher FOM can be used.

Considering the thermal limit indicated in **Fig. 2.17(a)**, it can be concluded that considering all resonant circuit topologies without output voltage limitation and a coil separation distance of 10 mm, a maximum total resonant circuit power loss of approximately 750 mW is

acceptable for the IPT resonant circuit, which corresponds to an efficiency of 97.6% at maximum output power. Note that the results given in **Fig. 2.17(a)** include the power losses of the resonant capacitors as well. Hence, the total permitted power loss in the energy transfer coils is slightly lower than 750 mW, as shown in **Fig. 2.17(b)**. In this case, the output voltage $U_{DC,2}$ limit is set to 35 V. A higher DC-link voltage beyond 40 V seems not advantageous, which is due to the increased secondary-side peak coil voltage and the increased switching losses in the subsequent hard-switched DC-DC converter stages, e.g. such as the battery charging converter. Hence, as shown in **Fig. 2.17(b)**, the series-series compensated IPT topology achieves a lower power loss in the secondary-side coil compared to the secondary-side parallel compensated IPT topologies and only few feasible designs remain for the SP and SSP system.

It is evident from **Fig. 2.18**, that the superior performance of the series-series compensated IPT topology comes at the expense of a much higher secondary-side coil voltage, when compared to the SP system, which limits the number of feasible designs and raises questions about the patient safety regarding the exposure to the electromagnetic field in the vicinity of the energy transfer coils, which is the topic of **Chapter 4**.

In summary, the comparison shows that the secondary-side series compensated IPT topology outperforms the parallel compensated resonant circuits at the power transfer level at hand. In addition, due to the continuous sinusoidal secondary-side current of the series-series compensated resonant circuit, a highly efficient synchronous rectifier circuit can be realized with little effort as presented in **Section 2.5**, which allows for high operating frequencies up to the MHz range [46]. Moreover, the secondary-side parallel compensated systems suffer even at low output power from high reactive power circulating in the secondary-side resonant circuit, which limits the secondary-side IPT system efficiency at partial load operation.

In the following, the focus is therefore on the series-series compensated IPT resonant circuit topology, i.e. the SSR-compensation and SSU-compensation. In a next step, a more detailed power loss model is introduced, which allows to estimate the overall power loss for both the SSU- and the SSR-compensated IPT system, including the inverter and the rectifier stage. A prototype IPT system is then realized, which is used to validate the power loss model and to verify the estimated energy transfer efficiency.

2.3 IPT System Power Loss Modeling

The simplified equivalent IPT circuit model is particularly useful for the design of the resonant tank, but a more detailed model was developed in [46] in order to accurately estimate the power losses of a practical realization of the IPT system, where parasitic components cannot be neglected. In addition, the detailed analysis of the inverter and the rectifier circuit operation allows for a better understanding of the impact of component parasitics on the IPT system operation. The power loss model in [46], which is presented in the following, further allows to investigate the power loss distribution within the IPT system, which is difficult to measure, but which is the basis for further optimizations.

2.3.1 Extended Load Model

In **Section 2.1.3**, a simple equivalent load model was introduced for the series-series compensated IPT topology, which is valid for purely sinusoidal secondary-side coil current and for an ideal operation of the full-wave rectifier circuit. However, in [45] it was observed that the time delay that it takes for the current commutation in the actual rectifier circuit cannot be neglected. This time delay arises, because at each current zero crossing, the parasitic capacitance of the diodes must be either charged or discharged, in order to commutate the current to the active branch of the rectifier circuit. During this time interval, there is no net energy supplied to the output of the rectifier which leads to a phase-shift between the secondary-side current i_2 and the fundamental of the rectifier input voltage $u_{2,(1)}$. This is particularly important if the system is operated at high switching frequencies, as it is the case for the TET system prototype. Furthermore, diodes - or active switches in case of a synchronous rectification - with low series resistivity have a large chip area, which further increases parasitic capacitance of the devices.

Therefore, in order to allow for an accurate calculation of the primary-side and secondary-side coil currents, the simplified equivalent load model given in (2.24) is extended to account for the rectifiers' parasitic capacitances.

Since the parasitic diode capacitances act as an equivalent capacitor connected in parallel to the input of an ideal full-wave diode rectifier, the equivalent load can be modeled similar to the load modelling presented in **Section 2.1.3** for the series-parallel compensated IPT topology.

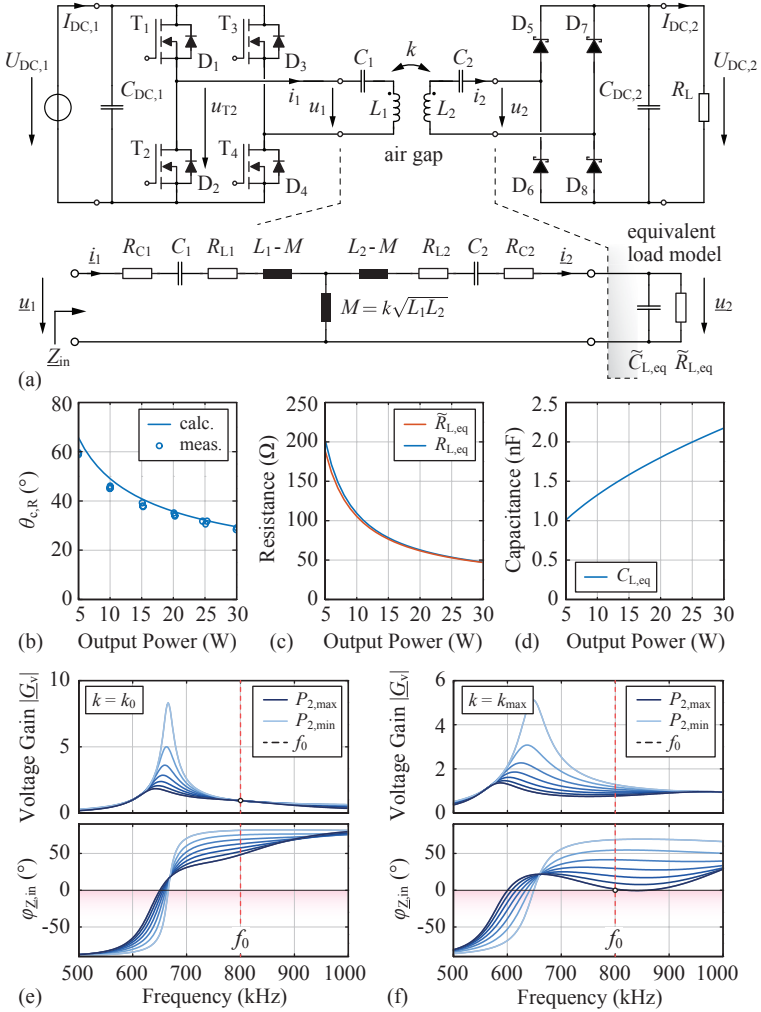


Fig. 2.19: (a) Detailed equivalent circuit of the series-series compensated IPT resonant circuit and the extended load modeling. (b) Measured and calculated rectifier input voltage transition time interval, expressed as phase angle $\theta_{c,R}$ (cf. **Fig. 2.20(a)**). (c)-(d) Calculated values of the equivalent load capacitance and resistance for the diode rectifier of the prototype IPT system presented in **Section 2.4**. (e)-(f) Voltage transfer characteristics and the phase angle of the input impedance of the IPT system prototype using the extended load model.

Accordingly, the equivalent load is modeled as a capacitor in parallel with a resistor [56] as illustrated in **Fig. 2.19(a)**. In order to obtain the equivalent load capacitance $\hat{C}_{L,\text{eq}}$, it is necessary to calculate the first harmonic $u_{2,(1)}$ of the rectifier input voltage, which requires the knowledge of the duration of the charging interval of the parasitic capacitances of the rectifier diodes, which is denoted by the angle $\theta_{c,R}$. The measured voltage and current waveforms of a switching transition of the synchronous rectifier, which is presented in **Section 2.5**, is shown in **Fig. 2.20(a)** (which are qualitatively equivalent to the waveforms of the diode rectifier at the secondary-side current zero crossing). During the time interval $\theta_{c,R}$ the net power flow to the output of the rectifier is zero while the parasitic capacitances of the rectifier diodes are charged or discharged by the current i_2 , which delivers the total charge ΔQ_1 . As indicated in **Fig. 2.20(b)**, the current i_2 is conducted through the upper and lower branch of the rectifier circuit simultaneously, connecting the parasitic capacitances $C_{p,D5}$ and $C_{p,D6}$ in parallel, which are additionally connected in series with the parallel connected capacitances $C_{p,D7}$ and $C_{p,D8}$. The non-linear parasitic diode capacitance of the diodes used for the IPT system prototype and the total parasitic capacitance $C_{p,\text{tot}}$, which is observed at the input of the rectifier circuit are shown in **Fig. 2.20(c)**. The (linear) charge-equivalent capacitance $C_{Q,\text{eq}}$ [67], given by

$$C_{Q,\text{eq}}(V) = \frac{1}{V} \int_0^V C_{p,\text{tot}}(v) dv, \quad (2.58)$$

is used to obtain the time interval $\theta_{c,R}$, which is given by

$$\begin{aligned} \theta_{c,R} &= \arccos\left(\frac{a_1 - b_1}{a_1 + b_1}\right) \\ a_1 &= (P_2 + P_{v,R})\pi \\ b_1 &= 2U_{\text{DC},2}\omega_0 C_{D,\text{Qeq}} \cdot (U_{\text{DC},2} + u_{\text{DR}}) \end{aligned}, \quad (2.59)$$

where $C_{D,\text{Qeq}}$ is the charge-equivalent capacitance of the total parasitic capacitance $C_{p,\text{tot}}$, evaluated at the voltage $V = (U_{\text{DC},2} + u_{\text{DR}})$, which is equal to the charge-equivalent capacitance of the single parasitic diode capacitance $C_{p,D}$ evaluated at the same voltage, since $C_{p,\text{tot}} = 2C_{p,D} \cdot \frac{1}{2}$. The rectifier diode forward voltage drop u_{DR} is much smaller than the output DC-link voltage $U_{\text{DC},2}$ and can be neglected in most of the cases. The rectifier power losses $P_{v,R}$ can be calculated iteratively in order to achieve the best accuracy. **Fig. 2.19(b)** shows the calculated and the measured charging time interval for the Schottky diode rectifier used in

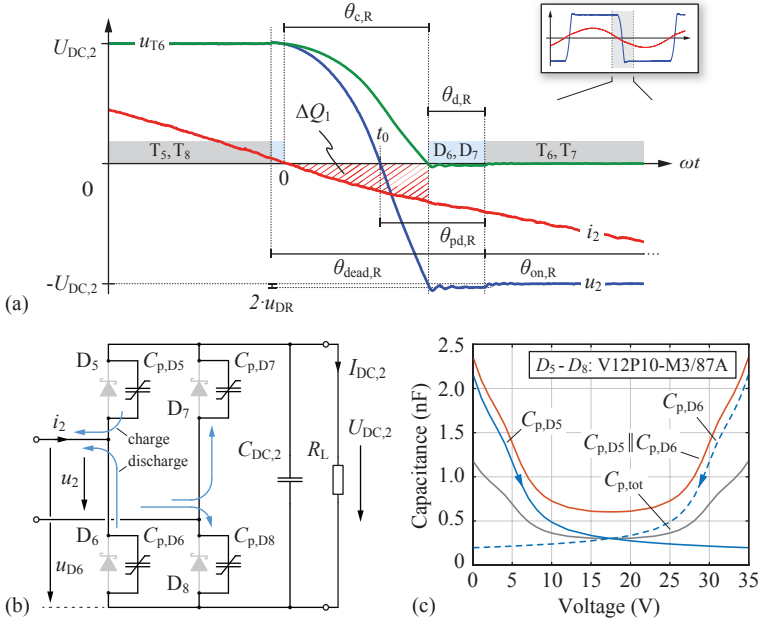


Fig. 2.20: (a) Measured switching waveforms of the synchronous rectifier input voltage and secondary-side coil current, during the current zero crossing time interval, including the labeling of the time intervals and designations used for the power loss modeling. (b) Illustration of the current flow in the diode rectifier during the time interval $\theta_{c,R}$. (c) Non-linear parasitic capacitance of the rectifier diodes used for the hardware prototype and the total parasitic capacitance $C_{p,tot}$, which is observed at the input of the rectifier circuit during the time interval $\theta_{c,R}$.

the prototype system with respect to variable load conditions. Despite the non-linearity of the diode junction capacitance and the assumption of purely sinusoidal currents in the resonant tank, the calculation fits the measurement with good accuracy.

Following the analysis reported in [56], the first harmonic $u_{2,(1)}$ of the rectifier input voltage can be calculated by means of calculating the first harmonic of the current delivering the charge ΔQ_1 which is required to charge and discharge the parasitic diode capacitances at each zero crossing of the current i_2 . The equivalent load resistance and

the equivalent load capacitance are then calculated according to

$$\tilde{R}_{L,\text{eq}} = \frac{a_2^2 + b_2^2}{2\omega_0^2 C_{D,\text{Qeq}}^2 (P_2 + P_{v,\text{R}})} \approx R_{L,\text{eq},\text{s}} \quad (2.60)$$

and

$$\tilde{C}_{L,\text{eq}} = \frac{b_2}{a_2 \omega_0 \tilde{R}_{L,\text{eq}}}, \quad (2.61)$$

using

$$\begin{aligned} \hat{I}_2 &= \frac{2\omega_0 C_{D,\text{Qeq}} (U_{\text{DC},2} + u_{\text{DR}})}{1 - \cos(\theta_{c,\text{R}})} \\ a_2 &= \frac{\hat{I}_2}{\pi} \sin^2(\theta_{c,\text{R}}) \\ b_2 &= \frac{\hat{I}_2}{\pi} \left[\theta_{c,\text{R}} - \frac{1}{2} \sin(2\theta_{c,\text{R}}) \right]. \end{aligned} \quad (2.62)$$

The calculated values of the extended load model are shown in **Figs. 2.19(c)** and **(d)** for the IPT system prototype. It can be observed in **Fig. 2.19(c)** that the simple equivalent load resistor model $R_{L,\text{eq},\text{s}}$, given in (2.24), is still valid for the design of the resonant circuit topology for maximum energy transfer efficiency and is a good approximation for the derived equivalent load given in (2.60). Nevertheless, the equivalent load capacitance given in (2.61) depends on the operating frequency as expected, but is also highly dependent on the output power, as shown in **Fig. 2.19(d)**, and is in the same order of magnitude as the primary-side and secondary-side compensation capacitances of the IPT system prototype (cf. **Tab. 2.2**).

As a result, the actual IPT resonant circuit transfer characteristics illustrated in **Figs. 2.19(e)** and **(f)** indicate the behaviour of a series-series-parallel compensated system. However, the load dependency of the phase angle of the input impedance does not change significantly at the operating frequency f_0 , which justifies the use of the simple load model given in **Section 2.1.3** for designing the IPT resonant circuit.

As a conclusion, the extended load model for the series-series compensated IPT system allows for an accurate calculation of the primary-side and secondary-side coil currents and hence allows to predict the coil power loss with higher accuracy.

2.3.2 Diode Rectifier Losses

Using the equations (2.59) and (2.62), the power loss of the full-wave diode rectifier can be calculated with

$$P_{v,\text{R}} = 2 \cdot \left(\frac{P_2}{U_{\text{DC},2}} u_{\text{DR},0} + I_{2,\text{RMS}}^2 r_{\text{DR},0} \right) \quad (2.63)$$

and

$$I_{2,\text{RMS}}^2 = \frac{\hat{I}_2^2}{2\pi} \cdot \left(\frac{1}{2} \sin(2\theta_{c,\text{R}}) - \theta_{c,\text{R}} + \pi \right), \quad (2.64)$$

using a simple rectifier diode model with the equivalent zero current diode forward voltage drop of $u_{\text{DR},0}$ in series with the diode's differential resistance $r_{\text{DR},0}$ evaluated at the average output current $I_{\text{DC},2}$.

2.3.3 Resonant Circuit Power Loss

The equivalent circuit of the IPT resonant circuit shown in **Fig. 2.19(a)** is used for the calculation of the primary-side coil current i_1 and the phase angle of the input impedance $\varphi_{\underline{Z},\text{in}}$. The parasitic resistances $R_{\text{L}1}$ and $R_{\text{L}2}$ of the energy transmission coils can be measured at the operating frequency or calculated using the analytical power loss model presented in **Section 2.1.5**. Assuming purely sinusoidal primary-side and secondary-side coil currents i_1 and i_2 , the total resonant circuit power losses are obtained with

$$P_{\text{v,ipt}} = \frac{\hat{I}_1^2}{2} (R_{\text{L}1} + R_{\text{C}1}) + \frac{\hat{I}_2^2}{2} (R_{\text{L}2} + R_{\text{C}2}). \quad (2.65)$$

The ESR $R_{\text{C}1}$ and $R_{\text{C}2}$ of the compensation capacitors are negligible in most of the cases where multiple high quality ceramic capacitors are used in parallel to build up the required compensation capacitance.

2.3.4 Inverter Losses

There are basically four loss mechanisms associated with the operation of the inverter circuit shown in **Fig. 2.19(a)**. These are the losses caused by the gate driver, the ON-state and the body diode conduction losses, as well as the switching losses. The occurrence of the last three loss mechanisms depends highly on the input impedance $\underline{Z}_{\text{in}}$ of the resonant circuit seen by the inverter, and therefore, depends also on the load conditions and the coil coupling factor. In order to validate the theoretical results presented in the previous sections, the SSU-compensated IPT system prototype presented in **Section 2.4** was designed such that the phase angle of the input impedance is zero at maximum coil coupling factor and maximum output power. However, a slightly inductive behaviour of the input impedance is needed in order to achieve soft-switching. Therefore, in a final design, depending on the switches used in the inverter circuit, the factor k_0 in (2.31) must be chosen with

some margin, such that the phase angle of the input impedance is large enough at the switching transition, such that the primary-side current i_1 provides sufficient charge to ensure soft-switching.

Regarding the power losses, there exist two distinct operating modes of the inverter. During nominal operation, the inverter is operated with a resistive/inductive load, such that the current i_1 is lagging the inverters' output voltage u_1 . A measurement of the inverter switching waveforms for this particular mode of operation is shown in **Fig. 2.21(a)**. At the time instant where the switches T_1 and T_4 are turned off, the primary-side current i_1 starts to discharge the parasitic output capacitance of the switches T_2 and T_3 , while the capacitances of the switches T_1 and T_4 are charged. In this case, the charge ΔQ_2 (cf. **Fig. 2.21(a)**) is large enough to discharge and charge the capacitances before the end of the dead-time interval denoted with $\theta_{\text{dead,T}}$. As soon as the voltage across the switch T_2 reaches zero, it is clamped by its body diode. Subsequently, the primary-side current i_1 is conducted by the diodes D_2 and D_3 until the switches T_2 and T_3 are turned on at almost zero voltage, which is referred to as ZVS operation. The turn-off process of the switches T_1 and T_4 is lossless as long as the switches are turned off fast enough, such that the gate voltage is below the FETs' threshold voltage before the voltage across the switch increases. Conduction losses are generated during both the body diode conduction interval $\theta_{\text{d,T}}$ and during the ON-time interval of the switch, which is due to the diode forward voltage drop and the ON-state resistance of the switch, respectively.

The switching waveforms of the second operating mode are shown in **Fig. 2.21(b)**. In this case, the charge ΔQ_2 provided by the inverter output current i_1 is not large enough to completely discharge the parasitic output capacitances of the switches T_2 and T_3 before the end of the dead-time interval and the switches are turned on at a finite voltage $U_{\text{s},0}$. In this case, the energy stored in the parasitic output capacitances is dissipated in the switches, which causes additional power losses and is referred to as hard-switching operation.

In order to calculate the total inverter power losses, it is necessary to determine the capacitive charging time interval $\theta_{\text{c,T}}$ and the interval θ_{T} , as well as the input voltage $U_{\text{DC},1}$. Similar to the considerations made in **Section 2.3.1**, it is assumed that the charging of the parasitic output capacitance of the switches is lossless and that no net charge is delivered from the power supply to the output of the inverter during

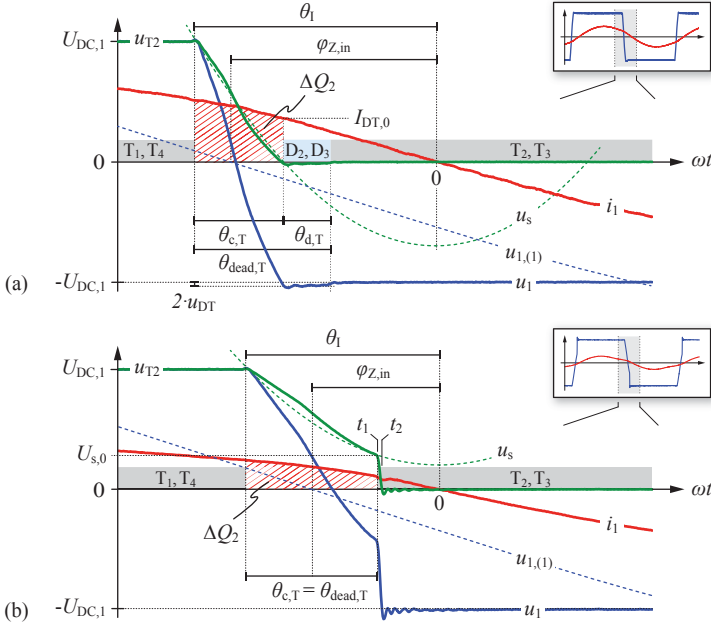


Fig. 2.21: Measured switching waveforms of the inverter output voltage and the primary-side coil current, including the labeling of the time intervals and designations used for the power loss model. In (a), the switching waveforms are given for case of soft-switching operation, and (b) shows the switching waveforms in case of hard-switching.

this time interval. Furthermore, it is assumed that the primary-side current i_1 is purely sinusoidal and that the phase angle of the input impedance $\varphi_{Z,in}$ is the same as the phase angle measured from the zero crossing of the primary-side current i_1 to the zero crossing of the inverter output voltage u_1 . Both assumptions allow to simplify the calculations significantly, but impose limitations to the model, as the two assumptions show only limited validity at high coupling factors and at high output power, where the inverter output current contains distinct higher order harmonic components and the zero crossing of the fundamental voltage component $u_{1,(1)}$ deviates significantly from the zero crossing of the actual inverter output voltage u_1 , i.e. specifically at partial hard-switching.

The input voltage $U_{\text{DC},1}$ can be calculated using the phase angle of the input impedance and the power delivered to the output of the inverter, and is given by

$$U_{\text{DC},1} = \frac{\pi (P_2 + P_{v,\text{tot}})}{2 (\hat{I}_1 \cos(\varphi_{\underline{Z},\text{in}}) + \omega_0 C_{\text{T,Req}} u_{\text{DT}})}, \quad (2.66)$$

where $P_{v,\text{tot}}$ is the total IPT system power loss and must be computed iteratively. The capacitance $C_{\text{T,Req}}$ is the charge equivalent capacitance (cf. (2.58)) of the parasitic output capacitance of the inverter switches, evaluated at the voltage $V = (U_{\text{DC},1} + u_{\text{DT}})$, where $U_{\text{DC},1}$ and the forward voltage drop of the FETs' body diode u_{DT} can be calculated iteratively as well. However, in most of the cases, the value of the term $\omega_0 C_{\text{T,Req}} u_{\text{DT}}$ is very small and can be neglected.

The time intervals $\theta_{c,\text{T}}$ and θ_{I} can be derived, assuming that the charge ΔQ_2 must fully charge and discharge the output capacitances of the corresponding switches within the time interval $\theta_{c,\text{T}}$ and can be expressed with

$$\theta_{\text{I}} = \arccos \left(\cos(\varphi_{\underline{Z},\text{in}}) - \frac{U_{\text{DC},1} \omega_0 C_{\text{T,Req}}}{\hat{I}_1} \right) \quad (2.67)$$

$$\theta_{c,\text{T}} = \theta_{\text{I}} - \arccos \left(\frac{2\omega_0 C_{\text{T,Req}} (U_{\text{DC},1} + u_{\text{DT}})}{\hat{I}_1} + \cos(\theta_{\text{I}}) \right). \quad (2.68)$$

Using (2.67) and (2.68), the power losses during the body diode conduction interval $\theta_{\text{d},\text{T}}$ can be calculated with

$$\begin{aligned} P_{v,\text{I,d1}} &= \frac{2\hat{I}_1 u_{\text{DT},0}}{\pi} (\cos(\theta_{\text{I}} - \theta_{\text{dead},\text{T}}) - \cos(\theta_{\text{I}} - \theta_{c,\text{T}})) \\ P_{v,\text{I,d2}} &= \frac{\hat{I}_1^2 r_{\text{DT},0}}{\pi} \left(\frac{1}{2} \sin(2(\theta_{\text{I}} - \theta_{\text{dead},\text{T}})) \right. \\ &\quad \left. - \frac{1}{2} \sin(2(\theta_{\text{I}} - \theta_{c,\text{T}})) - \theta_{c,\text{T}} + \theta_{\text{dead},\text{T}} \right), \quad (2.69) \\ P_{v,\text{I,d}} &= P_{v,\text{I,d1}} + P_{v,\text{I,d2}} \end{aligned}$$

using the equivalent zero current body diode forward voltage drop $u_{\text{DT},0}$ and the differential resistance $r_{\text{DT},0}$, evaluated at the diode current $I_{\text{DT},0}$ (cf. **Fig. 2.21(a)**).

The conduction losses due to the ON-state resistance $R_{\text{DS,on}}$ of the switches can be calculated using

$$P_{v,\text{I,on}} = \frac{\hat{I}_1^2 R_{\text{DS,on}}}{\pi} \left(\frac{1}{2} \sin(2\theta_{\text{I}}) - \frac{1}{2} \sin(2(\theta_{\text{I}} - \theta_{\text{dead},\text{T}})) - \theta_{\text{dead},\text{T}} + \pi \right). \quad (2.70)$$

The switching losses can be estimated by the evaluation of the energy balance, i.e. the evaluation of the energy that is stored in the inverter circuit at the time t_1 (cf. **Fig. 2.21(b)**), just before the turn-on of the switches T_2 and T_3 , with respect to the energy that is stored after the switching operation at the time t_2 . This approach is described in detail in [67] and will be explained in the following. The energy loss due to the overlapping of the load current and switch voltage at the switching instant is neglected since the switch current is small and the interval is very short.

In order to obtain the stored energies, the (linear) energy-equivalent capacitance of the parasitic output capacitance C_{oss} of the switches is required, which is evaluated at the voltage V , and which can be calculated with [67] as

$$C_{\text{E,eq}}(V) = \frac{2}{V^2} \int_0^V v_{\text{ds}} C_{\text{oss}}(v) dv. \quad (2.71)$$

At the time t_1 , the voltage across the switch T_2 is denoted with $U_{\text{s},0}$ and $(U_{\text{DC},1} - U_{\text{s},0})$ applies at the switch T_1 . The voltage $U_{\text{s},0}$ can be calculated approximatively with

$$U_{\text{s},0} \approx \frac{\hat{I}_1}{2\omega_0 C_{\text{T,Qeq}}} (\cos(\theta_1) - \cos(\theta_{\text{dead,T}} - \theta_1)) + U_{\text{DC},1}. \quad (2.72)$$

However, it is important to note that (2.72) is a rough estimation only, based on the total charge ΔQ_2 delivered to the output capacitances of the inverter switches, but neglects the actual resonant current and voltage transition during the dead-time interval.

The initially stored energy in the bridge leg consisting of the switches T_1 and T_2 can be calculated using

$$E_{\text{initial}} = \frac{1}{2} C_{\text{E,eq}}(U_{\text{s},0}) \cdot U_{\text{s},0}^2 + \frac{1}{2} C_{\text{E,eq}}(U_{\text{DC},1} - U_{\text{s},0}) \cdot (U_{\text{DC},1} - U_{\text{s},0})^2. \quad (2.73)$$

At the turn-on of switch T_2 , the energy that is stored in its output capacitance will be dissipated into heat. Additionally, in order to charge the output capacitance of the switch T_1 up to the primary-side DC-link voltage, additional charge has to be delivered by the power supply, which is causing conduction losses in switch T_2 . By using the charge-equivalent capacitance, the delivered energy can be calculated with

$$E_{\text{delivered}} = U_{\text{DC},1} (C_{\text{Q,eq}}(U_{\text{DC},1}) U_{\text{DC},1} - C_{\text{Q,eq}}(U_{\text{DC},1} - U_{\text{s},0}) \cdot (U_{\text{DC},1} - U_{\text{s},0})) \quad (2.74)$$

At the time instant t_2 , the final energy that is stored in the fully charged output capacitance of switch T_1 is described with

$$E_{\text{final}} = \frac{1}{2} C_{E,\text{eq}} (U_{\text{DC},1}) \cdot U_{\text{DC},1}^2 . \quad (2.75)$$

Both bridge legs experience the same amount of power losses, which occur twice within a switching period. Therefore, the total energy balance and the switching power losses can be calculated according to

$$\begin{aligned} E_{\text{dissipated}} &= 2 \cdot (E_{\text{initial}} + E_{\text{delivered}} - E_{\text{final}}) \\ P_{v,I,\text{sw}} &= 2 \cdot f_0 \cdot E_{\text{dissipated}} \end{aligned} . \quad (2.76)$$

Additional power losses are caused by the gate driver circuit. In the case of a boot-strap power supply of the high-side gate driver, the power losses are calculated with good approximation with

$$P_{v,I,\text{gd}} = 2 \cdot (2Q_{g,\text{tot}} U_{\text{gd}} f_0 + Q_{g,\text{tot}} u_{\text{DF,bs}} f_0) , \quad (2.77)$$

where $Q_{g,\text{tot}}$ is the total gate charge of the FET, U_{gd} is the gate drive power supply voltage and $u_{\text{DF,bs}}$ is the boot-strap diode forward voltage drop. The total inverter power loss is then described by the sum of all the individual loss components, which is given by

$$P_{v,I} = P_{v,I,d} + P_{v,I,\text{on}} + P_{v,I,\text{sw}} + P_{v,I,\text{gd}} . \quad (2.78)$$

The previously derived power loss model allows to predict the power loss distribution within the IPT system and will be verified in the following section using a hardware prototype of the SSU-compensated IPT system. Note that the model is not limited to series-series compensated systems only, but can be used also for the SP and SSP compensated IPT systems, as long as the input impedance $\underline{Z}_{\text{in}}$ has a resistive/inductive behaviour and as long as the primary-side and secondary-side coil currents are sinusoidal in shape.

2.4 Experimental Verification

In order to validate the power loss model and in order to verify the operation and the performance of the series-series compensated IPT topology, a hardware prototype is realized with the energy transmission coil set indicated in **Fig. 2.18**, operated at 800 kHz. In a first step, the

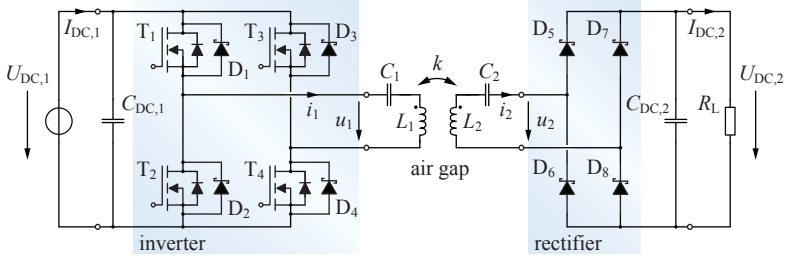


Fig. 2.22: Basic circuit schematic diagram of the IPT system hardware prototype shown in **Fig. 2.23**.

hardware prototype is used to explore the achievable performance of the SSU-compensated IPT system. Later in **Section 2.6**, the performance is also verified for the SSR-compensation and is compared to the SSU-compensation.

The following section gives insight into the realization of the hardware prototype.

2.4.1 IPT System Prototype

The basic circuit schematic of the implemented converter is shown in **Fig. 2.22** and a picture of the realized hardware prototype is shown in **Figs. 2.23(a)** and **(b)**. The latter shows the IPT system assembly including the prototype energy transfer coils. The technical specifications of the prototype coils and the main circuit components used for the hardware prototype are given in **Tab. 2.2**. The IPT coils have an outside diameter of 70 mm and are made of 17 turns of litz-wire on a single layer. The litz-wire consists of 300 strands with a strand diameter of 0.04 mm. The total litz-wire diameter is approximately 0.95 mm.

For simplicity, the primary-side and secondary-side circuit, i.e. the inverter and the diode rectifier circuit, are placed on the same Printed Circuit Board (PCB). The full-bridge inverter is based on the EPC2016 Gallium Nitride (GaN) FET [68]. The switch offers a low ON-state resistance of typically 12 m Ω and a low output capacitance of maximally 650 pF. Additionally, the GaN FET features a very low total gate charge of only 5 nC and can be driven with 5 V logic levels, which allows for a high switching frequency and which lowers the gate drive power losses considerably. Furthermore, the FET outline dimensions

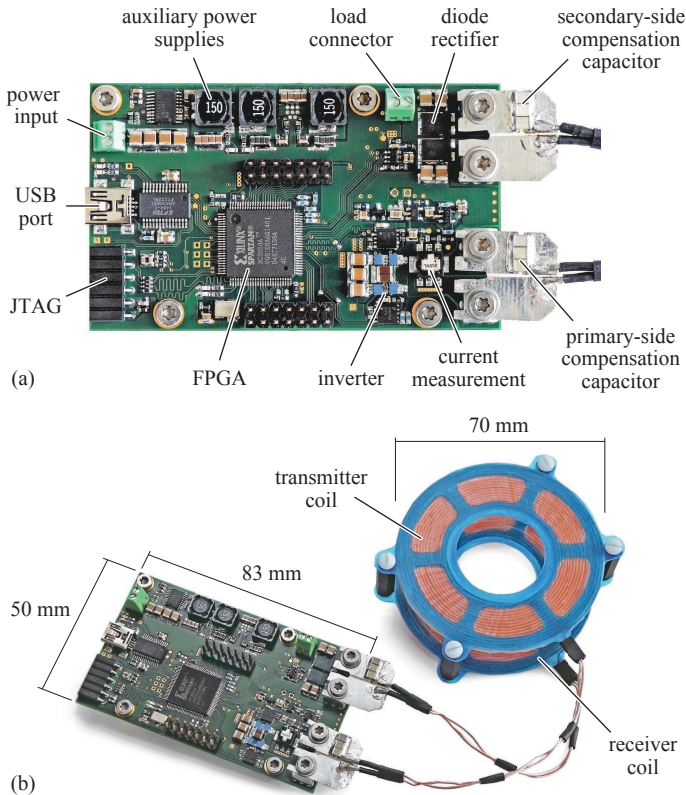


Fig. 2.23: (a) Prototype converter PCB and (b) the prototype IPT system assembly including the prototype energy transmission coils.

are as small as $2.1\text{ mm} \times 1.63\text{ mm}$, which allows for a PCB layout with ultra-low parasitic inductance in the commutation path of each half-bridge, and hence, increases the switching performance. The GaN FET has a source-to-drain forward voltage drop of approximately 1.5 V at a switch current of 1 A , which causes significant power losses during the body diode conduction interval. Therefore, as proposed in [69], each FET is equipped with an additional anti-parallel Schottky diode, i.e. the diodes D_1 - D_4 in **Fig. 2.22**, which reduce the inverter power losses significantly. The small package of the FET allows for low commutation inductance, which is needed for a fast commutation of the current

Test board components	Value
Power FET T ₁ -T ₄	EPC2016
Schottky diodes D ₁ -D ₄	MSS1P5-M3/89A
Rectifier diodes D ₅ -D ₈	V12P10-M3/87A
Resonant capacitors C ₁ , C ₂	2.97 nF / 1 kV
Energy transfer coils	
Inductance L ₁ , L ₂	18.8 μH, 18.4 μH
AC resistance R _{L1} , R _{L2}	210 mΩ, 204 mΩ
Litz wire	300 x 0.04 mm
Number of turns	17
Outside coil radius R _a	35 mm
Inside coil radius R _i	17 mm
Operating conditions	
Switching frequency f ₀	800 kHz
Output voltage U _{DC,2}	35 V
Output power P ₂	5 W - 30 W
Design coupling factor k ₀	0.268

Tab. 2.2: Component values and operating conditions of the IPT system prototype used for the measurements. The compensation capacitors are designed for the SSU-compensation, according to the equations given in **Tab. 2.1**.

from the FET to the anti-parallel Schottky diode. In addition, the high body diode voltage drop of the FET helps to reduce the commutation time. As a main disadvantage, the additional Schottky diodes increase the total parasitic output capacitance of each FET, and therefore, a higher inductive output current is required at the switching instant in order to allow for ZVS operation of the inverter switches.

The secondary-side full-wave rectifier is composed of four V12P10-M3/87A Schottky barrier diodes, which offer a low forward voltage drop of 0.38 V at a current of 1 A. The compensation capacitors of the resonant circuit are designed for the SSU system operation (cf. **Tab. 2.2**) and are mounted on separate PCBs, which are connected to the test board using screw terminals. The interchangeability of the resonant circuit simplifies the testing of different capacitive compensations and coil arrangements, but the bulky connectors and the PCBs for the compensation capacitors are not suited for a high-frequency operation and have a significant series resistance of about 32 mΩ at a frequency of 800 kHz, which was measured with an Agilent 4294A impedance analyzer.

Each GaN FET half-bridge is operated with the integrated bootstrap gate driver LM5113 [70] and the gate-signals are generated with a Field Programmable Gate Array (FPGA).

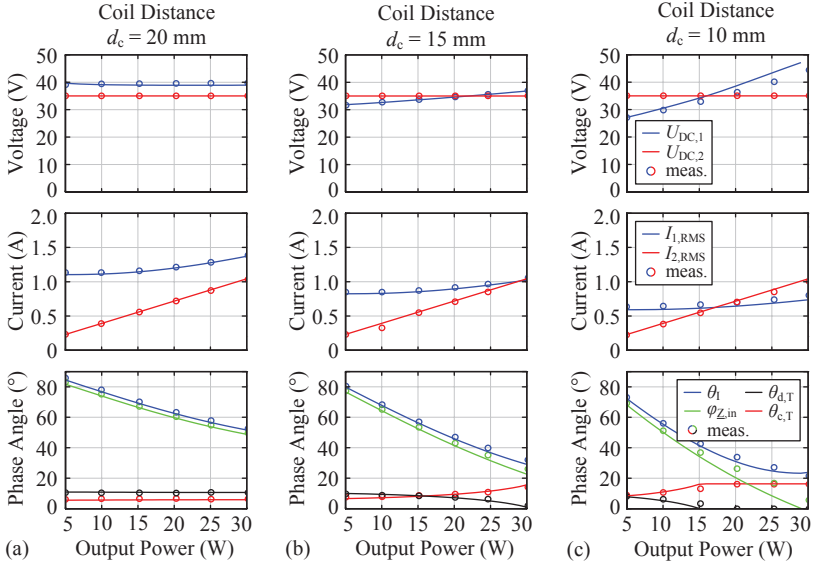


Fig. 2.24: Comparison of the measured operating characteristics and the values calculated with the mathematical model presented in **Section 2.3**, evaluated for different coil separation distances and for variable load conditions.

2.4.2 Measurement Results

In order to evaluate the performance of the prototype and to validate the analytical power loss models, extensive measurements were carried out and are discussed in the following.

The main electrical characteristics of the prototype IPT coils, such as the inductance value and the AC resistance are measured at the operating frequency with the Agilent 4294A impedance analyzer and are listed in **Tab. 2.2**. The measurement of the frequency dependency of the AC resistance and inductance of one of the two identical IPT coils is shown in **Figs. 2.12(b)** and **(c)**, respectively. The measurement of the coil coupling factor with respect to the coil separation distance and axial misalignment is shown in **Fig. 2.13**.

For the power loss measurements, the IPT system prototype is operated at a frequency of 800 kHz and a constant output voltage of 35 V, which is manually adjusted by varying the primary-side DC-link voltage

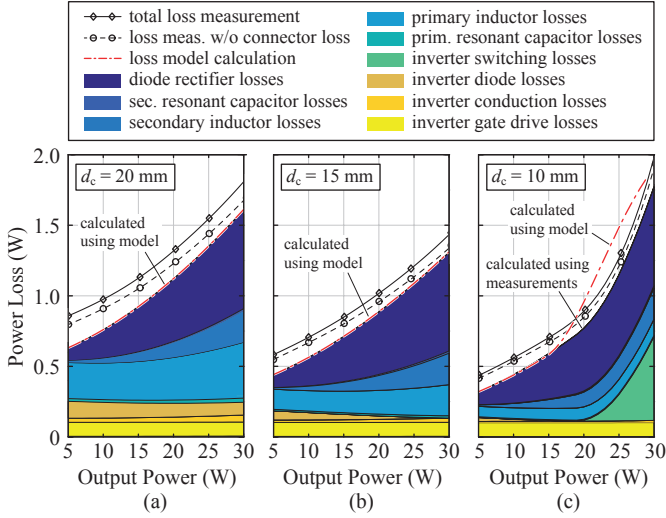


Fig. 2.25: Calculated power loss distribution and measurement of the total power loss of the IPT system prototype at different coil separation distances and variable output power. The red dashed line indicates the total power loss calculated with the analytical power loss model, whereas in (c) the power loss distribution is calculated with the mathematical model, but using measurements for the angles $\varphi_{Z_{in}}$, θ_I , $\theta_{c,T}$ and the voltage $U_{s,0}$ as an input to the model. Additionally, the figures indicate the total power losses with removed resonant circuit connector losses, since these losses are not covered by the mathematical model. Note that the power loss measurements do not include the constant power losses of 258 mW caused by the FPGA and the auxiliary power supply circuits.

$U_{DC,1}$. The dead-times for the inverter circuit are set to 56.4 ns and the rectifier output power is varied in a range of 5-30 W. The measurements are carried out at coil separation distances of 20 mm, 15 mm and 10 mm and perfect axial alignment, which correspond to a coil coupling factor of 0.263, 0.353 and 0.489, respectively.

The measured converter currents and voltages, and the comparison with the calculated values obtained with the analytical model are shown in **Fig. 2.24**. The calculated values of all the relevant converter operating characteristics fit the measurements with good accuracy. This is specifically true for large coil separation distances where the coil cou-

pling coefficient is small, and where the coil currents are almost perfectly sinusoidal. The limitation of the mathematical model becomes apparent at small coil separation distances, where the assumption of purely sinusoidal primary-side and secondary-side IPT coil currents loses its validity. As a result, as shown in **Fig. 2.24(c)**, the starting point of the inverter hard-switching operation is predicted at a lower output power than it is observed in the measurements.

The calculated power loss distribution of the IPT system prototype is shown in **Fig. 2.25** together with the measured total power loss. Note that the power loss measurements do not include the constant power losses of 258 mW caused by the FPGA and the auxiliary power supply circuits. Additionally, the power losses caused by the mentioned resonant circuit connectors are subtracted from the total power loss measurement as indicated in **Fig. 2.25**, since these losses are also not covered by the model.

In **Fig. 2.25(c)**, in order to overcome the limitations of the power loss model at small coil separation distances, measurements of the phase angles $\varphi_{Z,\text{in}}$, θ_I , $\theta_{c,T}$ and the measured voltage $U_{s,0}$ are used to calculate the power loss distribution. In this case, at maximum output power, the switching losses make up almost 70% of the total primary-side losses. This shows clearly, that a purely resistive operation of the IPT system is not practical and a minimum positive phase angle of the input impedance of the resonant circuit is needed, in order to ensure that the inverter output current is large enough to allow for ZVS operation.

On the secondary side, the diode rectifier power losses make the largest contribution to the total power loss within the IPT system, and account for almost 75% of the total secondary-side power losses. This is specifically undesirable, since in the final application, these power losses are generated within the patient's body. Therefore, a highly efficient synchronous rectifier was developed in order to significantly reduce the secondary-side power losses. The realization and the operation of the synchronous rectifier is shown in detail in the following section.

2.5 Synchronous Rectification

Using the improved power loss model, it is predicted that the diode rectifier power loss is approximately 700 mW at the maximum output power of 30 W. Due to the small volume of the rectifier diodes, the power loss density per diode is as high as 6 W/cm³, and is therefore

thermally difficult to handle within the implant. As a solution, a synchronous rectifier allows to reduce the power losses by replacing the rectifier diodes with actively controlled switches and thereby eliminating the high forward voltage drop of the rectifier diodes and the associated power losses.

There are few reported implementations of synchronous rectifier circuits intended for the use in TET system applications. The system with the highest reported efficiency is described in [33] with 93.4% at a coil separation distance of 5 mm and an output power of 46 W. The employed push-pull type synchronous rectifier circuit was operated at 160 kHz and uses the synchronous gate drive control circuit STSR30 manufactured by STMicroelectronics, which allows for operating frequencies up to 500 kHz [71]. Another synchronous rectifier circuit described in [72] is operated at 178 kHz and uses a push-pull type rectifier circuit as well.

The high operating frequency of the IPT system prototype of 800 kHz poses particular design challenges regarding the digital control, the operation of the gate drivers and the switches itself. The main objectives for the implementation of the synchronous rectifier are a high reliability, small volume and a high energy efficiency. Furthermore, the rectifier should be self-controlled, i.e. should generate the switching signals automatically based on the measurement of the rectifier input voltage.

2.5.1 Hardware Prototype

Fig. 2.26 shows the top and bottom side of the implemented synchronous rectifier prototype. The finally realized rectifier circuit for the TET implant prototype is shown in **Chapter 8** and has an area occupation of only 21×14 mm and is implemented on a four-layer PCB. GaN FETs are the optimal choice for low-power synchronous rectifier applications, which is due to the fast switching, the low ON-state resistance and the low total gate charge of the switches. Hence, the EPC2016 GaN FETs are used as well for the realization of the synchronous rectifier prototype. As for the inverter circuit, an additional Schottky diode is connected in anti-parallel configuration to each of the rectifier switches.

The detailed circuit schematic of the synchronous rectifier is shown in **Fig. 2.27** and can be subdivided into three sections: The digital control, the gate driver and the rectifier power stage. The control of the

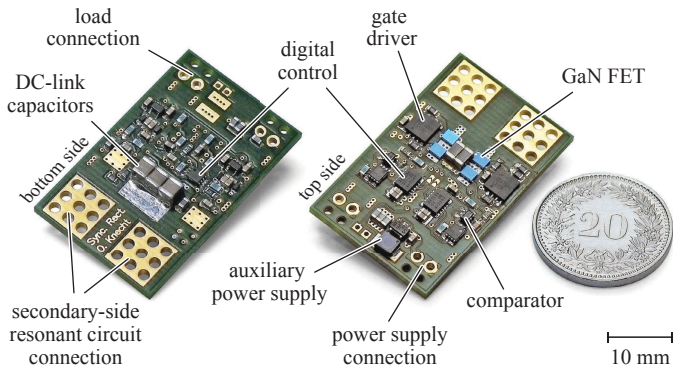


Fig. 2.26: Picture of the top and bottom side of the synchronous rectifier prototype.

rectifier circuit is based on the sensing of the zero crossing of the differential rectifier input voltage u_2 . Accordingly, the switch-node voltages $u_{sw,A}$ and $u_{sw,B}$ are compared to the half of the secondary-side DC-link voltage $U_{DC,2}$, which ensures the synchronization of the digital control to the operating frequency of the IPT system. As an alternative, the switch-node voltages could also be compared directly to each other, which would save a comparator in the circuit.

A detailed view of a switching transition of the synchronous rectifier is shown in **Fig. 2.20(a)**. The switches T_6 and T_7 are turned on with a delay of $\theta_{pd,R}$ after the zero crossing of the differential input voltage u_2 and during the time interval $\theta_{d,R}$, the Schottky diodes D_6 and D_7 , which are connected in parallel to the FETs, are conducting the secondary-side coil current i_2 .

As shown in **Fig. 2.27**, a one-shot circuit using the retriggerable monostable multivibrator 74AHC123 is used with adjustable ON-time to generate the gate signals. This allows to adjust the ON-state time interval such that the FETs are turned off just before the next zero crossing of the secondary-side coil current i_2 , preventing a power flow in the reverse direction due to a delayed turn-off. Using this concept, the implemented circuit could be operated at a fixed switching frequency of up to 2 MHz. In addition, in order to prevent a shoot-through condition or another erratic operation of the circuit, a digitally controlled interlock mechanism is implemented using D-type flip-flops and digital gates, which uses the Latch-Enable (LE) input of the comparators

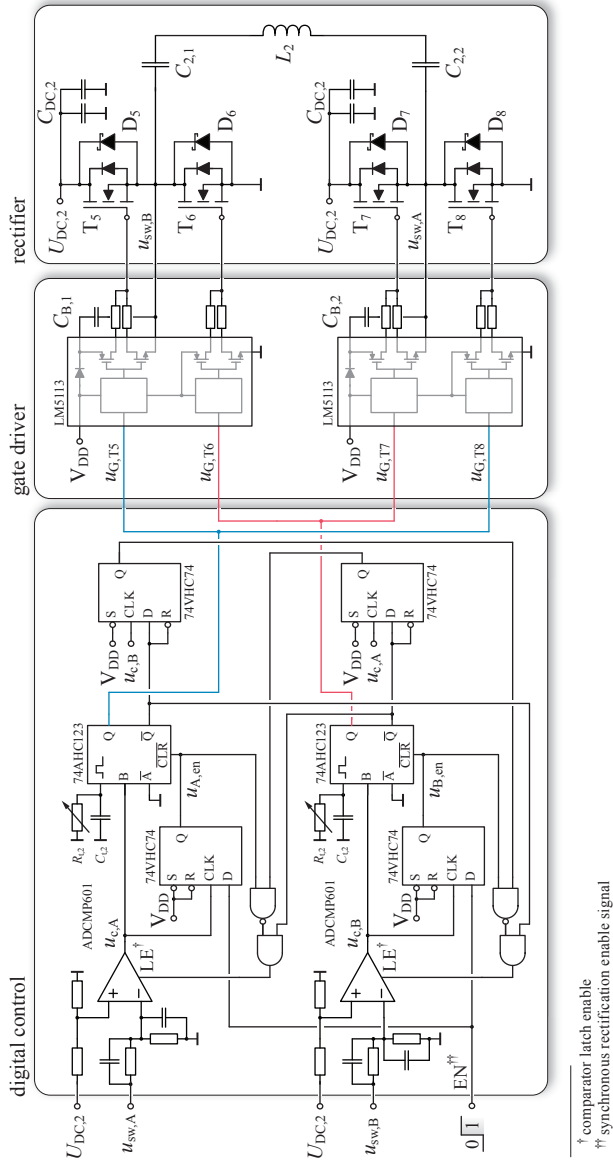


Fig. 2.27: Detailed circuit schematic of the synchronous rectifier.

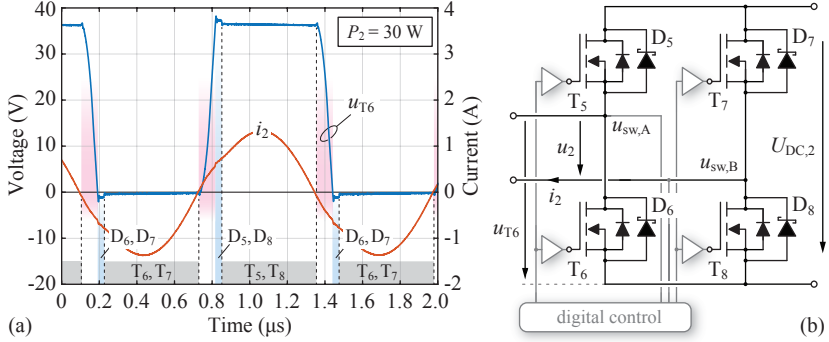


Fig. 2.28: (a) Synchronous rectifier input voltage and secondary-side coil current waveform of the final TET implant hardware prototype at an output power of 30 W. (b) Simplified synchronous rectifier circuit diagram.

to enable the corresponding comparator only for the voltage transition time interval $\theta_{c,R}$.

The voltage across switch T_6 and the rectifier input current waveform of the final implant hardware prototype, operated at the maximum output power is shown in **Fig. 2.28(a)**, and the corresponding simplified rectifier circuit diagram is shown in **Fig. 2.28(b)**. The total charging time of the parasitic output capacitance of the rectifier switches is about 175 ns within a switching cycle, which is 14 % of the total period. The diode conduction time, before the associated rectifier switches are turned on, is about 32.5 ns. This delay is due to the signal propagation times in the digital circuit and in the gate driver. Note that the turn-on propagation delay of the LM5113 gate driver itself is specified with 28 ns [70]. The ON-time interval of the switches is adjusted such that the rectifier switches are turned off automatically at the zero crossing of the rectifier input current i_2 , after a fixed time interval of about 50 ns.

In order to predict the performance and the power loss distribution of the synchronous rectifier circuit, the power loss model of the previous section is extended to account for the improved rectifier as well.

2.5.2 Power Loss Modeling

The charging time interval of the parasitic output capacitances of the FETs at the secondary-side current zero crossing can be calculated ac-

cording to (2.59). In this case, the charge-equivalent capacitance $C_{D, \text{Qeq}}$ includes the parasitic output capacitance of the GaN FET and the junction capacitance of the additional anti-parallel Schottky diode. The power loss due to the diode conduction time interval $\theta_{d, \text{R}}$ can be calculated with

$$P_{v, \text{SR}, d} = \frac{i_2^2 r_{\text{DR}, 0}}{\pi} \left(\frac{1}{2} \sin(2\varphi_1) - \varphi_1 - \frac{1}{2} \sin(2\varphi_2) + \varphi_2 \right) + \frac{2I_2 u_{\text{DR}, 0}}{\pi} (\cos(\varphi_1) - \cos(\varphi_2)) \quad , \quad (2.79)$$

using $\varphi_1 = \theta_{c, \text{R}}$ and $\varphi_2 = (\theta_{c, \text{R}} + \theta_{d, \text{R}})$. The conduction losses caused by the ON-state resistance of the FETs during the fixed ON-time interval $\theta_{\text{on}, \text{R}}$ is obtained with

$$P_{v, \text{SR}, \text{on}} = \frac{i_2^2 R_{\text{DS}, \text{on}}}{\pi} \left(\frac{1}{2} \sin(2\varphi_2) - \varphi_2 - \frac{1}{2} \sin(2\varphi_3) + \varphi_3 \right) \quad , \quad (2.80)$$

using $\varphi_3 = (\theta_{c, \text{R}} + \theta_{d, \text{R}} + \theta_{\text{on}, \text{R}})$. In addition, the gate drive power losses $P_{v, \text{SR}, \text{gd}}$ given by (2.77) and the auxiliary power supply losses $P_{v, \text{SR}, \text{aux}}$ caused by the control circuit must be taken into account. The total synchronous rectifier power loss is then given by

$$P_{v, \text{SR}} = P_{v, \text{SR}, d} + P_{v, \text{SR}, \text{on}} + P_{v, \text{SR}, \text{gd}} + P_{v, \text{SR}, \text{aux}} \quad . \quad (2.81)$$

In order to show the performance of the realized rectifier circuit, power loss measurements are carried out and compared to the measurements which are made with the IPT system prototype using the diode rectifier.

2.5.3 Measurement Results

A direct measurement of the total secondary-side power losses is difficult to achieve. Therefore, the estimation of the secondary-side power loss savings due to the synchronous rectifier operation is based on the measurement of the overall IPT system performance, either using the diode- or the synchronous rectifier, and on the secondary-side power loss calculation of the diode rectification. The reason being that the power loss of the diode rectifier can be calculated more accurately, which is due to its lower circuit complexity compared to the synchronous rectifier. The derived estimation of the secondary-side power loss for the diode rectifier and the synchronous rectification is shown in **Fig. 2.29(a)**.

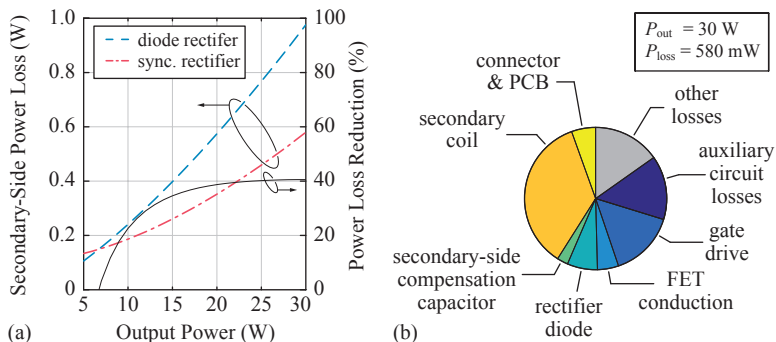


Fig. 2.29: (a) Calculated secondary-side power loss of the IPT system prototype using either the diode rectifier or the synchronous rectification. (b) Calculated secondary-side power loss distribution in case of synchronous rectification.

According to the calculation, by using the synchronous rectifier, the total secondary-side power losses are reduced by approximately 40% at the maximum output power. Hence, the secondary-side efficiency is increased from approximately 96.9% to 98.1% at an output power of 30 W and is above 97% for the entire load range. The diode rectifier shows an equal or slightly better performance at low output power, which is mainly due to the constant power consumption of the synchronous rectifier, which is caused by the gate drives and the digital control circuit. **Fig. 2.29(b)** illustrates the calculated distribution of the secondary-side power losses of the IPT system prototype including the synchronous rectifier at an output power of 30 W. The main power loss contributions in case of the rectifier circuit are the gate driver losses and the auxiliary circuit power losses, which include the power supplies, the digital control and the measurement circuits, and mainly determine the rectifier performance. The losses could be further reduced by using GaN FETs with lower total gate charge or by using a lower voltage of the digital circuit.

Fig. 2.30 shows the thermal images of the IPT system prototype, measured with a Fluke Ti9 thermographic camera. **Figs. 2.30(a)-(b)** show the inverter PCB and a close-up of the diode rectifier operated at 30 W output power and a coil separation distance of 15 mm. The ambient temperature was 26 °C and the PCB experienced passive air

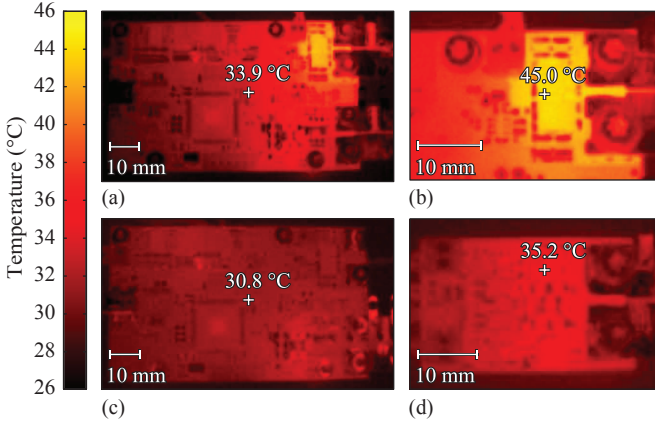


Fig. 2.30: Thermographic images of the prototype inverter PCB, operated at maximum output power and a coil separation distance of 15 mm, using either the diode rectifier (a) or the synchronous rectifier circuit (c). (b) Close-up of the top side of the diode rectifier and (d) shows the top side of the synchronous rectifier PCB at maximum output power.

cooling only. **Figs. 2.30(c)** and **(d)** show the thermal image of the IPT system operated at the same operating conditions, but using the synchronous rectifier circuit. As a result of the significantly reduced secondary-side power losses, the temperature of the synchronous rectifier is approximately 10°C lower compared to the diode rectifier.

The estimated secondary-side coil power loss of the prototype system is 206 mW at maximum output power, which is calculated using the measured coil AC resistance and the measured coil RMS current, and makes about 35.5% of the total secondary-side power losses. The maximum temperature of the human tissue surrounding the secondary-side TET coil is estimated for the maximum power transmission and minimum coil separation distance using the thermal model presented in **Chapter 3** and attains a value of 37.7°C , which is well below the thermal limit of 39°C given in [73].

The measurements of the DC-DC power conversion efficiency and the total power loss of the final IPT system prototype including the synchronous rectification are shown in **Figs. 2.31(a)** and **(b)**, respectively. The measurements include all power losses except the constant power loss of 258 mW caused by the FPGA and the auxiliary power supplies on

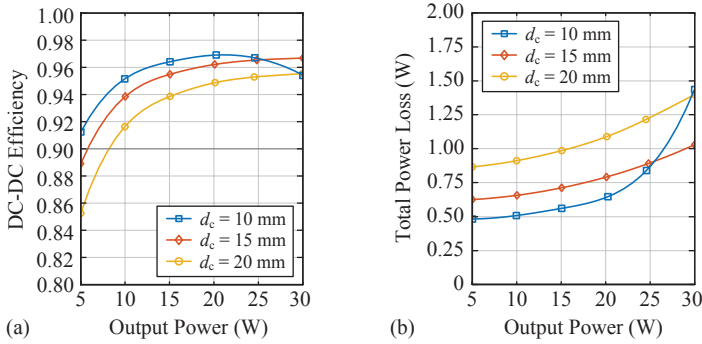


Fig. 2.31: (a) Measured DC-DC efficiency and (b) measured total power loss of the IPT system prototype using the synchronous rectifier. The total power losses caused by the FPGA and the primary-side auxiliary power supply of 258 mW, which would reduce the efficiency by 0.8% at maximum output power, are not included in the measurement.

the inverter PCB, which would reduce the DC-DC efficiency by 0.8% at maximum output power. However, the FPGA and the auxiliary circuits on the inverter PCB are not optimized for low power consumption.

The maximum measured DC-DC efficiency attains a value of 96.9% at a coil separation distance of 10 mm and an output power of 20 W, and is greater than 95% at maximum output power for all of the considered coil separation distances. In comparison to the IPT system using the simple diode rectifier, the efficiency increased by approximately 1% at the maximum output power.

The measurement of the DC-DC efficiency is carried out with the energy transmission coils operated in air. However, despite the comparably low electrical conductivity of the living tissue, the alternating magnetic and electric field in the vicinity of the energy transfer coils cause additional power losses in the tissue. In **Chapter 4**, an FE-simulation model of the human skin and the energy transfer coils is introduced, which allows to calculate the power loss in the tissue due to the electromagnetic field exposure. The simulation results show that at maximum output power and minimum coil separation distance of 10 mm, the total power loss in the tissue due to the electromagnetic field exposure, is below 20 mW, and is therefore only of minor importance for the system performance and the heating of the human tissue.

However, in the case of series-series compensation, the peak elec-

tric field strength in the tissue can attain very high values, which is addressed in detail in **Chapter 4**.

2.6 IPT System Operation and Control

It was shown in **Section 2.2** that the series-series compensated IPT topology outperforms the secondary-side parallel compensated systems for the considered maximum power transfer level at hand. And the performance measurements with the hardware prototype of the SSU-compensated IPT system has further shown that high energy transfer efficiencies can be achieved with a careful design of the IPT system.

Hence, in the following section, the operating modes of the series-series compensated IPT system are analyzed in more detail and the SSU-compensated IPT system is compared to the SSR IPT system operation, regarding several performance metrics, such as the energy transfer efficiency, the secondary-side coil power loss and the coil misalignment tolerance.

In addition, the control concept for the IPT system and the proposed overall TET system topology is shown for both operating modes. The large majority of control strategies reported in the literature involve a wireless feedback path, in order to implement a closed-loop controller. But there are also a few methods reported, which allow for a control of the energy transfer without using a wireless feedback path. For example in [74], a single primary-side controller is used to maintain a stable secondary-side output voltage. In this case, the voltage and current measurement at the primary side of a parallel-parallel compensated IPT resonant circuit is used to estimate the coil coupling and the secondary-side output voltage. Accordingly, the input voltage amplitude is adjusted by means of a duty-cycle control to maintain the output voltage set-point. In another work, the power transfer is controlled by adjusting the received power directly on the secondary side of the IPT system [75].

However, for the application at hand, a wireless communication channel is needed in any case, in order to transmit sensor data and in order to control the LVAD. Hence, the IPT system can be controlled as well based on a wireless feedback of the secondary-side current and voltage measurements. In general, there exist two degrees of freedom to control the power transfer in the IPT system, which are the input voltage amplitude of the resonant circuit and the operating frequency, or a

combination of the two [43, 76]. A comparative evaluation of different control methods is provided in [43, 76], and it is shown for a the SSR-compensation, that the voltage control, i.e. adjusting the primary-side and secondary-side DC-link voltages, achieves the best performance. Therefore, only voltage control will be considered for the SSR- and the SSU-compensated IPT systems.

2.6.1 SSR IPT System

A special property of the SSR-compensated IPT system is the fixed resonance frequency, that does not change with load or coil coupling variations, i.e. the operating frequency for a purely resistive input impedance of the resonant circuit does not change. Hence, the SSR system is operated at a constant switching frequency and according to (2.15), the equivalent load resistance at the output of the resonant circuit must be adjusted proportional to the coil coupling factor, in order to achieve the maximum power transmission efficiency. Accordingly, the adaptive impedance matching can be implemented by means of an additional DC-DC step-up and/or step-down converter, which allows to adjust the secondary-side DC-link voltage $U_{\text{DC},2}$ such that the optimal equivalent load resistance $R_{\text{L,opt}}$ is maintained at the output of the resonant circuit for any output power level and for any coil coupling factor. This operating scheme is referred to as *efficiency optimal control* and is described in detail in [43]. A brief summary will be given in the following.

The compensation capacitors for the SSR-operation are designed according to (2.4). As a result, assuming a lossless operation of the resonant circuit and assuming sinusoidal primary-side and secondary-side coil currents with peak values \hat{I}_1 and \hat{I}_2 , the simplified equivalent circuit shown in **Fig. 2.2(d)** can be used to calculate the power that is delivered to the resistive load, as shown in [43], which results in

$$P_2 = \frac{1}{2} \underbrace{\omega_0 M \hat{I}_1}_{\hat{U}_{2,(1)}} \hat{I}_2 = \frac{1}{2} \frac{\hat{U}_{1,(1)} \hat{U}_{2,(1)}}{\omega_0 M}, \quad (2.82)$$

where $\hat{U}_{1,(1)}$ and $\hat{U}_{2,(1)}$ denote the magnitude of the fundamental frequency component of the resonant circuit input and output voltage, which can be calculated with $\hat{U}_{i,(1)} = \frac{4}{\pi} U_{\text{DC},i}$, $i \in [1, 2]$, if a full-bridge rectifier and inverter stage with perfectly rectangular input and output voltage waveforms is assumed. Note that in case of the SSR-

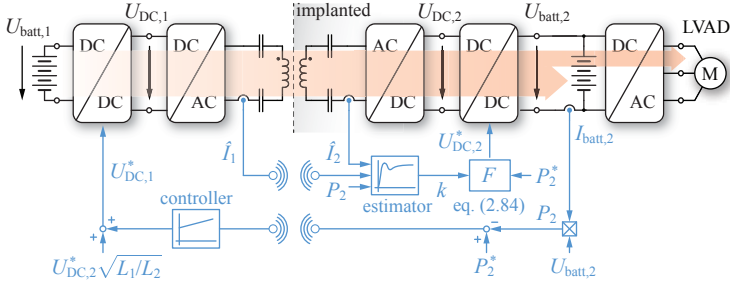


Fig. 2.32: TET system topology using the *efficiency optimal control* for the series-series compensated IPT system operated at resonance (SSR) [43].

compensation, the primary-side coil current is 90° phase shifted with respect to the secondary-side coil current.

Assuming a lossless operation of the circuit, the equation for the output power can be rearranged to

$$P_2 = \frac{8}{\pi^2} \frac{U_{DC,1} U_{DC,2}}{\omega_0 M}. \quad (2.83)$$

Hence, the primary-side and/or the secondary-side DC-link voltages, $U_{DC,1}$ and $U_{DC,2}$, can be used to control the transmitted power. As mentioned above, due to the current source behaviour of the SSR system, the secondary-side DC-link voltage $U_{DC,2}$ can be impressed and/or adjusted by the subsequent converter stage [43], which allows to control the equivalent load resistance at the output of the IPT system. Combining the equations for the optimal load resistance given in (2.17) and the equivalent load model given in (2.24), the optimum IPT system output DC-link voltage set-point is calculated according to

$$U_{DC,2,SSR}^* = \sqrt{\frac{\pi^2}{8} P_2^* k \omega_0 L_2}, \quad (2.84)$$

which is required to provide load matching for any output power level and coil coupling factor [43]. The input DC-link voltage set-point $U_{DC,1}^*$ follows directly from (2.6) and (2.17), and is calculated with

$$U_{DC,1}^* = \sqrt{\frac{L_1}{L_2}} U_{DC,2}^*. \quad (2.85)$$

The implementation of the *efficiency optimal control* according to [43] is illustrated in **Fig. 2.32**. Additional filtering stages which are required to protect the batteries from large voltage and current ripples are not explicitly shown in the figure. A key requirement for the controller implementation is the estimation of the coil coupling factor k , which is needed to evaluate equation (2.84). The coupling factor can be deduced from equation (2.82), using the measurements of the output power and the primary-side and secondary-side coil current amplitudes. Accordingly, the optimal IPT system output voltage $U_{\text{DC},2,\text{SSR}}^*$, calculated with equation (2.84), is set by the secondary-side DC-DC converter, in order to set the optimal load resistance for the IPT circuit. The output power set-point P_2^* is then maintained by adjusting the primary-side DC-link voltage $U_{\text{DC},1}$. As stated in [43], the dynamic performance of the SSR system can be improved by including a feed-forward of the primary-side DC-link voltage $U_{\text{DC},1}^*$ according to (2.85).

An interruption of the communication between the primary and secondary side, or a fault condition on the secondary side with a rapid change of the load condition can result in a high voltage at the output of the SSR system, which is due to the large voltage gain of the resonant circuit, and hence, raises questions about the operational safety of the SSR IPT system. In addition, since the input and output voltage vary over a wide range above and also below the primary-side and secondary-side battery voltage range of 12-16.8 V, a buck-boost type DC-DC converter is needed on either side of the IPT resonant converter, in order to provide the load matching.

In this case, the input voltage of the motor inverter is clamped to the battery voltage and during the battery charging process, both the charging power and the power to drive the LVAD must be supplied by the secondary-side DC-DC converter as indicated in **Fig. 2.32**. Consequently, the inductor of the DC-DC converter must be designed for the maximum power rating and hence, a relatively large inductor volume is needed in order to reduce the power loss in the implant.

Figs. 2.33(a)-(c) show the measured primary-side and secondary-side DC-link voltages, the phase angle of the input impedance $\varphi_{\underline{Z},\text{in}}$ and the DC-DC efficiency for the efficiency optimal operation of the SSR IPT system, using the hardware prototype shown in **Fig. 2.23** with the synchronous rectifier prototype presented in **Fig. 2.26**.

The operating conditions and the values of the compensation capacitors are given in **Tab. 2.3**. **Fig. 2.33(a)** shows the variation of

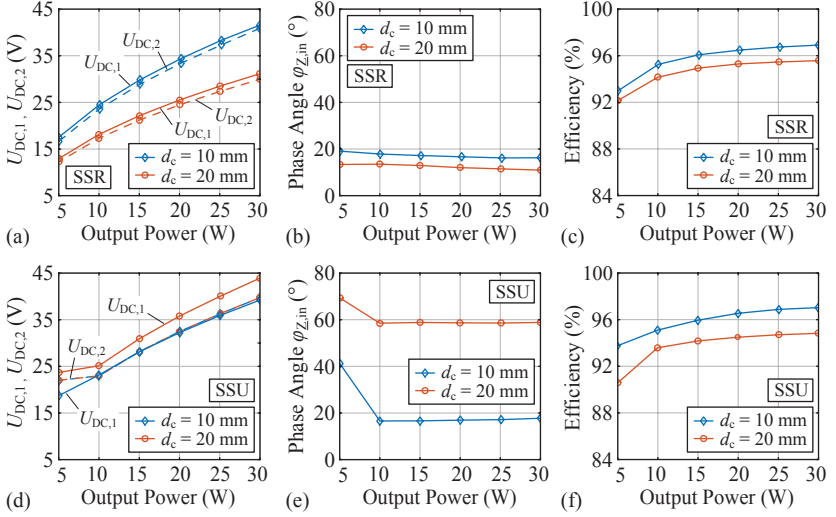


Fig. 2.33: (a)-(c) Measured input and output voltage, phase angle of the input impedance of the resonant circuit and DC-DC efficiency for the SSR IPT system operation and (d)-(f) for the SSU IPT system operation. The measurements are carried out with the IPT system hardware prototype and with the synchronous rectifier shown in the previous sections. Note that the constant power losses of 258 mW due to the primary-side FPGA and auxiliary power supplies are not included in the efficiency measurement.

the secondary-side DC-link voltage according to (2.84) with respect to the output power at a coil separation distance of 10 mm and 20 mm, respectively. As a result, as shown in **Fig. 2.33(b)**, the phase angle of the input impedance of the resonant circuit is almost constant with respect to the output power and attains values depending on the coil separation distance between 11° and 19° , which is required to allow for soft-switching operation of the inverter stage. The dead-time of the inverter is set to 65 ns for the measurements. The DC-DC efficiency is calculated from the input and output DC currents and DC voltages, which are measured using Agilent 34410A multimeters. The results are shown in **Fig. 2.33(c)**. Note that the constant power losses of 258 mW due to the primary-side FPGA and auxiliary power supplies are not included in the efficiency measurement.

According to the measurement accuracy specification of the mul-

Type	Parameter	Value	Parameter	Value
SSR	C_1, C_2	2.20 nF	L_1, L_2	18.8, 18.4 μ H
SSU	C_1, C_2	3.14 nF	f_0	800 kHz
	k_0	0.33	$k_{dc=10\text{mm}}$	0.489
	$U_{DC,2(\text{min})}$	22.0 V	$k_{dc=20\text{mm}}$	0.263

Tab. 2.3: SSR and SSU IPT system compensation capacitor values and operating conditions used for the performance measurement.

timer given in [77], the maximum relative error for the total power loss measurement is estimated with $\pm 0.34\%$ and $\pm 0.2\%$ at an output power of 5 W and 30 W, respectively. A maximum DC-DC efficiency of 96.9% is achieved at the minimum coil separation distance of 10 mm and the efficiency is larger than 92% in the entire output power range, even if the coil separation distance is as large as 20 mm. At an output power of 5 W and 20 mm coil separation distance, this is an efficiency improvement of 6.8% compared to the SSU IPT system operation with constant output voltage (cf. **Fig. 2.31(a)**). Furthermore, at a coil separation distance of 30 mm, i.e. at a coupling factor of 15%, the DC-DC efficiency is still larger than 90% and attains a maximum efficiency of 93.6% at the maximum output power. At a coil separation of 50 mm, i.e. at a coupling factor of merely 6%, the efficiency is still 85.2% at an output power of 10 W.

2.6.2 SSU IPT System

It was shown in **Section 2.5.3**, that the SSU IPT system operation with constant output voltage provides a high DC-DC efficiency at maximum output power and high coil coupling factor. But a main disadvantage of the constant output voltage operation is the increasing phase angle of the input impedance of the IPT resonant circuit at lower coil coupling and low output power, which causes an increase of the reactive power at the input and hence, increases the primary-side power losses significantly. Therefore, similar to the *efficiency optimal control* explained above, it is proposed to allow for a variation of the secondary-side DC-link voltage according to the output power demand. But in contrast to the SSR IPT system operation, the SSU-compensation shows a much lower voltage gain variation with respect to changes of the load conditions and coupling factor. Additionally, an estimation of the coil coupling factor is not required for the control of the SSU IPT system,

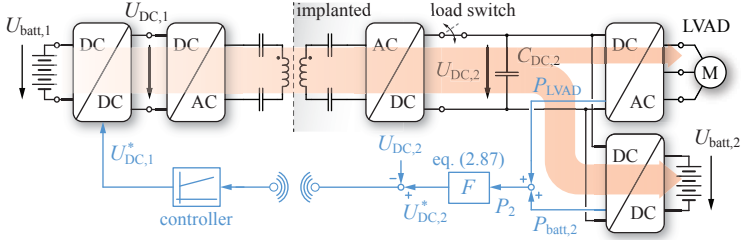


Fig. 2.34: TET system topology and control strategy for the SSU IPT system operation, i.e. for the operation near the frequency of load independent voltage gain.

as will be shown in the following.

An operation at exactly zero phase angle of the input impedance is not practical, since it would result in a hard-switching operation of the inverter stage. Hence, in order to design the IPT system for a desired phase angle of the input impedance $\varphi_{Z_{in,d}}$, which is large enough to ensure ZVS operation at maximum output power and maximum coil coupling, the factor k_0 is determined by

$$k_0 = \frac{k_{\max}}{\sqrt{3}} \sqrt{\tan(\varphi_{Z_{in,d}}) \sqrt{2} + 1}. \quad (2.86)$$

Accordingly, the primary-side and secondary-side compensation capacitors can be calculated using the design equations in **Tab. 2.1**. The secondary-side DC-link voltage is then varied according to the output power demand using [46],

$$U_{DC,2,SSU}^* = \frac{2^{3/4}}{4} \pi \sqrt{P_2 k_0 \omega_0 L_2}. \quad (2.87)$$

As a result, the equivalent load resistance of the SSU-compensated resonant circuit is kept at a constant value of

$$R_{L,eq,s}^* = \sqrt{2} k_0 \omega_0 L_2, \quad (2.88)$$

and this type of operation is therefore referred to as *constant load impedance control*.

The proposed structure and the control of the SSU-compensated IPT system is shown in **Fig. 2.34**. The power consumption of the LVAD and the battery charging converter (i.e. in charging mode) is

measured continuously and the set-point for the required IPT system output voltage $U_{\text{DC},2,\text{SSU}}^*$ is calculated using equation (2.87). On the primary side of the system, a DC-DC converter is then used to control the secondary-side DC-link voltage accordingly. By introducing a lower limit for the secondary-side DC-link voltage of 22 V, the buck-boost converter on the primary side and on the secondary side can be omitted and a simple bidirectional buck converter can be used for the battery charging converter and on the primary side, a simple boost converter can be employed. Hence, as shown in **Fig. 2.34**, the motor inverter and the buck-type battery charging converter are connected in parallel to the secondary-side DC-link. The inductor used for the buck converter can then be designed for a lower power throughput and therefore allows for a smaller volume compared to the inductor of the secondary-side buck-boost converter needed for the SSR IPT system shown in **Fig. 2.32**.

The control circuit of the battery charger continuously supervises the secondary-side DC-link voltage $U_{\text{DC},2}$ and if the voltage drops below the lower limit of 22 V, which may occur if the IPT system cannot transfer sufficient energy, the IPT system is disconnected from the DC-link using a load-switch and the battery charger takes over the power management and provides the energy supply for the LVAD inverter.

The experimental verification is again based on the hardware prototypes shown in **Fig. 2.23** and **Fig. 2.26**. The component values for the compensation capacitors are given in **Tab. 2.3**. **Figs. 2.33(d)** and **(e)** show the measured input and output DC-link voltages and the phase angle of the input impedance of the resonant circuit for the proposed SSU IPT system operation. Using the *constant load impedance control* method, the phase angle of the input impedance is kept constant at varying output power, but is increasing significantly at low coil coupling factors. The increase of the phase angle below 10 W in **Fig. 2.33(e)** is due to the minimum output voltage limit of 22 V. As a result, the increasing primary-side RMS current, which comes with the increasing phase angle of the input impedance, limits the power transfer capability at large coil separation distances and lowers the energy transfer efficiency, which is a main disadvantage of the SSU IPT system.

The measurement of the DC-DC efficiency is shown in **Fig. 2.33(f)**. At minimum coil separation distance, the efficiency is similar to the SSR IPT system using the *efficiency optimal control* and reaches a maximum of 97%. However, at a coil separation distance of 20 mm, the efficiency

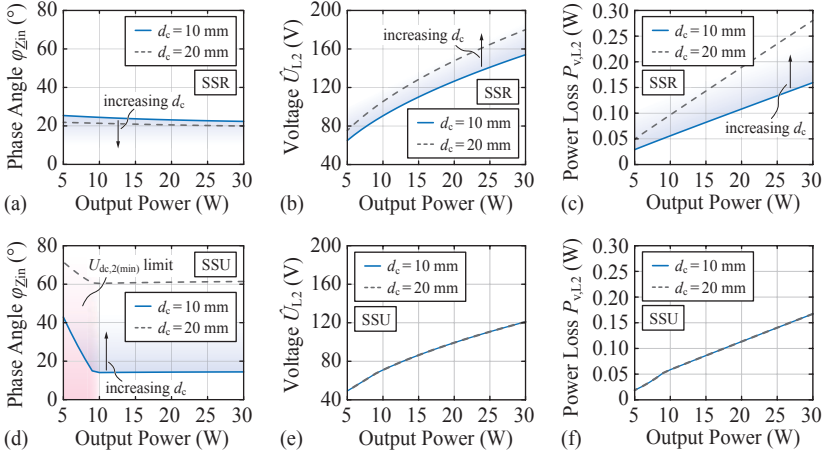


Fig. 2.35: (a)-(c) Performance indicators for the SSR-operation using the *efficiency optimal control*, and for the SSU-operation using the *constant load impedance control* in (d)-(f), calculated for variable output power and coil separation distances d_c of 10 mm and 20 mm, and the IPT resonant circuit parameters given in **Tab. 2.3**.

at minimum and maximum output power is 1.6% and 0.75% lower compared to the SSR IPT system operation, but above 90% in the entire operating range, which is a substantial improvement compared to the constant output voltage operation shown in **Fig. 2.31(a)**.

In the following, the two operating modes of the series-series compensated IPT systems are compared in more detail and the advantages or disadvantages of each system are highlighted, particularly with regard to the application at hand.

2.6.3 Discussion

Fig. 2.35 shows different performance indicators, which are particularly important for the TET system application at hand, calculated for the SSR-compensated and the SSU-compensated IPT systems, using the previously explained control strategies. These indicators are the phase angle of the input impedance $\varphi_{Z_{in}}$, the secondary-side coil peak voltage \hat{U}_{L2} and the secondary-side coil power loss $P_{v,L2}$, which are calculated for the IPT resonant circuit specifications shown in **Tab. 2.3**,

considering a variable output power and different coil separation distances. The implications of the analysis are summarized in the following:

- ▶ **Phase angle of the input impedance:** It was previously shown, that the phase angle of the input impedance is directly related to the energy transfer efficiency. For the SSR-compensation, using the *efficiency optimal control*, the phase angle of the input impedance is approximately constant, despite a varying output power, and is slightly decreasing with lower coil coupling factors (cf. **Fig. 2.35(a)**). In contrast, as shown in **Fig. 2.35(d)**, in case of the SSU-compensation, the phase angle of the input impedance increases significantly at large coil separation distances, which in turn reduces the energy transfer efficiency.
- ▶ **Secondary-side coil peak voltage:** A main disadvantage of the series-series compensated IPT system are the large IPT coil voltage amplitudes. Specifically on the secondary side, a large coil voltage bears several potential safety risks for the patient. The ISO 14708-1 international standard on the general requirements for safety of an active implantable medical device states, that any insulation of electrical conductors must withstand a dielectric strength test in which the applied voltage is no less than twice the peak voltage experienced by the part [73]. In order to maintain the mechanical flexibility of the implanted IPT coil, a silicone elastomer is preferably used for the encapsulation, which generally offers a very high dielectric strength of more than 20 kV/mm [78] and which is also available for medical device encapsulations [79]. Hence, an appropriate electrical insulation of the TET coils is easy to achieve and could be reinforced further with an additional layer of PTFE (Polytetrafluoroethylene), which offers excellent dielectric and mechanical properties.

However, as shown in [80], the large secondary-side coil voltage significantly contributes to the Electro-Magnetic Field (EMF) exposure of the human tissue, and even though there exists an appropriate solution to this problem, as shown in **Chapter 4**, the secondary-side coil voltage should be kept as low as possible. In case of the SSR-compensated system, the secondary-side coil peak voltage is increasing with increasing coil separation distance, which is due to the *efficiency optimal control*, where the equiv-

alent load resistance is decreased with decreasing coil coupling factor. As a result, at a fixed output power, the IPT system output voltage is reduced, which in turn increases the coil currents as well as the coil peak voltages, as shown in **Fig. 2.35(b)**.

In contrast, the secondary-side coil peak voltage of the SSU-compensated IPT system is independent of the coil separation distance, since the equivalent load resistance is kept constant, regardless of a varying coil coupling factor.

- ▶ **Secondary-side coil power loss:** Excessive heating of the human tissue surrounding the implanted IPT coil can cause discomfort to the patient or even permanent tissue damage. Therefore, it is important to reduce the power losses in the secondary-side coil to a minimum. In case of the SSR IPT system, the secondary-side coil power loss shows a proportionality according to $P_{V,L2} \propto P_2/k$. Consequently, the coil power loss is increasing substantially with increasing coil separation distance (cf. **Fig. 2.35(c)**), which is a main disadvantage of the SSR IPT system operation.

As with the secondary-side coil peak voltage, the secondary-side coil power loss of the SSU-compensated IPT system is independent of the coil coupling factor and is only proportional to the output power. This clearly shows the main difference between the two systems. In case of the SSR-compensation, the coil power losses are balanced between the primary-side and secondary-side coil and are increasing simultaneously if the coil coupling factor decreases [43]. In contrast, in case of the SSU-compensation, the power losses are asymmetrically distributed, i.e. with increasing coil separation distance, the primary-side coil power losses are increasing significantly, but the secondary-side coil power losses are not affected by a varying coil alignment.

In that sense, the power transfer capability of the SSR-compensated system is mainly limited by the EMF exposure and the heating of the human tissue at increasing coil misalignment. In case of the SSU-compensated IPT system, the power transfer capability is mainly limited by the primary-side power losses and the maximum tolerable inverter input voltage.

In summary, the SSR IPT system offers an impressive performance regarding the energy transfer efficiency and regarding the coil misalign-

ment tolerance. The main disadvantages of the SSR-compensated system using the *efficiency optimal control* are the increased control effort, which requires an online estimation of the coil coupling factor, the increased size of the secondary-side DC-DC converter stage and the increasing secondary-side coil power loss and peak voltage at increasing coil separation distance and constant power transmission.

In contrast, the SSU-operation allows for a simplified control scheme, i.e. the *constant load impedance control*, without the need for a coil coupling factor estimation, and offers a reduced hardware complexity. In addition, at constant power transmission, the SSU IPT system offers a constant secondary-side coil power loss, regardless of the coil separation distance. Furthermore, in case of an interruption or failure of the wireless communication, the SSU system benefits from a significantly lower voltage gain, which increases the functional safety of the TET system. As a main disadvantage, the coil misalignment tolerance of the SSU IPT system is limited by the large reactive power circulation on the primary side.

2.7 Summary of the Chapter

This chapter provides a brief, comprehensible introduction into the concepts of inductive/wireless power transfer. Further, the fundamental theory of the mutual coupling of energy transfer coils, capacitive compensation and load matching, i.e. the design for maximum energy transfer efficiency, are explained. Additionally, both analytical and numerical models are presented, which allow for a power loss estimation in the various components of the IPT system, and which allow for a feasibility assessment of a high power TET system. The most suitable IPT system topology is determined and a highly efficient IPT system prototype is designed in order to experimentally verify the system performance and the power loss models.

The final part of the chapter covers the optimal operation and control of the series-series compensated IPT system topology. The operating schemes are experimentally verified and the main advantages and disadvantages are revealed.

The main results of this chapter are summarized as follows:

- An introduction into the concepts and theory of IPT systems is

provided and simple and generally applicable design equations are derived for the series-series and the series-parallel compensated IPT resonant circuit topologies, using simple and meaningful electrical equivalent circuits. In addition, the design for maximum energy transfer efficiency is explained and an analytical model is provided, which allows to predict the power loss in the IPT coils.

- ▶ A comparative evaluation of three commonly applied IPT resonant circuit topologies is conducted and as a result, it is shown that the series-series compensated IPT topology outperforms the secondary-side parallel compensated topologies in terms of secondary-side coil power loss, which is specifically the case if the output voltage of the IPT system is limited by the application.
- ▶ The electrical characteristics of the series-series compensated IPT system are studied in more detail and it is shown that at high operating frequencies, the parasitic capacitances of the secondary-side rectifier circuit cannot be neglected for the power loss modeling. Therefore, the rectifier load model is refined and an extended power loss model is developed, which includes the inverter and rectifier circuit as well as its parasitic circuit elements.
- ▶ Based on the provided design guidelines, a highly efficient IPT hardware prototype is realized using latest GaN semiconductor technology and energy transfer coils with a diameter of 70 mm. A hardware prototype is used to experimentally verify the theoretical considerations and the power loss models. In order to further improve the energy transfer efficiency, a highly compact synchronous rectifier circuit is developed, which allows for a self-controlled, autonomous operation and which replaces the simple and lossy diode rectifier circuit. As shown, a careful design of the synchronous rectifier allows to reduce the secondary-side IPT power losses by up to 40 %.
- ▶ Measurements verify that the SSR-compensated IPT system, using the *efficiency optimal control* method, achieves the highest power conversion efficiency in the specified coil coupling and output power range, but comes at the expense of a complex control system that requires an online estimation of the coil coupling factor. The SSU-compensated IPT system, using a *constant load*

impedance control method, offers similar performance at high and moderate coil coupling factors, but suffers from a large reactive power circulation on the primary side at low coil coupling factors, and hence has only a limited power transfer capability at large coil separation distances.

- For coil separation distances up to 20 mm, the SSR-compensated IPT system allows for DC-DC efficiencies of more than 92%, and attains a maximum efficiency of 96.9% at a minimum coil separation distance of 10 mm and maximum output power. In case of the SSU IPT system using the *constant load impedance control*, the DC-DC efficiency is greater than 90% in the entire operating range, i.e. for coil separation distances up to 20 mm, and reaches a maximum of 97% at a minimum coil separation distance of 10 mm and ideal axial alignment. Note that these efficiency measurements cover the IPT power stage only and do not include the primary-side FPGA and auxiliary power supply power losses or the losses of any additional primary-side or secondary-side DC-DC converter stage needed for the TET system control.

The heating of the human tissue due to the power losses in the energy transfer coils is subject to applicable regulations and in case of an excessive heating may harm the patient. Consequently, the maximum feasible tissue temperature constitutes a main limitation on the IPT coil design and on the power transfer capability of the IPT system. Therefore, in the following chapter, a thermal simulation model is presented, which allows to predict the temperature in the human tissue in close proximity to the IPT coils, and hence, is used for the thermal safety assessment of the TET system prototype.

3

Thermal Model

THE TET System prototype presented in **Section 2.4.1** is designed for a maximum power transfer of 30 W. This power level is targeted to allow for the operation of LVADs for left- or bi-ventricular support or even for the operation of a TAH, including the capability to charge an implanted backup battery. Even if the TET system is optimized for highest energy efficiency, at high power transmission, a substantial power loss generation can be expected at the external and the implanted TET coil. Hence, the heating of the human tissue in close proximity to the TET coils can be significant and can cause discomfort or could even result in permanent tissue damage. Therefore, in order to assess the thermal safety of a TET system design, the estimation of the tissue temperature is important.

The aim of this chapter is to give a brief introduction into the heat transfer mechanisms in the human skin and subcutaneous tissue and to show the numerical thermal model which was used throughout this thesis to estimate the temperature rise in the human tissue due to the TET coil operation.

3.1 Heat Transfer in the Living Tissue

The thermoregulation of the human organism is a complicated process and involves different mechanisms of heat transfer in the living tissue, such as thermal conduction and convection due to blood perfusion. The main heat source of the body is the metabolic heat generation, which varies with the physical activity and the type of tissue [81]. Specifically the skin, as an interface to the external environment, plays an important

role in the thermoregulatory system of the human body [82].

In order to regulate the body core temperature to about 37°C , the body controls the metabolic heat production, the peripheral blood flow, i.e. by vasomotion, and the sweat production. The thermal interaction of the human body with the environment is mainly determined by conductive, convective and radiative heat transfer. As a last resort, in order prevent overheating, the human body is able to enhance the cooling significantly by the evaporation of sweat at the skin's surface [81,82].

For the application at hand, the focus is more on the localized thermal heat transfer rather than on the systemic thermoregulation of the whole body. Hence the following sections cover the thermal modeling of the tissue surrounding the implanted TET coil and are briefly discussing the adverse effects of excessive local heating of the tissue.

3.1.1 Bioheat Transfer Model

For the TET system implantation, it is assumed, that the energy receiving coil is inserted into the subcutaneous fat layer on top of the left or right pectoral muscle of the chest. Hence, the tissue layer structure includes skin, subcutaneous fat and muscle tissue in the vicinity of the implanted TET coil.

As stated in [83], the complex thermoregulatory system of the human body does not allow for an exact mathematical modeling and/or assumptions and simplifications must be made in order to allow for a practical model implementation, while including the main features of the heat transfer processes. The most widely applied mathematical model that describes the heat transfer in the living tissue, accounting for the heat generation and the blood perfusion, is the bioheat transfer model proposed by Harry Pennes in 1948 [84], and is used in this work as well. Pennes' bioheat equation is given by

$$\rho_T C_T \frac{\partial T}{\partial t} = \nabla \cdot (k_T \nabla T) + \omega_b \rho_b C_b (T_{\text{art}} - T) + q_m, \quad (3.1)$$

which is basically the standard thermal diffusion equation with two added terms to account for the blood perfusion and the metabolic heat source. In the equation, ρ_T , C_T and k_T denote the density, the specific heat and the thermal conductivity of the human tissue, respectively. The thermal effect due to the blood perfusion is modeled with ω_b , ρ_b and C_b , which are the blood perfusion rate, the density and the specific heat of the blood. T and T_{art} denote the temperature of the local

tissue and the arterial blood respectively. The metabolic heat source is described with q_m .

The simplicity of this mathematical model comes at the expense of some limitations which are due to the underlying assumptions, which are outlined in [81,83] and which are summarized in the following:

- ▶ It is assumed that the thermal equilibrium of the blood and the surrounding tissue occurs in the capillary bed, i.e. in (3.1), it is assumed that the arterial blood temperature T_{art} is equal to the body core temperature and the vein return temperature is equal to the local tissue temperature. However, in fact, the thermal equilibrium takes place in the pre-arteriole and post-venule blood vessels and the arterial and venous blood temperature vary continuously from the body core temperature to the periphery. Hence, the pre-arteriole blood temperature and the vein return temperature differ from the body core temperature and the local tissue temperature, respectively. Both approximations overestimate the effect of the blood perfusion on the local tissue temperature.
- ▶ The blood perfusion in the tissue is modeled as a homogeneous, isotropic heat source or heat sink, i.e. neglecting the different sizes of the blood vessels or the blood flow direction. But even within the same skin layer, such as the dermis or hypodermis, there exists a large inhomogeneity and anisotropy, which is due to the presence of different blood vessels [82].
- ▶ The skin itself is a complex, self-regulated thermal system, which can react to local heating or cooling, mainly by regulating the blood perfusion in the tissue.

In [85] it is reported that when the human forearm skin is heated locally in an area of 7 cm^2 to a temperature of $39\text{-}39.5^\circ\text{C}$, the local skin blood flow rate rises to the 6-fold of the normal value. However, the simple bioheat transfer model according to Pennes in (3.1) takes the blood perfusion rate and the metabolic heat source as a constant value and therefore neglects the thermoregulatory mechanisms of the skin, such as vasomotion.

The shortcomings that arise from the simplifications and assumptions promoted the development of more complex thermal models, that are summarized [81,83]. In general, the thermal modeling approaches

can be classified into four categories [82]: First, in the simple continuum models, the effect of the blood perfusion is included in an effective thermal conductivity of the tissue. Second, in the vascular models, the actual structure of the blood vessels is modeled in detail, and hence, requires detailed information on the blood flow, e.g. the direction, the velocity field or the local blood mass flux, and the detailed anatomical data of the vascular structure. Third, hybrid thermal models, which combine different vascular and continuum models and fourth, thermal models, where the perfused tissue is modeled as a porous media. In [86], Pennes' bioheat model is extended to account for a temperature-dependent blood perfusion rate by means of a vasodilatory component, that is linearly dependent on the tissue temperature and a temperature-independent basal blood perfusion rate.

However, the implementation of a more complex model is difficult in practice, which is mainly due to the lack of information on the model parameters and is beyond the scope of this thesis. Therefore, it was decided to use the simple bioheat transfer model in (3.1) for the tissue temperature estimation throughout this thesis. Further, there exist parameter databases such as in [66], which provide all parameters needed to implement the thermal model according to Pennes.

3.1.2 Thermal Tissue Damage

The human body has only limited capabilities to deal with body temperatures above 37°C . Whereas a body temperature in excess of 42°C is life-threatening, for localized excessive heating, the human body is to some extent able to prevent permanent damage to the tissue by increasing the cooling of the affected body part, i.e. by increasing the blood perfusion and hence, by distributing the heat over a larger surface area.

For the thermal safety assessment of the TET system, the local tissue temperature and the time duration of the heat exposure are important. In [87] it was found that a local exposure of the human skin to a temperature of 44°C for more than 6 hours causes cutaneous burns and irreversible damage at the epidermal cells can be observed. Between 44°C and 51°C , the time at which irreversible cellular damage occurs is halved for each degree rise of the skin surface temperature. Below 44°C , the rate at which burning of the skin occurs decreases rapidly.

The maximum permitted heating of an active medical implant is

regulated by the international standard ISO 14708-1 [73]. It states that the temperature rise of any outer surface of the active medical implant shall not be greater than 2°C above the nominal body temperature of 37°C at any circumstances, including failure modes. Hence, in order to comply with the regulation, a temperature of 39°C is taken as a limit for the thermal assessment of the TET coil operation. As a threshold for permanent tissue damage, a tissue temperature of 42°C is used as a maximum limit for the thermal safety assessment for both the skin surface and the subcutaneous tissue temperature.

However, the thermal limit defined in the ISO 14708-1 standard is very restrictive and as outlined in [88], a heating of the skin and the subcutaneous tissue in close proximity to the TET coils up to 42°C can be considered safe, since according to [87], a local skin surface temperature of 43°C and an exposure time of less than 12 hours does not cause irreversible tissue damages. But from the perspective of the patient, it is highly questionable, if even a short-term heating of the local skin tissue up to 42°C is comfortable and as reported in [89], several test persons even experienced mild pain, when the skin tissue was locally heated up to this temperature.

The following section describes the implementation of the numerical thermal model presented in [46], which is used for thermal safety assessment of the TET coils.

3.2 Numerical Thermal Model

The calculation of the tissue temperature in close proximity to the TET coils is based on the axis-symmetric two-dimensional thermal FE-model presented in [47]. The model was created with COMSOL Multiphysics and the model structure is shown in **Fig. 3.1**.

The TET coil windings are modeled as solid disks of copper, which are enclosed by a silicone layer that provides the electrical insulation and a biocompatible interface to the surrounding tissue. The heat sources are defined by the total primary-side and secondary-side coil power losses, which are distributed homogeneously across the corresponding coil winding.

The secondary-side coil is embedded in the fat layer on top of the muscle tissue. The primary-side coil is covered by a clothing layer and is separated from the skin surface by a cotton fabric layer, which provides a thermal insulation. The simulations have shown that the thermal

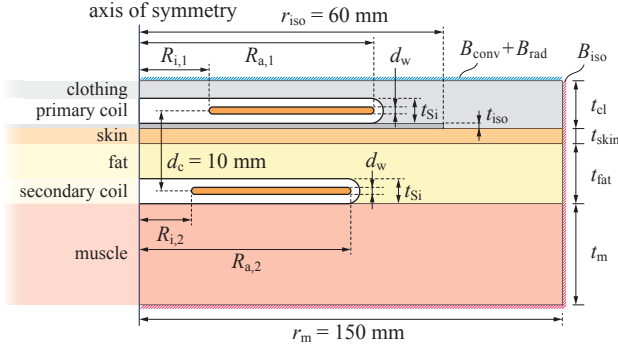


Fig. 3.1: Structure of the thermal simulation model.

insulation layer between the skin and the primary-side coil is important, since the power loss in the primary coil can contribute significantly to the heating of the skin and the subcutaneous tissue.

The dimensioning of the simulation model and the material parameter are summarized in **Tab. 3.1**. The physiological tissue material parameters used in this work are taken from the comprehensive tissue parameter database provided by the IT'IS Foundation [66]. Since for the thermal safety assessment only the steady-state temperature is of importance, the time derivative term in Pennes' bioheat equation (3.1) is set to zero. Hence, except for the blood, the material parameter values for the specific heat are not required, but are given in **Tab. 3.1** for the sake of completeness.

For the model at hand, as indicated in **Tab. 3.1**, the values for the blood perfusion rate and the metabolic heat source are reduced using scaling factors of 0.2 and 0.65 respectively. The reasons for this assumption and the derivation of these scaling factors are given later in **Section 3.4**.

As reported in [90], the neutral body core temperature, i.e. when the body is in a state of minimal thermoregulatory effort, is 36.8°C and the same value was used for the arterial blood temperature in (3.1). Initially, the skin layer was subdivided into two layers, to additionally model the epidermis with a thickness of $200\ \mu\text{m}$ and the same thermal parameter as for the skin given in **Tab. 3.1**, but without blood perfusion and without a metabolic heat source. However, the influence of this additional layer on the simulated temperatures is extremely small and

Parameter		Thermal	Density	Specific	Blood	Metabolic
Material	Length (mm)	conductivity (W/m/K)	(kg/m ³)	heat (J/kg/K)	perfusion ¹⁾ rate (1/s)	heat source ²⁾ (W/m ³)
Blood	-	0.52	1050	3617	-	0
Muscle	t_m 60	0.49	1090	3421	0.000672	991.9
Fat	t_{fat} 8.1	0.21	911	2348	0.000501	464.61
Skin	t_{skin} 1.4	0.37	1109	3391	0.001959	1829.85
Silicone	t_{Si} 3	0.23	1100	1300	-	-
Insulation	t_{iso} 0.5	0.026	327	1250	-	-
Clothing	t_{cl} 5.5	0.034	353	1250	-	-
Copper	d_w 1	400	8700	385	-	-

¹⁾ the blood perfusion rate values are scaled by a factor of 0.2 for the thermal simulations.

²⁾ the metabolic heat source values are scaled by a factor of 0.65 for the thermal simulations.

³⁾ IT'IS tissue properties database [66].

Tab. 3.1: Thermal model parameter used for the temperature estimation in the human tissue. The human tissue material parameters are taken from [66].

can be neglected and is therefore omitted in **Fig. 3.1**.

The selection of the model boundary conditions is difficult but yet important for a realistic prediction of the tissue temperatures. The thermal interaction of the human body with the environment is a complex process and the heat transfer is influenced by several factors, such as the ambient temperature, the air flow, the humidity, the radiative heat transfer and the thermal properties of the clothing. For the thermal model at hand, only the 'dry heat transfer' was considered, i.e. any evaporative heat loss was neglected. The heat transfer through the clothing layer is modeled considering conductive heat transfer only, with the thermal properties of the textile material taken from [91].

For the edge of the model towards the inside of the body, a thermal insulation boundary condition B_{iso} is defined as indicated in **Fig. 3.1**. With the thermal insulation boundary condition, the temperature 'deep inside the body' is mainly determined by the blood perfusion and the metabolic heat generation rate. A constant temperature boundary condition could be applied as well in order to better account for the well regulated body core temperature.

The total dry heat transfer from the human body to the ambient can be separated into convective and radiative heat transfer [92]. In previous work in [92, 93], the heat transfer coefficients for the convective and radiative heat transfer of the nude body was experimentally determined. The emissivity of the human skin is very high and the reported values range from 0.95 to 0.99 [93], and therefore shows the

properties of an almost perfect black body radiator.

According to [92], for the unclothed body, a linearized radiative heat transfer coefficient of $3.4 \text{ W}/(\text{m}^2\text{K})$ and $4.5 \text{ W}/(\text{m}^2\text{K})$ is reported for the chest for the human body in the standing and seating posture. The natural convective heat transfer coefficient is specified with $3.0 \text{ W}/(\text{m}^2\text{K})$ for both postures. In a more recent publication in [93], an emissivity of 0.98 was used for the evaluation of the radiative heat transfer and the linearized whole-body radiative heat transfer coefficient is specified with $4.4 \text{ W}/(\text{m}^2\text{K})$ for the standing human body posture. For the natural convection of the whole body, the measurement results in [93] have shown that the convective heat transfer coefficient is slightly rising for increasing skin-to-air temperature differences and attains a value of approximately $2.5 \text{ W}/(\text{m}^2\text{K})$ at a temperature difference of 10°C .

Hence, for the thermal model at hand, a heat transfer coefficient of $2.5 \text{ W}/(\text{m}^2\text{K})$ was used for the convective heat transfer boundary B_{conv} and for the radiative heat transfer boundary B_{rad} an emissivity of 0.95 was assumed at the clothing surface, which is equal to the reported skin surface emissivity. As a result, the total dry heat transfer coefficient, is approximately $8.5 \text{ W}/(\text{m}^2\text{K})$ at a clothing-to-air temperature difference of 10°C and 25°C ambient temperature, considering both the convective and the linearized radiative heat transfer. However, the surface emissivity of textile fabrics is greatly influenced by the surface structure and it was found later, that the assumed emissivity value is rather high and that for common textile fabrics, the emissivity is in a range of 0.55-0.85 [94, 95]. For the same temperature difference and ambient temperature specified above, the resulting average total dry heat transfer coefficient is calculated as $6.9 \text{ W}/(\text{m}^2\text{K})$ and the maximum value is $7.9 \text{ W}/(\text{m}^2\text{K})$. In [96], the dry heat transfer coefficients for the clothed human body was measured directly for different body segments and various wind speeds. In this case, an emissivity of 0.87 was reported for the clothing, and the total dry heat transfer coefficient was given with $10 \text{ W}/(\text{m}^2\text{K})$ for the chest at a wind speed of 0.2 m/s .

Hence, even though an emissivity of 0.95 of the clothing surface is overestimating the heat transfer in the thermal model at hand, the resulting total dry heat transfer coefficient is still in a reasonable range and therefore, the value was kept throughout the analysis.

In order to reduce the computation time for the temperature calculation of a large number of TET system designs, the maximum tissue temperature is calculated for four combinations of the primary-side and

secondary-side coil power losses only, i.e. for the 'power loss pairs' $[0,0]$, $[P_{v,L1},0]$, $[0,P_{v,L2}]$ and $[P_{v,L1},P_{v,L2}]$, where $P_{v,L1}$ and $P_{v,L2}$ denote the primary-side and secondary-side coil power losses at a selected operating point. With good approximation, the calculated temperatures are linearly dependent on the coil power losses, and hence, for a given coil geometry, the maximum tissue temperature at the surface of the implanted TET coil and the maximum skin surface temperature can be calculated for any coil power losses using linear interpolation. In order to allow for a variable coil geometry, a matrix of sample points is created with a coarse grid of the inside and outside coil radii $R_{a,i}$ and $R_{i,i}$, $i \in [1, 2]$ respectively, and hence allows to significantly reduce the number of FE-simulations. The maximum tissue temperature can then be calculated for each coil set and IPT system design in a post-processing step, using a six-dimensional linear interpolation function of the form

$$T_{\text{tissue(max)}} = f(R_{a,1}, R_{i,1}, R_{a,2}, R_{i,2}, P_{v,L1}, P_{v,L2}). \quad (3.2)$$

In order to verify the thermal safety of the TET system prototype at a power transmission of up to 30 W and to compare the thermal model with measured data, an animal experiment was conducted, which is described in the following section.

3.3 In-Vivo Experiment

In the course of the Zurich Heart project, several acute *in-vivo* experiments were conducted with adult male pigs in order to evaluate novel physiological control algorithms for the LVAD operation [97]. In two preliminary acute animal experiments, it was possible to additionally conduct a thermal experiment with the TET coil prototypes in parallel to the LVAD experiments, and hence, allowed to investigate the thermal safety of the TET system prototype.

Porcine skin has been used as a human skin model in many occasions. Since considering the general skin structure, thickness, hair follicle content, collagen and lipid composition, as well as the number, size and distribution of the dermal blood vessels, porcine skin has remarkable similarities with the human skin [87, 98, 99]. Therefore, the pig animal model is well suited for the thermal safety assessment of TET coils.

In order to avoid any Electro-Magnetic Interference (EMI) with the measurement equipment which was used for the LVAD experiments, it

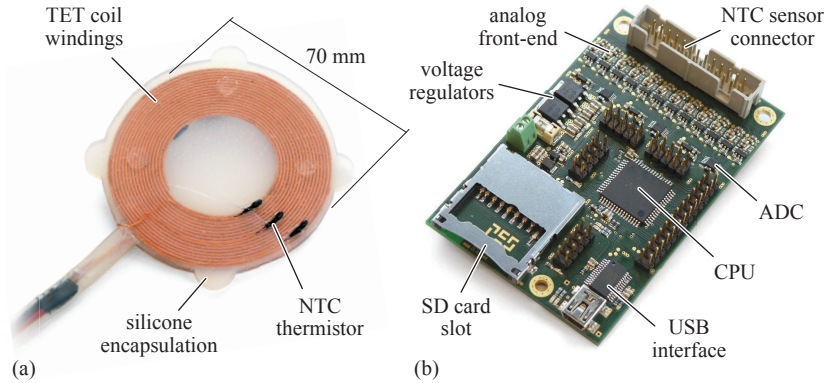


Fig. 3.2: (a) TET coil prototype used for the *in-vivo* experiment, including the attached NTC temperature sensors. (b) 12-channel temperature acquisition board.

was decided to simulate the TET system operation only by means of a direct electrical heating of each TET coil. The hardware realization of the identical external and implanted dummy TET coils is shown in **Fig. 3.2(a)**. The coil windings are built according to the prototype specifications given in **Tab. 2.2**. The two coils are encapsulated in RTV-3428 A&B silicone [100], which is a non-toxic two-component silicone that cures at room temperature. The resulting overall coil thickness is 3 mm and the silicone layer on each side of the coil winding is approximately 1 mm thick. In order to sense the temperature at different locations at the coils' surface, thermistors with Negative Temperature Coefficient (NTC) are used. In this case, the PS104J2 thermistors are selected, because of the small sensor volume and the high temperature accuracy of $\pm 0.1^\circ\text{C}$. The thermistors are connected to thin litz-wires and are coated with an acrylic paint for electrical insulation. The sensors are then attached at different positions on both sides of each TET coil. In total, six thermistors are distributed on both sides of the implanted coil and five sensors are placed on the external coil. An additional sensor was used to continuously log the ambient temperature. In order to record the measured temperatures, a specifically developed 12-channel temperature acquisition board was used, which is shown in **Fig. 3.2(b)**. Since the resistance value of the NTC thermistors are highly non-linear with respect to temperature, the tempera-



Fig. 3.3: *In-vivo* thermal experiment setup showing the implantation site of the secondary-side TET coil and the location of the external TET coil including the additional thermal insulation.

ture acquisition board logs the Analog-to-Digital Converter (ADC) raw data only, and the actual sensor temperatures are then computed in a post-processing step, using a look-up table of the sensor characteristics, which is provided by the sensor manufacturer.

Fig. 3.3 shows the implantation site of the secondary-side TET coil and the placement of the external primary-side TET coil, including its thermal insulation. Initially, an 8 cm long incision was made in the left abdomen and the skin and the subcutaneous tissue was removed from the muscle tissue. The secondary-side TET coil was then placed in the pocket, directly on top of the muscle tissue. The wound was then closed with surgical staples and the external TET coil was placed concentric to the implanted coil, in direct contact with the skin. The primary coil was then thermally insulated from the environment, using a 30 mm thick layer of polyurethane foam and everything was covered with surgical drapes.

The *in-vivo* temperature measurements of the preliminary experiment have confirmed, that the relationship between the steady-state tissue temperature and skin surface temperature is linear with respect to the power dissipation in the TET coils. Hence, in the second experiment, the steady-state temperature was measured for only four different operating points, which are defined by the coil power loss set-points. Accordingly, the obtained measurement data allow to infer the TET coil surface temperature at any sensor location for different TET coil

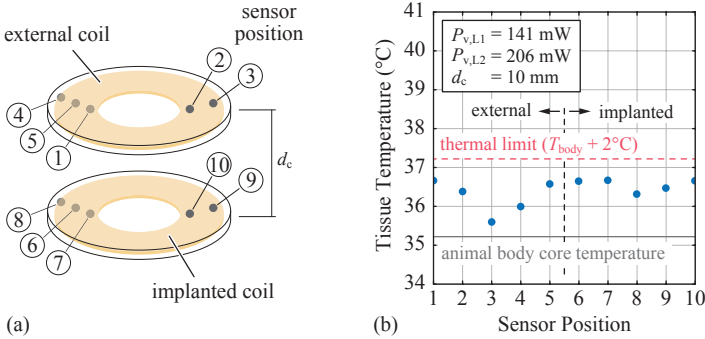


Fig. 3.4: (a) Temperature sensor distribution on the surface of the external and the implanted TET coil. (b) Interpolated steady-state sensor temperature for the operation of the TET coils, representing the SSU TET system prototype operation at an output power of 30.7 W and a coil separation distance of 10 mm.

power losses, using linear interpolation.

The positioning of each temperature sensor is shown in **Fig. 3.4(a)**. In this case, the coil separation distance is approximately 8-10 mm and the tissue thickness between the coils is about 5-7 mm. The power loss in each coil was generated using a DC power supply and was measured for both coils using Agilent 34410A multimeters. The measurement results of the steady-state sensor temperatures for the four different coil operating points are shown in **Fig. 3.5**.

The ambient temperature was slightly increasing throughout the experiment and had an average value of 25.26 °C. The measured animal body temperature was approximately 3.5 °C lower than the normal pig body core temperature of 38.6-39.2 °C. The reason for this hypothermia is mainly the anaesthetic-induced inhibition of the thermoregulatory control of the body [101]. In this case, also due to the cardiac surgery that was required for the LVAD experiments, the pig was put under deep anaesthesia, which was maintained with injections of propofol. In addition, a Constant Rate Infusion (CRI) of fentanyl was applied for pain relief [97]. Depending on the concentration of these anaesthetics, the thresholds for vasoconstriction and metabolic heat generation are reduced accordingly. Along with the air-conditioned environment of the surgery room, the body core temperature dropped substantially.

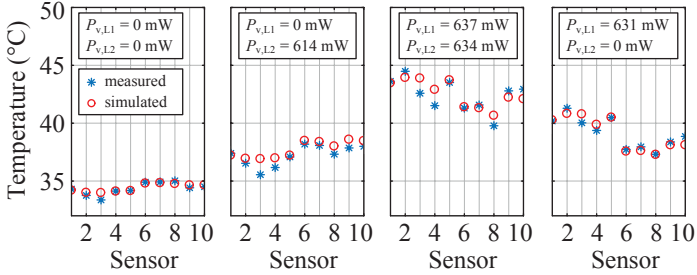


Fig. 3.5: Measured steady-state TET coil sensor temperature for different coil power losses and the calculated tissue temperature, obtained with calibrated FE-simulation.

Furthermore, for the conduction of the LVAD experiments, a cardiopulmonary bypass was installed, which further altered the heat content of the tissue and the heat distribution in the body [101]. However, the animal body temperature was supervised by medical personnel throughout the experiment and the body core temperature was stabilized at an average value of 35.2°C with a maximum temperature variation of 0.5°C .

Obviously, the thermal experiment has some limitations and it cannot fully reflect the real situation, but nevertheless, it provides a more realistic environment than an *in-vitro* experiment and furthermore, the animal experiment allowed for a more conservative thermal safety assessment of the prototype TET coil operation.

The measurements of the steady-state TET coil sensor temperatures shown in **Fig. 3.5** confirm that the external TET coil contributes significantly to the heating of the skin between the TET coils. For the maximum applied power loss of about 635 mW in each TET coil, a maximum tissue temperature of 43.6°C was measured at sensor position 1 (cf. **Fig. 3.4(a)**), which is located at the skin surface towards the inner winding of the external coil. Even if only the external TET coil is operated at a power loss of 631 mW, the temperature at the implanted coil attains values in a range of $37.3\text{--}38.9^{\circ}\text{C}$, which is $2.1\text{--}3.7^{\circ}\text{C}$ above the measured average body core temperature, and hence, underlines the importance of a thermal insulation between the two coils or an additional cooling of the primary-side TET coil.

Using the experimental data, the tissue temperature can be inferred for the operation of the SSU TET system prototype at maximum output

power and minimum coil separation distance, using linear interpolation. At an output power of 30.7 W and a coil separation distance of 10 mm, the primary-side and secondary-side coil power losses are calculated using the measured coil AC resistance (cf. **Tab. 2.2**) and the measured coil RMS currents, and attain values of 141 mW and 206 mW, respectively. The interpolated steady-state sensor temperatures are shown in **Fig. 3.4(b)**, and as a result, it is shown that each sensor temperature remains below a temperature rise of 2 °C with respect to the animal body core temperature. Hence, it can be concluded that the resulting TET coil surface temperatures are well below the harmful level and even comply with the ISO 14708-1 standard.

However, if the primary-side coil is misaligned, i.e. losing perfect axial alignment, the primary TET coil power loss and the skin surface temperature are increasing at constant power transmission, which again promotes a good thermal insulation between the skin surface and the primary coil. An additional heat-spreader could further help to remove the heat from the primary-side coil more effectively.

3.3.1 Comparison with the Numerical Model

In a next step, the temperature measurement is compared to the numerical simulation model. An axis-symmetric FE-simulation model similar to **Fig. 3.1** was created that represents the simplified structure of the animal skin and the implanted TET coil. For the model material parameters, the values from **Tab. 3.1** are used. The thermal insulation layer covering the external TET coil was modeled with a density of 30 kg/m³ and a thermal conductivity of 0.045 W/(m·K). At the boundary to the environment, a convective heat transfer coefficient of 2.5 W/(m²K), and for the radiative heat transfer, an emissivity of 0.95 was used. The ambient temperature was set to 25.26 °C and for the arterial blood temperature, the body core temperature of 35.2 °C was used for the simulation model. In order to compare the measurements and the simulations, the same coil power losses as in the experiment are used to model the heat source for each TET coil. In a post-processing step, after the simulation, the temperatures are evaluated in the model at the location of the actual sensor position. The comparison of the simulations with the measurement data has shown that the simulated steady-state temperatures and the temperature gradient among the various operating points are lower than the measured values.

Despite the existing model uncertainties, there are two reasons that possibly caused the discrepancy: First, as explained in **Section 3.1.1**, Pennes' bioheat equation shows some modeling limitations or shortcomings and overestimates the effect of the blood perfusion on the local tissue temperature. Furthermore, due to the anaesthetics, the thermoregulatory mechanisms of the animal body are inhibited to some extent.

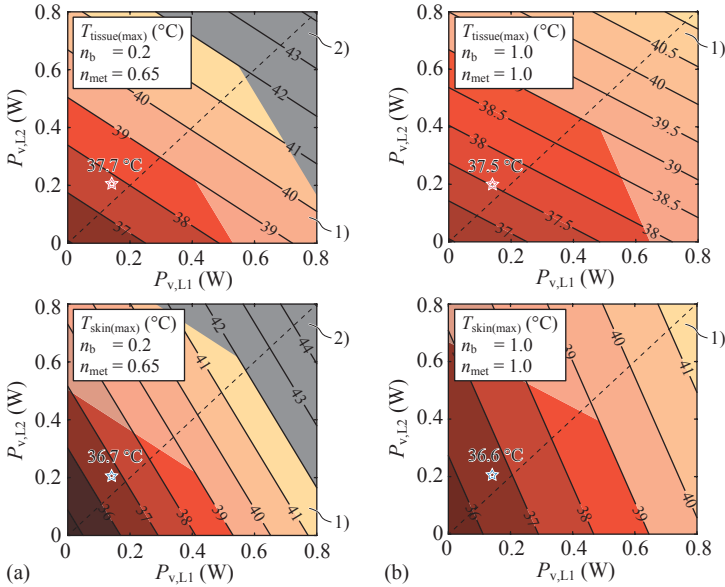
Hence, the model parameter for the blood perfusion rate and the metabolic heat generation given in **Tab. 3.1** are scaled with factors $n_b \in [0, 1]$ and $n_{\text{met}} \in [0, 1]$ respectively, in order to match the simulation, i.e. the gradient and the simulated steady-state temperatures, to the measured values. As a result, it was found that scaling factors of $n_b = 0.2$ for the blood perfusion rate and $n_{\text{met}} = 0.65$ for the metabolic heat source allow for a relative error of less than 4% between the simulated temperatures and the experimental data (cf. **Fig. 3.5**).

However, in reality, the thermal mechanisms and its interactions are highly complex and as highlighted above, the thermal model is subject to significant simplifications and parameter uncertainties. Hence, as an intermediate conclusion it is important to stress the following two points with regard to the model accuracy:

- ▶ First, the values for the blood perfusion rate and the heat generation rate reported in the literature, e.g. in [66, 82, 88], show large variations, e.g. for the muscle tissue, the maximum reported values deviate by a factor of up to five from the minimum value [66].
- ▶ Second, the boundary conditions are very important for an accurate estimation of the local temperature distribution. However, these conditions are rarely known with good accuracy and depend on many factors like the ambient temperature, air speed, humidity, thermal radiation, the clothing of the patient, implantation site, and other physiological factors, such as elevated body temperature due to increased physical activity.

It is hardly possible to account for all the mentioned model uncertainties. Therefore, the thermal safety assessment of the TET system prototype presented in the following section is an estimation only and is no guarantee that the thermal safety can be maintained under all circumstances.

Furthermore, it was decided to maintain the scaling factors for the blood perfusion rate and the metabolic heat source in the thermal



☆ ☆ SSU TET system prototype operating point ($P_2 = 30.7$ W, $d_c = 10$ mm)

- 1) $T_{\text{tissue(max)}} > 39^\circ\text{C} \cap T_{\text{skin(max)}} > 39^\circ\text{C}$
- 2) $T_{\text{tissue(max)}} > 42^\circ\text{C} \cap T_{\text{skin(max)}} > 42^\circ\text{C}$

Fig. 3.6: Interpolation of the maximum skin and tissue temperature in contact to the prototype TET coils for a primary-side and secondary-side coil power loss up to 800 mW. In (a), the average blood perfusion rate and the metabolic heat source values taken from [66] are scaled by the factors n_b and n_{met} respectively. (b) Simulation results for the unscaled tissue properties. In addition, the thermal limits are indicated in each figure, i.e. when either the skin or the secondary-side coil surface temperature exceeds a temperature of 39°C (according to ISO 14708-1) or 42°C , which represents the tissue damage threshold.

model, which was also used for the analysis carried out in **Chapter 2**, **Chapter 5**, and in **Chapter 9**. In this case, the thermal model allows for a more conservative temperature estimation and in a real life situation, it can be expected that the heating of the tissue is even lower than the predicted values.

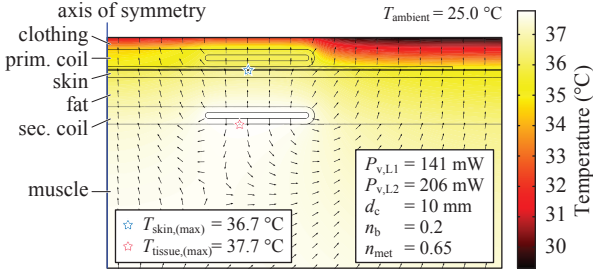


Fig. 3.7: FE-simulation result of the temperature distribution and heat flux for the SSU TET system prototype operated at a power transmission of 30.7 W and 10 mm coil separation distance.

3.4 Thermal Exposure Assessment

As the animal experiment with the prototype TET coils has already indicated, a power transmission of up to 30 W is feasible and the temperature rise complies with the ISO 14708-1 standard. In a next step, the thermal model from **Section 3.2** was used to investigate the thermal limits of the prototype TET coils, accounting for regular clothing of the patient. The simulation results for variable coil power losses up to 800 mW are shown in **Fig. 3.6(a)** and **Fig. 3.6(b)**, for the scaled blood perfusion- and heat generation rates and for the unscaled values, respectively. The maximum skin surface temperature and the maximum tissue temperature in contact with the implanted TET coil are indicated in the same figures for an operation of the SSU TET system prototype at 30.7 W and 10 mm coil separation distance. The corresponding simulated temperature distribution and heat flux is shown in **Fig. 3.7** for the scaled blood perfusion and metabolic heat generation. The skin and the subcutaneous tissue hot-spot temperature are located at the bottom side of each TET coil and attain values of 36.7 °C and 37.7 °C, respectively. At a distance from the TET coils, the steady-state temperature of the skin surface and clothing surface is 35.12 °C and 29.3 °C, respectively.

A comparison of **Fig. 3.6(a)** and **Fig. 3.6(b)** clearly shows the effectiveness of the blood perfusion. Even if the metabolic heat generation rate in **Fig. 3.6(b)** is higher than in **Fig. 3.6(a)**, the temperature gradient with respect to the coil power losses is much lower compared to the temperature values presented in **Fig. 3.6(a)**. For the

coil size at hand, in case of the scaled physiological tissue parameters, a primary-side coil power loss of 530 mW or an implant coil power loss of 500 mW could be tolerated at maximum, in order to comply with the ISO 14708-1 standard. With the unscaled blood perfusion- and heat generation rate the absolute maximum feasible power loss for the TET coils is 645 mW and 668 mW respectively, when the coils are operated individually. In the more realistic case, when both TET coils are active, the feasible coil power loss values decrease substantially, which is due to the mutual heating, as clearly visible from **Figs. 3.6(a)** and **(b)**.

For the SSU TET system prototype, the power loss of the secondary-side coil is largest at the maximum transferred power, and is independent of the coil alignment. Hence, from **Fig. 3.6(a)** it can be expected, that the primary-side coil power loss could be increased up to about 400 mW in order to still comply with the ISO 14708-1 standard and up to 800 mW until the thermal limit of 42 °C is reached at the skin surface.

In case of the SSR TET system prototype, the power loss in the primary-side and secondary-side coil increase simultaneously with decreasing coil coupling, which is due to the *efficiency optimal control* of the IPT system. In case of a symmetric IPT system, i.e. for identical TET coils, the power loss is equal in both coils. Hence, according to **Fig. 3.6(a)**, the total power loss in each TET coil could be about 300 mW and 575 mW in order to reach the 39 °C and the 42 °C thermal limit, respectively. In total, the SSR TET system is able to dissipate more heat in the TET coils, when compared to the SSU TET system. However, the increasing secondary-side TET coil power loss could still cause discomfort to the patient.

Note that the simulation results in **Fig. 3.6** are calculated for a coil separation distance of 10 mm and perfect axial alignment. Hence, the previously stated power loss limits are only an estimation for the skin and subcutaneous tissue hot-spot in case of lateral misalignment of the primary-side TET coil. Furthermore, the simulated values are valid only for the specific boundary conditions applied in the model at hand. If the clothing insulation layer is increased, or if the convective and/or radiative heat transfer coefficient at the clothing surface is changed, the simulation result might differ substantially.

In [36,102], an acute animal experiment with a sheep was conducted for the thermal safety assessment of a TET system. The primary-side coil diameter was 50 mm and the secondary-side coil diameter

was 40 mm. In this case, at a power transfer of 15 W, the maximum temperature rise was 5.5 °C and at 25 W, the temperature rise was approximately 8.4 °C. At an output power of 15 W and 10 mm coil separation distance, the maximum tissue temperature reached 42 °C and the primary-side and secondary-side TET coil power losses are reported with 300 mW and 426 mW, respectively. Hence, the area-related power loss densities of the primary-side and secondary-side coil are 65 mW/cm² and 34 mW/cm², respectively.

In contrast, for the TET system at hand, based on the conservative temperature estimation provided in **Fig. 3.6(a)** and assuming equal primary-side and secondary-side coil power losses, the maximum feasible area related power loss density is 15 mW/cm² for each coil, in order to ensure a tissue temperature of less than 42 °C. However, due to the mutual heating of the primary-side and secondary-side coil and due to the complex thermal system and variable environmental conditions, it is difficult to provide a generally applicable power loss density for the TET coils in order to simplify the thermal safety assessment of the TET system design.

3.5 Summary of the Chapter

A main objective of this chapter was to provide a thermal model that can be used for the thermal safety assessment of a TET system in a daily life situation. A main problem with the model implementation is the large parameter uncertainty, such as e.g. for the thermal boundary conditions, which are rarely known with good accuracy and may vary in a wide range.

The bioheat transfer model used in this work is based on Pennes' widely applied bioheat equation. However, the model contains some significant simplifications and has therefore only limited capabilities to reflect the actual thermal behaviour of the human tissue. Hence, the prediction of the actual temperatures of the tissue in contact with the TET coils is difficult and the thermal safety assessment of the TET system cannot rely only on thermal simulations, but must be experimentally verified. Nevertheless, the thermal model is easy to implement, uses only a limited parameter set and hence allows for a fast preliminary feasibility and safety analysis of a TET system design. Furthermore, if required, the thermal model can be extended easily, e.g. to allow for temperature-dependent blood perfusion.

The main results of this chapter are summarized as follows:

- ▶ A simple numerical thermal model based on Pennes' bioheat equation is provided with the full parameter set that is needed for the implementation, and which allows for the thermal safety assessment of the TET coils in a daily life situation.
- ▶ As pointed out in [81], it is likely that the effect of the blood perfusion is overestimated in Pennes' bioheat model. This is supported by the performed comparison of the measurement results with the simulated temperatures. Hence, the simulation model was calibrated using the measurement data in terms of a substantial reduction of the blood perfusion rate.
- ▶ Despite the limited ability of the animal experiment to represent the daily life situation for the TET system operation, it showed clearly, that with the TET system prototype at hand, a power transmission of up to 30 W is safe in terms of heating of the skin and subcutaneous tissue and that the temperature increase of the surrounding tissue can be kept below 2 °C.
- ▶ At maximum output power, the thermal simulation has shown for the SSU TET system prototype, that the primary-side coil power loss could increase up to about 400 mW and 800 mW to reach 39 °C and 42 °C, respectively. In case of the SSR TET system prototype, where the primary-side and secondary-side coil power losses increase simultaneously with decreasing coil coupling factor, the total power loss in each TET coil could increase up to 300 mW and 600 mW in order to comply with the 39 °C and the 42 °C thermal limit. Hence, the SSR TET system is able to dissipate more heat in the TET coils, but the increasing heating of the implanted TET coil could cause additional discomfort to the patient.
- ▶ In order to prevent the excessive heating of the tissue in contact with the implant or the TET coils, the temperature must be monitored continuously. Hence, when embedding temperature sensors into the TET coils, it is advantageous to use NTC thermistors with a high resistivity and a small volume in order to increase the noise immunity and to reduce the direct heating of the sensor due to induced eddy currents during TET system operation.

- ▶ Preferably, in order to enhance the coil alignment, the primary-side coil should be embedded in a close-fitting clothing item. And, in order to enhance the cooling of the primary-side coil, a flexible, thermally conductive polymer could be used to spread the heat over a larger surface area.

In this chapter, only the resistive power loss in the TET coils was considered as a heat source. However, during the operation of the TET coils, a strong electro-magnetic field is present in close proximity to the TET coils and the energy contained in that field is partly absorbed by the human tissue and is dissipated as heat. Accordingly, the exposure of the human body to the electro-magnetic field rises additional questions regarding the operational safety of the TET system. Hence, the interaction of the electro-magnetic field with the human body and its safety assessment are discussed in more detail in the following chapter.

4

Dielectric Model

THE analysis of the series-series compensated IPT system showed that due to the required high power transfer capability, large coil currents and voltages occur during operation. This imposes significant challenges for the design and optimization of the TET system and gives rise to major concerns regarding the potential safety risks. First, as outlined in chapter **Chapter 3**, the heating of the surrounding tissue due to the power losses in the energy receiver coil can lead to permanent tissue damage and must be taken into account during the design process of a high-power TET system. Second, the magnetic field, which is caused by the IPT coils, induces eddy currents in the tissue. These currents can evoke stimulation of nerve cells and muscle tissue, and cause additional heating. In the literature, the impact of magnetic fields on the human body is widely studied for IPT systems which are operated outside of the human body [103–106], as well as for low-power medical implants [107] and for a few TET systems powering an LVAD [108], [109]. In addition, depending on the power electronic converter topology and grounding scheme used for the TET system, the electric fields due to the large electric potential occurring at the power transfer coils can significantly contribute to the energy that is absorbed by the tissue and can excite electrically sensitive tissues, which is often neglected in the literature.

Therefore, based on the work presented in [80], the impact of the EMF exposure due to the TET system operation is investigated in this chapter, including the effects of the electric fields in the vicinity of the implanted energy receiver coil. In a first step, the dielectric properties of the various affected human tissues are introduced and the applicable regulations concerning the EMF exposure are summarized. In a second

step, a numerical simulation model is introduced, which allows to predict the electromagnetic field in the tissue at various operating points. The EMF exposure assessment is then demonstrated for the SSU IPT system prototype which was presented in the previous chapter. In addition, the resonant circuit topology and the grounding scheme of the implant are revised, with the objective to minimize the Common-Mode (CM) voltage at the implant IPT coil terminals, which tends to further increase the EMF exposure.

Finally, a shielding concept for the energy transmission coils is presented, which allows to reduce the peak electric field strength and the absorbed EMF energy in the human tissue.

4.1 Electrical Properties of Human Tissue

In order to evaluate the human exposure to the time-varying electromagnetic fields of an IPT system in close proximity or in direct contact with the human tissue, it is important to understand the basic electrical interactions of electromagnetic fields with the human body.

The human body has the permeability of air [110], i.e. $\mu_r = 1$, and therefore, the magnetic field that is generated by the IPT coils is barely disturbed by the tissue. However, the human tissue has the properties of a lossy dielectric material with frequency-dependent permittivity and electrical conductivity. Hence, an induced or an externally applied time-varying electric field generates conduction losses as well as dielectric losses within the tissue. Furthermore, the internal electric fields may excite electrically sensitive cells.

Assuming linear, homogeneous and isotropic materials, the current density in a lossy dielectric material caused by an applied electric field follows from the Maxwell's equations and is given by

$$\begin{aligned}
 \vec{J} &= \sigma \vec{E} + j\omega \vec{D} = \sigma \vec{E} + j\omega \underline{\varepsilon} \vec{E} \\
 &= j\omega \left(\underline{\varepsilon} - j \frac{\sigma}{\omega} \right) \vec{E} \\
 &= j\omega \left(\varepsilon' - j\varepsilon'' - j \frac{\sigma}{\omega} \right) \vec{E} \\
 &= j\omega \left(\varepsilon_0 \varepsilon'_r - j\varepsilon_0 \left(\frac{\sigma + \omega \varepsilon_0 \varepsilon''_r}{\omega \varepsilon_0} \right) \right) \vec{E}
 \end{aligned} \tag{4.1}$$

where $\underline{\varepsilon} = \varepsilon' - j\varepsilon''$ is the complex permittivity and σ is the conductivity of the material. As it is pointed out in [25], it is impossible to distinguish between σ and $\omega \varepsilon_0 \varepsilon''_r$, without knowledge of the atomic or molecular structure of the material. Therefore, the material parameters in (4.1)

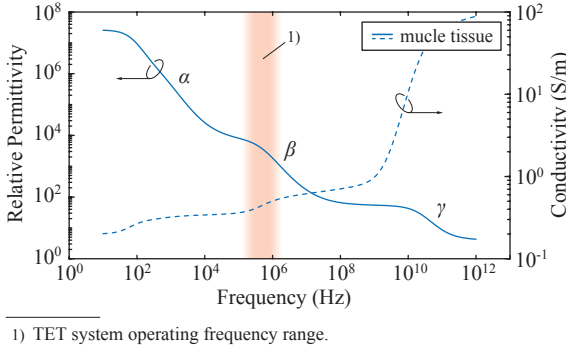


Fig. 4.1: Typical electrical properties of human tissue with its three main dispersion regions α , β and γ , shown at the example of muscle tissue [66].

can be replaced by a combined complex effective permittivity, which is given by

$$\underline{\varepsilon}_e = \frac{\vec{J}}{j\omega\vec{E}} = \varepsilon_0 (\varepsilon'_e - j\varepsilon''_e) = \varepsilon_0 \left(\varepsilon'_e - j \frac{\sigma_e}{\omega\varepsilon_0} \right), \quad (4.2)$$

where ε'_e determines the displacement current density contribution and is related to the amount of energy stored in the material due to an external electric field. The imaginary part ε''_e is related to the power loss generated within the tissue and is always larger than zero. Hence, the dielectric properties of the human tissue can be described with a real relative effective permittivity $\varepsilon_r = \varepsilon'_e$ and with an effective conductivity $\sigma_e = \omega\varepsilon_0\varepsilon''_e$, which accounts for both, conduction power losses and dielectric power losses, using the frequency $\omega = 2\pi f$ and the vacuum permittivity ε_0 [25, 111, 112]. Besides the strong frequency dependence, the dielectric properties depend on temperature as well, but to a lesser extent as reported in [111]; therefore, this dependency is neglected in this work.

The mathematical model that is used in this thesis to describe the dielectric properties of the human tissues, is provided by the work of Gabriel et al. [113] and is briefly summarized in the following. As explained in [111], the frequency-dependent permittivity of human tissues in the frequency range from the Hz to GHz can be divided into three main dispersion regions, referred to as α -, β - and γ -dispersion (cf. **Fig. 4.1**), which are characterized each by a different relaxation time constant given by the physical interaction, determining the time

Material Parameter	Cole-Cole Dispersion Model Parameter								
	ε_∞	σ_i (S/m)	$\Delta\varepsilon_1$	τ_1 (ps)	α_1	$\Delta\varepsilon_2$	τ_2 (ns)	α_2	
Skin (wet) ¹⁾	4.0	0.0	39	7.958	0.1	280	79.577	0.0	
Skin (dry) ²⁾	4.0	0.0002	32	7.234	0	1100	32.481	0.2	
Fat	2.5	0.035	9	7.958	0.2	35	15.915	0.1	
Muscle	4.0	0.2	50	7.234	0.1	7000	353.678	0.1	
Cortical Bone	2.5	0.02	10	13.263	0.2	180	79.577	0.2	
Bone Marrow	2.5	0.1	9	14.469	0.2	80	15.915	0.1	
Lung (inflated)	2.5	0.03	18	7.958	0.1	500	63.662	0.1	

Material Parameter	Cole-Cole Dispersion Model Parameter					
	$\Delta\varepsilon_3$	τ_3 (us)	α_3	$\Delta\varepsilon_4$	τ_4 (ms)	α_4
Skin (wet) ¹⁾	$3 \cdot 10^4$	1.592	0.16	$3 \cdot 10^4$	1.592	0.2
Skin (dry) ²⁾	0	159.155	0.2	0	15.915	0.2
Fat	$33 \cdot 10^3$	159.155	0.05	$1 \cdot 10^7$	15.915	0.0
Muscle	$12 \cdot 10^4$	318.310	0.1	$25 \cdot 10^6$	2.274	0.0
Cortical Bone	$5 \cdot 10^3$	159.155	0.2	$1 \cdot 10^5$	15.915	0.0
Bone Marrow	$1 \cdot 10^4$	1591.549	0.1	$2 \cdot 10^6$	15.915	0.1
Lung (inflated)	$25 \cdot 10^4$	159.155	0.2	$4 \cdot 10^7$	7.958	0.0

¹⁾ [113] ²⁾ [66]

Tab. 4.1: Cole-Cole dispersion model parameters and density of the human tissues [66, 113] used for the numerical simulation models.

dependence of the polarization of the material. In the GHz-range, dispersion arises mainly from the polarization of water molecules, whereas at hundreds of kHz, the polarisation and the structural changes of the cellular membranes, which control the flow of ions, are the main cause of dispersion. At low frequencies, the dispersion is due to ionic diffusion processes at the site of cellular membranes [111, 114].

According to [111] the dielectric properties of the human tissue in the frequency spectrum ranging from the Hz to the GHz regime can be described by a Cole-Cole dispersion model, comprising a total of four dispersion regions, which is given by

$$\varepsilon_e(\omega) = \varepsilon_0 \left(\varepsilon_\infty + \sum_{n=1}^4 \frac{\Delta\varepsilon_n}{1 + (j\omega\tau_n)^{(1-\alpha_n)}} + \frac{\sigma_i}{j\omega\varepsilon_0} \right), \quad (4.3)$$

where ε_∞ describes the permittivity in the terahertz frequency range and σ_i describes the ionic conductivity. Each dispersion region n is described by its relaxation time constant τ_n , the total permittivity variation $\Delta\varepsilon_n$ across the frequency range of the dispersion region and the parameter $\alpha_n \in [0, 1]$, which describes the broadening of the dispersion.

The dispersion model parameters for the tissues used in the FE-

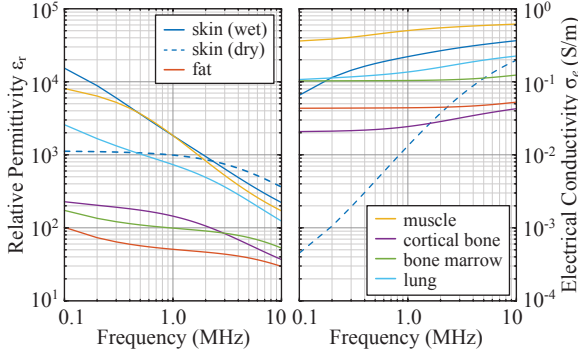


Fig. 4.2: Frequency dependency of relative permittivity and electrical conductivity of various human tissues, according to the material parameters given in **Tab. 4.1**.

simulations are summarized in **Tab. 4.1** and are taken from [66] and [113]. For the sake of completeness, the values are provided for the entire frequency spectrum ranging from the Hz to the GHz region. However, for the application at hand only the frequency range from 100 kHz to 2 MHz is of particular interest, which is mainly covered by the β -dispersion region, as indicated in **Fig. 4.1**. **Fig. 4.2** shows the relative permittivity and the electrical conductivity of the different tissues, calculated with (4.3) for the frequency range from 100 kHz to 10 MHz. It can be seen that specifically for the muscle and skin tissue, the permittivity and electrical conductivity vary by more than a decade in the considered frequency range.

4.2 Regulations on EMF Exposure

Today, there exists a variety of safety regulations and guidelines, which limit the exposure of the human body to time-varying EMF, such as the FCC 96-326 [115], the ANSI/IEEE C95.1-2005 [116], and the guidelines provided by the International Commission on Non-Ionizing Radiation Protection (ICNIRP) from 1998 [117] and from 2010 [110].

As stated in [110], in the frequency range between 100 kHz and 10 MHz, there exist mainly two potentially adverse health effects, that need to be considered. First, the induced and applied electric fields in

Frequency	RMS Current Density ($\frac{\text{mA}}{\text{m}^2}$)		RMS Electric Field Strength ($\frac{\text{V}}{\text{m}}$)	
	occupational	general public	occupational	general public
100 kHz - 10 MHz	³⁾ $f_{\text{Hz}}/100$	³⁾ $f_{\text{Hz}}/500$	¹⁾ $2.70 \cdot 10^{-4} \cdot f_{\text{Hz}}$	¹⁾ $1.35 \cdot 10^{-4} \cdot f_{\text{Hz}}$
3.35 kHz - 5 MHz	–	–	²⁾ $6.27 \cdot 10^{-4} \cdot f_{\text{Hz}}$	²⁾ $2.09 \cdot 10^{-4} \cdot f_{\text{Hz}}$

¹⁾[110] ²⁾[116] ³⁾[117]

Tab. 4.2: Basic restrictions on the induced current density and the internal electric field strength in the trunk of the human body [110, 116, 117].

the human tissue can excite nerve cells and other electrically sensitive tissues, which is of specific interest, since the TET system transfers the energy across the human skin, that contains peripheral nerve endings. Second, the ionic conduction loss and the dielectric power loss in the tissue generate heat, which may impair or even damage the cells.

Based on established health effects, the ICNIRP 1998 and 2010 guidelines provide exposure limits in terms of basic restrictions on the power loss generation, the induced current density and on the internal electric field strength [110, 117]. In the guidelines, there is an additional distinction between occupational and general public exposure. The occupationally exposed people are trained to be aware of the potential risks, where in contrast, the general public population, which includes individuals of all ages and medical conditions, is protected by more stringent safety limits [117] which are therefore more suitable for the safety assessment of a TET system.

In the latest guideline that was published by the ICNIRP in 2010, the induced current density has been replaced by the internal electric field strength as a limiting quantity, since it is the electric field that causes stimulation of nerve cells and electrically sensitive tissue in the frequency range up to 10 MHz [110].

Consequently, in the TET system operating frequency range in between 100 kHz and 2 MHz, EMF exposure can be quantified mainly in terms of internal electric field strength and the power loss generated within the human tissue. The latter is quantified by the Specific Absorption Rate (SAR), which is a measure of the time-average of the absorbed power per unit mass of tissue, specified as watts per kilogram. The peak SAR at each location within the tissue can be calculated according to

$$\text{SAR} = \frac{\sigma |E_{\text{RMS}}|^2}{\rho}, \quad (4.4)$$

Guideline	Averaging Mass		SAR ($\frac{W}{kg}$)	
	(g)	occupational	general public	
FCC 96-326 ¹⁾	1	8	1.6	
IEEE C95.1-2005 ²⁾	10	10	2	
ICNIRP 1998 ³⁾	10	10	2	

¹⁾[115] ²⁾[116] ³⁾[117]

Tab. 4.3: Basic restrictions on the local Specific Absorption Rate (SAR) evaluated for the specified averaging mass of tissue, for occupational and general public exposure [115–117].

where σ is the electrical conductivity, ρ is the density of the tissue material and $|\underline{E}_{RMS}|$ is the RMS electric field strength at the point of observation. For local EMF exposure assessment, the peak SAR is averaged over a contiguous tissue volume with a mass of 1 g or 10 g and is referred to as peak spatial-average SAR [116]. The tables **Tab. 4.2** and **Tab. 4.3** summarize the basic restrictions on SAR, internal electric field strength and induced current density for the frequency range from 100 kHz to 10 MHz.

The most restrictive SAR limit of 1.6 W/kg is proposed by the FCC 96-326 [115] for the general public exposure, averaged over 1 g of tissue. However, due to the large averaging volume of approximately 1 cm², some TET systems may comply with the regulations on peak spatial-average SAR, but the peak electric field strength may exceed the safety limits considerably. Therefore, in this work, according to the regulations provided by the ICNIRP in 2010 [110], the RMS electric field strength limit of $E_{RMS} = 1.35 \cdot 10^{-4} \cdot f_{Hz}$, which is specified for the general public exposure in the frequency range between 3 kHz and 10 MHz, is used for the exposure assessment. In this case, the safety limit is specified for a much smaller volume of human tissue compared to the SAR limits, i.e. as a vector average of the electric field in a contiguous tissue volume of $2 \times 2 \times 2$ mm³, and is therefore more suitable for the exposure assessment in close proximity to the implanted TET coil. In order to still provide a conservative assessment of the exposure levels, the spatial maximum value of the peak electric field strength is evaluated in the FE-simulations. Note that throughout the following analysis always peak values are considered instead of RMS values.

In the following sections, the numerical simulation model is introduced and the EMF exposure of the human tissue is assessed for the operation of the SSU IPT system prototype.

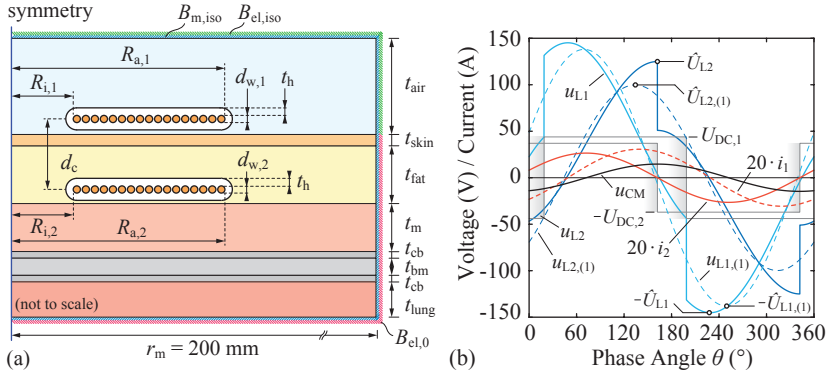


Fig. 4.3: (a) EMF simulation model geometry and (b) primary-side and secondary-side coil terminal voltages and currents for the SSU IPT prototype system, operated at maximum output power of $P_2 = 30 \text{ W}$ and 15 mm coil separation distance.

4.3 Simulation Model

In order to predict the magnitude of the internal electric field strength and the absorbed energy in the human tissue, an axis-symmetric, two-dimensional FE-simulation model of the human skin and the subcutaneous tissues was created, with the structure shown in **Fig. 4.3(a)**. Similar to the thermal model presented in **Section 3.2**, it is assumed that the energy receiving coil is implanted in the subcutaneous fat layer on top of the pectoral muscle.

The prototype TET coils are modelled with each single turn of the litz-wire winding, embedded in a silicone encapsulation. The dimensioning of the model and the electrical material properties of the human tissues are summarized in **Tab. 4.4**. The material properties are calculated according to (4.3) for the prototype TET system operating frequency of 800 kHz, using the dispersion model parameters given in **Tab. 4.1**. For the silicone insulation, a relative permittivity of 3.0 is used, according to the material parameters of the SILASTIC MDX4-4110 bio-medical grade elastomer [79]. The dissipation factor of the MDX4-4110 is specified in the data sheet with 0.001 at a frequency of 100 kHz. But in this case, the additional dielectric losses in the silicone layer are negligible and have no noticeable effect on the electric field strength and power loss in the human tissue, and hence, are neglected

Material Parameter	Length (mm)	Density (kg/m ³)	Relative Permittivity	Conductivity (S/m)	
Skin (wet) ¹⁾	t_{skin}	1.4	1109	2271.4 [†]	0.2070 [†]
Fat ²⁾	t_{fat}	13.6	911	52.4	0.0439
Muscle	t_{m}	15.0	1090	2336.9	0.4852
Cortical Bone	t_{cb}	1.5	1908	155.3	0.0235
Bone Marrow	t_{bm}	3.5	1029	102.0	0.1039
Lung (inflated)	t_{lung}	70.0	394	818.3	0.131
Air	t_{air}	120.0	1.2	1.0	0.0
Silicone	t_{h}	0.8-1.2	1100	3.0	2.50·10 ⁻¹⁴
Copper	d_{w}	0.95	8700	1.0	5.998·10 ⁷

[†]evaluated at $f = 800$ kHz.

¹⁾[113] ²⁾[66]

Tab. 4.4: Dimensioning of the EMF simulation model (cf. **Fig. 4.3**) and the electrical properties of the human tissue [66, 113], evaluated for the prototype TET system operating frequency of 800 kHz. The fat layer thickness is adjusted such that the coil separation distance d_c is 15 mm.

in the simulation.

The human tissue is exposed to the electromagnetic near field of the energy transmission coils. Therefore, in order to simplify the problem, a quasistatic approximation of the Maxwell's equations is used, such that the electric and the magnetic field can be calculated separately. This approximation is valid for the problem formulation at hand, since the coil geometry and the considered simulation volume is much smaller than the wavelength of the electromagnetic field in the human tissue at the considered operating frequency, and hence, the electric and magnetic fields are propagating instantaneously within the tissue [104, 118]. Furthermore, the TET system is operated at frequencies well below the self-resonance frequency of the energy transfer coils. Accordingly, the problem is split into an electro-quasistatic and magneto-quasistatic problem formulation. The total electric field and the current density in the tissue is then obtained from the superposition of the two solutions, which is valid as long as the material properties are linear with respect to the magnitude of the electric and magnetic field strength, which in this case is fulfilled.

The total power loss in the tissue volume V is calculated according to

$$P_{\text{v,tissue}} = \frac{1}{2} \iiint_V \sigma \vec{E} \cdot \vec{E}^* dV, \quad (4.5)$$

where \vec{E} is the vector of the complex total electric field amplitude that

is given by the superposition of the electric fields obtained from the electro- and magneto-quasistatic solution. Note that for the simulation model at hand, the power loss can be calculated separately in each quasistatic simulation and in the post-processing, and the power losses can be added up in order to obtain the total power loss. This however is a special case and is applicable only since in the model arrangement at hand, the electric field obtained from the electro-quasistatic solution is always perpendicular to the induced currents obtained from the magneto-quasistatic solution.

The boundary conditions used for the EMF simulation model are indicated in the model schematic in **Fig. 4.3(a)**. For the magneto-quasistatic problem, a magnetic insulation boundary condition $B_{m,iso}$ is used, enclosing the entire model geometry volume. For the electro-quasistatic problem formulation, a zero voltage potential boundary condition $B_{pot,0}$ is applied to the outer edges of the tissue model, in order to define the human tissue reference potential with respect to the TET coil terminal voltages and an electric insulation boundary $B_{el,iso}$, i.e. $\vec{n} \cdot \vec{J} = 0$, is used for the outer edges of the air volume.

In the following, the EMF exposure of the human tissue is assessed for the SSU IPT system prototype, operated at the maximum output power of 30 W and a coil separation distance of 15 mm. Accordingly, the calculated TET coil voltage and current waveforms shown in **Fig. 4.3(b)** are used as excitation sources of the EMF simulation model. For the magneto-quasistatic simulation, the excitation sources are defined by the amplitude and phase of the primary-side and secondary-side coil currents i_1 and i_2 . In addition, a homogeneous current distribution is assumed for each winding, which is ensured by the use of appropriate litz-wire. The sources for the electro-quasistatic simulation are defined by the primary-side and secondary-side coil terminal voltages.

Note that in [80], as a simplification it was assumed that the coil voltages u_{L1} and u_{L2} are sinusoidal and have an amplitude equal to the actual maximum coil terminal voltage, given by $\hat{U}_{L,i} = \hat{U}_{C,i} + U_{DC,i}$ ($i \in [1,2]$), which provides a worst case estimation of the peak electric field strength. Accordingly, the power losses and the peak electric field strength in the tissue are overestimated. Hence, it was decided to use the first harmonic of the coil voltages $u_{L1,(1)}$ and $u_{L1,(2)}$ (cf. **Fig. 4.3(b)**) as excitation sources of the electro-quasistatic simulation. With good approximation, the electric potential is distributed linearly

across the coil windings and accordingly, the voltage potential is defined for each individual turn of the TET coils.

But in order to calculate the electric field in the tissue, the electric potential of the surrounding tissue must be known with respect to the implant electronic circuit. This however raises the question of how the implanted electronic circuit is connected to the human body. Due to the capacitive coupling of the energy transmission coils to the surrounding tissue and depending on the grounding scheme of the implanted power electronic circuit, CM voltages can be present at the TET coil terminals, which in turn further increase the electric field strength in the tissue. This effect will be studied in more detail in the following section.

4.4 Influence of Common-Mode Voltage

In a first step, in order to predict the magnitude of the CM voltage, an electrical equivalent circuit model of the human skin and the subcutaneous tissue is considered. Second, the numerical simulation model presented in the previous chapter is used to evaluate the influence of the CM voltage on the EMF exposure. And third, the effect of the grounding scheme of the implanted power electronic circuit, i.e. the rectifier stage, is discussed and an experiment with the SSU IPT system prototype is carried out, in order to validate the theoretical considerations.

4.4.1 Equivalent Circuit Model

In order to analyze the CM current paths, an equivalent circuit of the prototype TET system and the subcutaneous tissue is considered as shown in **Fig. 4.4**, which models the electrical environment, in which the TET implant is operated. The model is used mainly to estimate the capacitive coupling of the energy transfer coils to the human tissue and to quantify the impedance of the tissue at the operating frequency. Similar to the method of impedances described in [119], the indicated resistors and capacitors which represent the electric impedances of the tissues are calculated for a very coarse mesh of sub-volumes. As a result, the estimated magnitude of the total tissue impedance $|\underline{Z}_T|$ between the implanted TET coil and the implanted controller is in a range of $250\ \Omega$ to $280\ \Omega$, considering the operation frequency of $800\ \text{kHz}$ and a distance of $200\ \text{mm}$ between the TET coils and the implanted controller.

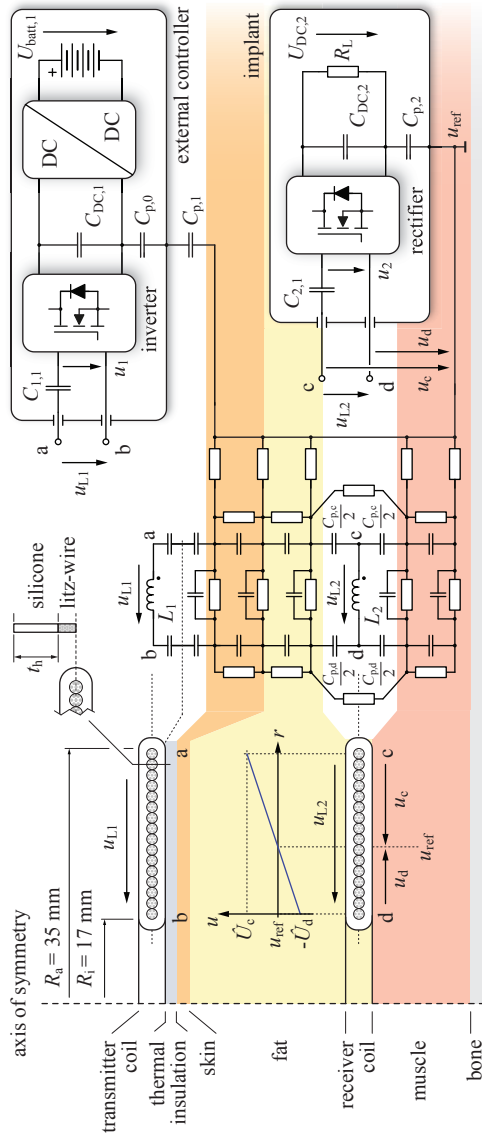


Fig. 4.4: Equivalent circuit of the human tissue, used to model the electrical environment in which the energy receiver coil and the implanted controller are operated.

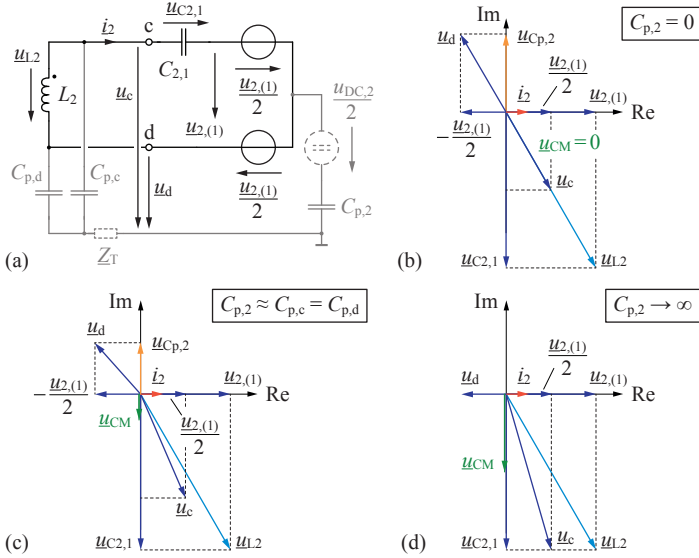


Fig. 4.5: (a) AC equivalent circuit of the implanted TET coil and the implanted rectifier circuit. (b)-(d) Phasor diagrams of the TET coil terminal voltages and CM voltage for different values of the parasitic capacitance $C_{p,2}$ and $C_{p,c}=C_{p,d}$.

The lumped parasitic capacitances $C_{p,c}$ and $C_{p,d}$ formed by the implanted coil and the surrounding tissue are estimated to be in a range of 65-100 pF for the prototype TET coil dimensions and a silicone insulation layer thickness ranging from 0.8 mm to 1.2 mm. The parasitic capacitance $C_{p,2}$ shown in **Fig. 4.4**, which couples the implant electronic circuit to the surrounding tissue is highly dependent on the actual design of the implanted controller and the power electronic circuit. Hence, the values of $C_{p,2}$ may vary in a wide range from 10 pF to more than 100 pF. Accordingly, the tissue impedance Z_T can be neglected in the first place when compared to the impedances of the parasitic capacitances at the operating frequency of the prototype TET system,

In the following analysis it is assumed that the capacitive coupling $C_{p,1}$ of the external controller to the human body is very small, such that the CM voltage at the transmitter coil terminals with respect to the human body is negligible.

In order to exactly calculate the CM voltage at the terminals of

the energy receiver coil, the AC equivalent circuit in **Fig. 4.5(a)** is used. Note that the AC voltage sources in **Fig. 4.5(a)** are consuming active power, as they simply represent the fundamental component of the rectifiers input voltage $\underline{u}_{2,(1)}$ across the equivalent load, that is observed at the rectifier input.

For the CM and the Differential-Mode (DM) voltage, the common definition

$$\underline{u}_{\text{CM}} = \frac{\underline{u}_{\text{c}} + \underline{u}_{\text{d}}}{2} \quad \text{and} \quad \underline{u}_{\text{DM}} = \underline{u}_{\text{c}} - \underline{u}_{\text{d}} \quad (4.6)$$

is used, where \underline{u}_{c} and \underline{u}_{d} denote the energy receiver coil terminal voltages with respect to the surrounding tissue. Hence, the coil terminal voltages can be calculated according to

$$\underline{u}_{\text{c}} = \frac{\underline{u}_{\text{DM}}}{2} + \underline{u}_{\text{CM}} \quad \text{and} \quad \underline{u}_{\text{d}} = -\frac{\underline{u}_{\text{DM}}}{2} + \underline{u}_{\text{CM}}, \quad (4.7)$$

using the equation for the receiver coil DM voltage given by $\underline{u}_{\text{DM}} = \underline{u}_{\text{C2},1} + \underline{u}_{2,(1)}$.

As indicated in **Fig. 4.5(a)** and as will be shown later, depending on the electrical connection between the implanted controller and the human tissue, there is also a DC CM voltage component present at the TET coil terminals, which is the result of the full-bridge rectifier operation. However, the DC component of the CM voltage does not affect the power loss generation in the tissue, as there is no DC current path through the tissue. Hence, only the AC equivalent circuit is considered, using the first harmonic component of the actual voltages and currents (cf. **Fig. 4.3(b)**).

Based on the equivalent circuit shown in **Fig. 4.5(a)**, and assuming that the impedance of the tissue Z_{T} is much smaller than the impedances of the parasitic capacitances $C_{\text{p},\text{c}}$, $C_{\text{p},\text{d}}$ and $C_{\text{p},2}$, the CM voltage at the TET coil terminals can be calculated with

$$\underline{u}_{\text{CM}} = \frac{\underline{u}_{\text{C2},1}}{2} + \underline{u}_{\text{Cp},2} = \frac{\underline{u}_{\text{C2},1}}{2} + \frac{\underline{u}_{2,(1)}(C_{\text{p},\text{d}} - C_{\text{p},\text{c}}) - 2C_{\text{p},\text{c}}\underline{u}_{\text{C2},1}}{2(C_{\text{p},\text{c}} + C_{\text{p},\text{d}} + C_{\text{p},2})}. \quad (4.8)$$

If it is further assumed that $C_{\text{p},\text{c}} = C_{\text{p},\text{d}} = C_{\text{p},i}$, equation (4.8) can be simplified to

$$\underline{u}_{\text{CM}} = \underline{u}_{\text{C2},1} \frac{C_{\text{p},2}}{2(2C_{\text{p},i} + C_{\text{p},2})}. \quad (4.9)$$

From (4.9) it can be seen that the CM voltage is in phase with the secondary-side compensation capacitor voltage $\underline{u}_{\text{C2},1}$ and its magnitude is dependent on the ratio of the parasitic capacitances $C_{\text{p},i}$ and $C_{\text{p},2}$.

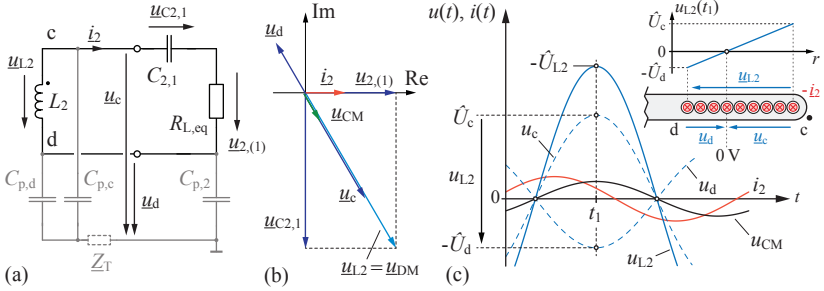


Fig. 4.6: (a) Simplified AC equivalent circuit of the energy receiver within the tissue. (b) Corresponding phasor diagram. (c) Asymmetric distribution of the TET coil voltage with respect to the human tissue due to a non-zero CM voltage.

Figs. 4.5(b)-(d) show the phasor diagram for the AC equivalent circuit shown in **Fig. 4.5(a)** for different values of the parasitic capacitance $C_{p,2}$. If ideally, $C_{p,2}$ is zero, the CM voltage at the TET coil terminals is zero as well, and the voltages u_c and u_d are equal in magnitude and exactly 180° phase-shifted with respect to each other, as shown in **Fig. 4.5(b)**. However, if the parasitic capacitance $C_{p,2}$ is not zero, the CM voltage is increasing, as shown in **Fig. 4.5(c)** for the case where $C_{p,2} \approx C_{p,c} = C_{p,d}$. In the extreme case, if the negative supply rail of the implanted power electronic circuit is connected by a low impedance to the implant enclosure and the surrounding human tissue, i.e. with $C_{p,2} \rightarrow \infty$, then the maximum CM voltage of $u_{CM} = u_{C_{2,1}}/2$ applies at the TET coil terminals and the voltages u_c and u_d differ substantially in magnitude, as shown in **Fig. 4.5(d)**.

Because of the circular coil winding it can be expected, that even with $C_{p,2} = 0$ a small CM voltage would apply to the TET coil, because in the model, the lumped coil capacitances $C_{p,c}$ and $C_{p,d}$ are not exactly equal. However, the exact distribution of the coil capacitance with respect to the surrounding tissue can be determined only by calculating the full capacitance matrix of the coil arrangement.

In order to get a more intuitive understanding of the TET coil voltage distribution and the influence of the parasitic capacitances, the AC equivalent model in **Fig. 4.5(a)** is simplified to the model shown in **Fig. 4.6(a)**, where the input of the rectifier is modeled with the equivalent load resistance $R_{L,eq}$. The associated phasor diagram is shown

in **Fig. 4.6(b)**. In this case, the voltages \underline{u}_c and \underline{u}_d are always 180° phase-shifted with respect to each other, and the CM voltage is in phase with the coil differential voltage, as long as \underline{Z}_T is negligible. This model implies that there is a turn in the receiver coil that has always the same potential as the surrounding tissue, and in presence of a CM voltage at the coil terminals, the potential is distributed asymmetrically across the winding with respect to the tissue, such that one coil terminal experiences a higher voltage stress than the other, as illustrated in **Fig. 4.6(c)**.

The asymmetric distribution of the TET coil voltage with respect to the tissue potential can be described for the simplified model with the ratio between the magnitudes of the CM voltage $\underline{u}_{\text{CM}}$ and the DM voltage $\underline{u}_{\text{DM}}$, given by

$$n = \frac{2\underline{u}_{\text{CM}}}{\underline{u}_{\text{DM}}} = \frac{\underline{u}_c + \underline{u}_d}{\underline{u}_c - \underline{u}_d} \approx \frac{C_{p,d} + C_{p,2} - C_{p,c}}{C_{p,d} + C_{p,2} + C_{p,c}}, \quad n \in [-1, 1], \quad (4.10)$$

which depends only on the capacitive voltage divider formed by the parasitic capacitances $C_{p,c}$, $C_{p,d}$ and $C_{p,2}$, assuming again that the tissue impedance \underline{Z}_T is much smaller than the impedances of the parasitic capacitances. Note that due to the model simplifications, the error of the calculated peak electric field strength is increasing with increasing CM voltage amplitude. For the expected parasitic capacitances of the TET coil and the implanted controller, a CM-DM ratio of $n = 0.05$ to $n = 0.45$ is expected. Within this range and for a coil insulation layer thickness of 0.8 mm, the calculated maximum electric field strength in the tissue is overestimated by a relative error of approximately 10 % at $n = 0.45$. Further note that mathematically, the ratio n can be negative as well, which simply means that the magnitude of the voltage \underline{u}_c is smaller than \underline{u}_d , i.e. if in the simplified AC model shown in **Fig. 4.6(a)** the coil terminals c and d are swapped.

4.4.2 EMF Exposure Assessment

Using the results from the previous section, the electric potentials at the receiver coil can be defined for the electro-quasistatic simulation and the EMF can be calculated in the surrounding tissue, including the AC component of the CM voltage at the TET coil terminals.

Fig. 4.7(a) shows the simulation results of the maximum electric field strength in the human tissue for different values of the parasitic capacitance $C_{p,2}$ with respect to the coil capacitances set to $C_{p,c} =$

$C_{p,d} = 100$ pF, calculated with the exact AC equivalent model shown in **Fig. 4.5(a)** for a maximum power transmission of 30 W. In this case, the coil separation distance is set to 15 mm and the silicone insulation layer thickness t_h is set to 0.8 mm. Note that for the simulation, the coil inductor current i_2 and the voltage $u_{2,(1)}$ are calculated according to the IPT system model presented in **Section 2.3**, which uses a resistive-capacitive equivalent load model that captures the operation of the synchronous rectifier more accurately. From **Fig. 4.5(a)** it is evident, that even if the parasitic capacitance $C_{p,2}$ is set to zero, the peak electric field strength exceeds the general public exposure limit of 152.7 V/m (at 800 kHz) as required by the ICNIRP 2010 guideline [110]. At the worst case, when the maximum AC CM voltage of $|\underline{u}_{C2,1}|/2$ applies at the receiver TET coil terminals (cf. **Fig. 4.5(d)**), the maximum electric field strength reaches 515 V/m and the peak SAR attains a value of 6.38 W/kg in the fat tissue, at the outer edge of the implanted TET coil, as shown in **Fig. 4.7(b)**.

More likely, the parasitic capacitance $C_{p,2}$ is in the range of the parasitic coil capacitances, i.e. $C_{p,2} \approx C_{p,c} = C_{p,d}$. This situation corresponds to the coil voltage and current waveforms depicted in **Fig. 4.3(b)**. The resulting magnitude of the simulated electric field strength and current density in the human tissue are shown in **Figs. 4.7(c)** and **(d)**, respectively. The peak power loss is generated in the fat tissue, at the outer edge of the implanted TET coil, where the electric field strength has its maximum. However, the highest current density is attained in the muscle tissue, directly below the implanted TET coil windings, and is due to the induced electric field, which is a result of the magnetic field, that is generated by the secondary-side TET coil. The maximum current density of 19.8 A/m² (198 μ A/mm²) exceeds the occupational exposure limit of the peak current density of 11.3 A/m² at 800 kHz, which is specified in the ICNIRP 1998 guidelines [117]. Nevertheless, the peak electric field strength in the muscle tissue is much lower than the basic restriction for general public exposure defined in the more recent ICNIRP 2010 guideline. Furthermore, the power loss density in the muscle tissue is also much lower than the peak power loss density in the fat tissue.

Figs. 4.8(a) and **(b)** shows the simulation results for the maximum internal electric field strength and the peak SAR for variable CM-DM ratios n and different coil silicone insulation layer thicknesses of 0.8 mm, 1.0 mm and 1.2 mm, according to the simplified AC equivalent model

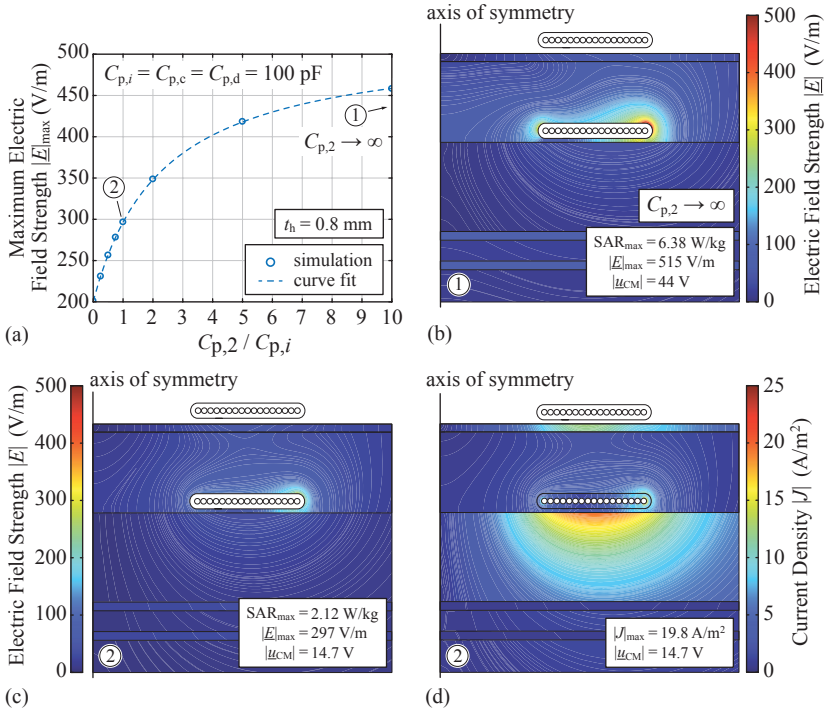


Fig. 4.7: (a) Simulation of the peak electrical field strength in the human tissue with respect to the ratio of the parasitic capacitances $C_{p,2}/C_{p,i}$, considering the exact AC equivalent circuit model shown in **Fig. 4.5(a)**. (b) Simulation result of the electric field strength in the human tissue for the maximum CM voltage, i.e. $C_{p,2} \rightarrow \infty$. (c)-(d) Simulated electric field strength and current density in the tissue at the operating point depicted in **Fig. 4.3(b)** and $C_{p,2} = C_{p,c} = C_{p,d} = 100$ pF.

shown in **Fig. 4.6(a)**. It can be seen that the maximum electric field strength rises almost linear with increasing CM voltage amplitude and the maximum SAR increases quadratically as expected from (4.4). Even small CM voltage amplitudes have a large impact on the EMF exposure, specifically on the electric field strength amplitude within the fat tissue. As indicated, a solution to reduce the peak electric field strength and the peak SAR, is to increase the thickness of the silicone insulation layer. However, in order to facilitate the TET coil implantation and

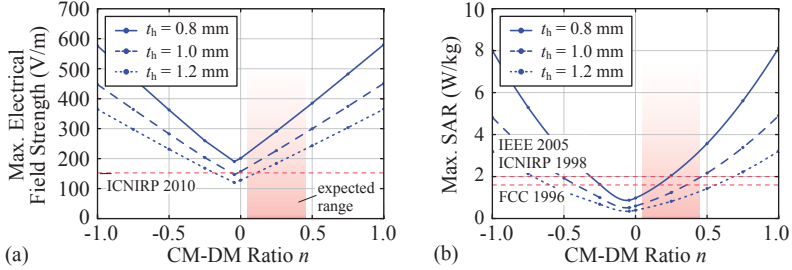


Fig. 4.8: (a) Simulation of the maximum electric field strength and (b) peak SAR in the tissue as a function of the ratio between the coil CM and DM voltage, $n = 2u_{\text{CM}}/u_{\text{DM}}$, with respect to the human body potential, according to the simplified equivalent circuit model shown in **Fig. 4.6(a)**.

in order to improve the wearing comfort for the patient, the receiver coil should be designed as thin as mechanically and electrically feasible. Another solution to mitigate the electric field strength in the tissue is to use an insulating material with lower relative permittivity, in order to confine the electric field within the insulation layer.

As a result of the simulations and the CM voltage analysis, it can be concluded, that specifically on the secondary side, the power electronic circuit topology depicted in **Fig. 4.4** causes substantial CM voltage magnitudes at the implanted TET coil, and hence, is not a feasible solution for TET systems, which are designed for an increased power transfer capability. Therefore, in the following, several topological improvements of the energy receiver circuit and the grounding scheme are investigated, which allow to suppress the CM voltage at the IPT coils.

4.4.3 Common-Mode Voltage Suppression

In order to validate the theoretical analysis of the common-mode voltage in the previous sections, an experiment was carried out using a dummy TET implant which includes a full-bridge diode rectifier circuit, the resonant tank capacitor and an external resistive load. The implant was built such that a parasitic capacitance of 84 pF between the negative rail of the rectifier circuit and a ground plane is formed. The ground plane has a size of 25×38 mm and is electrically connected to the tissue. As a model for the human skin, a $200 \text{ mm} \times 200 \text{ mm}$ piece of the chest of a pig, including skin, subcutaneous tissue, muscle and ribs was used.

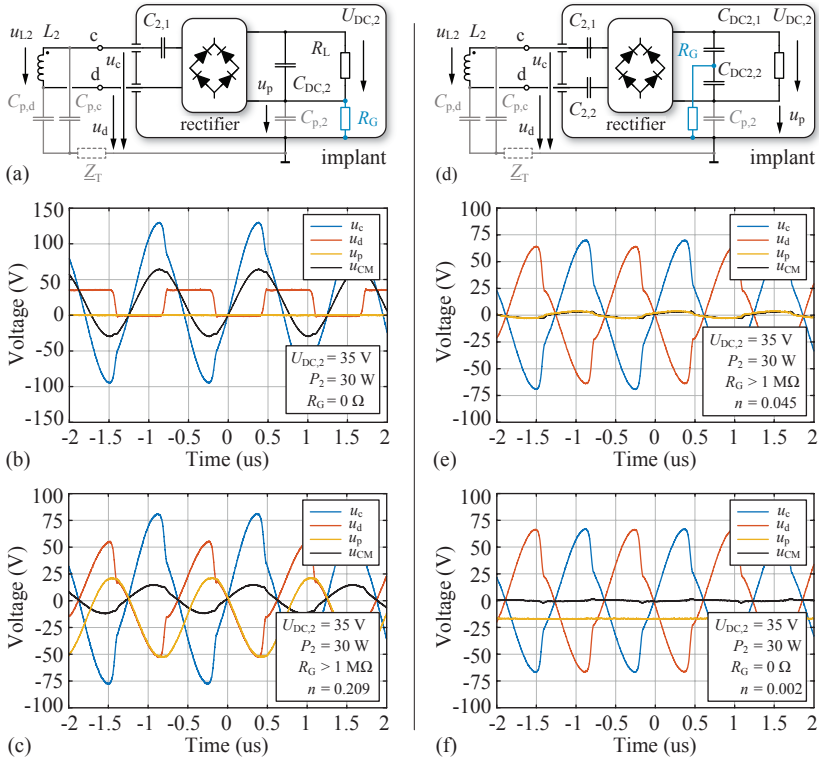


Fig. 4.9: (a) Basic energy receiver circuit topology and corresponding measured coil terminal voltages and the calculated CM voltage with respect to the surrounding tissue voltages in (b) and (c). (d) Improved circuit topology and the same voltage measurements as shown in (b) and (c) are depicted in (e) and (f).

The prototype receiver coil was inserted underneath the subcutaneous fat layer on top of the muscle in a distance of approximately 15 mm to the transmitter coil, which was placed directly on the skin's surface.

Two different types of the power electronic- and resonant circuit topologies are considered, including two different grounding schemes. The first topology comprises a single secondary-side resonant capacitor and either a low-impedance connection R_G or a capacitive coupling $C_{p,2}$ to the ground plane as indicated in **Fig. 4.9(a)**. The second topol-

ogy uses a balancing of the electrical circuit by means of a distribution of the secondary-side resonant capacitors between the two input terminals of the rectifier circuit, and either a low- or a high-impedance ground connection of the midpoint of the split DC-link, as indicated in **Fig. 4.9(d)**. The terminal voltages at the input of the receiver circuit and the voltage across the parasitic capacitance $C_{p,2}$ are measured with a LeCroy ADP305 differential voltage probe. The output voltage of the receiver circuit is set to 35 V and the maximum output power of 30 W is transferred across the tissue.

Fig. 4.9(b) shows the measured voltage waveforms for the basic receiver circuit topology depicted in **Fig. 4.9(a)**, using a low-impedance connection (i.e. $R_G = 0 \Omega$) between the negative DC voltage rail of the rectifier and the ground plane. In this case, the full differential voltage of the secondary-side TET coil is present at the coil terminal c with respect to the surrounding tissue, and hence, is causing a very high electric field strength in the tissue close to the edge of the TET coil. In addition, a DC CM voltage component of $U_{DC,2}/2$ is present at the TET coil terminal. This situation can be regarded as the worst case and should be avoided in any case.

Fig. 4.9(c) shows the voltage measurement for the same resonant circuit topology and for the case where the implant is just capacitively coupled to the surrounding tissue by the parasitic capacitance $C_{p,2}$. In this case, the CM-DM ratio n is approximately 0.21 and falls within the expected range of CM voltage magnitudes. However, the simulations have shown that in this case, the peak electric field strength exceeds the basic restrictions for all the considered coil insulation layer thicknesses. Therefore, the receiver circuit topology shown in **Fig. 4.9(a)** is not a feasible solution for the TET system at hand.

A substantial reduction of the CM voltage at the receiver coil terminals can be achieved with the circuit topology shown in **Fig. 4.9(d)**. In this case, the secondary-side resonant circuit is balanced by means of an equal distribution of the resonant capacitor to each input of the rectifier circuit. **Fig. 4.9(e)** shows the voltage measurement results for this topology and a parasitic capacitive coupling of the circuit to the surrounding tissue. As a result, the CM voltage is significantly reduced, but there is still an asymmetry observed between the coil terminal voltages. In order to further reduce the CM voltage, the circuit can be balanced completely by connecting the midpoint of the split DC-link to the ground plane of the dummy implant, i.e. with $R_G = 0 \Omega$. In this

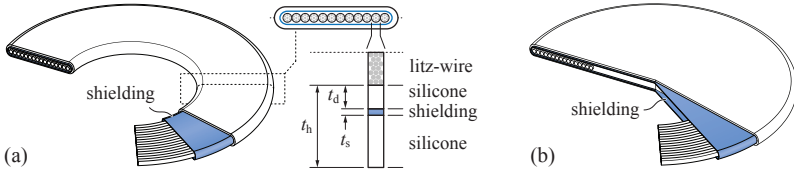


Fig. 4.10: (a) Schematic drawing of the TET coil shielding concept used for the numerical simulations (cf. **Fig. 4.11**). (b) Alternative TET coil concept including the electrical shielding.

case, as shown in **Fig. 4.9(f)**, the TET coil terminal voltages are fully symmetric and thus have the lowest voltage amplitude with respect to the tissue reference potential. However, the contact current might exceed the maximum permissible amount of 20 mA, which is specified as a reference level for the general public exposure in the ICNIRP 1998 and 2010 guidelines [110, 117]. Hence, the DC-link midpoint is preferably connected to the implant enclosure by means of a resistive or inductive connection, with an impedance of 100-500 Ω (at the operating frequency of 800 kHz).

According to **Fig. 4.8(b)**, for a silicone insulation layer thickness of 0.8 mm, the peak SAR can be reduced to 0.98 W/kg, using the improved circuit topology, and hence complies with the basic restrictions. However, the maximum electric field strength in the tissue of approximately 200 V/m still exceeds the basic restrictions significantly, if a coil insulation layer thickness of 0.8 mm is used. Therefore, in the following section, an additional electrical shielding technique is introduced for the TET coils, which allows to further reduce the maximum electric field strength and the peak SAR in the tissue.

4.5 Electrical Shielding

It was shown in **Figs. 4.7(b)** and **(c)** that the internal electric field strength has its maximum in close proximity to the receiver TET coil, which is due to the comparably low electrical conductivity and permittivity of the fat tissue. The simulation results obtained in **Section 4.4.2**, have shown that even with a fully balanced power electronic circuit, the basic restriction on the maximum electric field strength can be exceeded. As a solution, an additional layer of electrically conduc-

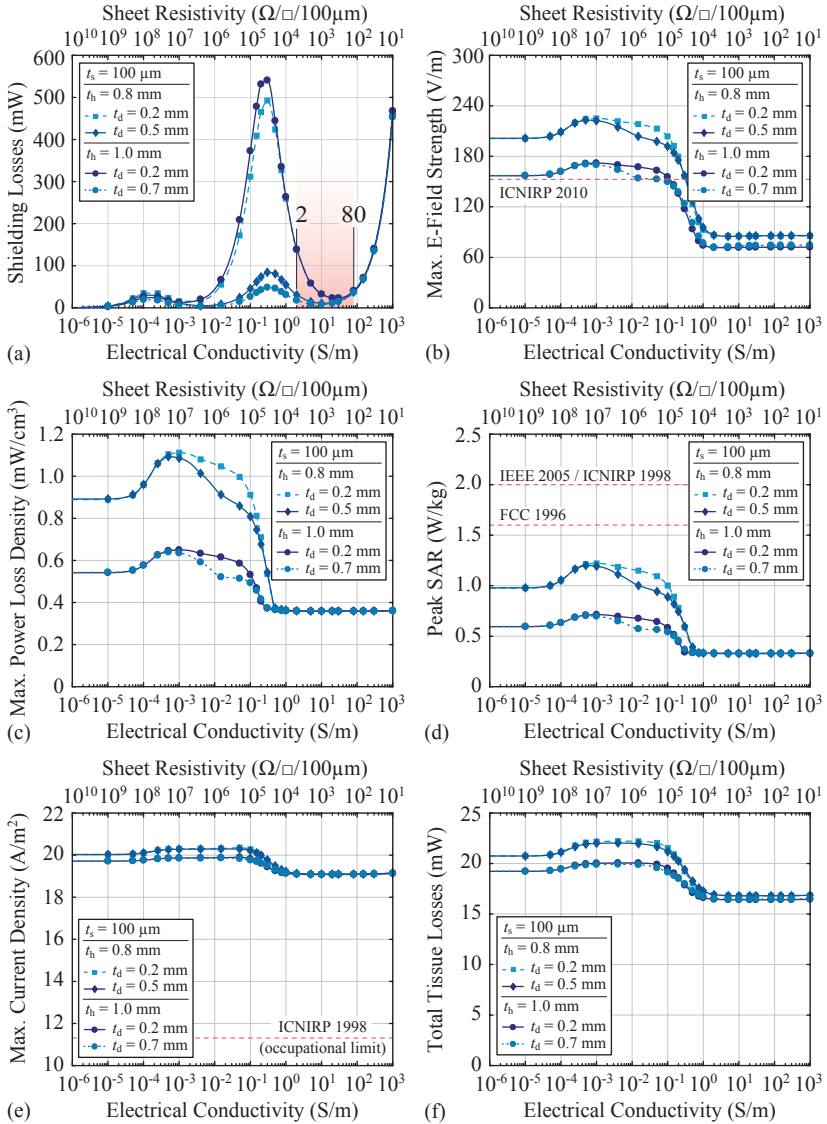


Fig. 4.11: TET coil shielding simulation: (a) shielding layer power loss, (b) max. electric field strength in the tissue, (c) max. tissue power loss density, (d) peak SAR, (e) max. current density and (f) total power losses in the tissue, with respect to the electrical conductivity of the shielding material.

tive material can be used within the silicone insulation of the TET coils, which acts as an electrical shielding and which allows to significantly reduce the electric field strength in the tissue.

In order to determine the optimal electrical conductivity of the shielding material, a parameter sweep was performed over a wide range of the electrical conductivity from 10^{-6} S/m to 10^3 S/m, using the numerical simulation model presented in **Section 4.3**. The shielding layer encloses the entire receiver coil winding and is embedded within the silicone insulation encapsulation, as illustrated in **Fig. 4.10(a)**. The thickness of the shielding layer t_s is set to 100 μm and it is assumed that the shielding material has the same relative permittivity as the silicone material, in order to eliminate the additional influence on the electric field distribution and magnitude. In addition, it was assumed that the IPT resonant circuit is fully balanced according to **Fig. 4.9(d)** and that the proposed optimal grounding scheme is used for the primary and secondary side of the TET system. In that case, any residual CM voltage can be neglected at the TET coil terminals. **Figs. 4.11(a)-(f)** show the simulation results of the total power loss in the shielding material, the maximum electric field strength in the tissue, the peak tissue power loss density, the peak SAR, the maximum current density and the total power loss in the tissue volume. The simulation was carried out for a coil insulation layer thickness t_h of 0.8 mm and 1.0 mm, and a variable distance between the shielding layer and the coil winding surface, according to the structure shown in **Fig. 4.10(a)**. From **Fig. 4.11(a)** it can be seen that if the electrical conductivity of the shielding material is increased to more than 0.01 S/m, the power loss in the shielding layer increases significantly, which is due to the increasing mobility of charge carriers, which are accelerated under the influence of the applied electric field. In turn, due to the displacement of the charge carriers, the applied electric field is partly cancelled, which is amplified as the shielding conductivity is increased. As a result, the power loss in the shielding material starts to decrease again. At this point, since the shielding layer starts to form an equipotential surface around the coil windings, the magnitude of the electric field strength in the tissue decreases significantly, as it is shown in **Fig. 4.11(b)**. However, if the electrical conductivity of the shielding material is further increased, the shielding power loss starts to increase again, which is due to the eddy currents that are induced in the shielding layer, caused by the strong magnetic field in close proximity to the TET coil. Hence, there exists

an optimal electrical conductivity of the shielding material in the range of 2-80 S/m, where the power losses in the shielding layer are at a minimum and the peak electric field strength in the tissue does not decrease any further. From **Fig. 4.11(a)** it is evident, that the shielding layer should be placed at the largest possible distance from the coil winding surface, in order to further reduce the shielding power loss. In this case, at the optimum electrical conductivity of 10 S/m, the shielding power loss of approximately 11 mW is about 1 % to the total IPT system power loss of 1.067 W, measured with the hardware prototype, operated at full output power and 15 mm coil separation distance (cf. **Fig. 2.31(b)**).

The electrical shielding layer cannot protect from the induced electric field, specifically in the muscle tissue, which is due to the strong magnetic field in proximity to the TET coil. Therefore, the maximum electric field strength, the peak SAR and the maximum current density are not decreasing any further if the electrical conductivity of the shielding material is increased beyond 1 S/m. In this case, the location within the tissue, at which the highest power loss is observed has moved from the fat tissue at the edge of the implanted coil to the muscle tissue, where the induced current density is the highest.

Materials with the desired electrical conductivity can be found in industry as carbon conductive composites, where a polymer is often used in combination with a conductive filler based on carbon black, which allows to control the conductivity of the compound in a wide range. As an example, conductive silicone rubbers, which are used for electromagnetic shielding applications [120, 121], are commercially available with a large variety of electrical conductivities ranging from 0.1 S/m to more than 100 S/m [78]. In another shielding application, semi-conductive tapes are used for the manufacturing of power distribution cables. In this case, the shielding layers ensure a uniform and gradual decrease of the electric field within the dielectric insulation of the cable [122].

As a result of the described electrical shielding method, the maximum electric field strength in the tissue can be reduced by a factor of up to 2.4 to about 85 V/m which reduces the peak SAR by a factor of 1.8 to 3 to about 0.33 W/kg, depending on the thickness of the silicone insulation layer. The achieved level of EMF exposure is therefore significantly lower than the basic restriction limits specified in the EMF exposure guidelines. However, the peak current density of 19.1 A/m² in the muscle tissue still exceeds the basic restriction limit provided by the ICNIRP 1998 guidelines. In this case, the only possibility to decrease

the current density in the muscle tissue is to use an additional shielding of the magnetic field below the receiver coil, which is beyond the scope of this work.

As stated in [116], other implanted electrically conductive objects, such as the LVAD may interact with the applied electromagnetic field, and may increase the EMF exposure of the tissue. Hence, in the final design stage, the exposure assessment of the TET system should be extended to the overall implanted system and should be performed using a more realistic 3D human body model, considering also nearby implanted electrically conductive objects.

4.6 Summary of the Chapter

In this chapter, the exposure of the human tissue to the time-varying electromagnetic fields in the vicinity of the TET coils is analyzed and discussed. The modeling of the dielectric properties of the human tissue is addressed and the applicable regulations on the EMF exposure are summarized. A numerical simulation model is introduced which allows for an EMF exposure assessment and the IPT resonant circuit topology as well as the grounding scheme of the secondary-side power electronic circuit is revised, in order to reduce the CM voltage at the implanted TET coil terminals. In addition, an electrical shielding technique is introduced, which allows to further reduce the EMF exposure of the human tissue.

The main results of this chapter are summarized as follows:

- ▶ It was shown that an EMF exposure assessment which is based only on the time-varying magnetic field and its induced electric field is not sufficient in the case of the series-series compensated IPT topology and the power transmission levels at hand. Because of the high voltages at the implanted TET coil terminals, the electric field strength in close proximity to the TET coil is increased and may exceed the basic restrictions significantly.
- ▶ Furthermore it was shown, that the magnitude of the internal electric field strength is highly dependent on the CM voltage magnitude applied to the receiver coil terminals, and depends also on the power electronic circuit topology of the implant. In order to

reduce the CM voltage and the EMF exposure to a minimum, the resonant tank of the TET system must be designed symmetrically and in addition, the midpoint of the split DC-link, located at the output of the rectifier circuit, must be connected to the implant enclosure, which in turn is electrically connected to the surrounding tissue.

- ▶ The internal electric field strength and the peak SAR can be further reduced by the use of an electrical shielding layer enclosing the energy transmission coils. For the prototype TET system at hand it was found that an electrical conductivity of the shielding material of 2-80 S/m is optimal in terms of minimizing the shielding power loss and enhancing the shielding effectiveness. In a practical realization, the shielding layer could be realized, e.g. using semi-conductive tapes or a carbon conductive silicone or coating, as part of the TET coils' encapsulation.
- ▶ Simulations have shown that using the electrical shielding, the maximum electric field strength and the peak SAR can be reduced from 202 V/m to 85 V/m and from 0.98 W/kg to 0.33 W/kg, respectively. Hence, both values comply with the applicable EMF exposure guidelines.

As a final remark, it must be noted, that the prediction of the magnitude and the distribution of the electromagnetic field in the human tissue is difficult, as the field distribution depends on many factors such as the electrical material properties of the tissues, the tissue distribution and its structure, which can hardly be captured completely by a numeric simulation. Therefore it is expected, that the effective EMF exposure in the living body may deviate considerably from the provided simulation results and a final exposure assessment can be provided only by means of a experimental verification. Nevertheless, the simplified electromagnetic simulations presented in this chapter allow for further optimizations of the TET system and allow to disclose the effects of the TET system operation on the EMF exposure of the human body.

Based on the thermal and the dielectric modelling presented in the previous chapters, the design limitations of the series-series compensated IPT system can be shown more generally for a large number of IPT system designs, which is the topic of the following chapter.

5

IPT System Design Limitations

BASED on the numerical models presented in the previous chapters, the design limitations of the series-series compensated IPT system are analyzed in more detail, regarding the heating and the electromagnetic field exposure of the tissue. In **Chapter 2**, it was shown that the energy transfer efficiency of the series-series compensated IPT topology can be increased using a higher operating frequency, i.e. by increasing the quality factor of the IPT coils, or by allowing higher IPT system operating voltages and therefore reducing the currents in the energy transfer coils.

It was then shown in **Chapter 4**, that higher IPT coil terminal voltages increase the local electric field strength in the tissue in close proximity to the implanted TET coils. On the other hand, small TET coil designs with low inductance values are operated at lower IPT system output voltages, and hence, are mainly limited by the heating of the human tissue due to the increased power loss density in the implanted TET coil.

Accordingly, the main objective of this chapter is to disclose the fundamental limitations imposed on the design space of the IPT system at hand, and to reveal the optimal operating frequency and output voltage range. The calculations are carried out for the SSU IPT system prototype specifications, but similar results are expected for the SSR IPT system operation, and the final conclusions are equally applicable to both operating modes.

5.1 IPT System Modeling

In a first step, an SSU IPT system is designed according to the design equations provided in **Tab. 2.1** for a vast number of feasible TET coil sets, which are generated according to the specifications given in **Fig. 2.10(b)** and considering an operating frequency range of 100 kHz to 2 MHz. In a next step, in order to evaluate the electric and the magnetic fields in the vicinity of the implanted TET coil of each SSU system design, the primary and secondary coil currents and voltages are calculated at the maximum output power of $P_2 = 30$ W and minimum coil separation distance of $d_c = 10$ mm. In addition, in order to estimate the total TET system efficiency and the maximum tissue temperature according to the thermal model presented in **Chapter 3**, the power loss of each circuit component is calculated using the power loss model presented in **Chapter 2**. In this case, the power loss calculations include the IPT resonant circuit as well as the primary-side inverter and the secondary-side synchronous rectifier circuit. Due to the capacitive load effect of the secondary-side synchronous rectifier explained in **Section 2.3.1**, the primary-side and secondary-side compensation capacitors are fine-tuned such that the input impedance of the resonant circuit seen by the inverter is slightly inductive with a phase angle in a range between 4.5° and 7° . The potential partial hard-switching operation of the inverter stage is neglected for the total power loss calculation and only the gate drive power losses, switch conduction losses as well as DC-link capacitor losses are considered. In the case of the synchronous rectifier, the conduction losses of the switches and diodes, as well as the gate drive and DC-link capacitor losses are considered. The dead-times of the rectifier switches are chosen such that the diode conduction time is 5 ns in each half-cycle and soft-switching of the rectifier is maintained in any case. The inverter and the rectifier switches are modelled with the EPC2016C GaN FET, including a MBR1H100SF Schottky diode connected in anti-parallel configuration to each switch.

The result of the efficiency calculation is shown in **Figs. 5.1(a)** and **(b)**. The calculated energy transfer efficiency attains values up to 98%. However, it is important to note that the calculation overestimates the system performance, as several sources of power losses are not considered in the calculation, such as the power losses caused by PCB tracks, the TET coil lead wires and connectors etc. Hence, the efficiency of the real system is expected to be considerably lower than the calculated

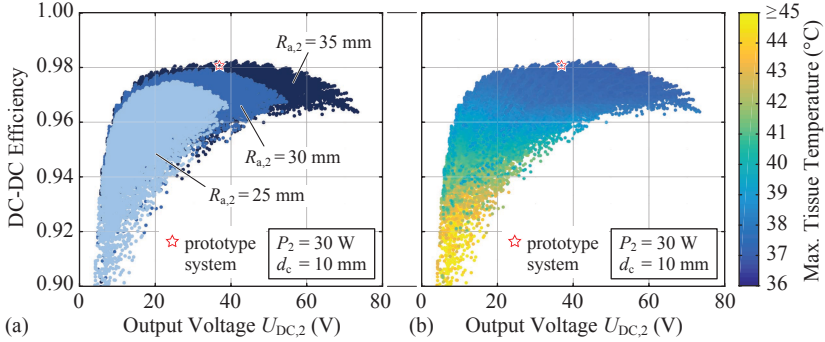


Fig. 5.1: Calculated DC-DC efficiency of the SSU IPT system with respect to the optimal output voltage at the maximum output power of 30 W and at 10 mm coil separation distance. (a) Distribution of the considered secondary-side outside radii. (b) Calculated maximum tissue temperature.

value, i.e. at 97%. Further note that the efficiency drops again for output voltages larger than 40 V. The reason is that these IPT system designs are operated also at a higher frequency and hence experience higher power losses in the synchronous rectifier and inverter circuit. As expected, the IPT system designs with a large secondary-side coil diameter achieve a higher energy transfer efficiency than smaller coil designs (cf. **Fig. 5.1(a)**), and also cause lower heating of the human tissue, as shown in **Fig. 5.1(b)**.

In a next step, the EMF exposure of the human tissue is evaluated for the designed IPT systems. The number of virtual IPT system designs in **Fig. 5.1** exceeds 50'000 designs. Hence, the computationally expensive FE-simulation of the electro-magnetic field cannot be performed for all designs within a reasonable amount of time. Therefore, only a subset of the thermally valid IPT system designs, i.e. the designs with a maximum tissue temperature of 39 °C, are extracted and are considered for the EMF simulation.

5.2 EMF Exposure Simulation

The procedure of the EMF simulation is described by the flow-chart shown in **Fig. 5.2**. The FE-simulation model is generated according to the structure and the dimensioning described in **Section 4.3**. For

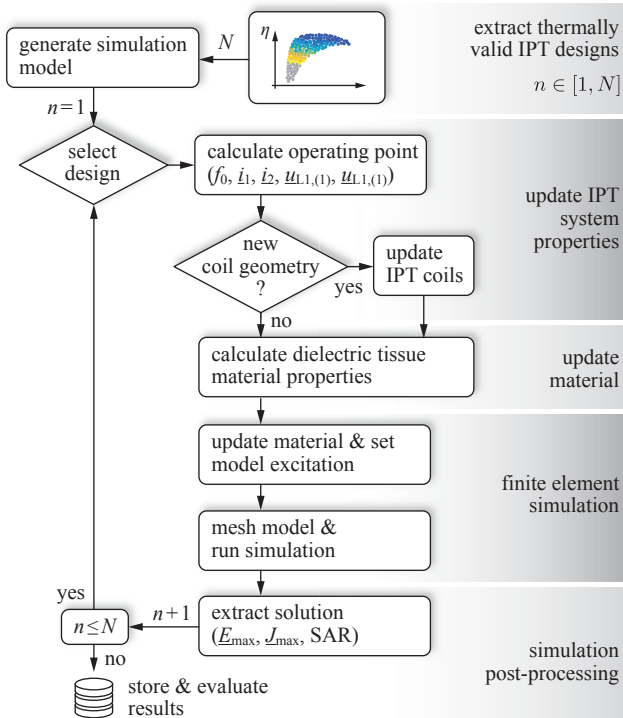


Fig. 5.2: Simulation flow-chart, describing the procedure of the electromagnetic field simulation, which is performed for the thermally valid IPT designs.

the EMF simulations, a total number of $N = 5'000$ thermally valid IPT system designs are considered and in order to further reduce the computation time, some minor modifications are applied to the simulation model, which are explained in the following.

A simplified schematic drawing of the axis-symmetric model of the IPT coils and the definition of the excitation sources, i.e. the applied voltages and currents, and the typical coil current/voltage waveforms that are considered for the EMF simulations, are shown in **Figs. 5.3(a)** and **(b)**, respectively.

The structure of the TET coils is schematically shown in **Fig. 5.3(a)**. In this case, it is assumed that the silicone encapsulation completely encloses the IPT coils and also fills the center hole of the coils. In addition,

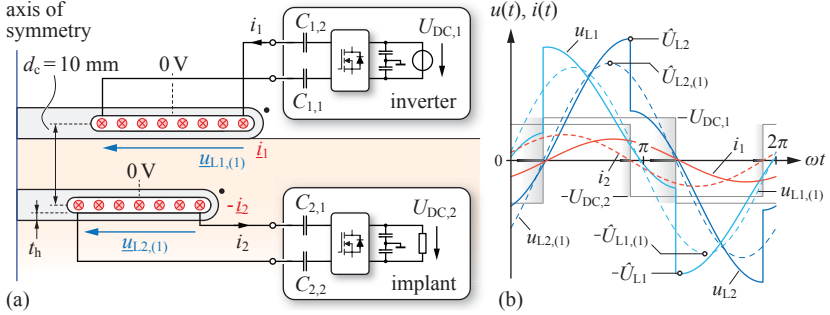


Fig. 5.3: (a) Simplified schematic drawing of the IPT system model and definition of the coil current and voltage excitations used for the EMF simulations. (b) Typical waveforms of the IPT coil currents and voltages.

in the model, the windings are simplified by using a lumped winding model with a homogeneously distributed current density, which is given by the total copper cross-section and the coil current at the specific operating point. Furthermore it is assumed, that all the measures for CM voltage suppression are applied to the primary and secondary side of the power electronic system, as proposed in **Chapter 4.4.3**. In this case, the differential coil voltages are distributed linearly and symmetrically across the coil windings, such that the turn in the center of the winding is always at the same electrical potential as the surrounding tissue, as indicated in **Fig. 5.3(a)**.

If the coil geometry has changed since the previous simulation run, the model geometry is updated. The fat layer thickness in the model is always adjusted, such that the coil separation distance is maintained at 10 mm and the thickness of the silicone encapsulation layer t_h (cf. **Fig. 5.3(a)**), surrounding the coil winding, is set to 1 mm for each coil.

In a next step, the dielectric properties of each tissue material are calculated for the operating frequency of the specific IPT system design, as explained in **Section 4.1**. The FE-simulation is then performed as described in **Section 4.3** and after the electro- and magneto-quasistatic simulation has finished, the total electric field, the total current density and the tissue power losses are calculated and stored for further post-processing steps.

The applicable regulations and guidelines, which limit the EMF exposure of the human body, are summarized in **Section 4.2**. In

this case, the EMF exposure assessment is based on the RMS electric field strength in the human tissue. In the considered frequency range of 0.1-2 MHz, the RMS electric field strength is limited to $E_{\text{RMS}} = 1.35 \cdot 10^{-4} \cdot f_{\text{Hz}}$ for the general public, averaged over a contiguous tissue volume of $2 \times 2 \times 2 \text{ mm}^3$ [110]. But in order to provide a conservative estimation of the exposure levels, the spatial maximum RMS electric field strength is evaluated in the FE-simulations and is then checked for compliance with the proposed exposure limit for each of the IPT system designs.

The spatial peak SAR is calculated as well, but is in this case not considered as a limiting factor for the IPT system design. The simulation results have shown that for all the valid IPT designs, i.e. the designs that comply with the thermal and the electric field strength limit, the maximum realized peak SAR is 3.55 W/kg and the maximum realized total tissue power loss is 72 mW, which is approximately 25 % of the secondary-side coil power loss of the same design. Both, the maximum SAR and the maximum tissue power loss are obtained for an IPT system design, which is operated at the maximum considered operating frequency of 2 MHz. However, the total tissue power losses, which are caused by the electromagnetic field exposure, are distributed over a much larger volume than the power losses generated within the secondary-side IPT coil. Therefore, the additional tissue power losses do not contribute significantly to the local heating of the tissue, which supports the considerations above.

5.3 Simulation Results

The results of the FE-simulations are depicted in **Fig. 5.4**. The maximum RMS electric field strength in the tissue volume is shown in **Fig. 5.4(a)** with respect to the power losses and the peak differential coil voltage \hat{U}_{L2} at the secondary-side coil. **Fig. 5.4(b)** shows the corresponding total tissue power loss caused by the EMF exposure. As a result of the EMF exposure assessment, only a fraction of the thermally valid designs are feasible in terms of compliance with the maximum RMS electric field strength limit. **Fig. 5.4(c)**, shows the Figure-of-Merit $FOM = k\sqrt{Q_1 Q_2}$ for each IPT coil set with respect to the optimal system output voltage at maximum output power. As expected, the system designs with lower FOM are limited by the heating of the tissue. With increasing primary-side and secondary-side coil qual-

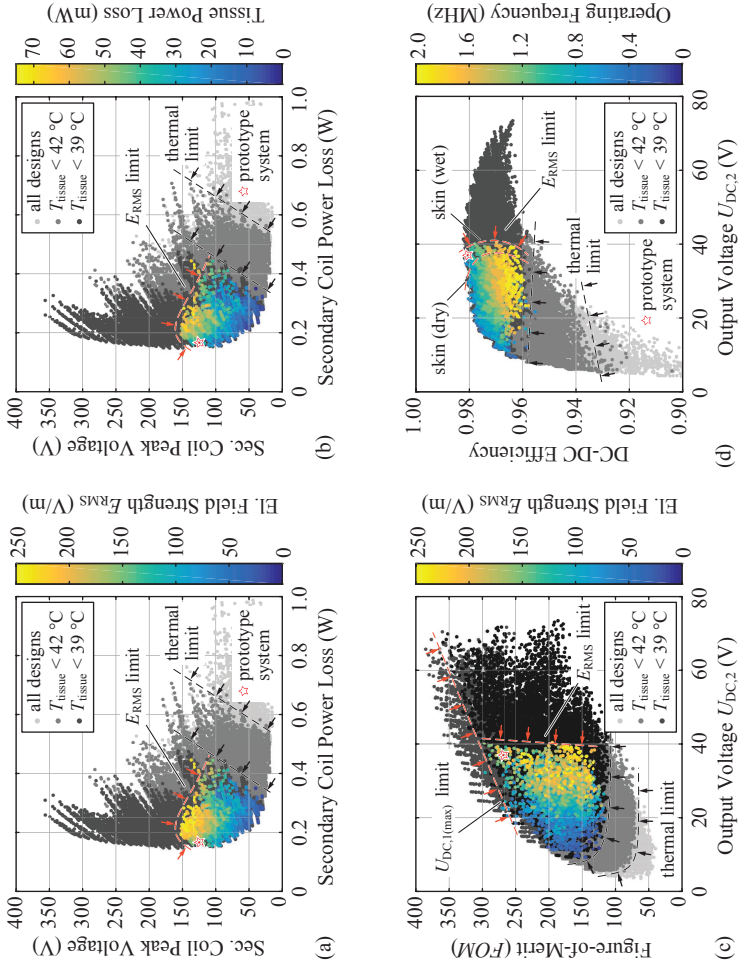


Fig. 5.4: (a)-(b) Max. RMS electric field strength and total tissue power loss of the feasible IPT system designs, plotted for the secondary-side coil power loss with respect to the peak secondary-side coil voltage. (c) Max. RMS electric field strength of the feasible designs with respect to the Figure-of-Merit $FOM = k\sqrt{Q_1 Q_2}$ and with respect to the optimal IPT system output voltage $U_{\text{DC},2}$. (d) Calculated DC-DC efficiency of the IPT system designs with respect to the output voltage $U_{\text{DC},2}$. In all the figures, the RMS electric field strength limit and the thermal limits are indicated. In addition, the calculated operating point of the SSU IPT system prototype (cf. **Chapter 2**) is indicated.

ity factor, i.e. with increasing operating frequency and coil inductance, the optimal IPT system output voltage is increasing and the total IPT coil power losses are decreasing. Concurrently, the peak secondary-side coil voltage and the maximum RMS electric field strength in the tissue are increasing. As a result, for a maximum power transmission of 30 W and for the considered coil specifications given in **Fig. 2.10(b)**, the maximum IPT system output voltage is limited to approximately 40 V. In addition, in this case, for the SSU IPT system, the feasible designs are also limited towards increasing FOM by the maximum feasible inverter input voltage, which is in this case set to $U_{DC,1(\max)} = 80$ V at maximum output power and minimum coil coupling factor, i.e. at the maximum considered coil separation distance of distance of 30 mm.

Fig. 5.4(d) shows the calculated DC-DC efficiency of the SSU IPT system designs with respect to the system's optimal output voltage at maximum output power. As described in **Section 5.1**, the efficiency calculation does include the power losses caused by the inverter circuit and the synchronous rectifier, but excludes auxiliary circuit power losses or conduction losses in the PCB tracks or in the TET coil lead wires. The power loss caused by the EMF exposure reduces the DC-DC efficiency of the valid designs by less than 0.22 % and is therefore neglected in the efficiency calculation. The envelope of the calculated efficiencies shows a rather flat optimum with respect to the IPT system output voltage and attains a maximum at an output voltage of approximately 40 V, which is delimited by the maximum RMS electric field strength limit.

Fig. 5.4(d) additionally indicates the influence of different dielectric properties of the skin tissue on the electric field strength limit. It was shown in **Fig. 4.2**, that the reported dielectric properties of dry skin deviate considerably from the properties of wet skin. In the considered frequency range of 0.1-2 MHz, this is specifically the case for the electrical conductivity, which in case of dry skin is up to two decades lower compared to the conductivity of wet skin. In the same frequency range, the relative permittivity of dry skin is almost constant and at 100 kHz it is more than one decade lower than the permittivity of wet skin. As a result, in case of dry skin, the maximum RMS electric field strength in the tissue is increased substantially, which restricts the design space even more. However, as explained at the end of **Chapter 4**, the simulated values for the RMS electric field strength give an indication of the range of the magnitudes only, and it is expected that the

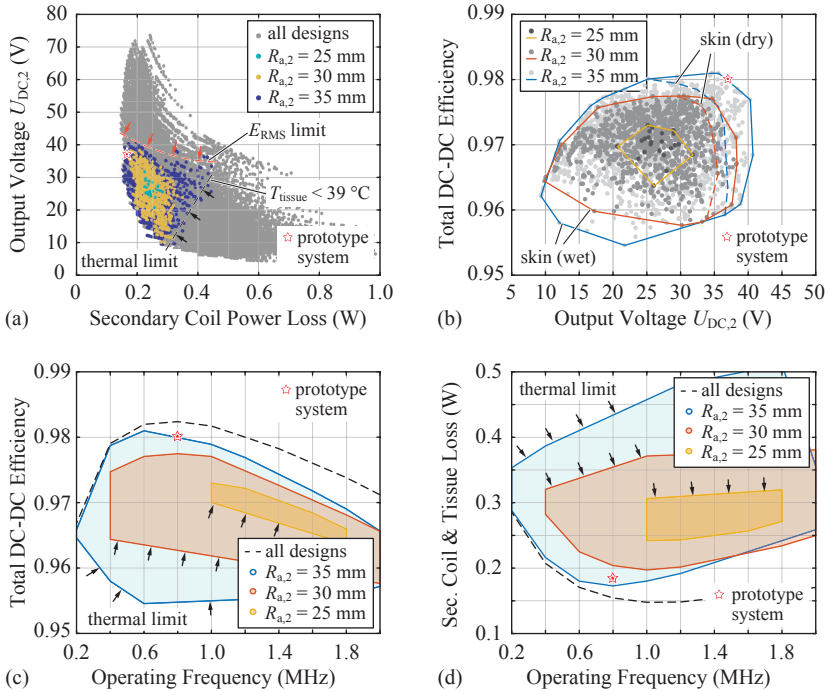


Fig. 5.5: (a) Secondary-side coil outside radius $R_{a,2}$ of the feasible IPT system designs, which comply with the thermal limit and the EMF exposure limit, with respect to the output voltage and the secondary-side coil power loss, at maximum power transmission. (b) Calculated total DC-DC efficiency of the feasible IPT system designs at maximum output power with respect to the output voltage, and in (c) with respect to the IPT system operating frequency. (d) Total secondary-side coil power losses and total tissue power losses caused by the EMF exposure with respect to the IPT system operating frequency. The dashed black line in (c) and (d) denotes the efficiency and the power loss boundary obtained for all IPT system designs, neglecting the limiting factors and the additional tissue power loss due to the EMF exposure.

effective electric field strength values in the human body may deviate considerably from the simulation results, which is due to the large parameter uncertainties and the simulation model simplifications.

Generally, in order to reduce the internal electric field strength and in order to mitigate the impact of the dielectric tissue material parameter variations, an electrical shielding can be applied to the primary-side and the secondary-side IPT coil, as it is described in detail in **Section 4.5**.

In **Figs. 5.5(a)** and **(b)** it is shown that for the maximum power transfer of 30 W only few feasible secondary-side coil designs with a diameter of 50 mm exist. As expected, the secondary-side coil designs with the largest diameter show the best performance in terms of tissue heating and in terms of the overall IPT system efficiency. Nevertheless, there exist designs with a secondary-side coil diameter of 60 mm which achieve a secondary-side coil power loss, which is similar to the performance of the 70 mm coils, but the overall coil misalignment tolerance is decreased for those designs, because the coil coupling factor decreases more rapidly with an increasing coil separation distance.

Fig. 5.5(c) shows the total DC-DC efficiency of all valid designs with respect to the operating frequency, including the tissue power losses caused by the EMF exposure. The dashed black line denotes the efficiency boundary obtained for all IPT system designs, neglecting the limiting factors and the additional tissue power losses, that are introduced by the EMF exposure. For the coil designs with an outside diameter of 70 mm, the maximum efficiency is obtained for an operating frequency of 600 kHz. For smaller secondary-side coil diameter the maximum efficiency is decreasing and is moved towards higher operating frequencies. Similar results can be observed in **Fig. 5.5(d)**, which shows the sum of the power losses caused within the secondary-side coil and within the tissue with respect to the operating frequency. In this case, the best performance is achieved at an operating frequency of 800 kHz and a secondary-side coil diameter of 70 mm.

5.4 Summary of the Chapter

The investigation presented in this chapter reveals the impact of the potentially adverse health effects on the IPT system design space. The analysis is carried out for a large number of electrically feasible IPT system designs, which are then checked for compliance with existing

regulations on the heating of the human tissue and on the exposure to electromagnetic fields. As a result, the maximum available IPT system design space and the optimum operating conditions are identified.

The main results of this chapter are summarized as follows:

- ▶ The main factors that limit the overall IPT system performance towards higher operating frequencies are the power losses that are generated in the inverter and in the synchronous rectifier circuit, i.e. in particular the gate drive power losses and the diode conduction losses.
- ▶ Considering the IPT resonant circuit, it can be concluded that secondary-side coil designs which offer a high quality factor, i.e. coils which have in general a large inductance value and are operated at high operating frequencies, require higher IPT system output voltage at maximum output power in order to achieve an efficiency optimal operation. As a result however, the power losses and the RMS electric field strengths in the tissue are increased, and may exceed the applicable safety limits. Hence, for the maximum power level at hand, the SSU IPT system should not be operated at output voltages beyond 40 V.
- ▶ In order to achieve a high energy transmission efficiency and a low secondary-side coil and tissue power loss, the operating frequency of the IPT system should be chosen in a range of 600 kHz to 800 kHz. For the previously mentioned reasons, it is not beneficial to increase the operating frequency beyond this frequency range.
- ▶ Furthermore it can be concluded that for the power transfer level at hand, a secondary-side coil diameter of at least 60 mm should be considered for a single layered secondary coil in order to provide a reliable and a safe operation of the TET system.
- ▶ The analysis was carried out for the SSU IPT system operation at maximum output power and minimum coil separation distance. Nevertheless, the final conclusions apply for the SSR IPT system as well, but, it can be expected that the design limitations are more restrictive in case of the SSR IPT system operation. The reason is that at a given output power, operating frequency and secondary-side IPT coil, the optimum output voltage of the SSR

IPT system is higher compared to the SSU IPT system design. Additionally, the compensation capacitances are smaller, which in turn results in a higher coil terminal voltage, and hence, increases the electric field strength in the tissue further. Additionally, it was shown in **Chapter 2**, that in case of the SSR system operation, the primary-side and secondary-side coil currents are increasing for a decreasing coil coupling factor. Hence, it can be expected, that the EMF exposure and the heating of the tissue are increasing at larger coil separation distances and constant power transfer.

- In order to mitigate the design limitations imposed by the restriction on the RMS electric field strength in the tissue, the IPT coils are preferably equipped with an electrical shielding, as proposed in **Section 4.5**. The shielding allows to enhance the operational safety of the TET system, but from the previous analysis it is not expected that it allows for IPT system designs with much higher overall IPT system efficiency.

In the previous chapters, the operation and the design of the IPT system was analyzed in detail and the design limitations are disclosed for the series-series compensated IPT system topology. The next chapter discusses the design and the optimization of the additional DC-DC converter stages at the input side and the output side of the IPT system that are required for the control of the wireless power transmission.

6

DC-DC Converter

IN **Chapter 2** it was shown, that it is beneficial to operate the IPT system at an input and output voltage $U_{DC,1}$ and $U_{DC,2}$, which is higher than the typical nominal battery pack output voltage of 14.8 V. Consequently, additional DC-DC converter stages must be inserted at the input and the output terminals of the IPT system, as indicated in **Fig. 6.1**.

In case of the SSR IPT system, the DC-DC converter stages provide the load impedance matching for the IPT system, which allow to operate the system at maximum power transfer efficiency, despite of a variable coil coupling and load conditions. Since the primary-side and secondary-side terminal voltages of the IPT system can take values below and above the nominal battery voltage, a buck-boost type DC-DC converter is needed on both sides of the IPT system, which can be realized as shown in **Fig. 6.2**.

According to the findings in **Section 2.6.2**, the SSU IPT system is designed to operate at output voltage levels above the nominal bat-

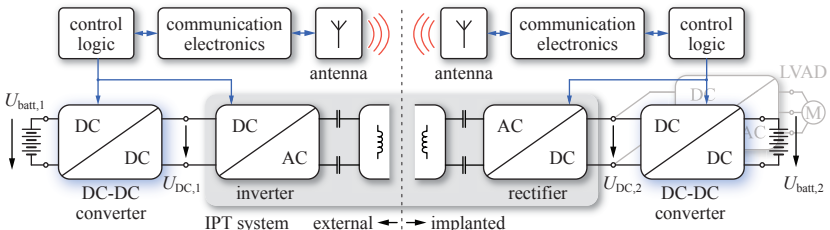


Fig. 6.1: TET system concept for a fully implantable MCS system.

tery voltage and the LVAD inverter is connected directly to the output terminals of the IPT system. Hence, on the primary side, an additional boost-type DC-DC converter is required between the main battery power supply and the IPT inverter. Similarly, on the secondary side, a bidirectional DC-DC converter is needed as battery charging converter, which is able to operate either in buck- or boost-mode, depending on the direction of the power flow, i.e. in buck-mode for battery charging and in boost-mode for autonomous operation of the TET implant. Possible implementations of the converter topology are shown in **Figs. 6.2(b)** and **(c)** and will be explained in more detail in the following sections.

The design of the implanted DC-DC converter is particularly challenging because of the limited available volume and the need for a high power conversion efficiency, in order to limit the heating of the surrounding tissue to a safe level. On the primary side, the requirements for the converter volume are less stringent, but nevertheless, a high power conversion efficiency is mandatory, in order to prolong the battery runtime.

In this chapter, different soft-switched, i.e. zero voltage switching, DC-DC converters are compared to the conventional hard-switched (HSW) converter solution, in order to investigate if the more advanced, but more complex soft-switched topologies, are able to outperform the conventional solution, and hence, allow to push the performance limit to higher power conversion efficiencies and higher power densities. The sections on the soft-switched DC-DC converter topologies are based mainly on the results published in [123,124], and the comparison is carried out at the example of the external boost-type DC-DC converter, which is used for the SSU TET system operation, but the final conclusions apply to the buck-type and the buck-boost converter as well.

6.1 Topology Overview

The very basic topology of the buck-boost or the simple boost converter, which can either be operated in hard-switched or soft-switched operation are shown in **Figs. 6.2(a)-(c)**, respectively. For the hard-switched operation, the inductor current is always positive and in boost-mode, i.e. $u_2 > u_1$, the low-side switch T_2 experiences a hard turn-on at the end of the time interval T_{off} , when the positive inductor current is commutated from the body diode of switch T_1 to the switch T_2 , as

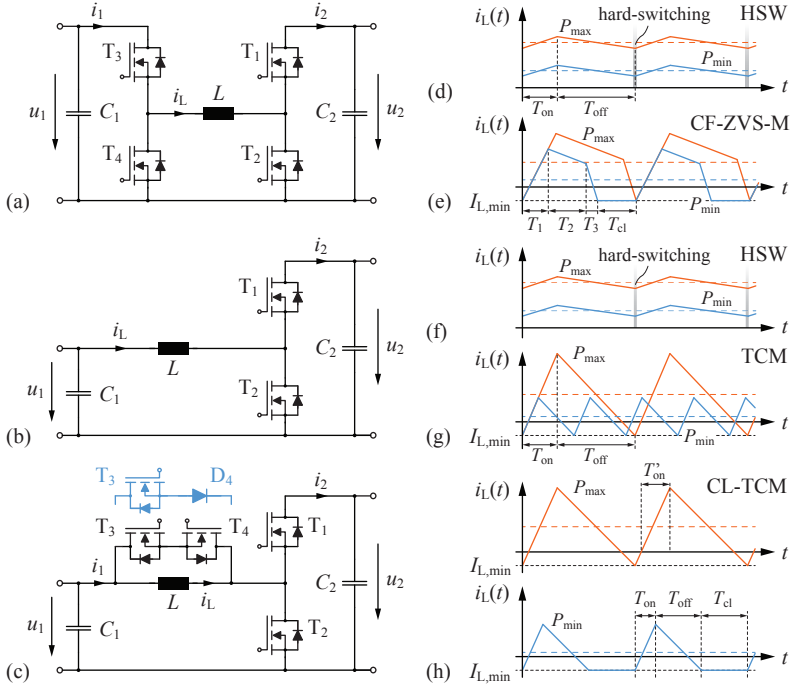


Fig. 6.2: (a) Basic buck-boost converter topology and the inductor current waveforms for the hard-switched operation (d) and for the soft-switched operation (e), according to the CF-ZVS modulation scheme proposed in [125]. (b) Conventional boost-type DC-DC converter topology and the inductor waveforms for hard-switched operation (f) and for the soft-switched operation (g), using the Triangular Current Mode (TCM) modulation scheme. (c) Clamp-Switch TCM (CL-TCM) boost converter topology [126, 127] and (h) the associated inductor current waveforms.

indicated in **Figs. 6.2(d)** and **(f)**. As a result, the power loss in the switch is increased significantly. For this type of operation, the switching loss limits the maximum feasible switching frequency and therefore also limits the minimum size of the passive components, such as the inductor L and the filter capacitors C_1 and C_2 .

Soft-switching of the converter, i.e. ZVS operation, can be achieved if the inductor current has a negative value at the end of the time interval T_{off} , which is large enough to deliver enough charge during the

dead-time interval to fully discharge the parasitic output capacitance of the switch T_2 and to charge the output capacitance of T_1 . In this case, switch T_2 can be turned on with negligible power loss.

A very promising implementation of a ZVS buck-boost DC-DC converter is the converter topology depicted in **Fig. 6.2(a)**, using the Constant-Frequency ZVS Modulation (CF-ZVS-M) scheme, according to [125]. The typical current waveforms for this type of operation are illustrated in **Fig. 6.2(e)**. Despite the complex modulation scheme, the converter offers a highly efficient operation and a compact design. The design and the implementation of the CF-ZVS-M buck-boost DC-DC converter is explained in great detail in [125] and will not be discussed any further.

ZVS buck- or boost-type converters are commonly realized using a Triangular Current Mode (TCM) operation with variable switching frequency [128–131] or a Synchronous Conduction Mode (SCM) operation with a fixed switching frequency [132–134]. In case of the SCM operation, the peak-to-peak current ripple in the inductor is set large enough to allow for zero voltage switching at maximum output power and fixed input and output voltages. However, as a consequence of the fixed switching frequency, the large peak-to-peak inductor current ripple is remaining constant at constant input/output terminal voltages, even at light load conditions, which in turn reduces the partial load efficiency significantly, and hence is a main disadvantage of the SCM converter operation.

A better performance is offered by the TCM operation, where the minimum inductor current $I_{L,\min}$ is kept at a constant value, just large enough to ensure ZVS of the low-side switch T_2 . The output power is then controlled by varying the ON-time interval T_{on} of the switch T_2 , as illustrated in **Fig. 6.2(g)** for minimum and maximum output power. As a result, the RMS inductor current is reduced at light load conditions, but the switching frequency is increasing significantly. Assuming a constant input voltage u_1 and a lossless operation of the converter, the switching frequency variation can be expressed with

$$n_{f,\text{TCM}} = \frac{f_{p,\max}}{f_{p,\min}} = \frac{(P_{\max} - I_{L,\min}u_1)(u_{2,\max} - u_1)u_{2,\min}}{(P_{\min} - I_{L,\min}u_1)(u_{2,\min} - u_1)u_{2,\max}}, \quad (6.1)$$

which depends on the output power and output voltage variation $u_2 \in [u_{2,\min}, u_{2,\max}]$. The maximum switching frequency $f_{p,\max}$ occurs at the minimum output power and the maximum voltage conversion

ratio. Depending on the range of operation, i.e. the output power range and the voltage conversion range, the switching frequency variation can be very large, which complicates the filter design and the implementation of the digital control, as the switching time intervals must be calculated and synchronized to the zero-crossings of the inductor current. As a possibility to limit the switching frequency variation, the TCM converter could be operated in a pulse skipping mode, which however suffers from hard-switching events, and is therefore not a viable solution.

In order to overcome these drawbacks, similar to the CF-ZVS-M buck-boost operation explained in [125], an additional clamp-switch can be introduced in parallel to the boost inductor, which allows for ZVS operation and facilitates a significant reduction of the switching frequency variation, while achieving a high partial load efficiency, similar to the TCM operation [126, 127, 135]. Such a topology is implemented in the Cool-Power[®] ZVS buck-type switching regulator series provided by Vicor Corp. [136] and its operation is described briefly in [135]. However, the realization of the clamp-switch itself is not revealed and the soft-switching operation is shown only for the main power switches.

The clamp-switch boost converter topology considered in this work is depicted in **Fig. 6.2(c)**. The converter comprises an active clamp-switch in parallel to the inductor, which is formed by the two anti-series connected switches T_3 and T_4 , allowing for a bidirectional voltage blocking capability [126, 127]. Note that the ON-state resistance of the clamp-switches can be higher compared to the main power switches T_1 and T_2 , since they are conducting a small current or only for a short time interval, as will be shown in the following section. Hence, switches with lower parasitic output capacitance can be used for the clamp-switches. As indicated in **Fig. 6.2(c)**, the converter complexity can be reduced by replacing the switch T_4 with the diode D_4 . In this case, ZVS operation can be achieved for unidirectional power flow only. More details on the operation of this converter topology and further hardware modifications are provided in **Appendix B**.

Typical inductor current waveforms of the CL-TCM converter are shown in **Fig. 6.2(h)**. At maximum output power, the converter operation corresponds to the TCM operation [126]. In this case, the inductor current has a triangular shape with a negative inductor current $I_{L,\min}$, which allows for ZVS of the two main switches T_1 and T_2 . However, at light load operation, the clamp-switch allows to introduce

a free-wheeling state for the inductor current after the turn-off of the switch T_1 and consequently, stretches the switching period, as shown in **Fig. 6.2(h)**. As a result, the switching frequency variation is reduced significantly, which in turn relaxes the requirements for the control circuit and allows to operate the converter at a higher switching frequency in the entire range of operation, when compared to a TCM converter, that is designed for the same maximum switching frequency.

In the following, this type of operation is referred to as CL-TCM operation and the operating principle and the fundamental design considerations are discussed in more detail in the following section, based on the work presented in [123].

6.2 CL-TCM Boost Converter Operation

The operation of the CL-TCM converter is based on the ZVS modulation scheme proposed in [127], which allows for ZVS operation of all four switches in the entire range of operation, i.e. in the input or output voltage and power range, and will be explained in detail in the following section. In addition, in **Section 6.2.2**, the electrical conditions for ZVS operation are revealed and finally, a controller implementation is proposed for the CL-TCM operation and the fundamental design considerations are provided.

6.2.1 ZVS Modulation Scheme

The detailed operating principle of the ZVS modulation scheme of the CL-TCM converter proposed in [127] is shown in **Fig. 6.3** for the boost operation. The inductor current i_L and switch-node voltage u_{sw} waveform belonging thereto are shown in **Fig. 6.4(a)**.

For the turn-off event of each switch, it is assumed that the gate driver's current sinking capability is large enough to remove the gate charge fast enough, such that the gate-to-source voltage drops below the FET's turn-on threshold voltage before the drain-to-source voltage increases. In this case, the FET is turned off lossless at zero voltage.

Starting with the first time interval $[t_0, t_1]$, switch T_2 is enabled and the inductor current rises linearly. The clamp-switch T_4 is in ON-state and the body diode of switch T_3 is in blocking state and prevents a short circuit of the input capacitor C_1 . As will be explained in **Section 6.2.3**, the inductor current zero crossing at time t'_0 is detected at

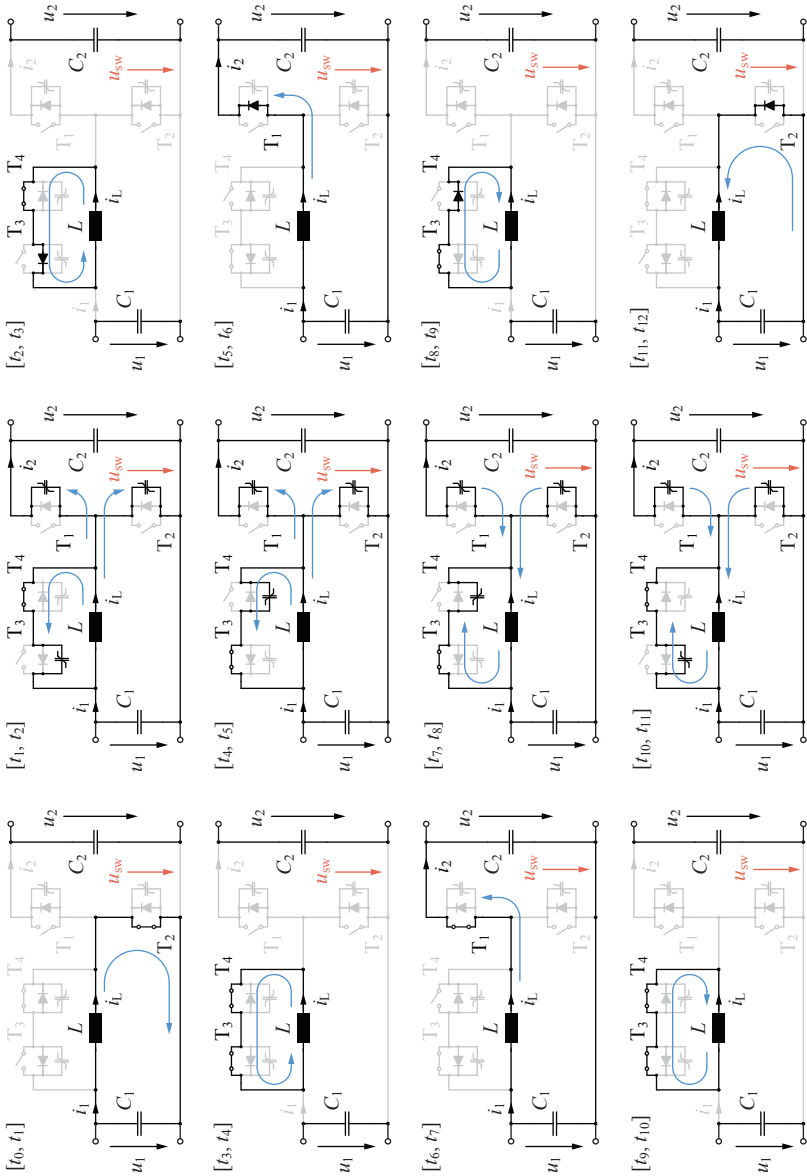


Fig. 6.3: Operating states of the proposed ZVS modulation scheme [127] for a full switching cycle $[t_0, t_{12}]$.

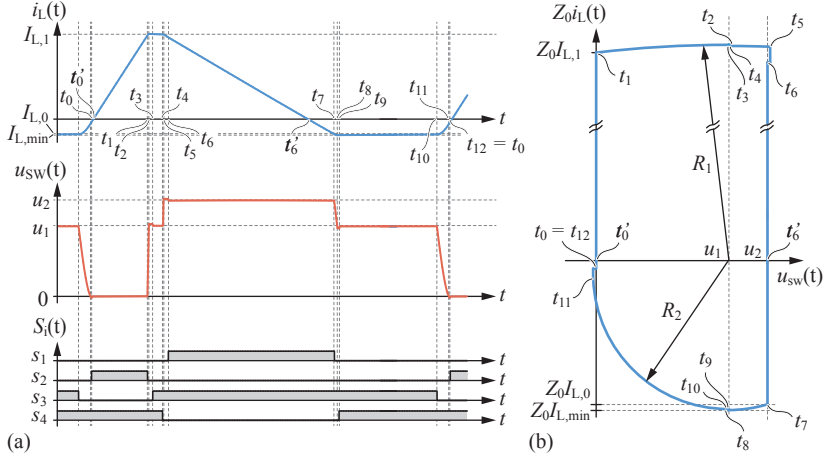


Fig. 6.4: (a) Typical waveforms of the inductor current i_L and the switch-node voltage u_{sw} and the indicated switching states t_1 to t_{12} . (b) State-plane diagram, showing the scaled inductor current $Z_0 i_L(t)$ with respect to the switch-node voltage $u_{sw}(t)$.

the low-side switch T_2 and is used to synchronize the timing of the gate control signals to the actual inductor current waveform. The remaining ON-time $T'_{on} = t_1 - t'_0$ of switch T_2 and the time T_{off} (cf. **Fig. 6.2(h)**) are calculated by the controller in order to turn off switch T_1 at t_7 at the negative inductor current $I_{L,0}$ which is required to achieve ZVS operation of the low-side switch T_2 later in the subsequent time intervals.

At t_1 , as soon as the inductor current reaches the value $I_{L,1}$, i.e. at the end of the time interval T'_{on} , switch T_2 turns off and the inductor current charges the parasitic output capacitance of switch T_2 , while discharging the output capacitances of T_1 and T_3 . During $[t_1, t_2]$, the voltage u_{sw} rises until the body diode of switch T_3 starts to conduct. In $[t_2, t_3]$ the inductor voltage is clamped to the diode forward voltage drop u_{DF} and switch T_3 can be turned on at nearly zero voltage at t_3 . The time interval $[t_3, t_4]$ is an intermediate state, where the inductor current is free-wheeling through the clamp-switches. In practice, this time interval must be set as short as possible in order to minimize the power loss in the clamp switches. However, the interval is important in order to swap the switching state of the clamp-switches - while allowing

for ZVS-operation - in order to block the voltage across the inductor in the subsequent time interval when the voltage polarity across the clamp-switches is reversed. Accordingly, at t_4 , switch T_4 is turned off and during $[t_4, t_5]$ the inductor current charges the parasitic output capacitance of the switches T_2 and T_4 and further discharges the output capacitance of T_1 . As soon as the parasitic output capacitance of switch T_1 is fully discharged, the anti-parallel diode starts to conduct at t_5 and clamps the voltage across the switch to u_{DF} , as shown in the time interval $[t_5, t_6]$. Consequently, switch T_1 can be turned on at nearly zero voltage at time t_6 . Note that the diode of switch T_4 is in blocking state and prevents a short circuit of the converter's input and output terminal. In the time interval $[t_6, t_7]$ the inductor current is supplied to the output and is decreasing linearly.

At t_7 , after the time interval T_{off} has expired, switch T_1 is turned off and the negative inductor current discharges the parasitic output capacitance of the switches T_2 and T_4 , while charging the output capacitance of switch T_1 during $[t_7, t_8]$. As soon as the voltage u_{sw} reaches a value of $(u_1 - u_{DF})$ at t_8 , the anti-parallel diode of switch T_4 starts to conduct and as a result, switch T_4 can be turned on at zero voltage at the time t_9 .

During the time interval $[t_9, t_{10}]$, the inductor current is free-wheeling in negative direction through the clamp-switch. In this time interval there is no energy delivered from the input to the output of the converter, and therefore, the length of the time interval can be used as a degree of freedom to control the switching period and the amount of power delivered to the load. During the clamping time interval, the inductor current amplitude is continuously decreasing, which is due to the power losses in the clamp switches and in the inductor. This has to be taken into account if the negative inductor current set-point is low and the clamping time interval is very large. In this case, the inductor current amplitude could fall below the minimum required value at t_{10} , where ZVS of switch T_2 cannot be achieved anymore in the following time intervals.

At t_{10} , switch T_3 is turned off and the negative inductor current continues discharging the parasitic output capacitance of switch T_2 until the switch-node voltage u_{sw} reaches zero and the diode of switch T_2 starts to conduct as shown in time interval $[t_{11}, t_{12}]$. The inductor current is rising and switch T_2 must be turned on before the current zero crossing, in order to allow for ZVS of T_2 . If switch T_2 is turned

on after the inductor current gets positive, soft-switching cannot be achieved. In this case, the parallel diode will block any current in the reverse direction and the parasitic capacitance of switch T_2 will be charged again and consequently, switch T_2 would need to be turned on at a voltage greater than zero.

The derivation of the fundamental conditions, which must be fulfilled in order to allow for the explained ZVS operation, will be shown in the following section.

6.2.2 ZVS Conditions

A useful representation for the analysis of the ZVS operation of the converter is provided by the state-plane diagram [137, 138], which in this case displays the switch-node voltage u_{sw} with respect to the inductor current i_L scaled by the characteristic impedance Z_0 of the resonant circuit, which is formed by the inductor and the parasitic output capacitances of the switches and diodes, and is shown in **Fig. 6.4(b)**. Assuming constant parasitic capacitances, the resonant voltage and current transitions are described by

$$\begin{aligned} Z_0 i_L(t) &= Z_0 I_{L,i} \cos(\omega_0 t) + (u_1 - U_{sw,i}) \sin(\omega_0 t) \\ u_{sw}(t) &= u_1 - (u_1 - U_{sw,i}) \cos(\omega_0 t) + Z_0 I_{L,i} \sin(\omega_0 t) \end{aligned} \quad (6.2)$$

which in the state-plane diagram represents a circle with the center located at $Z_0 i_L = 0$ and $u_{sw} = u_1$. At the beginning of the resonant transition, the inductor current has the value $I_{L,ini}$ and the switch-node voltage is $U_{sw,ini}$. The radius of the circle can be expressed with

$$R = \sqrt{(u_1 - U_{sw,ini})^2 + (Z_0 I_{L,ini})^2}, \quad \text{with} \quad Z_0 = \sqrt{\frac{L}{C_{tot}}}, \quad (6.3)$$

where C_{tot} is the total capacitance of the resonant circuit connected to the switch node. Similar to the analysis provided in [129] for the TCM operation, the state-plane diagram depicted in **Fig. 6.4(b)** is used to reveal the basic criteria, that must be met in order to achieve soft-switching of the switches after the resonant voltage transitions.

In order to account for the non-linearity of the parasitic capacitances of the switches $T_1 - T_4$, the resonant transition time and the required currents, needed to allow for ZVS, can be calculated with good approximation using the charge equivalent capacitance of the switches,

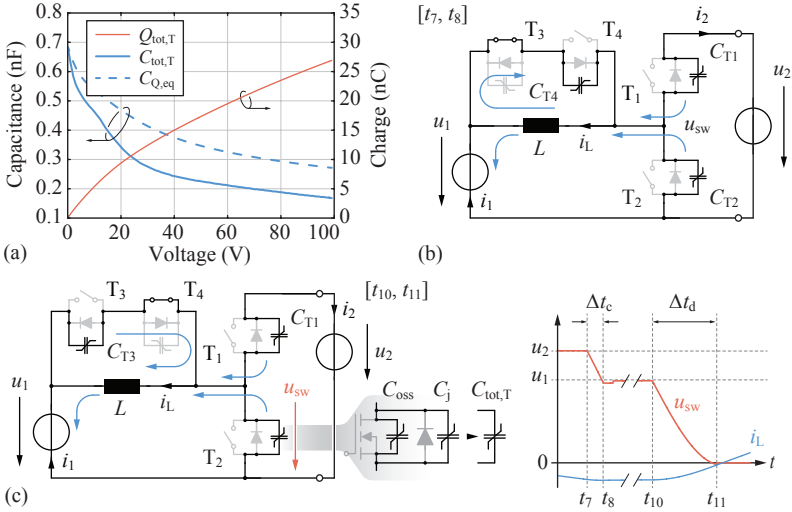


Fig. 6.5: (a) Total switch output capacitance, including the parasitic output capacitance of the EPC2016C GaN FET and the junction capacitance of the MBR1H100SF Schottky diode, derived from the data sheets [139, 140]. The calculated charge-equivalent capacitance and the stored charge are depicted in the same figure. (b) Illustration of the current flow during the resonant voltage transition in time interval $[t_7, t_8]$ and (c) in time interval $[t_{10}, t_{11}]$.

as explained in [129]. For the hardware prototype described in **Section 6.3.1**, each switch is composed of an EPC2016C GaN FET, placed in parallel with an additional Schottky diode, which lowers the voltage drop across the switch during diode conduction mode. The total capacitance $C_{\text{tot,T}}$ of the switch is therefore given by the sum of the switch output capacitance C_{oss} and the Schottky diode junction capacitance C_j . **Fig. 6.5(a)** shows the total capacitance of the EPC2016C GaN FET and the MBR1H100SF Schottky diode, used in parallel to the switch, as well as the total stored charge $Q_{\text{tot,T}}$ with respect to the applied voltage. In addition, **Fig. 6.5(a)** shows the charge equivalent capacitance, which can be calculated using [67]

$$C_{Q,\text{eq}}(V) = \frac{1}{V} \int_0^V C_{\text{tot,T}}(v) dv. \quad (6.4)$$

The resonant transition in the time intervals $[t_7, t_8]$ and $[t_{10}, t_{11}]$ is described in the state-plane diagram as a circle with the center at

$u_{sw} = u_1$ and $i_L = 0$ and a radius given by

$$R_2 = \sqrt{(Z_0 I_{L,0})^2 + (u_2 - u_1)^2}, \quad \text{with} \quad Z_0 = \sqrt{\frac{L}{C_{Q,eq,tot}}}. \quad (6.5)$$

As shown in **Fig. 6.5(b)**, during the time interval $\Delta t_c = (t_8 - t_7)$ the capacitance C_{T1} is charged from 0 V to $(u_2 - u_1)$, neglecting the forward voltage drop of the Schottky diode. The capacitances C_{T2} and C_{T4} are discharged from u_2 to u_1 and from $(u_2 - u_1)$ to 0 V, respectively. Assuming the same non-linear capacitance $C_{tot,T}$ for each switch, the total delivered charge and the associated charge equivalent capacitance can be calculated according to

$$\begin{aligned} \Delta Q_{C,T1} &= \int_0^{u_2 - u_1} C_{tot,T1}(v) dv \\ \Delta Q_{C,T2} &= \int_0^{u_2} C_{tot,T2}(v) dv - \int_0^{u_1} C_{tot,T2}(v) dv \\ \Delta Q_{C,T4} &= \int_0^{u_2 - u_1} C_{tot,T4}(v) dv \\ \Delta Q_{tot,c} &= \Delta Q_{C,T1} + \Delta Q_{C,T2} + \Delta Q_{C,T4} \end{aligned} \quad (6.6)$$

and

$$C_{Q,eq,tot,c} = \frac{\Delta Q_{tot,c}}{\Delta U_{tot,c}} = \frac{\Delta Q_{tot,c}}{(u_2 - u_1)}. \quad (6.7)$$

Similar considerations can be made for the time interval $\Delta t_d = (t_{11} - t_{10})$. In this case, at the end of the clamping time interval, the resonant transition is initiated with the turn-off of switch T_3 . The corresponding switching state and the current flow direction in the parasitic capacitances is shown in **Fig. 6.5(c)**. The capacitance C_{T2} is further discharged from u_1 to 0 V and the capacitances C_{T1} and C_{T3} are charged from $(u_2 - u_1)$ to u_2 and from 0 V to u_1 , respectively. The total delivered charge is then given by

$$\begin{aligned} \Delta Q_{C,T1} &= \int_0^{u_2} C_{tot,T1}(v) dv - \int_0^{u_2 - u_1} C_{tot,T1}(v) dv \\ \Delta Q_{C,T2} &= \int_0^{u_1} C_{tot,T2}(v) dv \\ \Delta Q_{C,T3} &= \int_0^{u_1} C_{tot,T3}(v) dv \\ \Delta Q_{tot,d} &= \Delta Q_{C,T1} + \Delta Q_{C,T2} + \Delta Q_{C,T3} \end{aligned}, \quad (6.8)$$

and the charge equivalent capacitance can be calculated with

$$C_{Q,eq,tot,d} = \frac{\Delta Q_{tot,d}}{\Delta U_{tot,d}} = \frac{\Delta Q_{tot,d}}{u_1}. \quad (6.9)$$

Hence, the total charge equivalent capacitance associated with the total resonant transition from t_7 to t_{11} can be calculated with

$$C_{Q,eq,tot} = \frac{\Delta Q_{tot,c} + \Delta Q_{tot,d}}{u_2}. \quad (6.10)$$

The minimum inductor current $I_{L,0}$ at the time instant t_7 , which is required for soft-switching of switch T_2 at the time t_{11} , can then be calculated using (6.5) and (6.10), according to

$$I_{L,0} \leq -\frac{1}{Z_0} \sqrt{u_2(2u_1 - u_2)}, \quad \text{for} \quad \left(u_1 \geq \frac{u_2}{2}\right). \quad (6.11)$$

In this case, the critical operating point, where soft-switching of T_2 could be lost, is at the minimum output voltage, regardless of the power delivered to the load.

Using the geometric relations depicted in the state-plane diagram in **Fig. 6.4(b)** and using the equation for the radius R_2 given in (6.5), the time interval $\Delta t_c = (t_8 - t_7)$ of the resonant transition can be calculated according to

$$\Delta t_c = \frac{1}{\omega_{0,c}} \left[\arctan \left(\frac{I_{L,0} Z_{0,c}}{u_2 - u_1} \right) + \frac{\pi}{2} \right], \quad (6.12)$$

using the characteristic impedance and the resonance frequency calculated with the charge equivalent capacitance given in (6.7),

$$Z_{0,c} = \sqrt{\frac{L}{C_{Q,eq,tot,c}}} \quad \text{and} \quad \omega_{0,c} = \frac{1}{\sqrt{LC_{Q,eq,tot,c}}}. \quad (6.13)$$

The negative peak inductor current can be calculated with

$$I_{L,\min} = -\frac{R_2}{Z_{0,c}} = -\frac{1}{Z_{0,c}} \sqrt{(Z_{0,c} I_{L,0})^2 + (u_2 - u_1)^2}. \quad (6.14)$$

Similar to the previous case, the resonant transition time interval $\Delta t_d = (t_{11} - t_{10})$ can be calculated using equation (6.13), substituted with the charge equivalent capacitance from (6.9), and is given by

$$\Delta t_d = \frac{1}{\omega_{0,d}} \arcsin \left(\frac{u_1}{|I_{L,\min}| Z_{0,d}} \right). \quad (6.15)$$

Due to the large inductor current $I_{L,1}$ at time t_1 , the resonant voltage-transition time intervals $[t_1, t_2]$ and $[t_4, t_5]$ are comparably short and can be neglected in the general case. The critical operating point where soft-switching of T_3 and T_1 at t_3 and t_6 could be lost is at the maximum output voltage and very low output power.

Note that the modelling of the resonant transitions using the constant charge equivalent capacitance is an approximation only. But as

shown in **Fig. 6.5(a)**, the total charge of the GaN FETs and the parallel Schottky diode does not show a high non-linearity with respect to the applied voltage. Hence, the equations (6.12)-(6.15) allow for an accurate modelling of the operation of the CL-TCM converter during the resonant voltage transitions and a relative error of less than 5% was obtained for time intervals Δt_c and Δt_d when compared to a circuit simulation. The required minimum negative inductor current $I_{L,0}$ can be predicted using equation (6.11). However, in this case, a relative error of up to 10% was obtained for the specifications and range of operation used for the prototype converter shown in **Section 6.3**.

Based on the operating principle shown in the previous sections, the timing of the switch control signals can be derived similar to [126] and is provided in the following section. In addition, a controller implementation is proposed for the CL-TCM converter operation.

6.2.3 CL-TCM Control

In case of the TCM operation, the ON-time of switch T_2 is the only degree of freedom available, in order to control the power delivered to the load. But in case of the CL-TCM modulation, the clamping time interval $[t_9, t_{10}]$ can be used in addition to control the switching frequency variation and the power delivered to the load. Considering the typical inductor current waveforms shown in **Fig. 6.2(h)**, it is beneficial to emulate TCM operation at maximum output power, i.e. by reducing the clamping time interval T_{cl} to zero [126], and hence reducing the inductor RMS current to a minimum, while maintaining ZVS operation. This however implies, that if the minimum inductor current $I_{L,\min}$ is fixed, the switching frequency will vary with changes in the input and/or the output voltage, due to the changing slopes of the inductor current. In contrast, if the terminal voltages are fixed and the output power is varied, the switching frequency is maintained constant by introducing the clamping time interval. In this case, the inductor RMS current could be reduced only by a significant variation of the switching frequency, which again is equal to the TCM operation. An alternative operating mode is described in **Appendix B.2**, where a constant switching frequency operation can be maintained, despite a variation of the terminal voltages. In this case, the minimum inductor current $I_{L,\min}$ is adjusted in addition to the clamping time interval, which has the disadvantage of an increased inductor RMS current at

larger voltage conversion ratios.

Therefore, the following analysis focuses on the first operating mode, which allows for a minimization of the switching frequency variation and simultaneous minimization of the inductor RMS current for variable output power $P_2 \in [P_{2,\min}, P_{2,\max}]$ and variable output voltage $u_2 \in [u_{2,\min}, u_{2,\max}]$. For the application at hand, i.e. for the primary-side DC-DC converter, a fixed input voltage u_1 is assumed, since the input of the boost converter is connected to the main battery supply. Note that the following calculations assume a constant input and output voltage over a switching cycle, which in a practical realization is ensured by an appropriate input and output filter design, which is described in more detail in **Appendix B.5**.

As reported in [126] for a constant switching frequency operation, and assuming a lossless operation of the converter, i.e. $P = P_1 = P_2$, the inductor must be designed according to

$$L = \frac{u_1^2 (u_{2,\max} - u_1)}{2u_{2,\max} f_{p,\max} (P_{1,\max} - u_1 I_{L,\min})}, \quad (6.16)$$

in order to achieve TCM operation at maximum output power, and such that a specified maximum switching frequency $f_{p,\max}$ is not exceeded for the specified range of operation, i.e. $u_2 \in [u_{2,\min}, u_{2,\max}]$.

The operation of the CL-TCM converter is determined mainly by the time intervals T_{on} , T'_{on} , T_{off} and T_{cl} (cf. **Fig. 6.2(h)**). The timing intervals are calculated such that the required average input current $I_{1,\text{avg}}$ and the negative inductor current $I_{L,\min}$ are achieved at any operating point. The timing calculations of the switch control signals are obtained for the boost operation, similar to the derivation given in [126].

The total ON-time of switch T_2 can be calculated for a desired average input current $I_{1,\text{avg}} = P_1/u_1$ according to

$$T_{\text{on}} = \frac{L}{u_1} \left(\sqrt{4I_{1,\text{avg}} \left(\frac{P_{1,\max}}{u_1} - I_{L,\min} \right) + I_{L,\min}^2 + |I_{L,\min}|} \right), \quad (6.17)$$

which is independent of the output voltage variation. Consequently, given the desired negative inductor current $I_{L,\min}$, the remaining ON-time T'_{on} , after the inductor current zero crossing, is calculated with

$$T'_{\text{on}} = T_{\text{on}} - \frac{L}{u_1} |I_{L,\min}|. \quad (6.18)$$

The switching time intervals T_{off} and T_{cl} (cf. **Fig. 6.2(h)**) can then be calculated with

$$T_{\text{off}} = T_{\text{on}} \left(\frac{u_1}{u_2 - u_1} \right) \quad \text{and} \quad T_{\text{cl}} = T_{\text{p,P(max)}} - T_{\text{on}} - T_{\text{off}}, \quad (6.19)$$

using the switching period T_{p} , evaluated for the nominal input power $P_{1,\text{max}}$, which follows directly from (6.16), and is given by

$$T_{\text{p,P(max)}} = \frac{2u_2L(P_{1,\text{max}}/u_1 - I_{L,\text{min}})}{u_1(u_2 - u_1)}. \quad (6.20)$$

Note that the equations (6.16)-(6.20) assume a lossless operation of the converter and the resonant transition times, as well as the short clamping time interval $[t_1, t_5]$, are neglected. However, in order to improve the accuracy of the inductance- and the timing interval calculations, the DC-DC efficiency $\eta_{\text{P(max)}}$ at maximum output power can be estimated in advance and the predicted maximum input power $P_{1,\text{max}} = P_{2,\text{max}}/\eta_{\text{P(max)}}$ can be used in (6.16)-(6.20).

The proposed implementation of the digital control circuit is illustrated in **Fig. 6.6(a)**. The inductor current zero crossing detection is the key feature that is required to implement the digital control of the CL-TCM modulation scheme. In the hardware prototype, it was intended to measure the inductor current directly in the inductor current path using a 10 m Ω shunt resistor. However, a more effective implementation of the zero crossing detection is shown in **Fig. 6.6(a)**, where the low-side switch current i_{T2} is sensed in order to detect the current zero crossing at the rising edge of the inductor current, as illustrated in **Fig. 6.6(b)**.

The timing values T'_{on} , T_{off} and T_{cl} are calculated by a Digital Signal Processor (DSP) and are transmitted to a Field Programmable Gate Array (FPGA), which implements the modulator in terms of a Finite State Machine (FSM), which is shown in **Fig. 6.6(c)** and which generates the gate control signals s_i , $i \in [1, 4]$, which are depicted in **Fig. 6.6(b)**.

A counter t_c within the FPGA is used to set the duration of the switching time intervals. After the remaining ON-time T'_{on} in state 1 has expired, the current zero crossing detector is disabled, i.e. $CDen = 0$, and the modulator enters state 2, which sets the first dead-time interval $T_{\text{dead},1}$ for the switches T_2 and T_3 . State 3 denotes the first intermediate clamping time interval $T_{\text{cl},0}$, which is preferably set as short as possible. After the second dead-time interval $T_{\text{dead},2}$, switch T_1 is enabled and the modulator enters state 5. With the expiration of the time interval

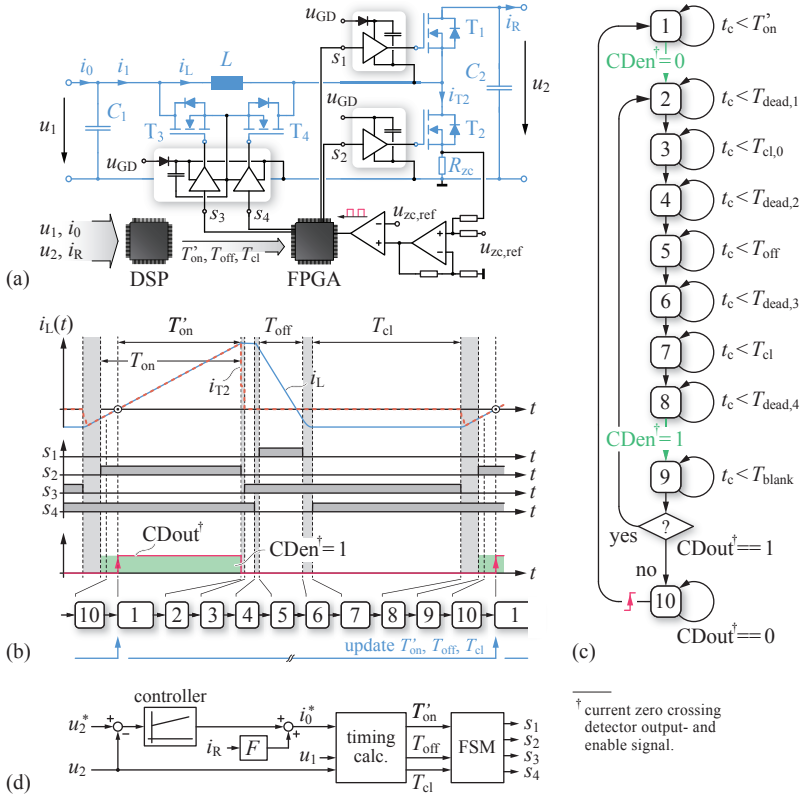


Fig. 6.6: (a) Realization of the control circuit and the proposed implementation of the inductor current zero crossing detection for the CL-TCM converter. (b) CL-TCM current waveforms, modulator states and (c) modulator state machine. (d) CL-TCM output voltage control with load current feed-forward.

T_{off} , and after the third dead-time interval $T_{\text{dead},3}$, the modulator enters the main clamping time-interval T_{cl} in state 7. After T_{cl} has expired and after the fourth dead-time interval in state 8, switch T_2 is turned on and the current zero crossing detector is enabled, i.e. $CDen = 1$. Initially, its output is blanked in order to prevent the detection of an erroneous current zero crossing due to the charging of the boot-strap capacitors of the high-side gate drivers or due to a hard-switching event at the turn-on of switch T_2 . After the blanking time interval, which should be chosen as short as possible, the current zero crossing detector output signal $CDout$ is evaluated. If the detector output is indicating that the inductor current is already positive, the state machine continues with state 2 in order to reduce the inductor current until its value is below zero when exiting state 9. If the inductor current is negative at the end of state 9, the modulator enters state 10 and waits for the detection of the current zero crossing, which then triggers the start of the modulation sequence from the beginning.

A very simple and yet effective implementation of the output voltage control of the converter is shown in **Fig. 6.6(d)**. A simple PI-controller and a load current feed-forward is used to set the average input current target i_0^* . Since the inductor current can be controlled directly cycle-by-cycle, the converter allows for a highly dynamic operation. However, since the evaluation of the timing values is computationally expensive, the values T'_{on} , T_{off} and T_{cl} may be updated only every n -th cycle, i.e. the modulator state machine runs with the same set of timing values for a few switching cycles until the values are updated at the beginning of the first modulator state (cf. **Fig. 6.6(b)**). Another solution to determine the timing values is to generate a look-up table with pre-calculated timing values and to interpolate the actual values online, using the look-up table together with the measured terminal voltages and the input current set-point.

As a result of the control scheme, the switching frequency variation is independent of the variation of the output power, and can be expressed with

$$n_{f,\text{CL}} = \frac{f_{\text{p,max}}}{f_{\text{p,min}}} = \frac{u_{2,\text{min}}}{u_{2,\text{max}}} \cdot \frac{(u_{2,\text{max}} - u_1)}{(u_{2,\text{min}} - u_1)}. \quad (6.21)$$

If the CL-TCM converter and the TCM converter are designed for the same maximum switching frequency $f_{\text{p,max}}$, the inductance value needed for the CL-TCM converter is much smaller than the inductance value needed for TCM operation. In this particular case, the ratio of

the inductance values is mainly given by the output power range and can be calculated according to

$$n_L = \frac{L_{CL}}{L_{TCM}} = \frac{P_{2,\min} - I_{L,\min,TCM} \cdot u_1}{P_{2,\max} - I_{L,\min,CL} \cdot u_1}. \quad (6.22)$$

On the other hand, if the CL-TCM converter is designed for the same minimum switching frequency as for TCM operation, with the same output voltage and output power range, the required inductance value is the same for both operating modes.

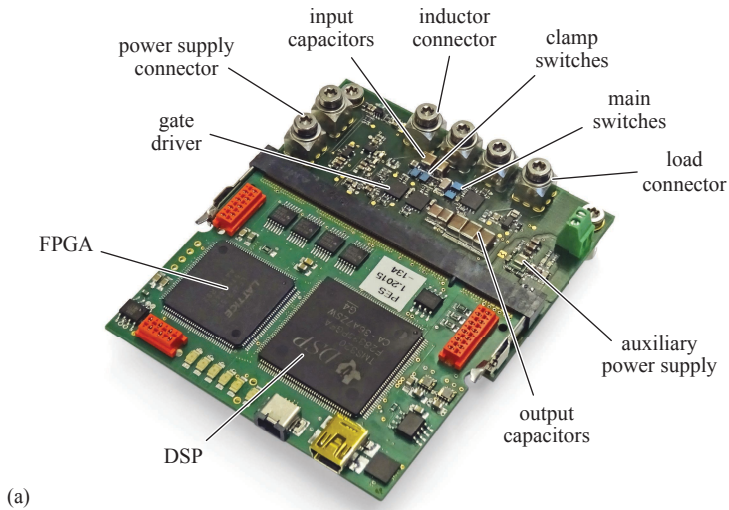
6.3 Experimental Verification

In order to verify the proposed operation of the CL-TCM converter, a hardware prototype was built and is presented in the following section. In addition, the converter performance is measured and is compared to the TCM operation.

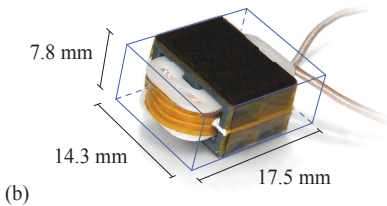
6.3.1 Hardware Prototype

Fig. 6.7(a) shows the hardware prototype of the CL-TCM converter. The EPC2016C GaN FETs are used for the switches, operated with the half-bridge gate driver LM5113. As already mentioned, an additional Schottky diode (MBR1H100SF) is placed in anti-parallel configuration to each switch. As illustrated in **Fig. 6.6(a)**, a boot-strap power supply is used as well for the clamp-switch gate drives, which allows for a very simple and compact design of the additional four-quadrant clamp-switch. The converter is controlled with a DSP/FPGA control board, comprising a Texas Instruments TMS320F28335 DSP and a Lattice LFXP2-5E FPGA. Note that the control board is not optimized for this converter and could be designed with significantly reduced footprint and power loss.

The prototype is designed according to the specifications given by the application for a nominal input voltage of 14.8 V and an output voltage range of 20-50 V. The output power range is set to 5-30 W. In order to directly compare the CL-TCM and the TCM operation of the converter, the same inductor is used for both modes of operation, such that both have the same minimum switching frequency. The hardware realization and the technical specifications of the realized inductors are shown in **Figs. 6.7(b)** and **(c)**. The inductor depicted in

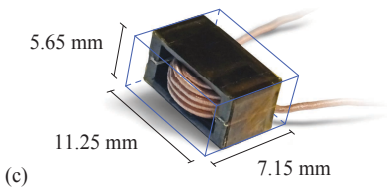


(a)



(b)

Parameter	Value
Inductance	7.51 μH
Litz wire	300 x 40 μm
Turns	9
Core material	N87
Core	2x EELP 14
Total air gap	0.56 mm
Power density	15.4 W/cm^3



(c)

Parameter	Value
Inductance	4.39 μH
Litz wire	135 x 40 μm
Turns	9
Core material	N87
Core	ER 11/5
Total air gap	0.46 mm
Power density	66.0 W/cm^3

Fig. 6.7: (a) Hardware prototype of the CL-TCM converter including the control board. (b)-(c) Realization and technical specifications of the inductors used for the performance evaluation of the CL-TCM converter.

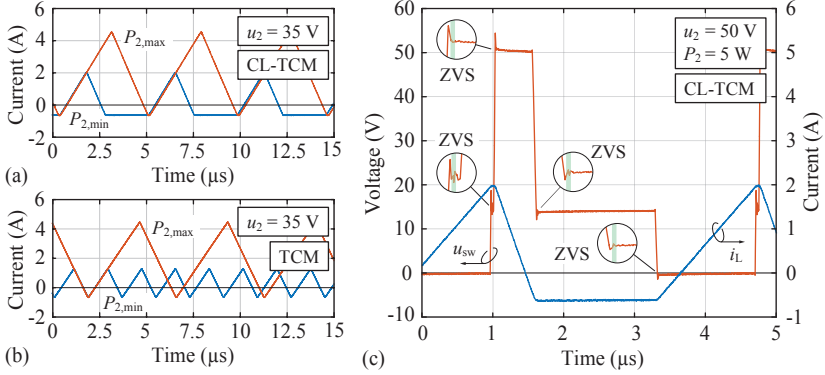


Fig. 6.8: (a)-(b) Measured inductor current waveforms of the prototype converter, operated in CL-TCM and TCM mode, respectively. (c) Measured CL-TCM converter switch-node voltage u_{sw} and inductor current i_L , indicating ZVS operation for all the four switches.

Fig. 6.7(b) is built using two EELP 14 core sets, manufactured from the TDK/EPCOS N87 ferrite material. The inductor is optimized for high-efficiency operation for a minimum converter switching frequency of 100 kHz and has therefore a rather low power density of 15.4 W/cm^3 at maximum output power. The second inductor shown in **Fig. 6.7(c)** is built using an ER 11/5 core set, in order to achieve a high inductor power-density of 66 W/cm^3 at maximum output power. In this case, the inductance value is designed such that the CL-TCM and the TCM converter have the same switching frequency at maximum output power, and such that the maximum switching frequency does not exceed $f_{p,\text{max}} = 1\text{ MHz}$ in TCM mode.

6.3.2 Performance Measurement

For the measurements, the output power range is set to 5-30 W and the output voltage is set to 20 V, 35 V and 50 V. The input voltage is kept in a range of 14.4-14.8 V. During the measurements, the converter was operated in open-loop mode and the timing values for the modulator state machine were calculated offline. The measurements presented in this section are conducted using the inductor shown in **Fig. 6.7(b)**.

The inductor current waveforms for minimum and maximum output power are shown in **Figs. 6.8(a)** and **(b)** for an output voltage of

35 V for the CL-TCM and the TCM operation, respectively. For the CL-TCM converter, soft-switching of the switches T_1 - T_4 is achieved at any point of operation, as indicated in **Fig. 6.8(c)** for minimum output power and an output voltage of 50 V. Note that the intermediate clamping time interval at the maximum inductor current is chosen as small as possible and is negligible, when compared to the total switching period. **Figs. 6.9(a)-(c)** shows the measured and the calculated inductor current characteristics, the switching frequency and the timing values T_{on} , T_{off} and T_{cl} , used for the modulator state machine for the CL-TCM operating mode. **Figs. 6.9(d)-(f)** shows the same measured and calculated parameters for the TCM operating mode. The negative peak inductor current $i_{L,min}$ was set to -0.67 A for both modes of operation, such that the total dead-time needed for the time intervals $[t_7, t_9]$ and $[t_{10}, t_{12}]$ is not exceeding 100 ns, and hence, allows to neglect the dead-times for the timing calculations for the open-loop operation of the converter. However, the magnitude of the negative inductor current $I_{L,min}$ could also be chosen lower in order to slightly reduce the inductor RMS current. In general, in case of the TCM operation, the magnitude of the minimum inductor current can be chosen lower compared to the CL-TCM operation, which is due to the lower parasitic switch capacitance that must be charged during the switching transitions to allow for ZVS operation.

As expected for the CL-TCM operating mode, the peak inductor current at maximum output power is similar to the TCM operation and the operating frequency measurement in **Fig. 6.9(b)** confirms the constant switching frequency of the CL-TCM operation at fixed converter terminal voltages and variable output power. As explained in **Section 6.2.3**, at low output power, the constant frequency operation comes at the expense of a higher peak and RMS inductor current when compared to the TCM operation, as shown in **Fig. 6.9(a)** and **Fig. 6.9(d)**.

In case of the TCM operating mode, the switching frequency varies by a factor of 6.4 from 103 kHz to 662 kHz, whereas the operating frequency of the CL-TCM converter varies only by factor of 2.7 from 99 kHz to 266 kHz, which is in good agreement with the result obtained with equation (6.21). As predicted by the equations (6.17)-(6.20), the clamping-time interval T_{cl} approaches zero at the nominal output power of 30 W (cf. **Fig. 6.9(c)**), which corresponds to the TCM operation.

The input and output power of the converter was calculated based

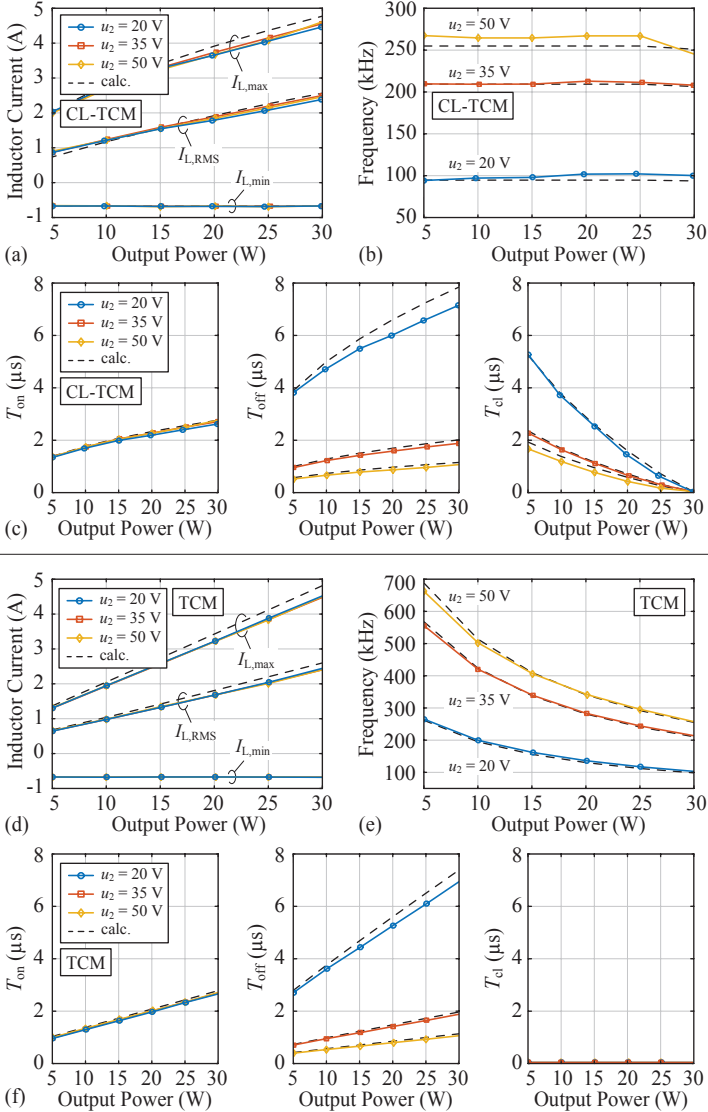


Fig. 6.9: (a) Measured and calculated minimum, maximum and RMS inductor current values of the prototype CL-TCM converter. (b) Measured and calculated switching frequency and (c) ON-, OFF- and clamping-time intervals of the CL-TCM converter. (d)-(f) show the same parameters, measured and calculated for the TCM operating mode.

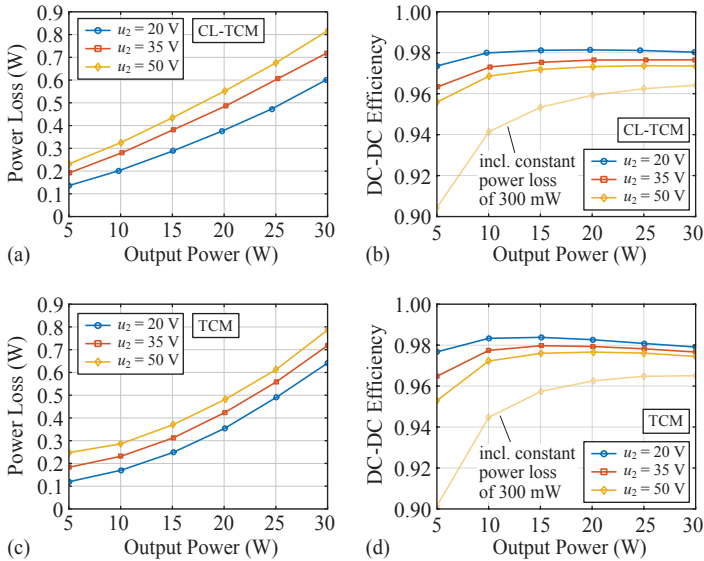


Fig. 6.10: (a)-(b) Measured power loss and DC-DC efficiency of the CL-TCM boost converter at variable output power and different output voltages. (c)- (d) Measured boost converter performance for the TCM operating mode. Note that these measurements do not include the constant power loss of the DSP/FPGA control board.

on the measurement of the input and output terminal voltages and currents, using four Agilent 34410A multimeter. The power loss and the achieved DC-DC efficiency of the CL-TCM and TCM converter are shown in **Fig. 6.10**. The constant power loss caused by the current and voltage measurement circuit of the converter is measured separately and attains a value of 37.2 mW. The gate drive power losses are measured separately as well and are also included in the total power loss measurement.

As mentioned before, the DSP/FPGA board is not optimized for the application at hand and causes a total constant power loss of about 994 mW, where the DSP accounts approximately for 87% of the losses. These constant power losses could be reduced significantly, down to 200-300 mW, using state-of-the-art low-power microcontrollers and FPGAs. Therefore, these constant power losses are not included in the power loss and efficiency measurement. As indicated in **Figs. 6.10(b)** and

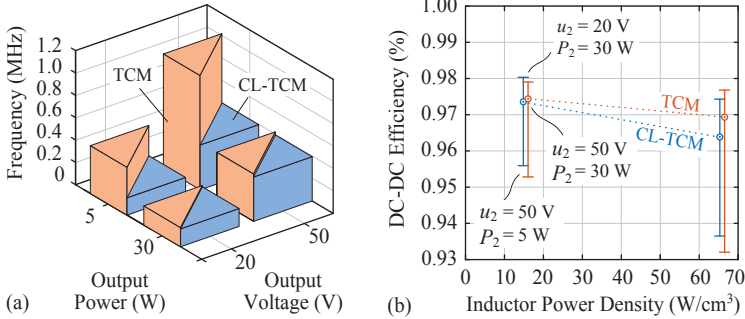


Fig. 6.11: (a) Measured switching frequency variation of the CL-TCM and TCM converter, operated with the inductor shown in **Fig. 6.7(c)**. (b) Measured DC-DC efficiency of the CL-TCM and the TCM converter with respect to the power density of the two inductors shown in **Figs. 6.7(b)** and **(c)**. Note that the efficiency does not include the power losses of the DSP/FPGA control board.

(d), a constant power loss of up to 300 mW could be accepted for the control circuit in order to achieve a DC-DC efficiency above 90% in the entire range of operation.

The CL-TCM and TCM converters show almost the same efficiency at minimum and maximum output power. Due to the increased switching frequency of the TCM operating mode at low output power, it was expected, that the power losses are higher compared to the CL-TCM operation. However, the measurements show that this is not the case. The reason is that, as the switching frequency of the TCM converter increases, the RMS inductor current decreases linearly with decreasing output power, and hence, compensates for the increased AC losses in the inductor core and winding.

In order to compare the degradation of the performance with increasing power density of the inductor, the switching frequency variation and the DC-DC efficiency was measured for both converter operating modes with the inductor shown in **Fig. 6.7(c)**. **Fig. 6.11(a)** shows the measured switching frequency variation. With TCM operation, the operating frequency varies by a factor of 5.96 from 171 kHz up to 1.02 MHz. The CL-TCM converter instead has a maximum switching frequency of 400 kHz and the frequency varies by a factor of 2.6 only.

The results of the efficiency measurement are shown in **Fig. 6.11(b)**

for both prototype inductors. Again, the constant power loss of the DSP/FPGA control board is not included in this measurement. Additionally, due to the reduced inductance value, the negative peak inductor current was increased to -0.75 A in order to achieve ZVS within the 100 ns total dead-time during the time intervals $[t_7, t_9]$ and $[t_{10}, t_{12}]$. Again, the two converter operating modes show very similar efficiencies. However, for the worst case operating point which is at an output voltage of 50 V and an output power of 30 W, the efficiency of the CL-TCM converter is decreasing with a steeper slope towards higher inductor power density, when compared to TCM operation. As explained in **Section 6.2.3**, the CL-TCM emulates TCM operation at maximum output power. Hence, at this operating point, the clamping time intervals are reduced to 35 ns, but are not completely omitted during the measurements, in order to maintain the ZVS modulation scheme for the entire range of operation. Hence, the associated power losses in the clamp-switch and the gate driver are a main reason for the lower efficiency of the CL-TCM converter, when compared to the TCM converter at this specific operating point, as shown in **Fig. 6.11(b)**.

The experimental evaluation and the comparison of the TCM and the CL-TCM boost converter have revealed the advantages and disadvantages, as well as the performance limits of the two more advanced soft-switched boost converter topologies. In order to get the full picture, the focus of the following sections is on the optimization of the conventional hard-switched boost converter and its performance comparison with the soft-switched TCM and CL-TCM operating modes.

6.4 Hard-Switched Boost Converter

The conventional hard-switched boost-type DC-DC converter topology shown in **Fig. 6.2(b)** is the most simple solution in terms of circuit complexity and control effort, and is therefore widely used in industrial applications. As it was mentioned at the beginning of this chapter in **Section 6.1**, the conventional boost converter operation suffers from hard turn-on events of the low-side switch at the beginning of each switching period, as indicated in **Fig. 6.2(f)**. During the hard-switching events, the inductor current is commutated from the body-diode of the high-side switch to the low-side switch, but unless the current commutation is complete, the voltage across the low-side switch cannot decrease to zero. As a result, a large amount of energy is dissipated in the low-

side switch, which is due to the overlapping of the non-zero voltage and current in the switch.

The total converter power losses are mainly consisting of the switching losses and the power losses caused by the inductor. The inductor core and winding power losses are related to the peak-to-peak inductor current ripple and the switching frequency, whereas the total switching losses are determined by the switching frequency, the switching speed and the voltage and current applied to the switch during the switching transition. As shown in **Fig. 6.2(f)**, the hard-switching event occurs always at the minimum inductor current (which is also true for the buck-type operation, where the high-side switch experiences the hard-switching). Hence, at a fixed output power and operating frequency, the switching losses can be reduced, by increasing the inductor current ripple, i.e. by choosing a smaller boost inductance, which in turn reduces the inductor current at the hard-switching instant. However, the increased current ripple causes additional power losses in the inductor. Concurrently, choosing a high switching frequency allows for a more compact converter design, i.e. a smaller inductor volume, but causes significant switching losses and therefore reduces the efficiency of the converter.

In order to find the optimal converter design in terms of power density and DC-DC efficiency, a multi-objective optimization of the hard-switched boost converter was carried out, and is explained in more detail in the following section.

6.4.1 Multi-Objective Optimization

A comprehensive introduction into multi-objective optimization of power electronic converters is given in [141], which was also the basis for the DC-DC converter optimizations carried out in this work.

The simplified optimization routine is shown in **Fig. 6.12** and is implemented using MATLAB. First, the type of converter, i.e. hard-switched, TCM or CL-TCM operation is selected, and the voltage range and output power are specified. In case of the hard-switched boost converter, the optimization process is based on parameter sweeps of the switching frequency and the inductor current ripple specification. For each loop through the specified sweep parameter range, a boost converter is designed and the exact operating point is calculated, i.e. all the relevant component voltages and currents, as well as the FET and

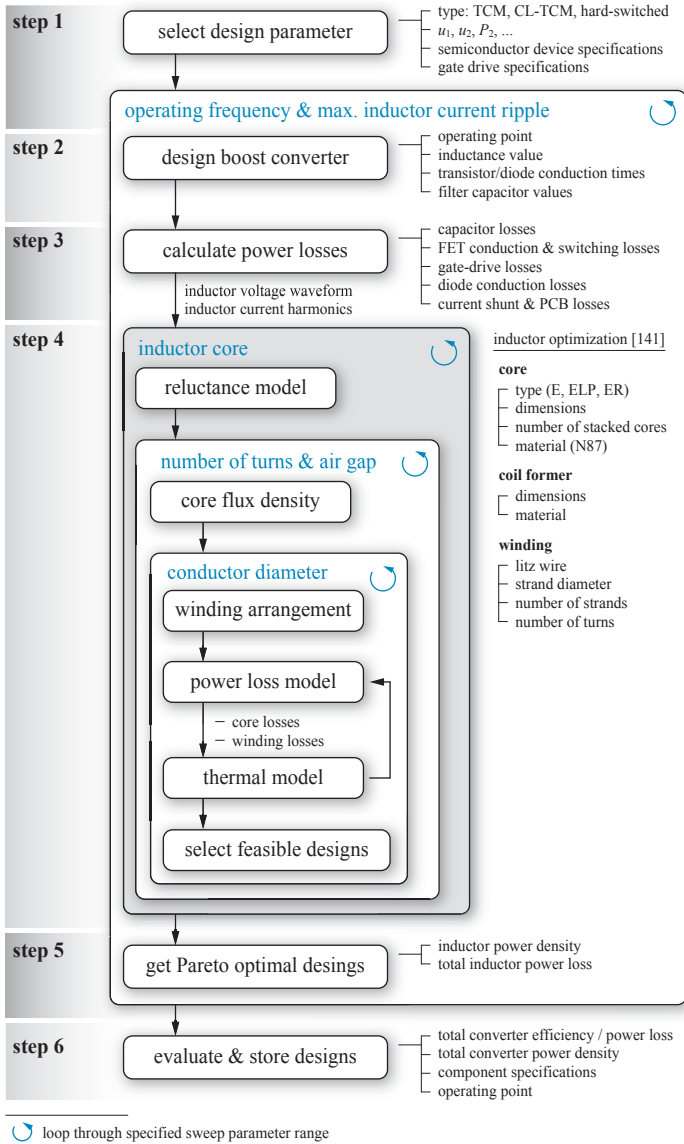


Fig. 6.12: DC-DC boost converter optimization process. The inductor optimization routine is taken from [141].

diode conduction times. In a next step, the power losses are calculated for the switches, the diodes, the current measurement shunts, the PCB and the filter capacitors. The estimation of the switching power losses is a particular challenge and is discussed in the following.

Switching Loss Estimation

An accurate measurement of the switching losses of the EPC2016C GaN half-bridge is extremely difficult, which is mainly due to the small size of the circuit, e.g. the GaN FET outline dimensions are $1.6\text{ mm} \times 2.1\text{ mm}$. A widely applied method to measure the switching losses is to use a double-pulse test setup to directly measure the voltage and current waveforms at the low-side switch of the half-bridge during turn-on and turn-off [141,142]. The switching energy loss is then calculated by integrating the product of the switch voltage and current over the switching transition time interval. As reported in [141,142], the main limitations of this method arise from measurement errors, e.g. caused by a mismatch of probe delays, which is particularly critical when measuring fast switching transients. Another source for measurement error is due to the modification of the commutation loop inductance of the half-bridge, when introducing the current measurement shunt into the switching circuit, which in turn can alter the shape of the switching transient.

An alternative solution to measure the switching power losses is to perform a calorimetric measurement [142,143]. However, the main disadvantage of this method is the increased measuring period, which is due to the large thermal time constants of the calorimetric measurement setup. In addition, the measurement results contain the total loss of the switching cell, i.e. the FET, the PCB and the diode conduction losses, as well as the switching losses, which makes a distinction extremely difficult or even impossible.

Consequently, it was decided to estimate the switching losses by means of a virtual switching loss measurement using a SPICE simulation. The simulation circuit model of the EPC2016C GaN FET is provided by the manufacturer and the SPICE simulation allows for a fast and simple switching loss estimation in a wide range of operating conditions. However, the author is aware of the limited accuracy of this approach, as the simulation results are only as good as the model of the GaN FET itself. Furthermore, the switching loss estimation depends also on the modeling of the gate drive circuit and the parasitic inductances in the commutation loop of the half-bridge circuit. In ad-

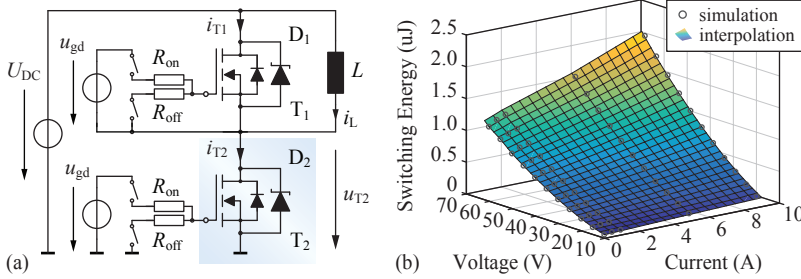


Fig. 6.13: (a) Schematic diagram of the SPICE simulation model, which was used to extract the switching loss data of the EPC2016C GaN FET, including the anti-parallel connected MBR1H100SF Schottky diode.

dition, the simulation does not consider any thermal effects, i.e. the temperature dependence of the ON-state resistance of the GaN FET.

Accordingly, the derived switching loss energies are an estimation only and most likely underestimate the actual switching losses of the hard-switched FETs.

Fig. 6.13(a) shows a simplified schematic diagram of the SPICE simulation model. The low- and high-side gate drive sections of the half-bridge gate driver LM5113 are modeled with an ideal voltage source of $u_{gd} = 5\text{ V}$ and the approximate internal turn-on and turn-off resistances $R_{on} = 4.2\ \Omega$ and $R_{off} = 1\ \Omega$, which are calculated using the peak source and current sinking capabilities reported in the LM5113 data sheet [70]. Due to the small package of the GaN FETs and the parallel Schottky diode, the half-bridge can be designed with very low commutation loop inductance and is therefore neglected in the simulation. However, in order to enhance the simulation stability, an inductance of $100\ \text{pH}$ is included in series to each switch. As with a double-pulse measurement, the total energy loss during hard-switching of the low-side FET is obtained for several operating points, i.e. different DC-link voltages U_{DC} and different commutation currents, by integration of the instantaneous power loss of both switches over the hard-switching time interval. The obtained power loss map is shown in **Fig. 6.13(b)** and is used for the optimization routine, in order to derive the switching loss at a specific operating point using interpolation.

Boost Inductor Optimization

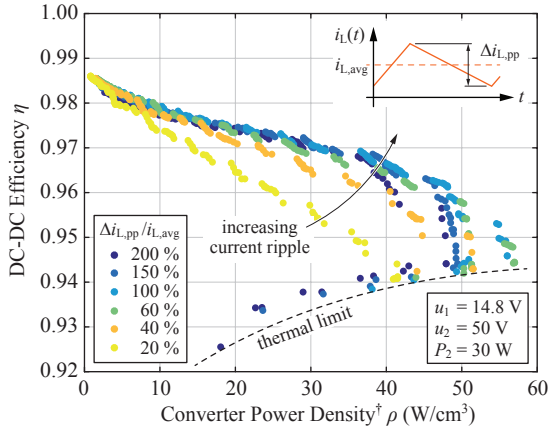
The modeling and the optimization of the boost inductor is performed using the same routines as in [141], and which are described in great detail therein. The design space of the inductor optimization routine is determined mainly by the core type, the core material and the coil winding type, i.e. using magnet wire or litz-wire. In this case, different E-, ELP- and ER-type ferrite cores, the TDK/EPCOS N87 ferrite material and a wide range of different litz-wires are considered. As shown in **Fig. 6.12**, the inductor optimization routine loops through all selected core geometries and for each core, a set of feasible numbers of turns and air-gap sizes is calculated, which allow for the desired inductance value. In a next step, for each core and winding arrangement, the feasible range of litz-wire, i.e. strand diameter and number of strands is determined.

The total winding and core power losses are then calculated for each feasible inductor design, as described in detail in [141]. Whereas for the winding loss calculation, analytical models are available [59], the core loss estimation is based on the improved improved Generalized Steinmetz Equation (i^2 GSE) [59], using a measured power loss map of the TDK/EPCOS N87 ferrite material, provided in [141]. A thermal model is then used to predict the hot-spot temperature of the inductor and according to a thermal limit of 100 °C, only the feasible inductor designs are selected and stored for further processing.

Optimization Results

The thermally feasible inductor designs are merged with the previously calculated boost converter design and the total power loss and the overall power density of the converter are calculated. Note that the volume of the converter considers the boxed volume of the inductor, the volume of the GaN FET half-bridge of 212 mm³ and the size of the DC-link capacitors only.

Finally, the Pareto-optimal designs are extracted for each inductor current ripple specification. The resulting Pareto fronts are shown in **Fig. 6.14**, which illustrate the trade-off between the DC-DC efficiency and the overall converter power density at the maximum output power. In this case, the operating frequency ranges from 100 kHz to 1 MHz and the inductor current ripple $\Delta i_{L,pp}$ is specified in a range of 20 % to 200 % of the average inductor current at the maximum output power of



[†] considering the lumped volume of the inductor, the half-bridge components and DC-link capacitors.

Fig. 6.14: Calculated η - ρ Pareto front of the hard-switched boost converter for different current ripple specifications, using a litz-wire winding for the boost inductor. The calculation of the efficiency does not include any auxiliary power supply or control circuit power losses.

30 W and an output voltage of 50 V. The input voltage has a fixed value of 14.8 V. The inductor core dimensions are swept continuously based on the geometric relations of a TDK/EPCOS E 14/8/4 ferrite core-set. For the sweep, the minimum boxed core-set volume is set to 0.1 cm^3 . However, the simulation showed that the minimum feasible magnetic core cross-section is 5 mm^2 , which corresponds to a boxed core-set volume of 0.13 cm^3 . As a result, the boxed volume of the smallest inductor including core and winding is 0.296 cm^3 and the largest core that is considered in the calculations has a magnetic cross-section of 114 mm^2 .

From **Fig. 6.14** it is evident, that if the inductor current ripple is increased beyond 20% of the average inductor current, the DC-DC efficiency and the power density of the converter can be increased significantly. However, as the inductor current ripple increases beyond 60% of the average inductor current, the Pareto front is not significantly pushed further towards higher efficiencies and higher power densities. Specifically, the achievable inductor power density decreases again at large inductor current ripples. This is mainly due to the increasing high frequency power losses in the inductor core and winding.

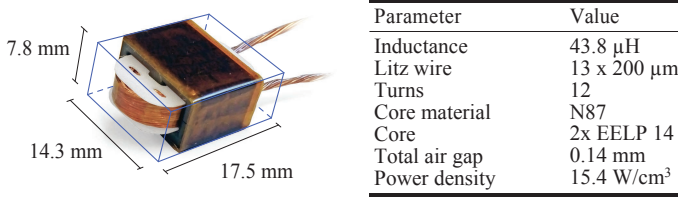


Fig. 6.15: Hardware prototype and specifications of the boost inductor, optimized for the hard-switched boost converter operation.

Therefore, it can be concluded that for the application at hand, using a litz-wire winding and an inductor current ripple specification of $\Delta i_{L,pp}/i_{L,avg} = 60 - 100\%$ is an optimal choice for the hard-switched boost converter design.

6.4.2 Performance Measurement

Fig. 6.15 depicts the hardware realization of the optimized inductor for the hard-switched boost converter. The inductor is designed for the same power density as the inductor used for the CL-TCM converter in order to provide a fair comparison. The optimum switching frequency of the hard-switched converter is 200 kHz and the inductor is designed for a maximum inductor current ripple specification of $\Delta i_{L,pp}/i_{L,avg} = 60\%$ at the maximum output power of 30 W and the maximum output voltage of 50 V, which yields a maximum current ripple of 1.2 A. For the measurements, the input voltage is kept at a constant value of 14.8 V.

Figs. 6.16(a) and **(b)** show the measured inductor RMS current and the peak-to-peak inductor current. As shown in **Fig. 6.16(b)**, at the maximum output voltage, towards higher output power, the inductor current ripple increasingly deviates from the theoretical current ripple specification. The reason is that at large current ripples and increasing DC-magnetization, i.e. at increasing output power, the inductor core is operated already close to the non-linear regime. As a result, at high magnetic flux densities, the core permeability is decreasing, which decreases the total inductance and hence, increases the peak inductor current as well as the overall current ripple. As a solution, the core cross section area could be increased, or additional turns could be added to the winding. In this case, the non-linearity of the inductor does not affect the operation of the converter and a significant increase

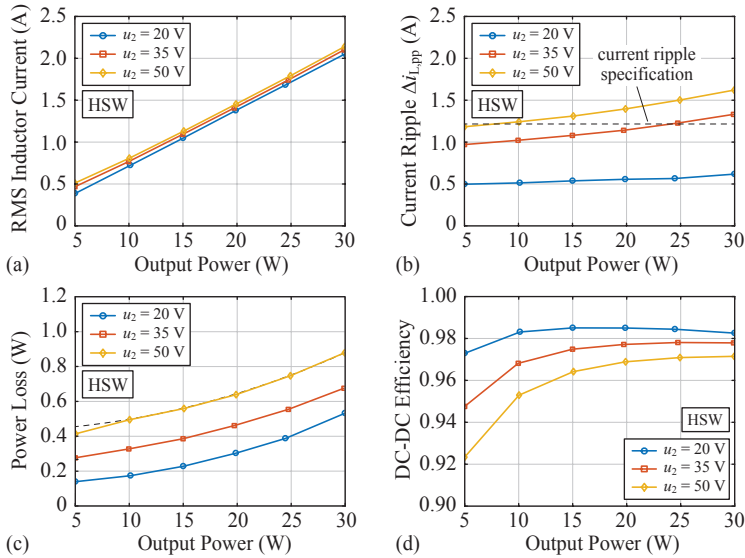


Fig. 6.16: (a) Measurement of the RMS inductor current and the peak-to-peak inductor current ripple (b) for the hard-switched boost converter operation. (c)-(d) Measured power loss and DC-DC efficiency of the hard-switched boost converter at variable output power and different output voltages. Note that the power loss and efficiency measurements do not include the constant power loss of the DSP/FPGA control board.

of the power loss could not be noticed.

The power loss of the hard-switched boost converter was measured with the same hardware prototype board (cf. **Fig. 6.7(a)**) as for the TCM and the CL-TCM converter. Similar to the TCM operation, the clamp switches are not operated and are kept in OFF-state throughout the measurements. Note that the clamp switches add additional capacitance to the main power switches and therefore slightly increase the switching power losses. The power loss measurement results are shown in **Fig. 6.16(c)**. Again, the measurements do not include the large constant power loss of 994 mW of the DSP/FPGA control board. As expected, due to the hard-switching operation of the converter, the power loss increases significantly with increasing output voltage. Hence, the DC-DC efficiency shown in **Fig. 6.16(d)** is reduced substantially at partial load operation. Nevertheless, at low input-to-output voltage

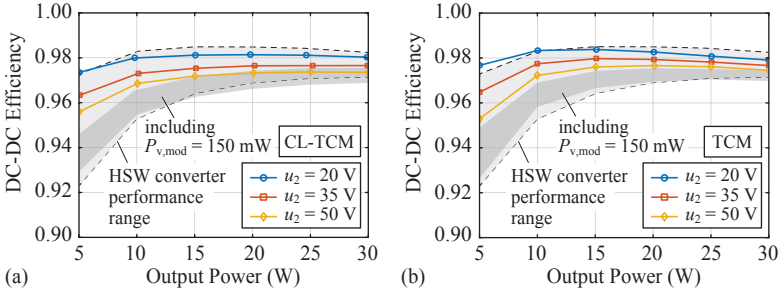


Fig. 6.17: (a)-(b) Comparison of the CL-TCM and the TCM boost converter DC-DC efficiencies with the hard-switched boost converter performance range. Additionally, the performance range of the soft-switched converter solutions is indicated, if an additional power loss of 150 mW is considered for the ZVS modulator. Note that the power loss and efficiency measurements do not include the constant power loss of the DSP/FPGA board.

conversion ratios, the DC-DC efficiency attains very high levels, i.e. more than 98%. It is interesting to note, that due to the large inductor current ripple at maximum output voltage, the total power loss at minimum output power is lower than expected from the power loss curve, as indicated in **Fig. 6.16(c)**. The reason is that at this operating point, the inductor current reaches a negative value at the turn-off of switch T_1 and allows for a partial soft-switching of switch T_2 , which in turn reduces the switching losses substantially.

In the following section, the performance of the hard-switched boost converter is compared to the TCM and the CL-TCM operating modes.

6.5 DC-DC Converter Comparison

The comparison of the achieved DC-DC efficiency of the soft-switched and the hard-switched boost converter is shown in **Figs. 6.17(a)** and **(b)**, respectively. It is important to note, that again, these efficiencies do not include the power losses of the DSP/FPGA control board. In order to determine the most suitable converter solution for the application at hand and to provide a fair comparison, the additional power losses of the ZVS modulator $P_{v,mod}$ must be included for the CL-TCM and the TCM converter. In this case, as indicated in **Figs. 6.17(a)** and **(b)**, an additional power loss of about 150 mW could be accepted

for the modulator circuit of the soft-switched converters in order to keep the efficiency within the performance range of the hard-switched boost converter at partial load operation. This is hardly achievable with currently available off-the-shelf components, such as CPLDs or FPGAs. Nevertheless, using state-of-the-art CMOS process technologies, an Application Specific Integrated Circuit (ASIC) could be designed to implement the CL-TCM ZVS modulator circuit, optimized for ultra-low power consumption, and hence, may allow to outperform the conventional hard-switched solution. This however, is beyond the scope of this thesis. Consequently, in terms of power loss and circuit complexity, it must be concluded, that the conventional hard-switched topology is the most appropriate solution for the application at hand.

In order to give a starting point for further optimization, the power loss distribution is calculated for each boost converter topology for the operating points at minimum and maximum output voltage and output power, as shown in **Fig. 6.18**. Specifically in case of the TCM and the CL-TCM converter it is striking, that the power losses caused by the current shunt measurements and the PCB make up a large part of the total power losses. In this case, in order to measure the input and the output current, a $5\text{ m}\Omega$ current shunt resistor was used and the inductor current was measured using a $10\text{ m}\Omega$ shunt. These losses could be reduced by implementing the current zero crossing detection as described in **Section 6.2.3**. The power losses in the PCB are determined using the measured DC-resistance at the converter input and output and the measured AC resistance in the inductor current loop, including the inductor lead wires and screw connections. These power losses could be further reduced by a careful PCB layout in the inductor current path and by directly integrating the inductor into the converter, i.e. as close as possible to the switches. The prototype converter presented in **Section 6.3** is convenient for the evaluation of different operating modes and different boost inductors, but as explained, allows for further design and layout improvements.

In case of the hard-switched boost converter, at maximum output power, the total inductor power loss and the power losses related to the semiconductor switches are approximately equal in magnitude. In this case, the inductor current measurement shunt was replaced by a $5\text{ m}\Omega$ resistor and the inductor lead wires are directly soldered to the PCB. Hence, the PCB and the shunt power losses are reduced. As expected, at maximum output power, the hard-switching power losses make up a

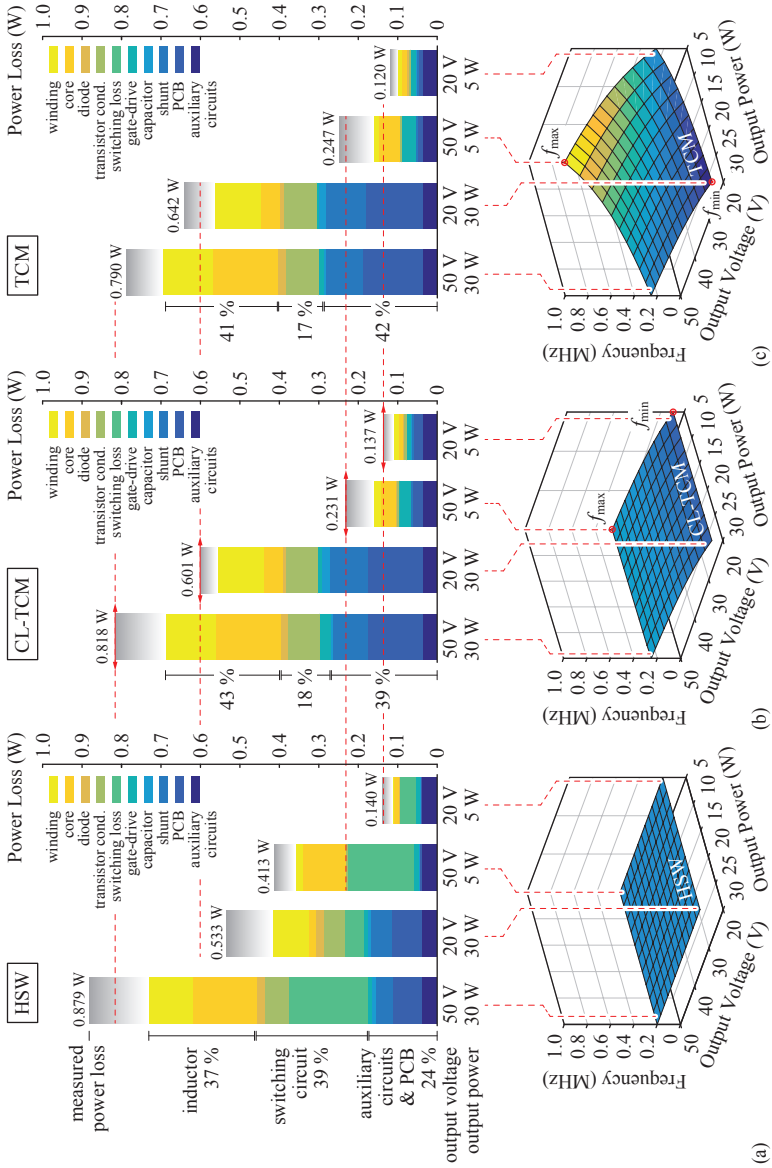


Fig. 6.18: Calculated power loss distribution and switching frequency variation of the hard-switched (a), the CL-TCM (b) and the TCM boost converter (c).

large part of the total power loss. Furthermore, when comparing the calculated and the measured total power loss, it can be expected that the switching losses are underestimated at maximum output power and maximum output voltage. It is likely that the switching energy loss increases at a higher rate with increasing switching current than predicted by the switching loss simulation results shown in **Fig. 6.13(b)**. In addition, the calculation neglects any switching power losses occurring during soft-switching operation, which applies also to power loss calculations of the TCM and the CL-TCM converter.

6.6 Summary of the Chapter

For the control of the wireless power transmission, additional DC-DC converter stages are needed, in order to convert the external and the internal battery voltages to the required IPT terminal voltages. This chapter shows the realization and the comparison of two soft-switched converter topologies and the conventional hard-switched converter topology, at the example of the external boost converter, which is required for the SSU TET system topology. For the implementation of the soft-switched converters, the TCM and the CL-TCM topology are considered. Since the CL-TCM converter is less well known in the literature and/or no soft-switching scheme has been described so far, its operation and implementation is explained in more detail.

The main results of this chapter are summarized as follows:

- ▶ The CL-TCM DC-DC buck or boost converter allows for ZVS of all switches and offers a significantly reduced switching frequency variation when compared to the traditional TCM operation, which in turn simplifies the filter design in EMI-sensitive applications and relaxes the requirements for the digital control.
- ▶ The control effort for the TCM and the CL-TCM converter is similar and the additional clamp-switch and boot-strap gate driver, needed for the CL-TCM converter, do not significantly increase the circuit complexity in the case of a low voltage/low power application.
- ▶ In cases where a high power conversion efficiency is desired, the CL-TCM and the TCM converter achieve similar performance at

a low power density of the inductor. However, in applications where a very high power density is needed, the TCM converter shows a superior performance in terms of efficiency and power density, which is mainly because of the lower number of switches required for the TCM operation.

- ▶ The optimization of the hard-switched boost converter has revealed, that a large inductor current ripple and the use of a litz-wire winding allows to achieve a similar DC-DC efficiency and power density as obtained for the CL-TCM and the TCM converter operation.
- ▶ It turned out for the low voltage/low power application at hand, that the switching losses in the hard-switched converter are not the main decisive factor which determines the most suitable converter topology and/or modulation scheme, which is mainly due to the significant improvements in modern wide-band-gap semiconductor technology. A far more important factor is the constant power loss generated by the control circuit, which has a significant impact on the outcome of the comparison between soft-switched and hard-switched converters. In conclusion, only a careful and application-specific analysis of the converter topologies and modulation schemes reveals the advantages and limitations of each topology and hence, allows to select the most suitable solution for the application at hand.

The following chapter covers the realization of the wireless communication channel, which is needed for the remote monitoring of the implant and the closed-loop control of the IPT system.

7

Wireless Communication

THE CONTROL schemes of the series-series compensated IPT system topology presented in **Section 2.6** require both an adaptation of the load resistance at the IPT system output, which depends on the transferred power and/or on the coil coupling factor. Hence, in both cases, a closed-loop control of the IPT system output voltage is needed and therefore, a wireless communication channel is required for the feedback of the secondary-side operating point. In addition, the wireless communication channel is not dedicated solely to the TET system control, but is also required for the control of the LVAD and for the transmission of physiological sensor data.

There are mainly three solutions for the implementation of a wireless communication link between the implanted and extracorporeal part of the TET system. The first method is to use the IPT system itself for a simultaneous power and information transfer by means of an amplitude modulation of the energy transfer carrier signal, using a Load Shift Keying (LSK) modulation technique or by modulating the resonance frequency of the IPT resonant tank [21, 22, 144, 145]. These methods are often used for low power implantable medical devices. As a main disadvantage, the information can be transferred only if the power transmitter is in operation and is located close to the power receiver coil. In case of the TET system application at hand, another disadvantage of the mentioned methods is the limited achievable bandwidth of the communication, which is due to the low frequency of the carrier signal of a few hundred kilohertz.

Hence, for higher power transfer, it is advantageous to separate the power and data transmission channels. In this case, dedicated data transmission coils can be embedded in the energy transfer coils, which

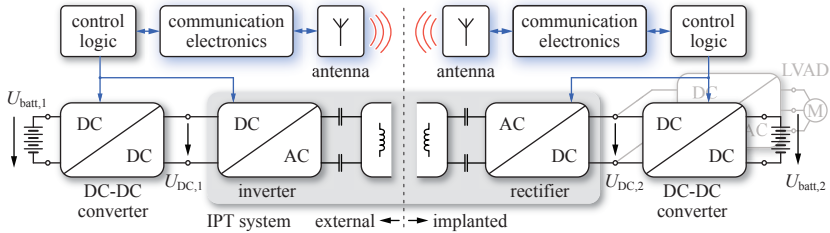


Fig. 7.1: TET system concept for a fully implantable MCS system.

allow for a short-range communication, even if no power is transmitted to the implant [23, 24, 146]. In addition, a higher carrier frequency can be chosen for the data transmission coils, which allows for higher data rates. A main disadvantage of this technique is the electrical interference between the energy- and the data transfer channel, which is due to the mutual coupling between the two links.

The third possibility for the implementation of the wireless communication channel is to use dedicated Radio Frequency (RF) transceivers and additional RF antennas on the primary and secondary side of the TET system, which are fully decoupled from the energy transfer system, as it is illustrated in **Fig. 7.1**.

The main advantage of this implementation is that the implant can be monitored and controlled over a much larger distance, e.g. when the patient does not wear the external power supply and the TET system is not used. Furthermore, highly integrated versatile RF transceivers are available as off-the-shelf components, which allows to implement reliable bidirectional communication links with data rates up to 1 Mbps using Frequency Shift Keying (FSK) modulation techniques. Therefore, in the case at hand, this type of communication system is considered the most appropriate solution for the transmission of control and sensor data, as well as for the remote monitoring of the implanted blood pump.

A particular challenge is the design of the implantable antenna, as it must be able to operate within the electrically difficult environment of the human body. Hence, the main focus of this chapter is on the design, the implementation and integration of the implantable antenna, as presented in [147]. In addition, a prototype of the RF transceiver electronics is realized and the electrical performance of the implantable antenna is experimentally verified and the antenna is checked for

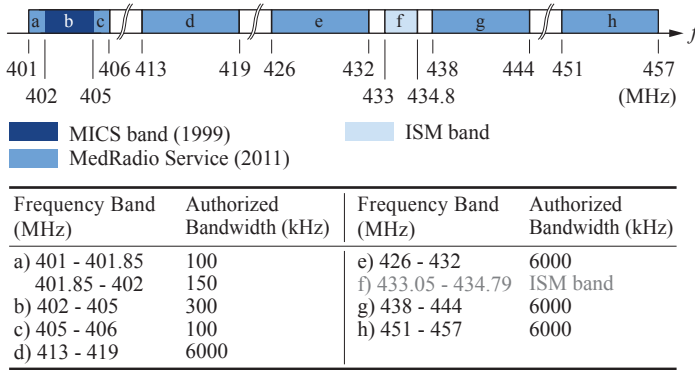


Fig. 7.2: Medical Device Radiocommunications Service (MedRadio) frequency spectrum overview and authorized bandwidths [148].

compliance to EMF exposure limits using FE-simulations.

7.1 Medical Device Radiocommunications Service

Active implantable devices such as cardiac pacemakers and defibrillators are allowed to communicate in dedicated frequency bands, such as the Medical Implant Communication Service (MICS), which was established by the FCC in 1999 and covers the frequency range of 402-405 MHz. In 2009, the FCC extended the frequency range to 401-406 MHz, which is today known as the Medical Device Radiocommunications Service (MedRadio) frequency band, and added 24 MHz of additional spectrum to the MedRadio band in the frequency range of 413-457 MHz in 2011 [148]. The distribution of the MedRadio band between 400 MHz and 500 MHz is illustrated in **Fig. 7.2**.

The RF transceiver and the implantable antenna described in the following sections, are designed for an operation within the MICS band at a center frequency of 403.5 MHz. The maximum radiated power within the MICS band is limited to a maximum Equivalent Isotropically Radiated Power (EIRP) of -16 dBm (25 μ W) [149], in order to minimize the risk of interference with other medical devices, which are operating in the same frequency range. Further, the authorized band-

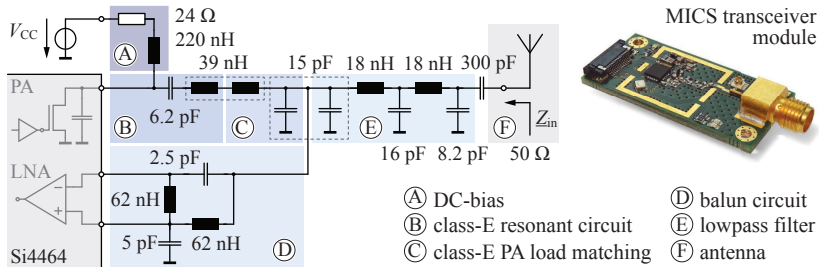


Fig. 7.3: RF transceiver front-end circuit.

width is limited to 300 kHz. If a higher bandwidth is required, the RF transceiver and the antenna design can be adapted easily to operate at a higher frequency, e.g. in the range of 413-419 MHz, where the authorized bandwidth is specified with 6 MHz (cf. **Fig. 7.2**).

In the following, the implementation of the RF transceiver module and the design of the extracorporeal MICS band antenna is presented briefly and second, the design of the implantable antenna is covered in more detail.

7.2 MICS Band Transceiver

The key component of the MICS band RF transceiver implemented in this work, is the Integrated Circuit (IC) component Si4464 [150]. This high performance RF transceiver allows for an operation in a wide frequency range from 119 MHz to 960 MHz. The maximum data rate is up to 1 Mbps using a 4-FSK modulation scheme, and the receiver sensitivity is specified with up to -97 dBm at a data rate of 500 kbps.

The RF front-end circuit is shown in **Fig. 7.3** and a detailed description of the design of the analog front-end is given in [151]. Its basic functionality is summarized in the following. The Power Amplifier (PA) of the Si4464 transceiver is operated in Class-E mode, which allows for zero-voltage switching of the RF MOSFET and thus offers a highly efficient operation. The drain terminal of the RF MOSFET is connected to the DC bias circuit, which protects the DC supply from the high-frequency signal and which is used to limit the output power of the transceiver circuit. In this case, the bias circuit is designed such that the maximum output power attains 14.4 dBm (27.6 mW) into a

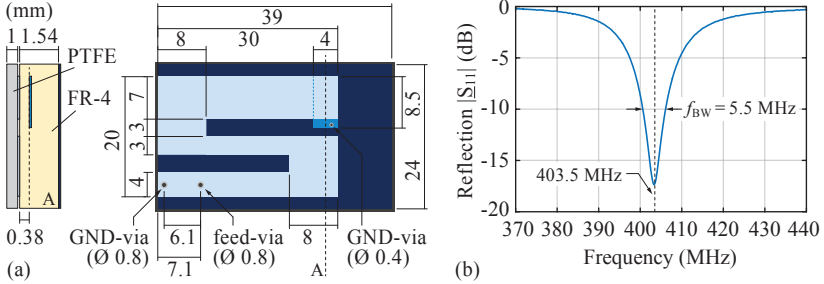


Fig. 7.4: (a) Dimensioning of the extracorporeal MICS band antenna, designed for an operation at 403.5 MHz. (b) Measurement of the reflection coefficient of the fabricated antenna.

50 Ω load. As it will be shown later, in the case of the implanted transceiver, the output power of the transceiver has to be reduced to 9.35 dBm (8.6 mW) in order to comply with the maximum allowed EIRP of -16 dBm (25 μ W). The resonant circuit connected in series to the RF MOSFET drain terminal is tuned to the center frequency of 403.5 MHz and the subsequent matching network transforms the antenna impedance of 50 Ω to the PA load impedance that allows for class-E operation. In order to suppress the higher harmonic content in the PA output signal, a 5th order Chebyshev low-pass filter is added to the output of the transmitter [151].

In the receiving signal path, a 4-element balanced-to-unbalanced (balun) circuit is inserted, which converts the single-ended antenna signal into a differential signal at the input of the Low Noise Amplifier (LNA) and which simultaneously provides the required impedance matching [151].

For the implementation of the extracorporeal Planar Inverted-F Antenna (PIFA), an FR-4 substrate is used and the antenna is fabricated using standard PCB production methods. The dimensioning of the antenna patch and the layer stack of the PCB is shown in **Fig. 7.4(a)**. The antenna patch is meandered in order to increase the electrical length of the antenna and the additional capacitive load at the open end of the antenna and the PTFE superstrate allow for a further reduction of the overall antenna dimensions. The measurement of the reflection coefficient at the antenna input terminal in **Fig. 7.4(b)** shows that the impedance matching is sufficient for a reliable communication, but it

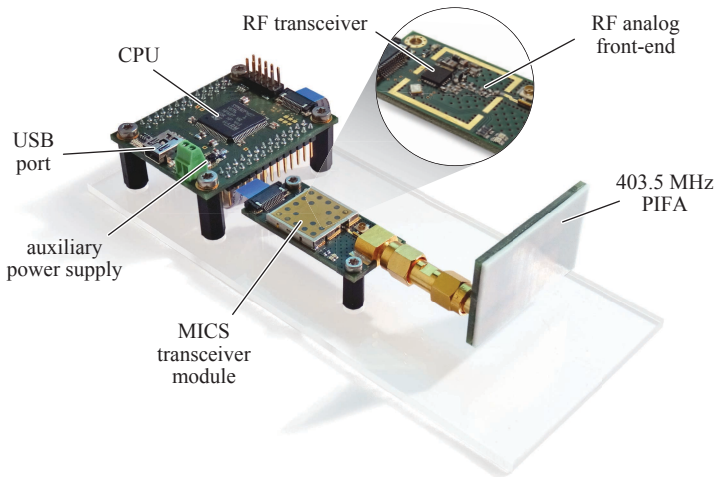


Fig. 7.5: Hardware prototype of the MICS transceiver.

could be further improved by adjusting the distance between the GND-via and the antenna feed-via.

The hardware prototype realization of the transceiver module is shown in **Fig. 7.5**. The quality of the communication channel is evaluated by measuring the received signal strength, i.e. the Received Signal Strength Indicator (RSSI), and the ratio between the number of failed data packet transmissions to the total number of transmitted data packets, using two identical transceiver modules, operated in air. The measurement was performed at a data rate of 1 Mbps and a total number of 10'000 data packets were transmitted, each containing 10 bytes of payload data. A packet transmission is considered successful, if the packet is received correctly and is successfully acknowledged by the receiver. As a result, for an average RSSI of -71 dBm, a packet error ratio of less than 2% is achieved. However, if the received signal power is lower than -80 dBm, the packet error ratio increases significantly.

The measured power consumption of the module in receive-mode is 51.1 mW, but during the duration of the data transmission of 260 μ s, the power consumption rises up to 217 mW. Hence, for an effective data rate of 50 kbps, i.e. transferring the 10 bytes of user data at a rate of 625 Hz, the total average power consumption is estimated with 78 mW.

The antenna shown in **Fig. 7.4(a)** is designed to operate in air and

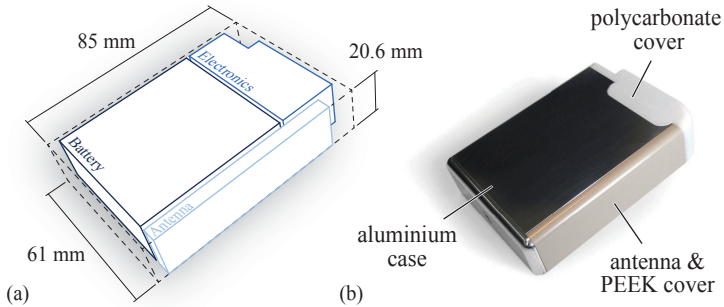


Fig. 7.6: (a) Distribution and space occupation of the main electrical components of the TET implant, i.e. the backup battery, the power and control electronic components and the antenna. (b) Implant dummy enclosure and integrated antenna assembly, which was used for the experimental verification of the antenna performance.

is heavily detuned in close proximity to human tissue, which is due to the distinct dielectric properties of the tissue. Hence, in the following sections, the realization of an implantable antenna and the influence of the human tissue on the antenna characteristics are discussed in more detail.

7.3 Implant Antenna Design

A main objective of the design of implantable antennas is to minimize the antenna volume. However, the allowed volume occupation of the antenna is highly dependent on the actual implant design and its dimensions. In order to maximize the antenna performance, i.e. the gain and radiation efficiency, the antenna should be built using the maximum space available that is feasible for the implant at hand. **Fig. 7.6(a)** illustrates the allocation of the electronic components and the volume occupation for the preliminary design of the implantable part of the TET system. The boxed volume of the implant is 10.7 cl, and is mainly determined by the backup battery, which occupies the largest amount of the volume and which defines the overall thickness of the implant. The antenna is placed on the side of the enclosure, such that the implant can be built as thin as possible, while offering a large surface area of 69 mm \times 20.6 mm for the antenna design. The total height of the an-

tenna assembly, including the superstrate material is 5 mm. Hence, the total boxed volume of the antenna is 0.71 cl, which accounts for 6.65 % of the total boxed implant volume.

In [25, 152] it was shown that magnetic dipoles, i.e. loop antennas, offer higher radiation efficiencies than electric sources such as a patch antenna or the electric dipole antenna, when operated within the human body. As discussed in **Section 4.1**, the human tissue is non-magnetic and barely interacts with the magnetic field. Hence, the strong magnetic near field of the antenna is not absorbed. However, placing a loop antenna near to the surface of the metallic enclosure of the implant increases the power losses and disturbs the magnetic field significantly. Therefore, it was decided to chose the PIFA for the antenna implementation, which benefits from the large reference ground plane formed by the implant enclosure, which in turn shields the internal electronics from the electromagnetic field generated by the antenna. Furthermore, the PIFA offers a highly compact design with a low profile and offers higher radiation efficiency within the human body when compared to conventional microstrip antennas (e.g. spiral-type microstrip antennas), as it was shown in [153].

Following the design guidelines reported in [25], the antenna was first designed in air in order to reveal the critical geometric design parameters and in a second step, the lossy tissue material is added to the model and the previously revealed design parameters are then used to optimize the antenna with the objective to maximize the input impedance matching, the antenna gain and the radiation efficiency.

In the following sections, the influence of the geometric design, the antenna substrate and superstrate material, as well as the influence of the human tissue on the antenna performance are analyzed.

7.3.1 Antenna Patch Design

The numerical simulations are performed using the Ansys High Frequency Structure Simulator (HFSS). In [154], it was shown that the size of the PIFA's ground plane has a significant influence on the bandwidth, the radiation pattern and the achieved gain of the antenna. Therefore, the antenna assembly is simulated together with the implant case, which is modelled as solid block of aluminium with a polycarbonate top cover. The ground plane of the PIFA is electrically connected to the implant enclosure and is thereby increased in size. As a result, the radiation

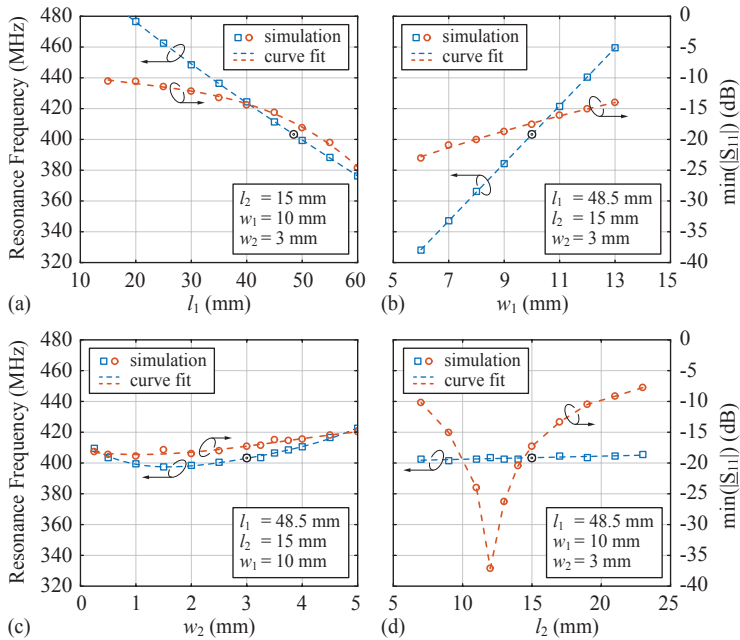


Fig. 7.8: Influence of the variation of the main patch design parameter l_1 , l_2 , w_1 and w_2 (cf. **Fig. 7.7(b)**) on the resonance frequency and on the input impedance matching of the antenna.

the lossy tissue. As shown in **Figs. 7.8(a)** and **(b)**, the resonance frequency of the antenna is mainly determined by the parameters l_1 and w_1 . As the length of the slot l_1 is increased, the resonance frequency is decreasing linearly due the increase of the electrical length of the antenna. A similar effect can be observed with the variation of the distance w_1 . By moving the slot further away from the ground via, the current density on the other side of the slot, opposite to the ground via, is decreasing and hence, the effective electrical length of the patch is decreased as well. Note that the tuning of l_1 and w_1 also takes a significant influence on the impedance matching of the antenna.

The width of the slot, denoted with w_2 , has a less prominent influence on the resonance frequency and on the impedance matching of the antenna and can be used for fine-tuning, as shown in **Fig. 7.8(c)**. As the width of the slot is increased, the resonance frequency rises because

of the increasing impedance of the delimited part of the patch, which in turn decreases the effective electrical length of the antenna. On the other hand, if the slot width is much smaller than the thickness of the substrate, the capacitive coupling between the separated parts of the patch becomes dominant and the resonance frequency rises again since the slot loses its effectiveness.

First, as explained above, the parameters l_1 , w_1 and w_2 are used to tune the antenna for an operation at the desired resonance frequency. Then, in a second step, the distance l_2 between the ground via and the feed-via is used to tune the antenna's input impedance, as shown in **Fig. 7.8(d)**. Note that the diameter of the GND-via, as well as the diameter of the feed-via are critical for the matching of the antenna, since the diameter of the vias directly influences the inductance of the current loop seen at the antenna input.

7.3.2 Substrate Material

The substrate material properties and layer thickness have a significant influence on the resonance frequency, radiation efficiency and the fractional bandwidth of the antenna [155–157]. A substrate material with high relative permittivity increases the electrical length of the antenna, which decreases the resonance frequency and hence allows for a more compact design of the antenna, but the bandwidth of the antenna decreases as well, i.e. the quality factor of the antenna is increased. The bandwidth of the antenna can be enhanced by increasing the height of the substrate, as reported in [155, 157]. But considering the specified total height of 5 mm of the antenna assembly, a thicker substrate comes at the expense of a reduced superstrate thickness, which is not preferred, as pointed out in the following section.

Following these considerations, and given the large area available for the antenna design, a substrate material with low permittivity and low profile is used. In addition, a material with a low dissipation factor is preferred in order to minimize the power loss in the substrate. Therefore, the substrate material Duroid 5880 was used with a standardized thickness of 1.575 mm. The relative permittivity of this material is $\epsilon_r = 2.2$ and the dissipation factor is as low as $\tan(\delta) = 0.0004 - 0.0009$, and therefore, allows to substantially enhance the efficiency of the antenna.

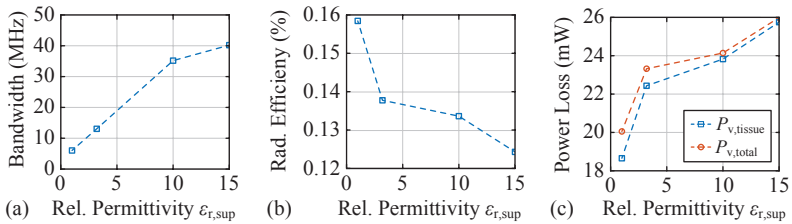


Fig. 7.9: Simulation of the influence of the superstrate permittivity $\epsilon_{r,\text{sup}}$ on the impedance matching bandwidth (i.e. the bandwidth at $|\underline{S}_{11}| = -10$ dB) (a), the radiation efficiency (b) and on the total tissue power loss (c), at a radiated power of $32.5 \mu\text{W}$.

7.3.3 Superstrate Material

The superstrate of the antenna has a particularly important role in the design of implantable antennas. The superstrate layer insulates the antenna patch from the electrically conductive tissue material and furthermore, it acts as a buffer layer that allows to confine the high electrical near field component within the superstrate layer, due to the much higher permittivity of the biological tissue compared to the insulation layer. Hence, the power loss in the biological tissue can be reduced significantly, which in turn improves the radiation efficiency of the antenna, as described in detail in [25, 158, 159].

It is reported in [160], that the loading of the antenna with a high permittivity superstrate material allows to reduce the size of the antenna and decreases the antenna bandwidth. The simulation results depicted in **Fig. 7.9(a)** seem to be in contradiction to this statement, as the impedance matching bandwidth is increasing with increasing superstrate permittivity. But it is important to note that in this case, the increase in bandwidth is due to the higher amount of power loss introduced into the human tissue (cf. **Fig. 7.9(c)**), which in turn lowers the overall quality factor of the antenna. The increased bandwidth should therefore not be confused with the 'useful bandwidth', as it reflects mainly the increased power losses in the tissue [25].

As a conclusion, an increase of the permittivity of the superstrate material is not advantageous as it results in higher tissue power losses and therefore in a reduced radiation efficiency. Hence, a thick layer of low-loss superstrate material with low permittivity is preferred.

For the application at hand, PEEK (polyetheretherketone) is used

Parameter	Muscle	Skin	Fat
Relative Permittivity [†]	57.1	46.7	11.6
El. Conductivity (S/m) [†]	0.797	0.69	0.08
Density (kg/m ³)	1090	1109	911

[†]evaluated at $f = 403.5$ MHz.

Tab. 7.1: Dielectric properties of selected human tissues at an operating frequency of 403.5 MHz [66].

as insulation material, which has a relative permittivity of $\epsilon_r = 3.2$ and a dissipation factor of $\tan(\delta) = 0.003$ [161]. As pointed out in [25], PEEK is not the optimal solution to maximize the performance of the antenna, but it offers good mechanical properties and it is a biocompatible material, which is widely accepted for the use in medical implants [162].

7.3.4 Influence of the Human Tissue

In this study a simple homogeneous muscle tissue model was used for the simulations and the design of the antenna. But as will be shown in the following, the dielectric properties of the human tissue surrounding the implant have a significant influence on the electrical characteristics of the antenna.

Due to the high relative permittivity of the biological tissue (cf. **Tab. 7.1**), the resonance frequency is decreased significantly, which allows to further reduce the size of the antenna or to choose a substrate and superstrate material with lower permittivity and therefore, enhancing the fractional bandwidth of the antenna. The influence of the type of human tissue on the resonance frequency is shown in **Fig. 7.10(a)** and the dielectric properties of the considered tissues are summarized in **Tab. 7.1** for the design frequency of 403.5 MHz [66]. According to **Fig. 7.10(a)**, the composition of the tissue in close proximity to the antenna has a significant influence on the resonance frequency. E.g. a high fat content in the surrounding tissue shifts the antenna resonance frequency towards higher frequencies, which is due to the low permittivity of fat tissue.

Therefore, for the final antenna design, a more complex model of the human tissue needs to be considered and hence, also the implant location of the device must to be known prior to the final tuning of the antenna.

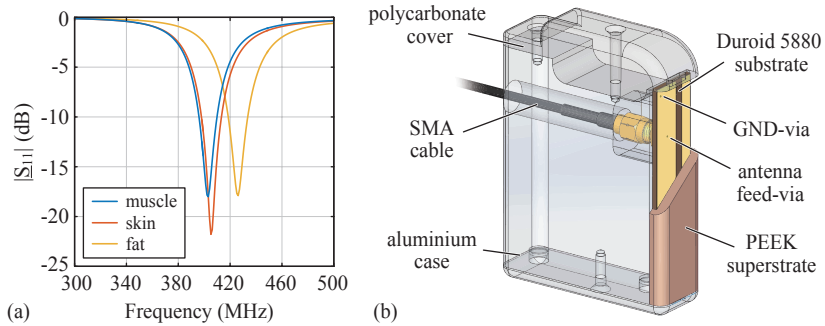


Fig. 7.10: (a) Influence of different human tissues on the resonance frequency of the final antenna design. (b) Schematic drawing of the hardware design of the final antenna assembly and the dummy implant used for the experimental verification.

7.3.5 Hardware Prototype

Fig. 7.10(b) shows a schematic drawing of the hardware prototype of the antenna assembly and the dummy implant. The PEEK superstrate covers the entire PIFA and has a thickness of 3.425 mm at the surface of the antenna patch. The ground plane of the antenna is electrically connected to the solid aluminium implant dummy enclosure, which provides a feed-through for the antenna supply cable that is connected to the antenna feed-point. The top cover of the dummy implant, which represents the connector block for the connection of the TET coil and the driveline of the LVAD, is manufactured from polycarbonate. The final fabricated hardware assembly, which was used for experimental verification, is shown in **Fig. 7.6(b)**.

7.4 Experimental Verification

For the measurement of the resonance frequency, the input impedance matching and the radiation pattern of the antenna, the implant dummy was immersed in a muscle tissue mimicking liquid with a total volume of 5.6 l and the same dimensions as for the simulation model, as illustrated in **Fig. 7.13**. The antenna substrate is positioned at the location $\Delta x = 77.5$ mm, $\Delta y = 21.5$ mm and $\Delta z = 52$ mm within the tissue model (cf. **Fig. 7.13**).

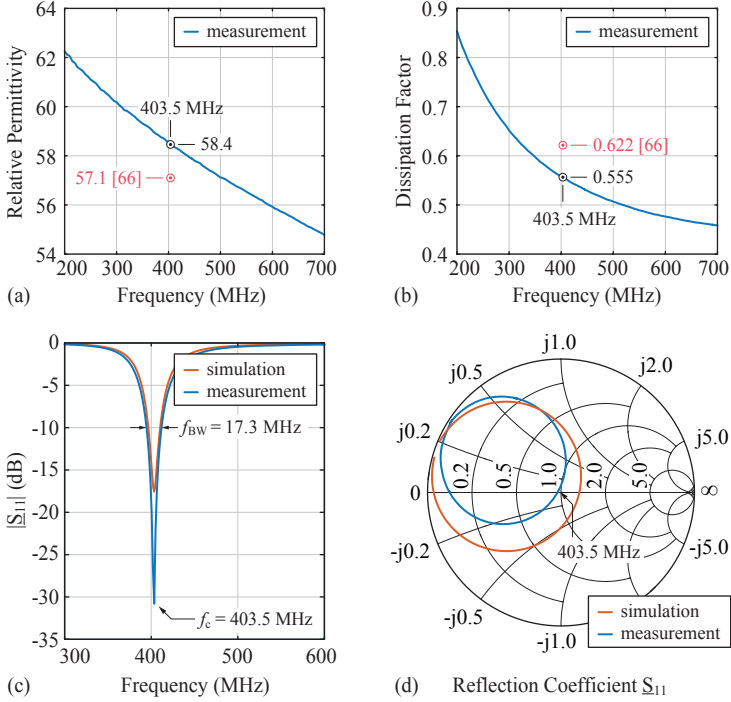


Fig. 7.11: Measurement of the relative permittivity (a) and the dissipation factor (b) of the muscle-mimicking liquid. (c)-(d) comparison of the measured and the simulated reflection coefficient S_{11} .

For the manufacturing of the muscle tissue mimicking liquid, the recipe provided in [25] was used, which contains 51.3% (weight percentage) de-ionised water, 47.3% sugar and 1.4% pure NaCl (sodium chloride). At a temperature of 22 °C, the liquid solution exhibits dielectric properties equivalent to living muscle tissue at a frequency of 403.5 MHz and at a temperature of 37 °C. The relative permittivity and the dissipation factor are measured with a Vector Network Analyzer (VNA), using a HP (Keysight) 85070B dielectric probe kit [163]. The results are shown in **Figs. 7.11(a)-(b)**. The relative error of the measured relative permittivity with respect to the value provided by [66] is 2.3% and -10.8% for the dissipation factor.

The measured and simulated reflection coefficient at the feed-point

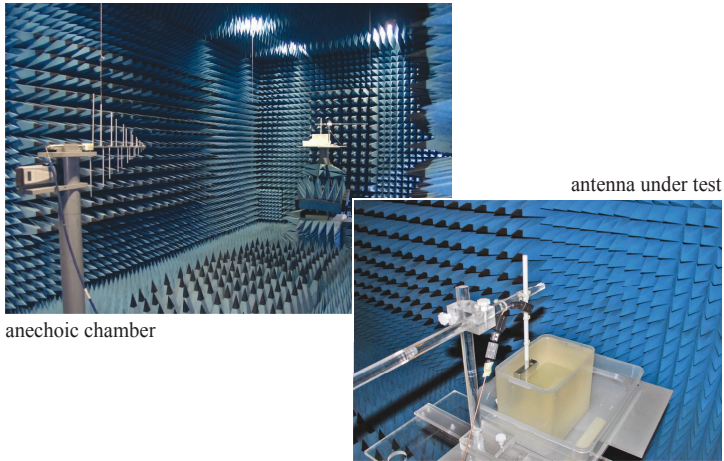


Fig. 7.12: Antenna gain measurement in the anechoic chamber and the dummy implant hardware immersed in the human-mimicking liquid.

of the antenna are shown in **Figs. 7.11(c)** and **(d)**. The resonance frequency of the realized antenna is exactly at 403.5 MHz and a return loss of more than 25 dB was achieved at the center frequency. The impedance matching bandwidth at a return loss of 10 dB is 17.3 MHz, which is much larger than the bandwidth needed for this application.

The gain of the antenna was measured in an anechoic chamber with the setup shown in **Fig. 7.12**. The dummy implant is placed in the muscle tissue-mimicking liquid with the orientation and placement shown in **Fig. 7.13**.

First, the free-space damping was experimentally determined using two identical wideband logarithmic-periodic antennas, which have a known gain of $G_{\text{ref}} = 5$ dBi. At a separation distance of 3.85 m between the two antennas, a damping of 25.17 dB was measured at 403.5 MHz, which is close to the theoretical damping of 26.26 dB. In a next step, one of the reference antennas is replaced by the implant test setup and the gain of the prototype antenna within the tissue-mimicking liquid is calculated according to

$$G_{\text{DUT},(\text{dBi})} = 10 \cdot \log_{10} \left(\frac{P_{\text{Rx}}}{P_{\text{Tx}}} \right) + 20 \cdot \log_{10} \left(\frac{4\pi x}{\lambda} \right) - G_{\text{ref},(\text{dBi})}, \quad (7.1)$$

where λ is the free-space wavelength at the operating frequency and

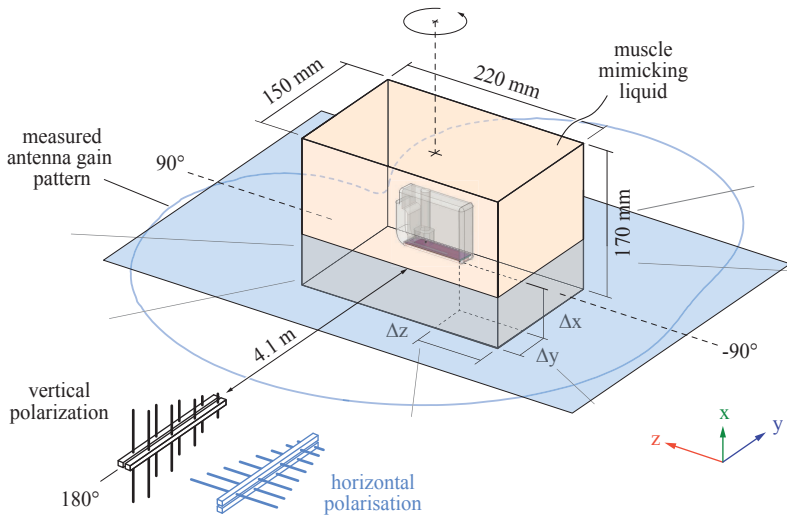


Fig. 7.13: Measurement setup and orientation of the dummy implant during the gain measurement in the anechoic chamber.

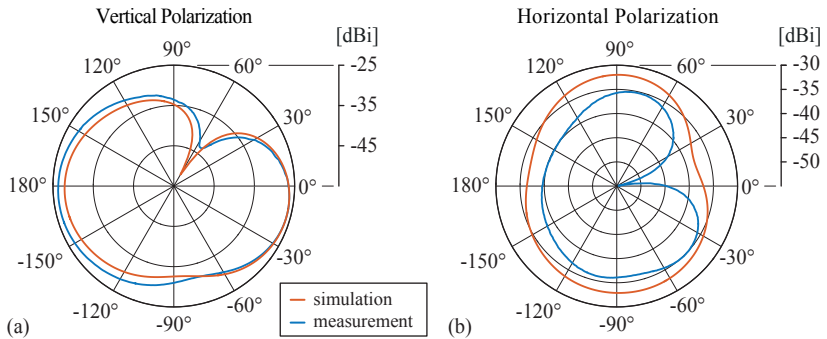


Fig. 7.14: (a)-(b) Measurement of the antenna gain in the y - z -plane for vertical polarization (i.e. polarization in x -direction) and horizontal polarization (i.e. polarization in z -direction) of the antenna.

Parameter	Simulation	Measurement
Resonance Frequency	403.3 MHz	403.5 MHz
Max. Return Loss	17.5 dB	30.8 dB
Matching Bandwidth	13.0 MHz	17.3 MHz
Antenna Gain [†]	-27.9 dBi	-26.3 dBi
Radiation Efficiency	0.135 %	—

[†]antenna gain in the direction towards 180°, out of the muscle-mimicking liquid, as defined in Fig. 7.13.

Tab. 7.2: Summary of the simulated and measured antenna parameter.

P_{Rx} and P_{Tx} are the measurements of the received and the transmitted power, respectively. In this case, the reference antenna is located on the same level as the prototype antenna at a free-space distance of $x = 4.1$ m, as indicated in Fig. 7.13. The gain of the implantable antenna was measured in the direction of vertical polarisation, i.e. with the reference antenna polarization oriented in the x -direction, and in the direction of horizontal polarisation, i.e. with the reference antenna polarization oriented in z -direction.

The results of the gain measurements are shown in Figs. 7.14(a) and (b). The measured radiation pattern in the direction of vertical polarization is in good agreement with the simulated values. In this case, the measured antenna gain in the direction towards 180°, i.e. outwards of the muscle-mimicking liquid, attains a value of -26.3 dBi, despite the large 'implantation depth' of 20 mm. The gain in the direction of horizontal polarisation is much lower compared to the vertical polarization, which was expected, considering the planar structure of the PIFA.

The simulated and measured performance characteristics of the realized PIFA, operated in the muscle-mimicking liquid, are summarized in Tab. 7.2. The simulated peak gain attains a value of -25.35 dBi and the peak directivity is 3.33 dBi. Accordingly, the simulated radiation efficiency of the antenna attains a value of 0.135 %, and is limited mainly by the high power loss in the tissue material surrounding the implant.

7.5 Exposure Assessment

A summary of the applicable regulations used for the assessment of the exposure of the human body to time-varying electromagnetic fields is given in Section 4.2. In the megahertz range the exposure is generally assessed in terms of specific absorption rate. The SAR limits for the

general public exposure are defined in [116] and [117] as 2 W/kg for 10 g averaging volume and as 1.6 W/kg for the 1 g average in [115]. The highest power loss in the tissue is observed at the edges of the antenna assembly and therefore, the 1.6 W/kg (1 g average) SAR limit is considered as the most appropriate exposure limit for the application at hand.

With the simple muscle tissue model used in this study a power of 17.1 dBm (51 mW) could be supplied at the antenna input terminal in order to comply with the 1.6 W/kg SAR limit. However, in order to comply with the maximum allowed equivalent isotropically radiated power of -16 dBm specified in [149], and considering the simulated peak gain of -25.35 dBi, a maximum power of only 9.35 dBm (8.6 mW) could be supplied at the antenna input, which in turn results in a maximum spatial-average SAR of 0.27 W/kg. This value is a factor of six below the most stringent SAR limit is therefore considered safe for the human body. However, as pointed out in [25], for a final exposure assessment, a detailed heterogeneous human body model must be considered.

7.6 Summary of the Chapter

In this chapter, the practical realization of a wireless communication link between the implant and the external part of the TET system is described, which is operated in the MICS band and which is intended to be used for the control of the IPT system and the monitoring of the implant. Whereas for the RF transceiver and the extracorporeal antenna exist readily available solutions, the design of the implantable antenna poses particular challenges. Consequently, the design approach and the critical design considerations for the realization of the implantable antenna are covered in more detail.

The main results of this chapter are summarized as follows:

- The MICS band transceiver module is realized using off-the-shelf components and achieves a good performance with very little hardware effort and a small volume occupation. Measurements with the implantable antenna immersed in the tissue-mimicking liquid have shown that a reliable communication with the external transceiver module can be established, even at a separation distance of 5 m. In this case, the data rate was set to 1 Mbps, and

a total number of 10'000 data packets are transmitted, achieving a packet error ratio of less than 1 %.

- ▶ The implantable antenna must be designed and optimized for the specific application, considering the actual material and dimensioning of the implant enclosure. In addition, the antenna volume should be maximized within the limits given by the implant design, in order to enhance the gain and the radiation efficiency of the antenna.
- ▶ An important design parameter for the implant antenna is the material and the thickness of the superstrate. A thick superstrate with low permittivity is preferred in order to confine the high electric near field of the antenna in the insulation layer, which allows to decrease the power losses in the tissue. Given the volume of the PIFA assembly, the substrate thickness should be reduced and a low permittivity substrate material should be used in order to enhance the bandwidth of the antenna.
- ▶ The final implant antenna prototype is designed for an operation at 403.5 MHz and achieves a gain of -26.3 dBi, even when immersed in the lossy muscle tissue-mimicking liquid in a depth of 20 mm from the surface.
- ▶ With the simple tissue model at hand, the numerical simulation show that the implant antenna design complies with the regulations on SAR.

The following chapter shows the realization of the hardware prototype of the TET implant and the performance measurement of the total TET system at variable operating conditions.

8

Hardware Prototype

IN the previous chapters, the design considerations and the implementation of each electrical building block of the TET system was discussed in detail and the functionality of each component was experimentally verified on its own. In a next step, the electrical sub-assemblies are combined and the overall system performance is shown for both the SSU and the SSR IPT system operation.

A particular challenge is the design and the implementation of the TET system implant, because of the small available volume and the required high energy efficiency of the system, in order to prevent excessive heating of the surrounding tissue. Hence, as presented in [3], it was decided to build a demonstrator prototype for the SSU TET system implant, because of the high secondary-side power conversion efficiency and the reduced system complexity. The implant for the SSR TET system can be built very similar, with minor modifications of the hardware, but due to its increased hardware complexity, it is expected, that the volume of the implant is increased.

In the following, the design and the hardware realization of the TET system implant is shown and subsequently, the overall TET system performance is experimentally verified for both operating modes and a summary of the achievements is given at the end of the chapter. Note that this chapter is based to a large part on the results published in [3].

8.1 TET Implant Design

The volume occupation is a particularly critical parameter for implantable medical devices and it is a main requirement to reduce the implant

size as much as possible, in order to facilitate the implantation of the device and to increase the wearing comfort for the patient. The few reported volumes of implant controllers of fully implantable MCS systems are typically above 200 cm^3 , i.e. the LionHeart implant controller has a size of 277 cm^3 [27] and the Reinheart implant controller has a fairly large size, occupying 360 cm^3 [18], but it is still in a prototype stage. The TET system implant controller developed by Minnetronix has a volume of 245 cm^3 and contains all electronic components related to the TET system, i.e. communication and control electronics, backup battery and the LVAD driver [38]. Compared to the volume of modern ICDs of less than 60 cm^3 , the TET system implants are rather large, which is mainly due to the large backup battery. In discussion with medical experts, it was concluded that a maximum volume of 100 cm^3 (10 cl) should be targeted for the TET implant. This volume should include all the electronic building blocks, such as the IPT energy receiver, the communication electronics and the backup battery as well as the control electronics. In this case, the inverter circuit, which is used to drive the LVAD, is not included in the TET implant prototype. It is the opinion of the author that the inverter and its controller should be integrated preferably into the LVAD itself. In this case, the connection with the LVAD incorporates only the DC power supply and few control signals. More important, the total implant power losses, i.e. from the TET implant and the LVAD inverter, are spread over a larger volume, which facilitates the cooling of the system. Specifically the inverter could be cooled more efficiently in the LVAD, due to the continuous blood flow.

Fig. 8.1 shows the concept of the system integration. It was decided to use a modular design approach which allows for higher flexibility and a compact design. The functionality of the electronics is divided into four sub-modules, which contain the system controller, the battery charger, the IPT front-end (i.e. the synchronous rectifier) and the electronics for the wireless communication. In order to allow for a compact design, the four PCBs are stacked on top of each other, which yields a total volume of the electronics assembly of approximately 22 cm^3 and hence, occupies about 22% of the total implant volume.

The MICS-band antenna is integrated into the implant enclosure as shown in **Chapter 7**, and makes up about 7% of the total implant volume.

The implant enclosure is manufactured from aluminium and 3D-

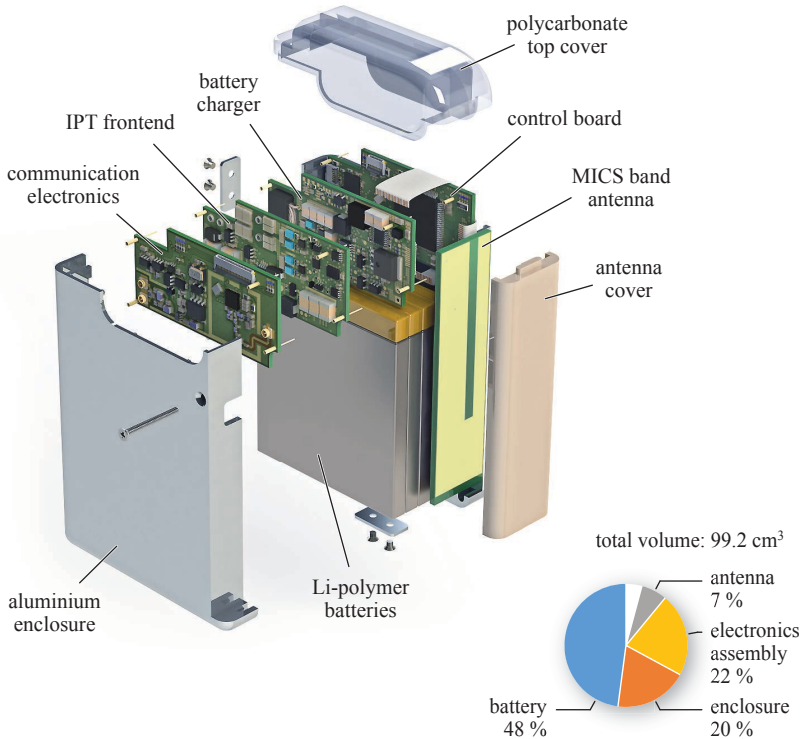


Fig. 8.1: Explosion view of the CAD drawing of the TET implant prototype and the distribution of the volume.

printed polycarbonate and occupies almost the same volume as the electronics assembly. However, almost 50% of the total implant volume is occupied by the backup battery.

8.1.1 Rechargeable Battery

The backup battery is included in the TET implant to allow for a completely untethered operation of the LVAD, or if excessive coil misalignment prevents the transmission of the required power, the battery allows to bridge the supply gap. In this case, the requirements for the implanted backup battery are considerably high. The major requirements for the implantable battery are a high operational safety, high

reliability and a high energy density. Furthermore, the battery should offer high charge and discharge capabilities, low power loss, low self-discharge and a high number of charge/discharge cycles, as well as a high retention of the original capacity. Today, lithium-based batteries offer most of these characteristics and are widely used as primary power sources for implantable biomedical devices, such as cardiac pacemakers, implantable defibrillators, drug delivery systems, neurostimulators, and are also used as secondary power source for fully implantable LVAD and TAH system prototypes [15, 164, 165].

The runtime of the LVAD and the TET implant is limited mainly by the available battery volume. In case of the LionHeart system, the implanted battery allowed for an operation of the LVAD for about 20 minutes without the external power supply [28].

Today's medical-grade lithium-based rechargeable batteries have volumetric energy densities of up to 255 Wh/l, i.e. such as the lithium-ion battery Xcellion R220, which is manufactured by Greatbatch Medical [20]. In this case and assuming a battery volume of 5 cl, a total capacity of 12.75 Wh would be available for the LVAD operation. Hence, with an average LVAD power consumption of 7 W, a battery runtime of up to 55 minutes could be achieved at a Depth-of-Discharge (DoD) of 50 %.

A higher volumetric energy density of the battery is therefore preferred in order to prolong the battery runtime with the same battery volume, but this comes at the expense of an increased safety risk due to the large amount of stored energy. Furthermore, for long-term use, such as for destination therapy, the life-time of the batteries must be increased. As a conclusion, the *ideal* battery for the application at hand is not yet available. The conventional lithium-ion batteries using cobalt-based materials for the positive electrode, such as lithium-cobalt-oxide LiCoO_2 are easy to produce and offer very high energy densities of more than 500 Wh/l, but the batteries are sensitive to overcharging and mechanical damage, which likely causes a thermal runaway and hence could have fatal consequences, when implanted in the patient. In contrast, one of the most promising, more recently developed lithium-ion technologies uses lithium-iron-phosphate (LiFePO_4) for the positive electrode material, which has many advantages compared to previous developments, specifically with respect to operational safety and cost. The LiFePO_4 powder is non-toxic, chemically stable and does not show any thermal runaway. Furthermore LiFePO_4 batteries have a large

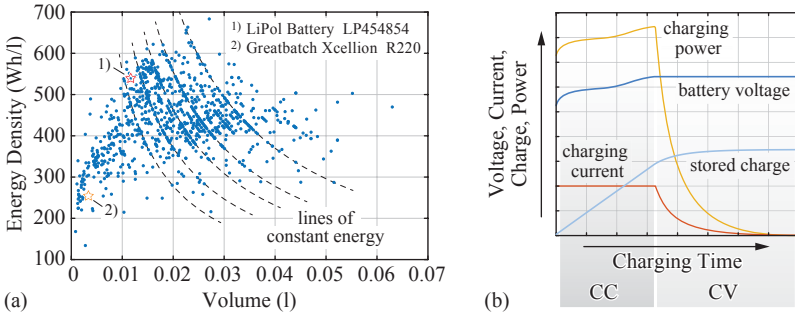


Fig. 8.2: (a) Energy densities and volumes of the rechargeable lithium-polymer batteries manufactured by LiPol Battery Co. [167]. (b) Typical Constant Current (CC), Constant Voltage (CV) charging profile of rechargeable lithium-ion batteries.

overcharge tolerance, offer high charging current, very long cycle life of more than 4000 charge/discharge cycles and a lifespan of more than five years. However, the increased safety comes at the expense of a considerably lower volumetric energy density of up to 330 Wh/l. [26, 166]

For the TET implant prototype it was decided to use commercially available general purpose lithium-polymer batteries, which has the advantage, that a solid electrolyte is used and hence does not require a sealed protective case. Therefore, high volumetric energy densities are achievable and the battery cells can be manufactured in a wide range of different shapes, which increases the design flexibility and reduces the prototyping cost. For the implant prototype illustrated in **Fig. 8.1**, the lithium-polymer battery LP454854 is used, which has a nominal cell voltage of 3.7 V, offers a capacity of 1.7 Ah and has an expected lifetime of more than 500 charge/discharge cycles [167]. However, it is important to note that this battery does not meet the demanding safety requirements. Consequently, the TET implant prototype is not suitable for *in-vivo* experiments, unless the batteries are replaced by certified implantable batteries.

Fig. 8.2(a) shows the energy density of a large number of lithium-polymer batteries available from the manufacturer LiPol Battery Co. [167]. As indicated, the battery that is used for the prototype offers a high energy density of 539 Wh/l. In order to achieve the nominal battery pack voltage of 14.8 V, four cells are connected in series. The

battery pack has a total boxed volume of about 4.8 cl, weighs 136 g, stores a nominal energy of 25.2 Wh and the nominal continuous power that can be delivered by the battery pack is 25 W. Hence, the LVAD could be operated independent from an extracorporeal power source for about 1.8 h, assuming an average power consumption of 7 W and a DoD of 50 %. In order to prevent battery damage, each battery includes an overcharge and -discharge protection circuit. The battery is charged using the typical Constant Current (CC), Constant Voltage (CV) charging profile, which is illustrated in **Fig. 8.2(b)**. With a charging current of 0.5 C, i.e. at maximum charging power of 14.3 W, the battery pack could be fully charged within two hours.

8.1.2 Hardware Realization

The hardware realization of the PCBs is shown in **Fig. 8.3**. The main component of the IPT energy receiver PCB shown in **Fig. 8.3(a)** is the synchronous rectifier circuit (cf. **Fig. 2.27**) and the secondary-side compensation capacitors. In this case, the synchronous rectifier is updated with the improved EPC2016C GaN FETs [139], which are also used for the battery charging converter. In addition, current and voltage measurement circuits are included and a load switch allows to disconnect the IPT system from the load, whenever the LVAD is powered by the backup battery.

Fig. 8.3(b) shows the bidirectional buck-type battery charging converter. In order to protect the battery from the large current ripple in the inductor, an additional LC-filter stage is connected in series with the battery. Furthermore, in order to prevent any damage of the battery in case of a malfunction of the charger, it can be disconnected from the circuit using an additional load switch. The PCB contains also the 3.3 V and 5 V auxiliary power supplies and the voltage and current measurement circuits, which are used to control the battery charger. More details on the design and the performance of the battery charger are provided in **Section 8.2.1**.

The heart of the TET implant prototype is a 32-bit ARM Cortex-M4 CPU, i.e. the microcontroller STM32F407VG, which is placed on the control board shown in **Fig. 8.3(c)**. The microcontroller implements all the functionality needed to control the synchronous rectifier and the battery charging converter and provides the interface for the wireless communication. In addition, the temperature of the backup battery and

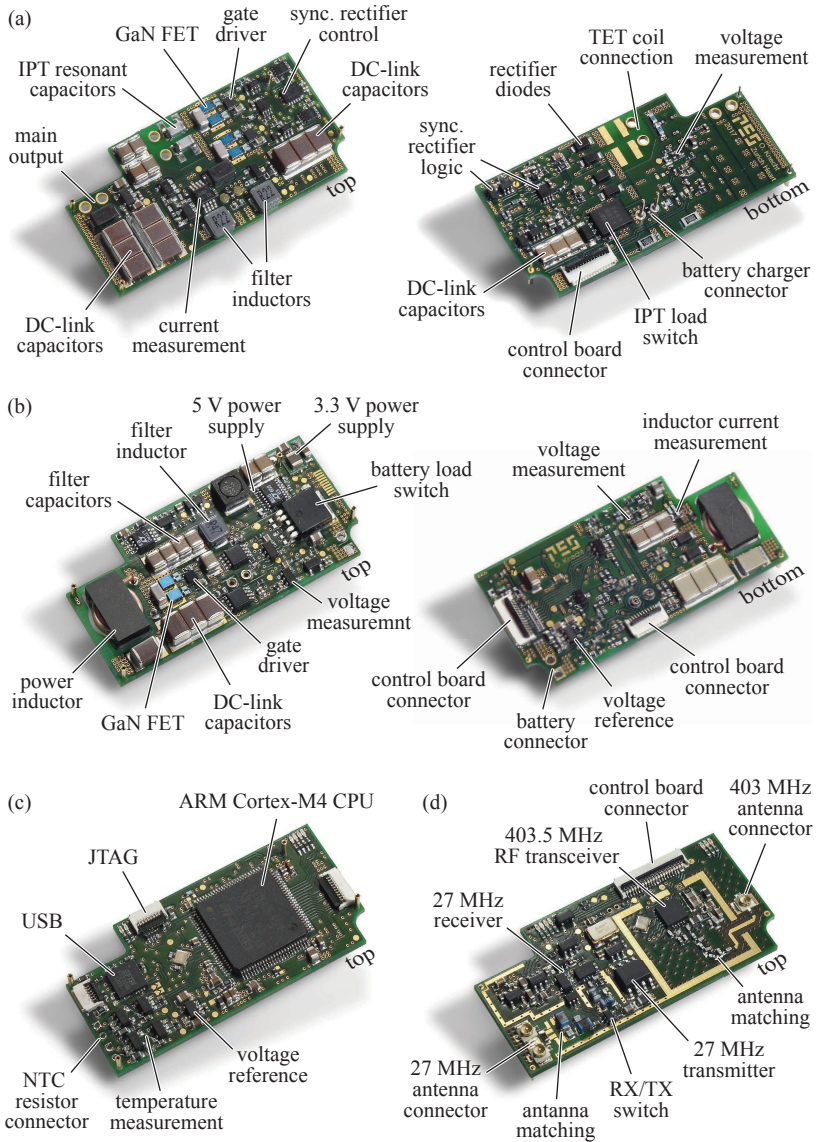


Fig. 8.3: (a) IPT energy receiver PCB. (b) Battery charger PCB. (c) Control board and (d) communication electronics PCB.

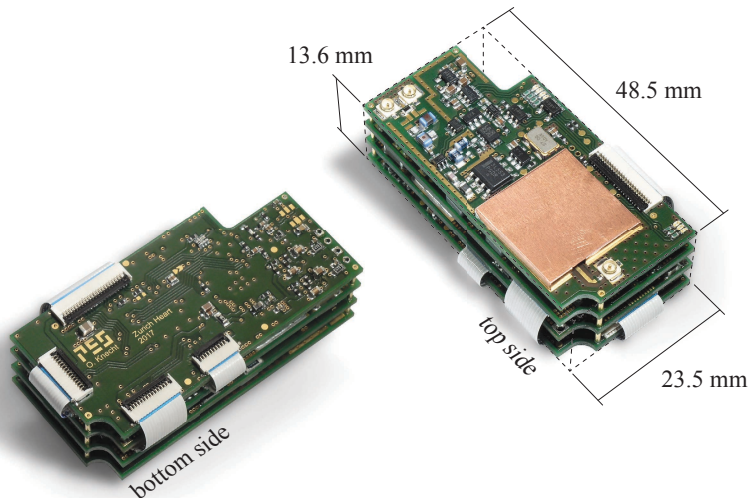


Fig. 8.4: PCB assembly of the TET implant prototype.

the temperature of the battery charger inductor can be monitored using NTC sensors. The CPU clock frequency of the microcontroller is set to 100 MHz and the typical power consumption is about 160 mW [168]. The power consumption could be further reduced down to 60 mW by using a specialized low power microcontroller, such as the STM32L471, running at 80 MHz core clock frequency [169].

The circuits for the wireless communication are placed on a separate PCB which is shown in **Fig. 8.3(d)**. The components are placed mainly on the top side of the PCB and a large ground plane on the bottom side prevents any interference with the noisy power electronic stage of the IPT front-end. The main RF transceiver, which is used for the top-level communication and which is operated in the MICS-band at 403.5 MHz, is implemented as explained in **Section 7.2**. In addition, a second bidirectional Near Field Communication (NFC) channel is implemented. The loop-antennas are embedded directly into the final TET coil prototypes. The NFC link operates in the ISM-band at 27 MHz and uses a simple On-Off-Keying (OOK) modulation scheme for the data transmission. Data rates of up to 500 kbps are achieved and a stable communication can be maintained for a coil separation distance of at least a TET coil diameter, which is by far more than the

feasible power transmission range. However, the simple OOK modulation scheme is prone to interferences with the switching noise of the IPT system and a careful NFC antenna design is required to electrically separate the NFC antennas from the TET coils as much as possible. The idea is to dedicate the NFC channel exclusively to the control of the IPT system, such that the MICS-band communication can be used for uncritical high-level tasks, such as the control of the LVAD and the monitoring of physiological sensor data.

The assembled electronic building block is shown in **Fig. 8.4**. Each PCB is connected to the control board using Flat Flexible Cables (FFC) which allow for a very compact design. The NFC loop antenna and the MICS-band antenna are connected on the front side of the communication electronics PCB using coaxial RF connectors and the MICS-band transceiver is additionally shielded to suppress EMI.

The two finally realized TET coil prototypes have the same specifications and the secondary-side TET coil is shown in **Figs. 8.5(a)** and **(d)**. The winding layer of both TET coils has an outside diameter of approximately 69 mm and an inside diameter of 35 mm. The single-layered coils consist of 17 turns of litz-wire with 330 strands and a strand diameter of 40 μm . As for the TET coil prototypes used in the *in-vivo* thermal experiment, described in **Section 3.3**, the coil windings are encapsulated in RTV-3428 A&B silicone [100]. Including the silicone encapsulation, the TET coils have an overall outside diameter of 73 mm, a thickness of 3 mm and a weight of 26 g.

The measured inductance and AC resistance of the secondary-side coil, with respect to the operating frequency, are shown in **Figs. 8.5(b)** and **(c)** respectively. The lead wire length is 200 mm and its AC resistance was measured using a twisted pair litz-wire cable of the same length. At the operating frequency of 800 kHz, the measured self-inductance and AC resistance of the primary-side TET coil are 19.16 μH and 240 m Ω , respectively. In this case, the lead wires have a length of about 275 mm. Even though a litz-wire with a larger number of strands was used, the measured AC resistance is larger compared to the first TET coil prototype presented in **Section 2.4.1**. A possible reason for the overall larger AC resistance might be a non-ideal twisting of the litz-wire, which in this case leads to larger proximity effect losses [61]. The difference of the AC resistance between the two final TET coil prototypes is possibly due to a poor electrical connection of a number of strands at the secondary-side coil terminals. The quality factors of the

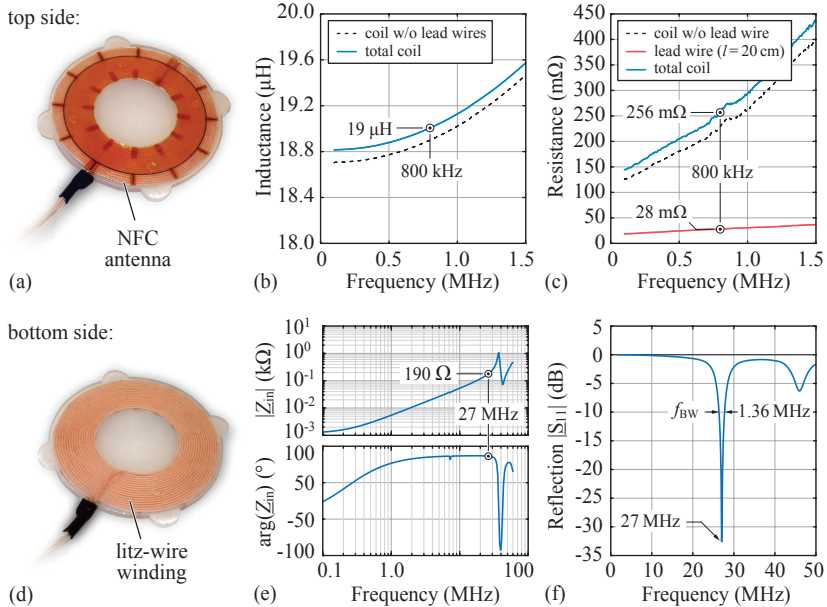


Fig. 8.5: (a) Top side of the final implant TET coil prototype. (b) Measured inductance and (c) AC resistance of the TET coil. (d) Bottom side view of the TET coil prototype. (e) Measured impedance of the embedded NFC antenna. (f) Measured reflection coefficient of the NFC antenna at the input of the balun circuit and impedance matching.

two coils are in a range of 373 to 401 at the operating frequency and the self-resonance frequency in air is about 6.85 MHz for both coils.

As indicated in **Fig. 8.5(a)**, the NFC loop antenna is mounted on top of the litz-wire winding and consists of one single turn at the outer edge of the IPT coil and two turns at the inner edge of the IPT coil winding, which are wound in the direction opposite to the outer loop. The coil arrangement and winding scheme is optimized such that the magnetic coupling between the energy transfer coil and the NFC antenna is minimized, as described in [23]. The measured magnetic coupling between the TET coil and the NFC coil is very low and attains a value of only 2.7% at 800 kHz. However, it is important to note that a measurement of such a low coupling coefficient is difficult and the measured value is subject to variations.

Fig. 8.5(e) shows the measurement of the input impedance of the NFC antenna. The self-inductance is 845 nH over a wide frequency range, but the loop is operated close to the self-resonance frequency of 37.14 MHz, which is not desirable. Hence, in order to shift the self-resonance frequency to higher frequencies, the overall diameter of the NFC coil could be decreased, in order to decrease the inductance of the coil. Nevertheless, as shown in **Fig. 8.5(f)**, a very good impedance matching is achieved at the center frequency of 27 MHz and the matching bandwidth (i.e. at a return loss of 10 dB) is 1.36 MHz.

Finally, the TET coil, the NFC antenna and the backup battery are attached to the electronics assembly, which is then inserted into the 3D-printed top cover. The inside of the realized TET implant prototype assembly is shown in **Fig. 8.6(a)**, whereas **Fig. 8.6(b)** shows the final prototype and its dimensions. The TET implant prototype has a boxed volume of 10.3 cl and a weight of 188 g, which is mainly due to the large battery pack. It should be noted, that the implant prototype can be used for short-term in-vivo experiments when the backup battery is removed, but in its current state, the prototype is not hermetically sealed and is therefore not suited for long-term experiments.

8.2 Performance Measurement

The following sections provide a comprehensive experimental performance evaluation of the TET system prototype. First, the performance of the battery charger is evaluated by means of power conversion efficiency measurements at different operating points. Second, the total TET system performance is determined on a system level, i.e. with power loss measurements including all power conversion stages from the external battery supply to the output of the implant. Third, in order to compare the SSU TET system performance, the power loss and the DC-DC efficiency is measured for the SSR TET system as well for different operating points and TET coil separation distances.

8.2.1 Battery Charging Converter

The battery charger is optimized as described in **Section 6.4.1** and is operated at a switching frequency of 300 kHz. The inductor is built using an ER 11/5 ferrite core set and 13 turns of litz-wire consisting of 135 strands with a strand diameter of 40 μm . For the core, the

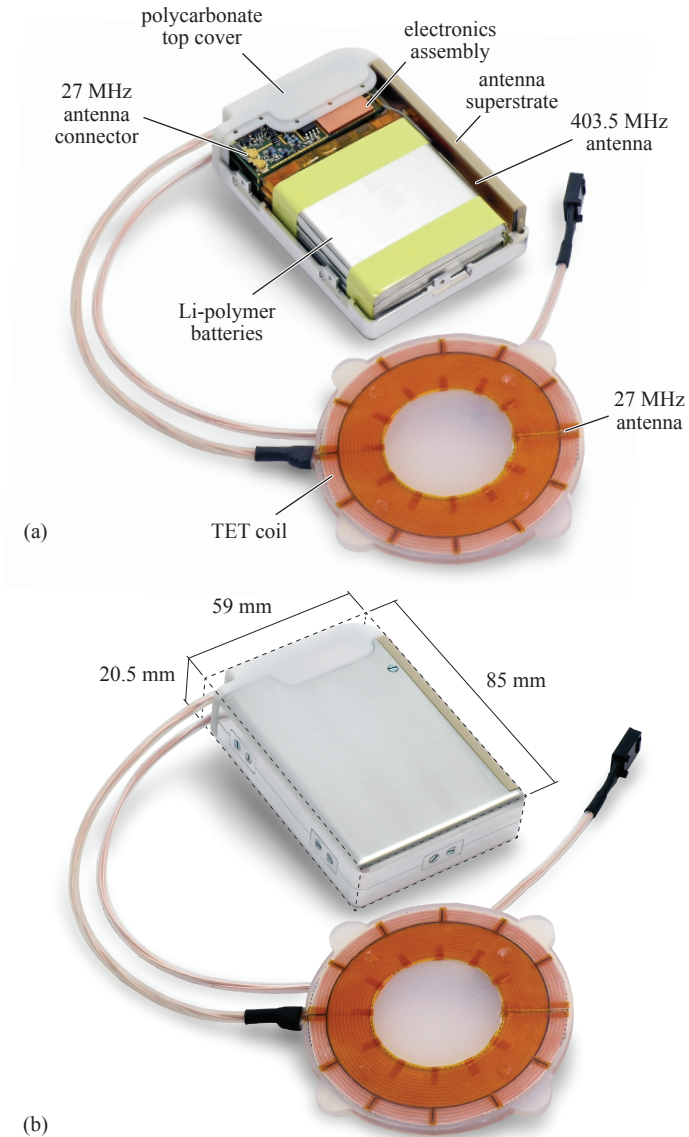


Fig. 8.6: Final TET implant hardware prototype.

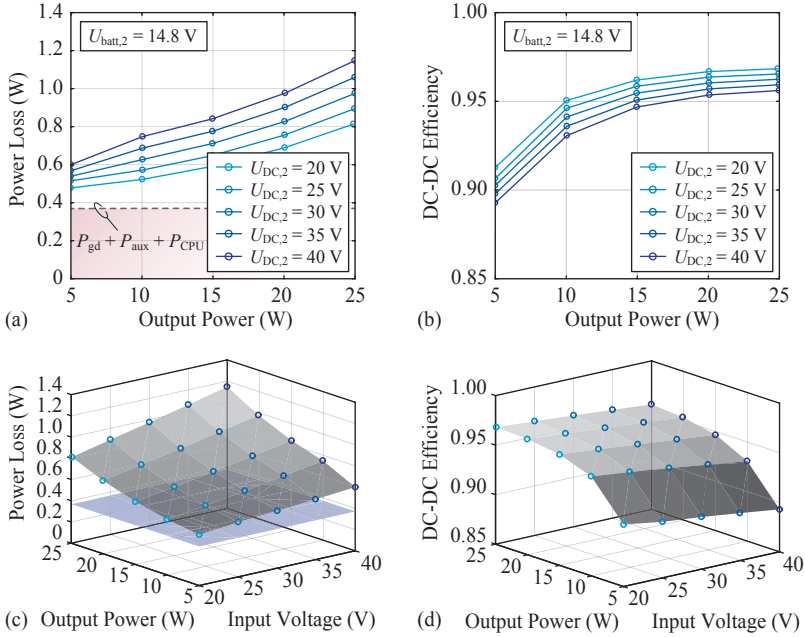


Fig. 8.7: (a) Measured power loss and (b) efficiency of the buck-type battery charger DC-DC converter prototype.

TDK/EPCOS N87 ferrite material was selected. The measured inductance value is $27.9 \mu\text{H}$ and is designed such that the peak-to-peak inductor current ripple is about 70% of the maximum average inductor current at a battery voltage of 14.8 V , a DC-link voltage of $U_{\text{DC},2} = 40 \text{ V}$ and a maximum output power of 25 W . In order to protect the battery from the large peak-to-peak current ripple at maximum DC-link voltage, a filter capacitance of $30 \mu\text{F}$ is placed at the output of the buck converter. In addition, a filter inductance of 470 nH is placed in series with the battery, in order to further reduce the current ripple.

The dead-time of the switch control signals is set to 40 ns and is selected such that in buck-mode, soft-switching of the low-side switch is achieved at a minimum output power of 5 W and the maximum DC-link voltage of 40 V . The power loss and DC-DC efficiency measurement of the converter in buck-mode are shown in **Figs. 8.7(a)-(d)** for an output power range of $5\text{-}25 \text{ W}$ and an input voltage range of $20\text{-}40 \text{ V}$. The

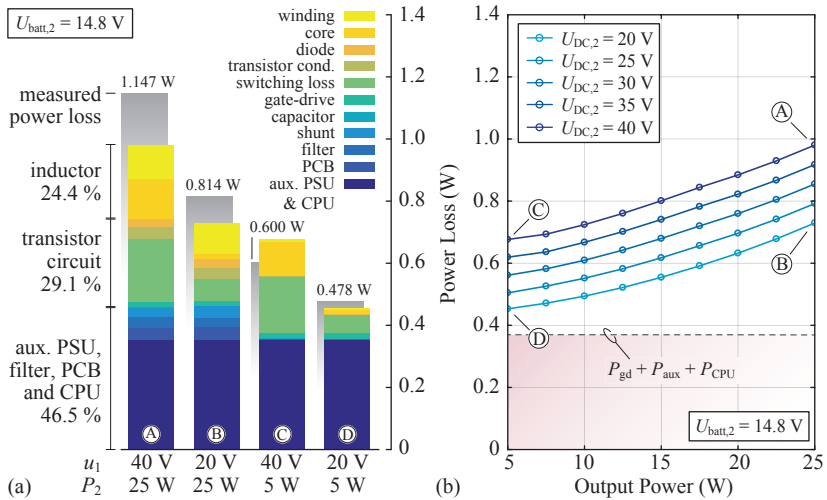


Fig. 8.8: (a) Calculated power loss distribution and (b) power loss of the prototype battery charger DC-DC converter.

output voltage is set to a constant value of 14.8 V and the measurements include all control and auxiliary circuit power losses.

As indicated in **Fig. 8.7(a)**, a large part of the total power loss is caused by the constant power loss of almost 370 mW, which is due to the control circuit, i.e. the microcontroller, the auxiliary power supplies, the measurement circuits and the gate driver. However, it should be noted, that the CPU executes many tasks that are not related to the battery charging converter, such that only a part of the constant power loss can be associated with the buck converter operation.

The DC-DC efficiency is larger than 90% over a wide range of operating conditions and as expected, the maximum efficiency is achieved at maximum output power and minimum input voltage, and attains a value of 96.8%.

Fig. 8.8(a) shows the distribution of the calculated converter power losses at the operating points indicated in **Fig. 8.8(b)**. The power losses are calculated using the numerical simulation explained in **Section 6.4.1**. The PCB power losses are estimated based on the calculated currents and the measured DC-resistances of the tracks on the final prototype PCB. For the control and the auxiliary power supply

losses, the measured value is taken.

At maximum output voltage and maximum output power, the calculated switching power losses are almost equal to the total inductor power loss. However, as explained in **Section 6.5**, it is expected that the switching energy loss increases at a higher rate with respect to the switching current, compared to the predictions from the switching loss simulations. At low output power, the numerical model fits the measured power loss values very well. At minimum output power and high input voltages, the inductor current is negative at the turn-on of the high-side switch and as a result, the power loss is decreased due to partial soft-switching. This is the reason why the measured power loss at the operating point denoted with (C) (cf. **Fig. 8.8(a)**) is lower than the calculated power losses, since this effect is not modeled in the numerical calculation.

At maximum output power and at maximum DC-link voltage, the inductor core temperature reaches $60.4\text{ }^{\circ}\text{C}$ in air at $25\text{ }^{\circ}\text{C}$ ambient temperature. The hard-switching, high-side GaN FET attains a temperature of $58.5\text{ }^{\circ}\text{C}$ and does not require any additional cooling. An increased temperature of the inductor core is advantageous, since the core losses decrease with increasing temperature and are reaching a minimum at approximately $100\text{ }^{\circ}\text{C}$. During battery charging operation, the power loss of the implanted battery charger contributes significantly to the heating of the implant as a whole. As an approach to reduce the charging power loss, the inductor volume should be maximized within the available implant volume. Consequently, considering the larger feasible inductance value, the battery charging converter could be operated at a reduced switching frequency, which in turn reduces the power losses associated with the semiconductors.

In the following section, the performance of the SSU TET system prototype is measured on a system level, including all the power losses that are generated in the conversion stages in between the external battery supply and the TET implant output and the internal backup battery.

8.2.2 SSU TET System

For the proposed SSU TET system, two separate operating modes are considered, since the battery charger is connected in parallel to the output of the TET implant. In the first mode, denoted with *mode*

A, the power is delivered directly to the LVAD, without the operation of the backup battery charger. The second operating mode, denoted with *mode B*, considers a constant power supply for the LVAD and the simultaneous operation of the battery charger with variable output power.

The external part of the TET system is realized using the inverter circuit presented in **Section 2.4.1**. The inverter stage is supplied by a boost-type DC-DC converter, which is implemented with the same battery charger PCB as used for the TET implant prototype. However, in this case, the converter is operated in boost-mode only and the boost inductance is optimized for a high power conversion efficiency, since for the extracorporeal device, the power density is of minor importance.

The inductor is manufactured from two stacked EELP 14/3.5/5 core sets made of the N87 ferrite material and has a similar volume as the inductor shown in **Fig. 6.15**. The winding is realized with 12 turns of litz-wire with 9 strands and 200 μm strand diameter. The air-gap of the inductor is adjusted such that the inductance value attains 39.7 μH at the operating frequency of 150 kHz and the dead-time of the switch control signals is set to 40 ns.

It is important to note that for the performance measurement, the power loss was measured for each converter stage separately, in order to show the power loss distribution. In this case, it is important that the voltage and the input/output power is matched at the converter interface. More precisely, in this case, the power loss is measured first for the IPT converter stage for different operating points. Then in a second step, the power loss is measured for the external DC-DC converter, such that the output voltage and output power of the DC-DC converter matches the input voltage and the input power of the IPT converter stage for each considered operating point.

The TET system performance was measured for a IPT coil separation distance d_c of 13 mm and 23 mm, such that the distance between the TET coil encapsulations is exactly 10 mm and 20 mm. Accordingly, the measured coupling factors are 0.390 and 0.219, respectively. The primary-side and secondary-side compensation capacitances $C_{1,1}$, $C_{1,2}$ and $C_{2,1}$, $C_{2,2}$ have a value of 5.6 nF each and are designed for $k_0 = 0.262$. Hence, according to (2.87), the optimum secondary-side DC-link voltage $U_{\text{DC},2}$ at maximum output power is 36.2 V. The primary-side inverter is operated at a switching frequency of 800 kHz and the dead-time of the 50 % duty-cycle switch control signals is set

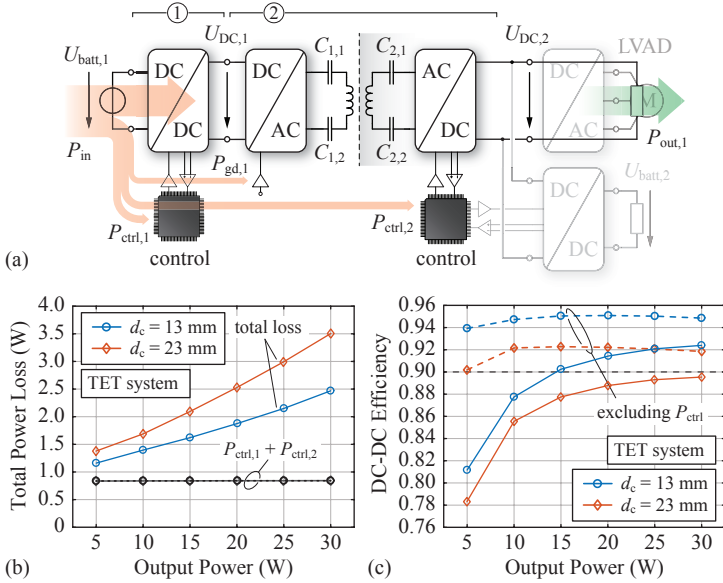


Fig. 8.9: (a) Schematic circuit diagram of the SSU TET system prototype operated in *mode A* and the illustrated components of the input and output power considered for the total system performance evaluation. (b) Measurement of the total SSU TET system prototype power loss and (c) total DC-DC efficiency.

to 65 ns. For the 3-phase motor inverter, which is supposed to drive the LVAD, it is assumed that an absolute maximum input voltage variation of a factor of two can be compensated, using PWM modulation. Consequently, the lower limit for the IPT system output voltage is set to $U_{DC,2} = 20$ V. If the secondary-side DC-link voltage drops below this limit, it is the idea that the IPT system is disconnected from the subsequent power electronic stages and that the backup battery provides the power supply for the LVAD. In this case, the battery charger is operated in boost-mode and controls the inverter DC-link voltage to a constant value of 20 V.

Fig. 8.9(a) illustrates the structure of the SSU TET system prototype for the *operating mode A*, where the power is transferred directly to the LVAD, without charging of the implant backup battery.

The power loss components that are additionally considered for the

total system input power P_{in} , but which are measured separately, are the losses caused by the primary-side and secondary-side control board, including auxiliary power supplies, measurement circuits, as well as the gate drivers for the boost converter and the IPT inverter stage, as indicated in **Fig. 8.9(a)**. Note that the power loss of 258 mW of the FPGA and its auxiliary power supplies, which generates the control signals for the full-bridge inverter, is not included in the performance evaluation of the TET system, since in a final realization of the external control unit, the signals are generated directly by the MCU. Further, the wireless communication is not included in the performance measurements, and was disabled in the implant hardware prototype. The output power is measured at a load resistor, which models the power consumption of the LVAD, and the external battery supply is replaced by a programmable laboratory DC power supply.

Fig. 8.9(b) shows the results of the total power loss measurement. The power loss was measured for an output power range of 5-30 W, but it is most unlikely that a single LVAD consumes more than 12 W. However, for systems providing bi-ventricular support or for a TAH, the power consumption of the circulatory support system could reach up to 20 W or even more. The total measured power loss ranges from 1.16 W up to 3.51 W depending on the output power and the coil separation distance. The total implant power loss at maximum output power is calculated as 0.917 W and is independent of the coil separation distance. It should be noted, that the constant power loss of the combined primary-side and secondary-side control and auxiliary circuit reaches about 840 mW and offer great potential for further improvements and optimization.

The resulting DC-DC efficiency is shown in **Fig. 8.9(c)**. At maximum output power, the efficiency reaches up to 92.4%. However, due to the constant power losses, the efficiency drops down to 78.3-81.2% at the minimum output power of 5 W and at a coil separation distance of 23 mm and 13 mm, respectively. In order to show the potential room for improvement, the efficiency is calculated in addition for the energy transmission system only, neglecting the control and auxiliary circuit power losses, and is plotted in the same figure. Even if this is only a theoretical consideration, it is evident that the system performance could be improved specifically at low output power up to 10 W by reducing the constant power losses, e.g. of the microcontroller and by a more efficient design of the 3.3 V and 5 V auxiliary power supplies.

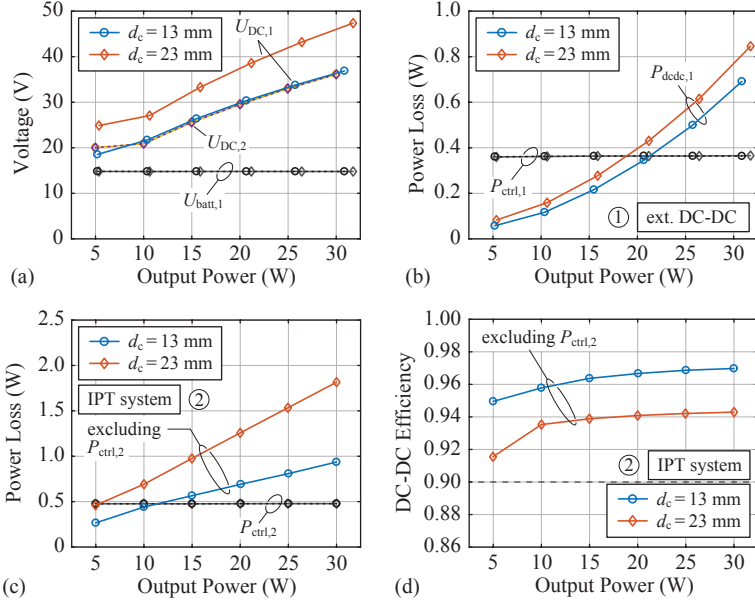


Fig. 8.10: (a) Input and output voltage of the IPT system. (b) Power loss of the external boost-type DC-DC converter stage and the separately measured primary-side control and auxiliary circuit power losses. (c) Power loss of the IPT system power stage, obtained from the measured inverter input power and rectifier output power, including the inverter gate drive power loss. Additionally, the secondary-side control and auxiliary circuit power losses are indicated in the same figure. (d) Corresponding DC-DC efficiency of the IPT system power stage, excluding the secondary-side control losses.

The measured primary-side and secondary-side DC-link voltages and the measured power loss of the primary-side boost converter and the IPT system power stage are shown in **Figs. 8.10(a)-(d)**. Note that the power losses are derived from the measurement of the input and output power of each individual power stage in **Fig. 8.9(a)**, denoted with 1 and 2. The control and auxiliary circuit power losses $P_{\text{ctrl},1}$ and $P_{\text{ctrl},2}$ are measured separately and are given in addition in **Figs. 8.10(b)** and **(c)**, respectively. As the only exception, the constant inverter gate drive power loss $P_{\text{gd},1}$ of 75 mW is already included in the IPT stage power loss measurement.

As explained in **Section 2.6.2**, the output voltage of the SSU TET

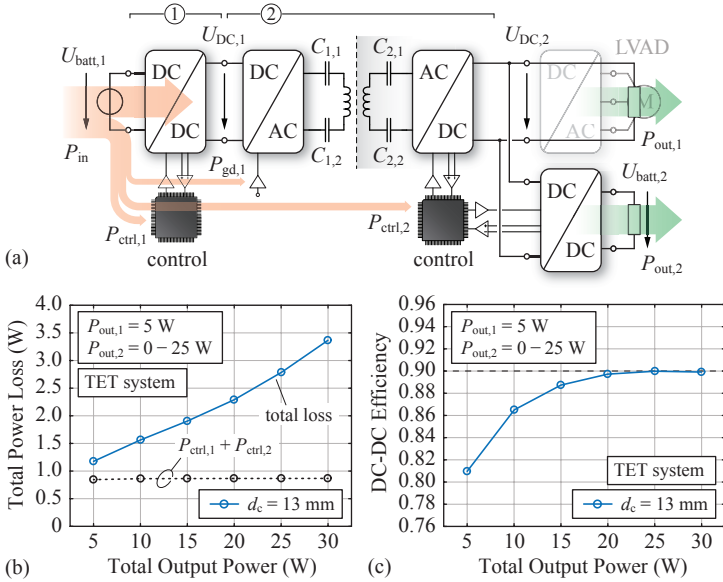


Fig. 8.11: (a) Schematic circuit diagram of the SSU TET system prototype operated in *mode B* and the indicated input and output power components that are considered for the total system performance measurement. (b) Total SSU TET system prototype power loss and (c) total DC-DC efficiency.

system is varied according to the output power of the IPT system and is limited to a minimum output voltage of 20 V, such that there is no need for a buck-boost DC-DC converter on either side of the IPT power stage. As already stated, a main disadvantage of the SSU TET system is the increasingly inductive behaviour of the input impedance of the IPT resonant circuit, when the coil separation distance is increased. Hence, at low coil coupling factors, the primary-side DC-link voltage must be increased in order to maintain the required energy transfer across the skin. As a consequence, the power loss on the primary side increases significantly with increasing coil separation distance (cf. **Fig. 8.10(c)**). Nevertheless, the secondary-side power losses are small and are independent of the coil separation distance, which is an advantage of the SSU TET system.

As shown in **Fig. 8.10(d)**, the IPT power stage attains DC-DC efficiencies of up to 97% at the minimum coil separation distance of

13 mm. However, as explained above, the efficiency drops significantly with decreasing coil coupling factor down to 91.6%, which is measured at minimum output power and 23 mm coil separation distance.

The SSU TET system performance was also measured for the *operating mode B*, which considers a constant power supply of 5 W for the LVAD and an additional variable battery charger output power. The TET system schematic and the considered input and output power components for the *operating mode B* are illustrated in **Fig. 8.11(a)**. For the measurements, both the LVAD and the backup battery are modeled with an adjustable load resistor. The battery charger is operated in buck-mode and controls the output voltage to the nominal battery pack terminal voltage of 14.8 V. The load resistance is varied such that the output power $P_{\text{out},2}$ ranges from zero to 25 W. The load resistor, which models the power consumption of the LVAD and the 3-phase inverter, is adjusted such that a constant power of 5 W is consumed. The power loss measurement was performed at a coil separation distance of 13 mm and the result is shown in **Fig. 8.11(b)**. The total primary-side and secondary-side control and auxiliary circuit power losses attain a value of 866 mW and are indicated in the same figure. Again, the power loss of the wireless communication is not included in the measurements and the module is disabled in the implant prototype. Further it should be noted that due to the small phase angle of the input impedance of the IPT resonant circuit at minimum coil separation distance, the primary-side inverter is partially hard-switching at an IPT system output power of 10-30 W. However, the switch voltage at the hard-switching instant is in a range of only 4.6-6.3 V and hence does not contribute significantly to the total power losses.

The total DC-DC efficiency is shown in **Fig. 8.11(c)** and confirms that the TET system prototype is able to deliver a constant power of 5 W to the LVAD and simultaneously, a power of up to 25 W can be delivered to the internal backup battery with a total DC-DC efficiency of up to 90%. The distribution of the secondary-side power losses for the TET implant prototype operated in *mode B* at maximum output power of 30 W, is shown in **Fig. 8.12(a)**, and is calculated using both measurements and numerical models. The estimated total secondary-side power loss is about 1.63 W and the secondary-side IPT coil power loss is calculated as 252 mW, which is only 15% of the total secondary-side losses. The power loss in the implant (excluding power losses in the implant battery) is 1.38 W and **Fig. 8.12(b)** shows the corresponding

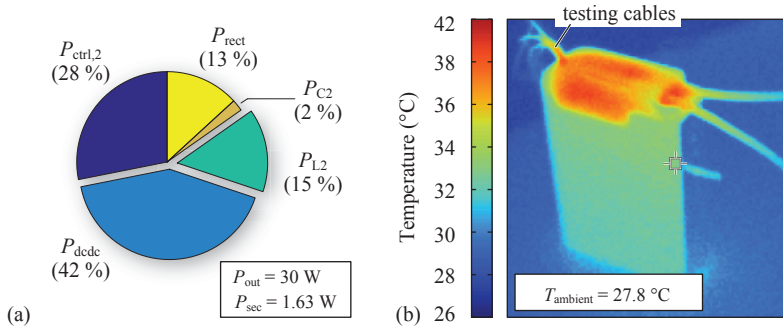


Fig. 8.12: (a) Calculated distribution of the implant power losses for the power loss measurement shown in **Fig. 8.11(b)**. (b) Thermal image of the implant hardware prototype, operated at a total output power of 30 W, including the battery charger output power of 25 W (cf. **Fig. 8.11**). The ambient temperature is 27.8°C .

thermal image of the implant prototype operated at maximum output power. The maximum temperature at the top cover of the prototype reaches 42°C in air with an ambient temperature of 27.8°C . Note that for the performance measurement, the charging of the battery was simulated using a variable load resistor. However, the battery charging is not a lossless process. For a nominal battery voltage of 14.8 V, a reasonable charging power of 20 W and assuming a DC-resistance of $100\text{ m}\Omega$ for each battery, the total power loss of the battery pack is estimated with 730 mW. Therefore, it is expected that the surface temperature of the aluminium enclosure is much higher than depicted in **Fig. 8.12(b)**. But due to the large surface area of the implant, it can also be expected that the batteries are cooled more effectively, when implanted in the human body. An assessment of the thermal safety of the TET implant prototype is difficult as it would require a more complex thermal model of the human body and additional information on the location of implantation, i.e. the type and structure of the surrounding tissue. A final thermal safety assessment of the implant can be provided only by an experiment.

In order to compare the measured performance of the SSU TET system prototype, the same measurements are also performed for the SSR TET system, and the results are presented in the following section.

8.2.3 SSR TET System

The performance evaluation of the SSR TET system operation (cf. **Section 2.6.1**) is carried using the inverter circuit, the IPT coils and the synchronous rectifier stage presented in **Section 2.4.1**. Similar to the previous measurements, the power loss is measured separately for each power electronic converter stage with matched input and output voltage/power at the DC-link interfaces. For the primary-side and secondary-side DC-DC converter, the same battery charger PCB as for the TET implant prototype is used and is operated either in buck-, or with reversed terminal connections, in boost-mode, whichever is required for the operating point. The DC-DC converter stages are operated at 150 kHz and the same inductor is used as for the external DC-DC converter of the SSU TET system prototype. However, in this case, the power losses of the DC-DC converters are slightly underestimated, i.e. about 60 mW at maximum output power, because of the missing additional on-state resistance of the switch in continuous conduction mode, which is present in the conduction path of the idle branch of a four-switch buck-boost converter (cf. **Fig. 6.2(a)**).

The IPT system is operated at 800 kHz and the primary-side and secondary-side compensation capacitances C_1 and C_2 have a value of 2.2 nF. A simplified schematic circuit diagram of the SSR TET system prototype is shown in **Fig. 8.13(a)**. The power loss measurements are performed for coil separation distances of 10 mm and 30 mm, which corresponds to coil coupling factors of 0.489 and 0.15, respectively. The LVAD and its inverter stage are modeled with an adjustable load resistor. The voltage at the load resistor is set to a constant value of 14.8 V that represents the backup battery voltage, and the power at the load resistor is varied in a range of 5-30 W. In order to control the DC-DC converter stages, the same control board as for the SSU TET system prototype is used. The power loss is measured for each power conversion stage individually, which are denoted in **Fig. 8.13(a)** with numbers 1, 2 and 3. The constant power losses P_{ctrl} of the control and the auxiliary circuits, which are used to operate the DC-DC converter stages, are measured separately. In addition, the primary-side inverter gate drive power loss $P_{\text{gd},1}$ and the secondary-side synchronous rectifier gate drive and auxiliary circuit power losses P_{sync} are measured, and are included in the total IPT system power loss measurement. Similar to the previous measurements, the power losses due to the wireless communication and due the FPGA of the IPT inverter stage are not

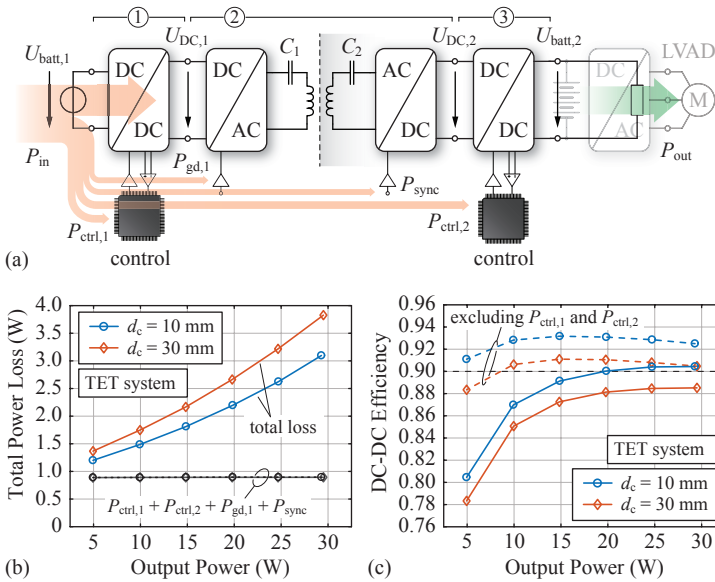


Fig. 8.13: (a) Schematic circuit diagram of the SSR TET system prototype and the illustrated components of the input and output power considered for the total system performance evaluation. (b) Total SSR TET system prototype power loss and (c) total DC-DC efficiency.

included in the performance evaluation.

The results for the total power loss measurement and the total system efficiency are shown in **Figs. 8.13(b)** and **(c)**, respectively. Due to the symmetry of the particular circuit, the power losses are distributed approximately in equal parts between the primary and the secondary side. Therefore, it can be inferred with good approximation, that the implant power losses are about half of the measured total power losses. Again, as shown in **Fig. 8.13(b)**, the total constant power loss which is due to the control circuit, the inverter gate drive and the auxiliary circuit of the synchronous rectifier, has a value of 893 mW and contributes significantly to the total power loss. The total DC-DC efficiency depicted in **Fig. 8.13(c)** reaches values of up to 90.4% at maximum output power and minimum coil separation distance. And even at a large coil separation distance of 30 mm, efficiencies of up to 88.5% are achieved. As indicated in the same figure, the efficiency could be signif-

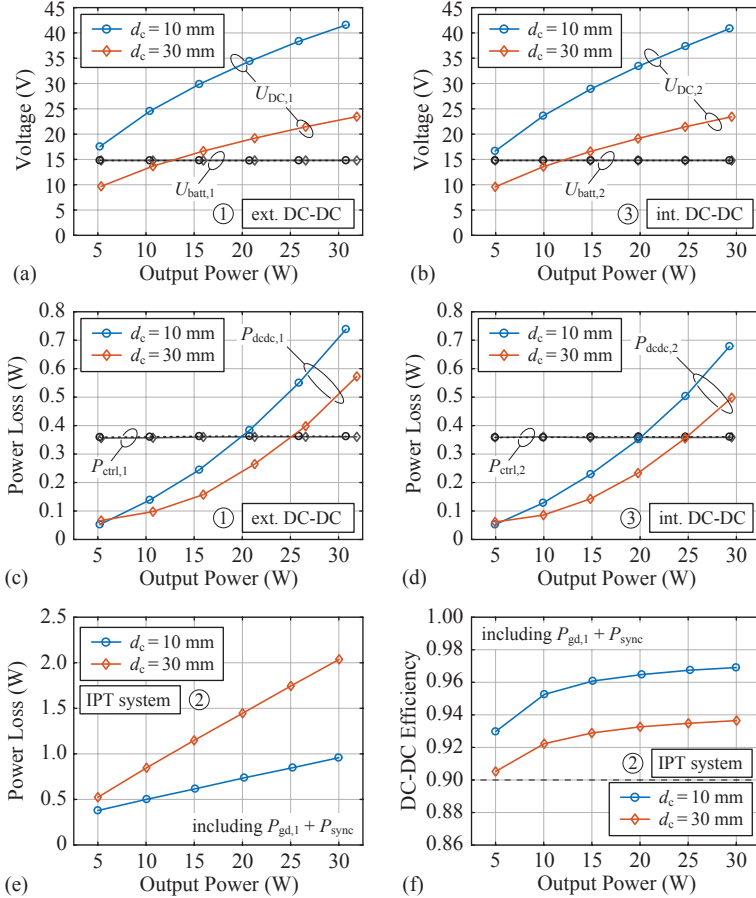


Fig. 8.14: Performance measurement of the SSR TET system prototype. (a)-(b) Input and output voltage of the primary-side and secondary-side DC-DC converter stages. (c) Power loss of the primary-side and (d) of the secondary-side DC-DC converter stage and the additional control and auxiliary circuit power losses. (e) Power loss of the SSR IPT system, including the inverter gate drive and the synchronous rectifier power losses. (f) Corresponding DC-DC efficiency.

icantly improved, if the power loss of the primary-side and secondary-side control circuit and the auxiliary power supplies are reduced.

Figs. 8.14(a) and **(b)** show the primary-side and secondary-side input and output voltages $U_{\text{batt},1}$ and $U_{\text{batt},2}$, as well as the DC-link voltages $U_{\text{DC},1}$ and $U_{\text{DC},2}$ for the SSR TET system operation. As explained in **Section 2.6.1**, at large coil separation distances, the primary-side and secondary-side DC-link voltages are decreased in order to maintain an efficiency-optimal operation. Accordingly, the overall IPT system efficiency is optimized, but the primary-side and secondary-side coil power losses are increased simultaneously for a decreasing coil coupling factor and constant output power, which causes additional heating of the TET coils and hence, is a main disadvantage of the SSR TET system operation. At minimum coil separation distance, the primary-side and secondary-side DC-DC converter stages operate in boost- or buck-operation only, but as the coil separation distance increases, the optimum DC-link voltages drop below the nominal battery voltages and the DC-DC converter stages are switching from boost to buck operation and vice versa.

The primary-side and secondary-side DC-DC converter power losses are shown in **Figs. 8.14(c)** and **(d)**, respectively. In addition, the total primary and secondary control and auxiliary circuit power losses are indicated in the same figures. The SSR TET system operation has the advantage, that at large coil separation distances, i.e. at low coil coupling factors, the DC-link voltage is decreased and hence reduces the switching losses in the DC-DC converter stages.

The power loss of the IPT stage increases linearly with increasing output power, as shown in **Fig. 8.14(e)**. The active load matching which is a result of the *efficiency optimal control* of the SSR IPT system allows to reduce the power losses significantly at large coil separation distances. As a result, the DC-DC efficiency of the IPT system, which is shown in **Fig. 8.14(f)**, is above 90 %, even at a large coil separation distance of 30 mm, and reaches a maximum value of up to 96.9 % at the minimum coil separation distance and maximum output power. However, due to the decreasing phase angle of the input impedance of the IPT resonant circuit at increasing coil separation distance, the primary-side inverter stage experiences increasing switching losses, which is due to partial hard-switching. At the minimum coil separation distance of 10 mm, the partial hard-switching occurs at very low switch voltages, e.g. as low as 5 V at maximum output power. At larger coil separa-

tion distances, i.e. at a coil separation distance of 30 mm, the partial hard-switching losses contribute substantially to the total losses, since at maximum output power, the switch voltage at the switching instant has a value of about 2/3 of the input DC-link voltage. At a coil separation distance of 50 mm, i.e. at a coil coupling factor of only 6%, and for an output power of 5 W, the DC-DC efficiency of the IPT stage is still 83.7% and 85.2% at 10 W output power. Consequently, the wireless power supply for the LVAD can be sustained even at significant coil misalignment. However, it should be noted that in this case, the primary-side inverter is fully hard-switching, which is due to the small phase angle of the input impedance.

8.3 Summary of the Chapter

This chapters describes the design and the hardware realization of the TET implant prototype for the SSU TET system concept and the performance measurements are shown for the SSU and the SSR TET system topology. The measurement results clearly indicate the capabilities of each TET system type and the efficiencies that can be achieved with a careful design of the power electronic converter stages. The comparison of the two concepts shows that both solutions achieve about the same DC-DC efficiencies at the minimum specified coil separation distance. However, the SSR TET system shows a better performance at an increased TET coil misalignment. It was further shown that the constant power losses, which are due to the auxiliary power supplies and the control circuit, are a main contributor to the total power losses and must therefore be reduced in order to further improve the overall system performance.

The main results of this chapter are summarized as follows:

- ▶ A fully functional and compact TET implant prototype was realized, including the IPT synchronous rectifier circuit, the battery charging converter as well as the backup battery, the control circuit and two separate wireless communication interfaces, including the antennas. The demonstrator implant prototype has a boxed volume of only 10.3 cl and weighs 188 g.
- ▶ In case of the SSU TET system prototype, an output power of 5 W can be delivered to the LVAD with DC-DC efficiencies ranging

from 78.3% to 81.2% at coil separation distances of 23 mm and 13 mm, respectively. The efficiency is mainly limited by the large constant power loss, which is associated with the control circuit and the auxiliary power supplies. At the maximum output power and coil separation distances of 23 mm and 13 mm, the DC-DC efficiency attains values of 89.5% and 92.4%, respectively.

- ▶ In case of simultaneous battery charging converter operation, an overall DC-DC efficiency of up to 90% was achieved for the SSU TET system prototype at a maximum power transmission of 30 W and minimum coil separation distance of 13 mm.
- ▶ The SSR TET system prototype shows a superior coil misalignment tolerance and even at a coil separation distance of 30 mm and 5 W output power, an overall DC-DC efficiency of 78.3% (i.e. 1.37 W total power loss) was achieved. At the rated maximum power transmission of 30 W, the system efficiency is as high as 90.4% at 10 mm coil separation distance and drops to 88.5% at 30 mm coil separation distance. The DC-DC efficiency of the IPT stage itself is very high and reaches values of up to 96.9% at the minimum coil separation distance and maximum output power. For coil separation distances of less than 30 mm, the DC-DC efficiency is always above 90%.

Up to this point, the TET system was designed and optimized stage-by-stage and the 3-phase inverter, which drives the LVAD, was not considered. Therefore, in the next chapter, an extended numerical optimization is presented, which allows to optimize the overall TET system, including each power electronic stage between the external battery supply and the LVAD.

9

TET System Optimization

In the previous chapters, each power electronic converter stage was analyzed individually and was optimized as a single stage for the maximum output power and ideal coil alignment, i.e. at the minimum coil separation distance. However, the individual converter stages are interconnected and share the same DC-link at the interfaces. Hence, the optimization of one stage could result in increased power losses in the subsequent converter stage, e.g. as the switching power losses are increased due to a larger DC-link voltage. Even if it is important to design the converter stages for the maximum output power, i.e. for the maximum power loss, the TET system is usually operated only for short time intervals close to the maximum power transfer capability, i.e. during the charging process of the implanted backup battery. But for most of the time, the TET system has to cover the LVAD power consumption only. Therefore, it is equally important to optimize the TET system for a high partial load efficiency. Furthermore, it was shown in the previous chapter, that the SSU and the SSR IPT system operation differs quite significantly in terms of the operating conditions, i.e. considering the control of the internal DC-link voltages and the share of the power losses within the overall system, which both are mainly dependent on the coil alignment. Hence, in order to account for these effects, it was decided to optimize the overall TET system in terms of a weighted efficiency, calculated for the following four operating points

$$\text{OP}(n) = \left[\begin{array}{cccc} P_{2,\max} & P_{2,\min} & \tilde{P}_{2,\max} & P_{2,\min} \\ \underbrace{k_{\max}}_{n=1} & k_{\max} & k_{\min} & k_{\min} \end{array} \right], \quad n \in [1, 4], \quad (9.1)$$

which are characterized each by the specified IPT converter stage output power P_2 and coil coupling factor k . The weighted efficiency for the maximum power transmission and partial load operation is then defined for the operation at each coupling factor with

$$\begin{aligned} \eta_{w,k(\max)} &= \alpha_1 \eta_1 + \alpha_2 \eta_2 & \text{and} & \quad \alpha_1 + \alpha_2 = 1, \\ \eta_{w,k(\min)} &= \alpha_1 \eta_3 + \alpha_2 \eta_4 \end{aligned} \quad (9.2)$$

where η_i , $i \in [1, 4]$, denotes the total DC-DC efficiency of the overall TET system at the operating point 1 to 4. The efficiency weights α_1 and α_2 represent the percentage of the time per day at which the IPT system is operated either at maximum output power or at partial load conditions. In this case, it was assumed that within a single day, the TET system is in charging mode for about one hour, i.e. at which the maximum power is delivered to the implant. In the remaining time, the TET system is delivering the power for the LVAD operation only. Hence, the efficiency weight α_1 is set to 0.04 and accordingly, α_2 is set to 0.96. The maximum output power $P_{2,\max}$ at maximum coil coupling factor k_{\max} is set to 30 W and the minimum output power $P_{2,\min}$ is set to 5 W. It was assumed that a constant IPT system output power of 5 W is used to operate the LVAD and any excessive transferred power is used to charge the implanted backup battery. The maximum coil coupling factor k_{\max} is obtained at the minimum coil separation distance of $d_{c,\min} = 10$ mm and at a specified maximum coil separation distance of $d_{c,\max} = 30$ mm, i.e. at k_{\min} , the maximum IPT converter stage output power is reduced to $\tilde{P}_{2,\max} = 20$ W.

In order to account for the coil coupling variations as well, the total weighted efficiency is then calculated according to

$$\eta_{w,\text{tot}} = \alpha_3 \eta_{w,k(\max)} + \alpha_4 \eta_{w,k(\min)} \quad \text{and} \quad \alpha_3 + \alpha_4 = 1. \quad (9.3)$$

Since any activity or movements of the patient are likely to cause a misalignment of the TET coils, the carrying device or harness for the external IPT coil must include measures for the positioning of the coil. Additionally, the TET system could provide a feedback to the patient, which indicates if the coil alignment is not sufficient, especially during high power transmission. It can therefore be expected, that it is more likely that a reasonable coil coupling is achieved and that an operation of the TET system at the specified maximum coil separation distance is minimized. Accordingly, the efficiency weights α_3 and α_4 are set to 0.6 and 0.4 for the maximum and the minimum coil coupling factor, respectively.

9.1 Optimization Procedure

Due to the large design space and the extensive calculations, the optimization process is split into several parts and the design results are continuously evaluated and checked for feasibility in order to eliminate poor system designs at an early stage. The remaining results are merged at the end of the simulation.

The optimization procedure is shown in **Fig. 9.1** and starts with the generation of feasible IPT coil sets. As described in **Section 2.2.1**, a large number of feasible coil sets is generated for a wide range of coil geometries (cf. **Fig. 2.10**) with maximum coil radii of 35 mm and 40 mm for the implanted and the external coil, respectively. The minimum outside coil radius is set to 25 mm. Only the coil sets, which have a primary-side coil outside diameter greater or equal to the secondary-side coil diameter are considered for the optimization. The minimum inside radius is set to 5 mm for both coils. For the single-layered coil windings, commercially available litz-wires with 32-71 μm strand diameter and 200-320 strands are considered. Then, using an FE-simulation, the coil self inductance and the mutual inductance are calculated for the minimum and maximum coil separation distance of 10 mm and 30 mm.

In a next step, an IPT system is designed according to the simulation flow-chart illustrated in **Fig. 9.2**, considering eight equally spaced operating frequencies in the frequency range of 0.2-1.6 MHz, as well as at 100 kHz. For each operating frequency only the coils with a minimum coil quality factor of $Q_{\min} = 200$ are considered. Then, in *step 3* in **Fig. 9.2**, an IPT system is designed for each feasible coil pair for the SSU and the SSR IPT system operation, according to the design equations given in **Tab. 2.1**. For the SSU IPT system, the minimum secondary-side DC-link voltage $U_{\text{DC},2}$ is limited to 20 V, such that the battery charging converter can be realized as simple bidirectional buck-type DC-DC converter, which reduces the implant hardware complexity, as it is explained in **Section 2.6.2**.

In *step 4* in **Fig. 9.2**, the performance of each IPT system design is calculated for the four operating points specified in (9.1). In a first step, the coil currents, the IPT system input voltage and the input impedance of the resonant tank are calculated for the operating points. In addition, the IPT coil AC resistances are calculated according to the analytical model provided in **Section 2.1.5**. In this case, the calculated

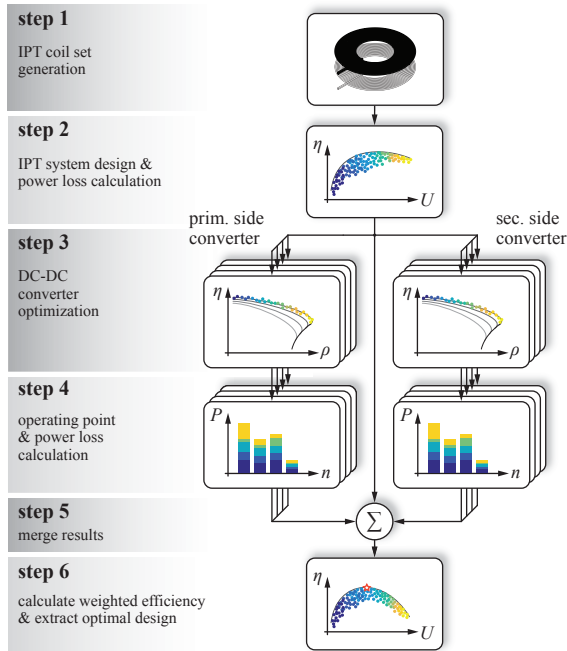


Fig. 9.1: Flowchart of the overall TET system optimization.

AC resistances are scaled by a factor of 1.15 in order to partly account for the coil lead wires, which are not explicitly modeled in the numerical simulation, and to account for litz-wire twisting imperfections.

In the next step, the total power losses are calculated for each IPT system design, including the inverter and synchronous rectifier power losses. The dead-time for the inverter is set to 50 ns and it is assumed that soft-switching of the inverter is achieved at any operating point, i.e. potential partial hard-switching at small phase angles of the input impedance is neglected. For the synchronous rectifier it is assumed that the diode conduction time is as low as 5 ns before the rectifier switches are turned on (cf. **Fig. 2.28(a)**). For both the inverter and the synchronous rectifier switches it is assumed that the EPC2016C GaN FET is used together with the MBR1H100SF Schottky diode, which is placed in anti-parallel configuration to each FET, as shown in **Fig. 2.22** and **Fig. 2.27**.

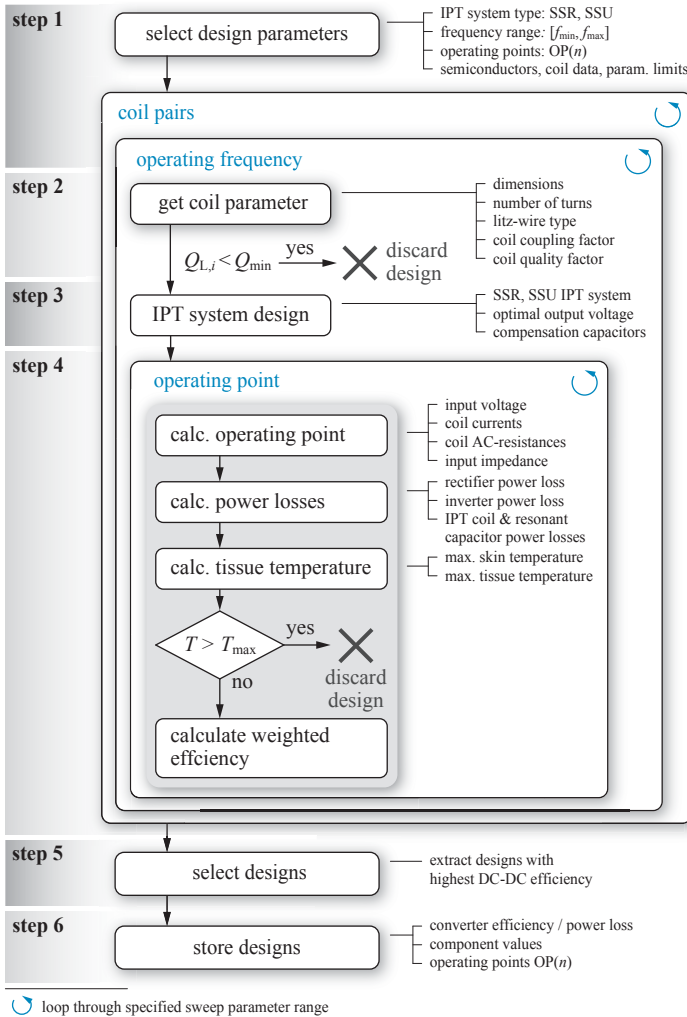


Fig. 9.2: Flowchart of the IPT system design and performance calculation.

After the secondary-side IPT coil power loss calculation, the maximum skin and tissue temperatures are calculated for the minimum coil separation distance and the maximum output power, based on the thermal model presented in **Chapter 3**. Only the thermally valid designs, i.e. the designs with a tissue temperature below 39°C , are considered for the further calculation.

Finally, the weighted efficiency is calculated for each IPT system design according to (9.2) and (9.3) and only the designs with the highest weighted DC-DC efficiency with respect to the IPT system output voltage at maximum output power and minimum coil separation distance are selected for the further calculations. At this point, from a total number of about 40'000 IPT system designs, a group of 300-500 designs is considered for each the SSR and the SSU IPT system for the further overall system optimization.

The DC-DC converter stages at the input and at the output of the IPT system are optimized in terms of a multi-objective optimization, as described in **Section 6.4.1**. The DC-DC converter stages are designed as necessary for the IPT system design at hand, i.e. for the SSR or the SSU IPT system operation, as a hard-switched buck, buck-boost or as a simple boost converter. The external and the internal battery voltage is set to a nominal value of 14.8 V and the considered switching frequencies include several equally spaced frequencies in a range of 100-600 kHz for the external converter, and a range of 100-400 kHz for the internal DC-DC converter stage. The specification for the maximum peak-to-peak inductor current ripple is defined such that the ripple does not exceed 80 % of the average inductor current at maximum output power. For the design of the inductor, a litz-wire winding and a wide range of commercially available E-, ELP- and ER ferrite cores is considered. For the core material, the TDK/EPCOS N87 ferrite material is used.

Consequently, for each feasible IPT system design, a large number of external and internal DC-DC converter stages is designed. In order to reduce the computation time, the optimization process is split into multiple smaller parts that are computed in parallel, as illustrated in **Fig. 9.1**. The interface between the IPT system and the DC-DC converter stages is defined by the common DC-link voltage at the interconnections and the transferred power.

For each IPT system design, the DC-DC converter stages are optimized for the worst-case operating point, i.e. for the highest inductor current, in order to select only the thermally valid designs. For each

considered switching frequency, a large set of feasible inductors with different power densities are designed. Additionally, the total converter volume is calculated as well as the power loss of each converter component. In order to reduce the number of designs, only the Pareto-optimal designs, i.e. in terms of converter efficiency and power density, are stored. After the completion of the switching frequency sweep, the designs are merged and again, only the Pareto-optimal designs are selected for the further processing. In *step 4* in **Fig. 9.1**, the total power loss is evaluated for each of the DC-DC converter stages for the four considered operating points of the associated IPT system design.

At this stage, each considered IPT system design is equipped with a large number of Pareto-optimal external and internal DC-DC converter designs. In addition, the total power loss is already calculated for each power conversion stage for each of the four specified operating points. Hence, in *step 5* and *step 6* shown in **Fig. 9.1**, the individual power conversion stages are cascaded and the total system power loss is calculated for each combination of the primary-side and secondary-side DC-DC converter stages that belong to the same IPT system design. Note, that at this point, the total number of considered TET system designs exceeds a number of 1 million designs.

The 3-phase inverter, which is needed for the LVAD operation, is considered as well, but only a very simple power loss model is used, which accounts only for the gate drive and the hard-switching power losses. In order to further simplify the calculation, it was assumed that the switching loss arises only from the dissipation of the energy which is stored in the output capacitances of the switches. Further it is assumed, that the inverter uses a PWM scheme with a fixed operating frequency of 150 kHz.

For the SSR IPT system, the total power loss is obtained by cascading each power conversion stage, beginning at the external DC-DC converter and continuing towards the 3-phase inverter. For the SSU IPT system, the secondary-side battery charging converter is connected in parallel to the 3-phase inverter. In this case, the battery charger is not operated at the minimum output power of the IPT system and therefore, does not cause any power losses at this specific operating point.

The simulation procedure in **Fig. 9.1** is terminated with the calculation of the total weighted efficiency according to (9.3) and for each IPT system design, only the DC-DC converter stage combination is stored, which achieves the highest overall weighted efficiency. Note that the

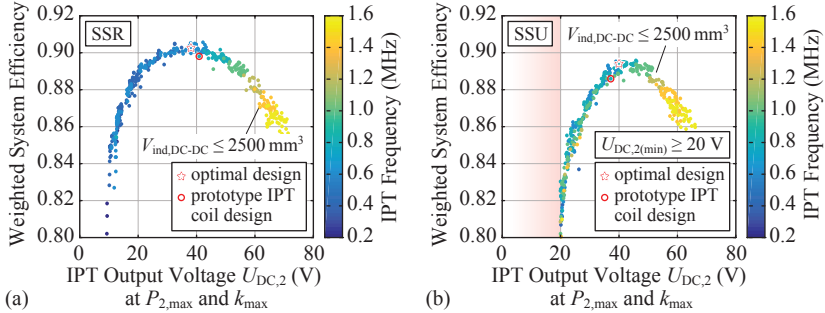


Fig. 9.3: (a)-(b) Calculated total weighted efficiency $\eta_{w,tot}$ of the optimal SSR and SSU TET system designs, with respect to the IPT output voltage at maximum power transmission and minimum coil separation distance, and excluding the power losses of the control circuit and the auxiliary power supplies.

constant power losses caused by the control circuit and the auxiliary power supplies are not considered in the optimization process.

9.2 Optimization Results

Since each DC-DC converter stage can achieve a higher power conversion efficiency if the inductor size is increased, the maximum feasible inductor volume must be chosen prior to the selection an optimal design. **Figs. 9.3(a)** and **(b)** visualizes the optimal SSR and SSU TET system designs for a maximum DC-DC converter inductor boxed volume $V_{ind,DC-DC}$ of 2500 mm^3 . The total weighted system efficiency $\eta_{w,tot}$, excluding the power losses of the control circuit and the auxiliary power supplies, is plotted with respect to the optimal IPT system output voltage at maximum power transmission and minimum coil separation distance. If larger inductor volumes of the DC-DC converters are allowed, the overall system efficiency of each design is improved.

Both TET system types have an efficiency maximum about $U_{DC,2} = 40 \text{ V}$, but the optimum is more distinct for the SSU TET system and a deviation from the optimum results in a significant decrease of the overall system performance. Furthermore, as expected, it can be noted that the SSR TET system achieves a higher overall system performance and the optimal IPT system operating frequency is lower compared to

the SSU TET system.

As indicated in **Figs. 9.3(a)** and **(b)**, the calculated weighted efficiency of the TET system design, which uses the IPT coil pair that has the same design specifications as the prototype IPT coils, is not far from the optimal design, when considering maximum DC-DC converter inductor volumes of 2500 mm^3 . However, the overall implant volume is a critical design parameter and therefore, for the selection of a feasible TET system design, the inductor volume limit is reduced for the implanted DC-DC converter to a maximum boxed volume of 1200 mm^3 . In order to provide a fair comparison, the same inductor volume limitations are used for both IPT system operating modes. In addition, the maximum IPT system output voltage is limited to 40 V. The optimal designs that meet these criteria are indicated in **Figs. 9.3(a)** and **(b)**, and the overall performance of the selected designs is only slightly lower than the global optimum, which is due to the higher power density of the implanted DC-DC converter stage. A summary of the design parameters and the circuit schematic of the proposed power electronic converter stages of the selected system optima are given in **Tab. 9.1** and **Fig. 9.4** for the SSR TET system and in **Tab. 9.2** and **Fig. 9.5** for the SSU TET system, respectively.

In order to give an interpretation of the results, the power loss distribution is calculated for each of the considered operating points for both TET system designs, and is shown in **Fig. 9.6**. On both sides of the TET system, a constant total power loss of 350 mW is included, in order to account for the external and the internal control circuit and auxiliary power supply losses.

A main difference of the SSR and the SSU TET system operation is the share of the power losses that are generated in the implant and in the extracorporeal part of the TET system, which is visualized in **Fig. 9.6**. In case of the SSR TET system, the power losses are shared almost equally between the internal and the external part of the system. For the operation at large coil separation distances and constant output power, the power loss in the IPT system increases significantly on both sides, which is due to the lowering of the IPT system input and output voltage. But concurrently, the switching power losses in the primary-side and the secondary-side DC-DC converter stages are decreasing due to the lower DC-link voltages. The LVAD inverter experiences the same power loss for each operating point, since in case of the SSR TET system, the inverter is connected directly to the backup

Optimal SSR TET System Design			
IPT system parameter		Secondary-side DC-DC converter	
Operating conditions			
Frequency	600 kHz	Frequency	150 kHz
Max. input voltage	$U_{DC1,max}$ 33.2 V	Dead time	t_{dead} 41 ns
Max. output voltage	$U_{DC2,max}$ 38.1 V	Battery voltage	$U_{batt,2}$ 14.8 V
Min. coil distance	$d_{c,min}$ 10 mm	Max. current ripple ²⁾	$\Delta I_{L,pp(max)}$ 80 %
Max. coil coupling	k_{max} 0.51	Inductor design	
Min. coil coupling ¹⁾	k_{min} 0.17	Inductance	$L_{B,2}$ 38 μ H
IPT coil (primary side)			
Inductance	L_1 14.46 μ H	Strand diameter	d_i 100 μ m
Outside radius	$R_{a,1}$ 40 mm	Number of strands	n_i 33
Strand diameter	$d_{i,1}$ 50 μ m	Number of turns	N 28
Number of strands	$n_{i,1}$ 320	Core material	N87
Number of turns	N_1 15	Core type	E 10/5.5/5 set
IPT coil (secondary side)			
Inductance	L_2 20.44 μ H	Stacked core sets	N_c 1
Outside radius	$R_{a,2}$ 35 mm	Total air gap	s_{sig} 0.443 mm
Strand diameter	$d_{i,2}$ 40 μ m	Inductor volume	V_{ind} 1108 mm ³
Number of strands	$n_{i,2}$ 300	Min. DC-link capacitance	
Number of turns	N_2 19	Input capacitor	$C_{DC,B3}$ 5.6 μ F
IPT compensation capacitors			
Primary-side cap.	C_1 4.87 nF	Output capacitor	$C_{DC,B4}$ 6.1 μ F
Secondary-side cap.	C_2 3.44 nF	System efficiency	
		Total efficiency ³⁾	$\eta(n)$ 92.3 %
		Weighted efficiency	$\eta_{w, tot}$ 81.3 %

¹⁾ at an axial coil separation distance of 30 mm.

²⁾ specified as percentage of the maximum average inductor current

³⁾ total TET system efficiency at each operating point $OP(n) = [(P_{2,max}, k_{max}), (P_{2,min}, k_{min}), (P_{2,max}, k_{min}), (P_{2,min}, k_{max})]$, cf. Fig. 9.6(a), including the estimated L/VAD inverter losses and the constant primary-side and secondary-side control and auxiliary circuit power losses of 700 mW.

Tab. 9.1: Component parameter of the selected optimal SSR TET system design indicated in Fig. 9.3(a).

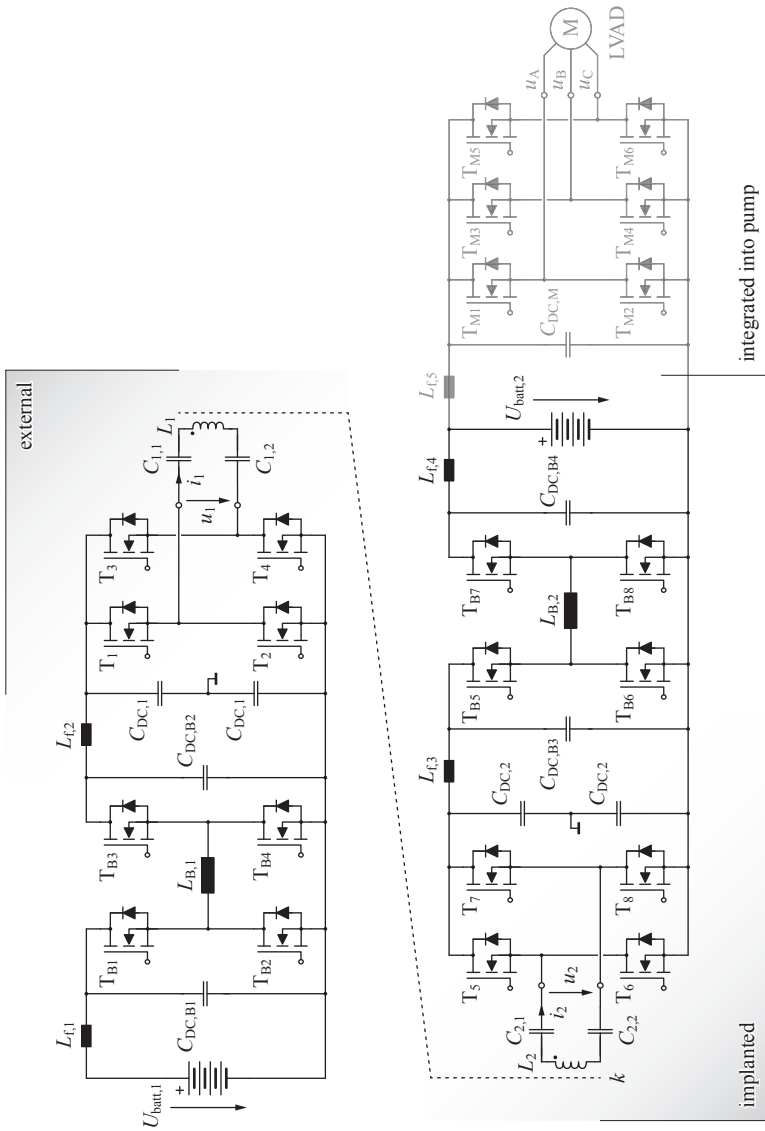


Fig. 9.4: Circuit schematic of the power electronic converter stages of the SSR TET system.

Optimal SSU TET System Design		
IPT system parameter	Primary-side DC-DC converter	Secondary-side DC-DC converter
Operating conditions		
Frequency	150 kHz	150 kHz
Max. input voltage ¹⁾	50.3 V	f_0
Max. output voltage	40 V	t_{dead}
Min. coil distance	10 mm	$U_{\text{batt},1}$
Max. coil coupling	0.47	Max. current ripple ³⁾
Min. coil coupling ²⁾	0.17	$\Delta I_{L,\text{pp}}(\text{max})$
IPT coil (primary side)		
Inductance	20.44 μH	Inductor design
Outside radius	40 mm	Inductance
Strand diameter	40 μm	Strand diameter
Number of strands	300	Number of strands
Number of turns	15	Number of turns
IPT coil (secondary side)		
Inductance	22.22 μH	Core material
Outside radius	35 mm	Core type
Strand diameter	40 μm	Stacked core sets
Number of strands	300	Total air gap
Number of turns	21	Inductor volume
IPT compensation capacitors		
Primary-side cap.	C_1	Min. DC-link capacitance
Secondary-side cap.	C_2	Input capacitor
		Output capacitor
System efficiency		
Total efficiency ⁴⁾	$\eta(n)$	Total efficiency
Weighted efficiency	$\eta_{\text{w, tot}}$	Weighted efficiency
	91.6	91.6
	86.8	86.8
	76.8	76.8
	%	%
	80.1	80.1

¹⁾ at the operating point OP(3) = [$P_{2,\text{max}}, k_{\text{min}}$]

²⁾ at an axial coil separation distance of 30 mm.

³⁾ specified as percentage of the maximum average inductor current

⁴⁾ total TET system efficiency at each operating point OP(n) = [$P_{2,\text{max}}, k_{\text{max}}$], [$P_{2,\text{max}}, k_{\text{min}}$], [$P_{2,\text{min}}, k_{\text{max}}$], [$P_{2,\text{min}}, k_{\text{min}}$]], cf. Fig. 9.6(b), including the estimated L.VAD inverter losses and the constant primary-side and secondary-side control and auxiliary circuit power losses of 700 mW.

Tab. 9.2: Component parameter of the selected optimal SSU TET system design indicated in **Fig. 9.3(b)**.

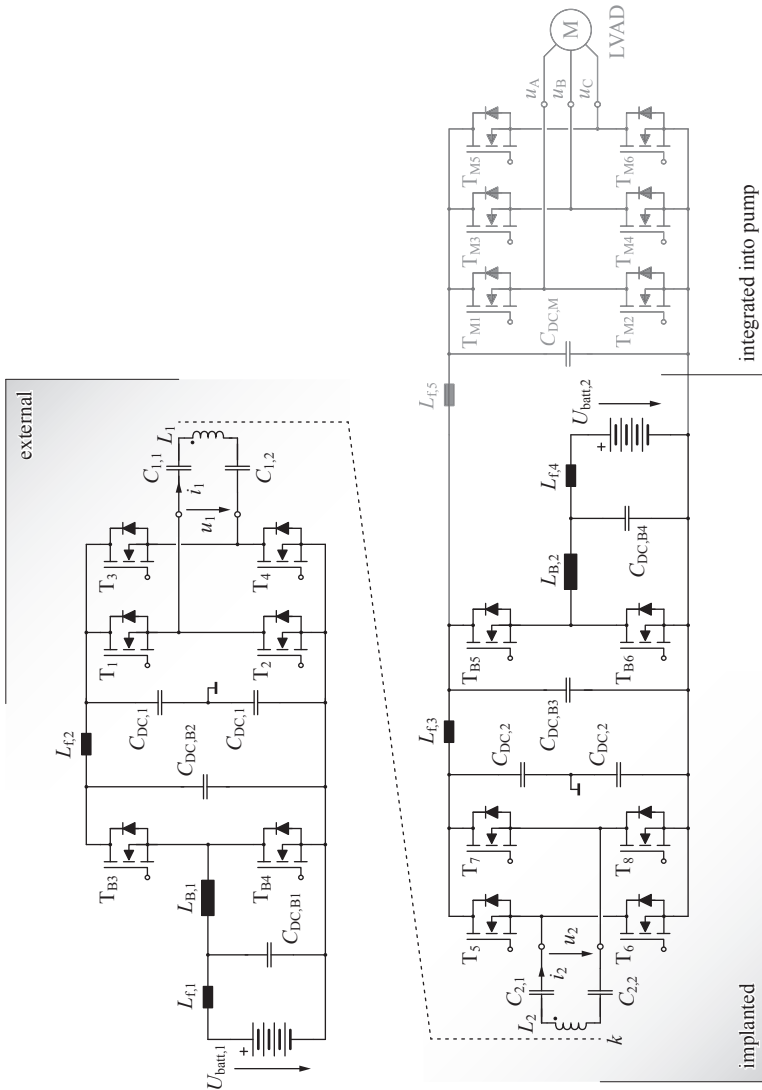


Fig. 9.5: Circuit schematic of the power electronic converter stages of the SSU TET system.

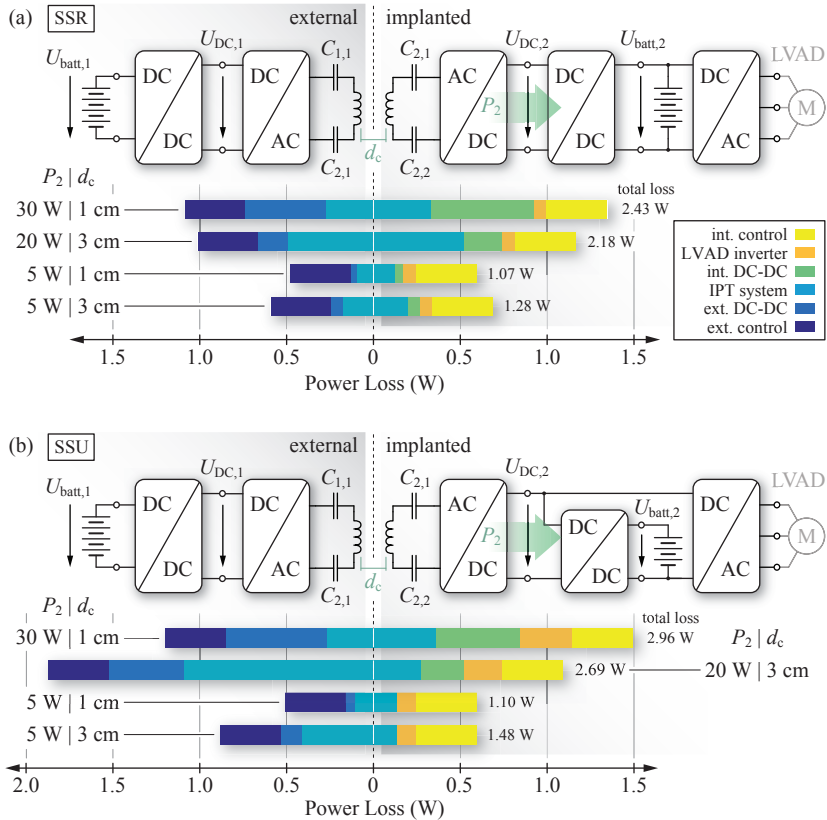


Fig. 9.6: (a)-(b) Calculated power loss distribution of the selected optimal SSR and SSU TET system design indicated in **Figs. 9.3(a)** and **(b)**, respectively.

battery as shown in **Fig. 9.6(a)**.

In case of the SSU TET system design, the power loss distribution between the primary and secondary side of the IPT system is asymmetrical. For large coil separation distances, the power loss in the external part of the TET system is increased significantly, which is due to the increasingly inductive behaviour of the input impedance of the IPT resonant circuit. This is aggravated by the fact, that due to the increasing primary-side DC-link voltage $U_{DC,1}$, the switching power losses in the

primary-side boost converter are increasing as well. On the other hand, the power losses that are generated in the implant are independent of the coil separation distance. In addition, as shown in **Fig. 9.6** for the maximum power transfer and minimum coil distance, the power loss in the implanted DC-DC converter of the SSU TET system is smaller compared to the SSR TET system. The reason is, that in case of the SSR TET system, the total transferred power has to be delivered by the internal DC-DC converter, whereas in case of the SSU TET system, the power is split at the output of the IPT system and only a part is processed by the battery charging converter. On the downside, in case of the SSU TET system, the switching losses that are generated in the LVAD inverter stage are increased at high IPT output power levels, which is due to the increased IPT system output voltage $U_{DC,2}$. Therefore, the power loss savings in the battery charging converter are compensated by the increased inverter power losses, such that the total secondary-side power losses of the SSU and the SSR TET system are very similar.

In the most frequent case, where only the power for the operation of the LVAD must be transmitted, the battery charger of the SSU TET system is not operated and the additional power losses can be saved. In case of the SSR TET system, the secondary-side DC-DC converter is operated in any case. But at low output power, the DC-link voltages are reduced due to the *efficiency optimal control* (cf. **Section 2.6.1**) and therefore, the switching losses in the DC-DC converter stages are reduced as well. On the one hand, considering the implant power losses only, it is expected from **Fig. 9.6** that both TET system types achieve a similar performance. But the SSU TET system benefits from lower secondary-side IPT coil power losses at large coil separation distances, and therefore allows for a lower heating of the subcutaneous tissue that is in contact with the implanted TET coil. On the other hand, considering the total primary-side power losses, it is obvious that the SSU TET system shows a lower performance, which is mainly due to the increasing reactive power at the input of the IPT resonant circuit at large coil separation distances.

The calculations are verified at the example of the SSR TET system prototype presented in **Section 8.2.3**. The measured power loss distribution of the SSR TET system prototype is shown in **Fig. 9.7(a)** and the calculated distribution is shown in **Fig. 9.7(b)**. In this case, the calculations account for the partial hard-switching operation of the

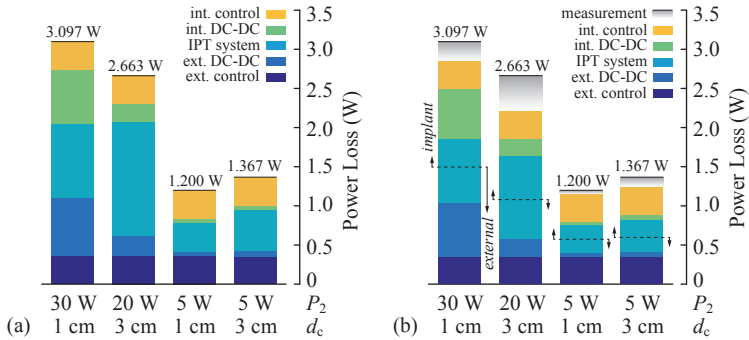


Fig. 9.7: (a) Measured power loss distribution of the SSR TET system prototype at different operating points, according to the experimental verification presented in **Section 8.2.3**. (b) Calculated power loss distribution of the SSR TET system prototype.

primary-side inverter according to the observations made during the performance measurements with the SSR TET system prototype. The calculated distribution matches the measurement with good accuracy, specifically in case of the primary-side and secondary-side DC-DC converter stages. However, at maximum coil separation distance and at an output power of 20 W, the numerical power loss model underestimates the power loss caused by the partial hard-switching operation of the IPT inverter stage, which explains the rather large discrepancy between the measured and the calculated total power loss in the IPT system.

9.3 Summary of the Chapter

It was shown in **Section 2.6**, that for the optimal IPT system operation, the load resistance of the IPT system must be adjusted depending on the operating point, i.e. depending on the load conditions or the coil coupling factor. In this case, the adaptive load matching is provided by additional DC-DC converter stages at the input and the output of the IPT system. Each DC-DC converter stage shares a common DC-link with the IPT system and hence, specifically in the case of hard-switched DC-DC converters, the design of the IPT system and the selection of the operating frequency have an impact on the total DC-DC converter

power losses. Therefore, in this chapter, a numerical optimization routine was presented, which allows to find the optimal overall TET system design for an extensive design parameter space.

The main results of this chapter are summarized as follows:

- ▶ The numerical optimization is based on the calculation of the weighted efficiency of the TET system, which allows to capture the system performance under real-life conditions more effectively, i.e. by accounting for the partial load operation, which is the main operating mode of the TET system.
- ▶ The optimization was performed for the SSU and the SSR TET system, considering all the power electronic stages in the energy transmission path from the external main battery supply to the implanted backup battery. The impact of the LVAD inverter operation is quantified by means of a simple switching loss estimation. The numerical calculations are finally verified at the example of the SSR TET system prototype.
- ▶ As expected, it was shown, that at maximum output power both the SSR and the SSU TET system reach the maximum weighted efficiency at a similar IPT system output voltage. However, the overall weighted efficiency of the SSU TET system is lower, which is due to the increased primary-side power losses at large coil separation distances.
- ▶ An optimal design is selected for both the SSR and the SSU TET system and a full set of design parameters is provided, which allows for the implementation of either TET system type.

The overall TET system optimization and the experimental verification of the TET system operation complete the TET system design. Final conclusions of this work and a critical review of several of the addressed topics are given in the following chapter.

10

Conclusion & Outlook

WIRELESS power transfer is a promising technology that allows to eliminate the percutaneous driveline of the LVAD and is the next logical step towards a fully implantable mechanical circulatory support system.

A fully implantable solution reduces the risk of severe infections and improves the quality of life for the patient. On the other hand, it must be emphasized that the complexity and the volume of the electrical system is increased substantially and most important, when implanted, is no longer accessible for maintenance. Therefore, achieving the required operational safety is the most significant challenge, which is also due to the high power transfer capability of the TET system application at hand, which is unique among today's medical implants. As a main objective, the aim of this work is to optimize the TET system for highest energy transfer efficiency and thereby reducing the heating of the human tissue, which is surrounding the energy receiving coil and the implanted controller. In addition, other safety aspects are addressed, such as the exposure of the human tissue to the electromagnetic fields. Finally, a demonstrator prototype of the TET implant is realized in order to verify the performance of the power electronic system and to show the achievable implant volume.

A summary and a short discussion of the important results is provided at the end of each chapter. The aim of the following sections is to highlight the main conclusions and to give a critical review of some selected topics. The thesis is then concluded with suggestions and proposals for further research.

10.1 Results & Conclusions

This work provides a framework that allows for the design and the efficiency optimization of TET systems for medical implants with increased power consumption, such as ventricular assist devices or total artificial hearts. The main topics include the fundamental theory, the power loss modeling and the performance evaluation of different IPT circuit topologies, as well as the optimization of the DC-DC converter stages and the implementation of the wireless communication channel, which are both needed for the control of the wireless energy transfer system. In addition, aspects of the operational safety, such as the heating of the skin and the EMF exposure of the human tissue are discussed and analyzed as well.

The comparative evaluation of several IPT resonant circuit topologies, i.e. in particular the secondary-side parallel and series compensated resonant circuit topologies has revealed, that for the power levels at hand, the primary-side and secondary-side series compensated IPT system outperforms the secondary-side parallel circuit. The focus of the further investigation was therefore on the operation of this particular IPT circuit topology, which was analyzed in more detail.

It was shown that for the power levels at hand, it is not sufficient to focus only on the differential-mode properties of the IPT converter stage. Due to the distinct electrical properties of the human tissue and its capacitive coupling to the implanted TET coil, common-mode currents may appear, which have an adverse effect on the EMF exposure of the tissue. Hence, a fully symmetrical topological design of the power electronic resonant converter stage is important, in order to reduce common-mode currents and voltages in the system.

Based on the numerical calculations, it was shown that for the maximum power transfer of 30 W, a secondary-side coil diameter of at least 60 mm should be considered in order to allow for a high overall IPT system efficiency and a moderate heating of the tissue. The optimal maximum IPT system output voltage is around 40 V and the optimum operating frequency is in a range of 600-800 kHz. An operation of the IPT system beyond this frequency range is not advantageous, since the power loss that is induced in the tissue is increasing significantly with higher operating frequencies.

The internal environment of the human body is highly complex, both thermally and electrically, and is difficult to fully capture the

properties with simplified numerical simulation models that allow for a moderate computation time. In addition, there is often a large parameter variation and parameter uncertainty associated with simulations that model the living tissue. Consequently, the thermal and the electromagnetic simulations are only giving approximate results and only an experimental study can confirm the thermal and electromagnetic safety of the TET system for the entire range of operating conditions. Specifically, the impact of the electromagnetic exposure is difficult to assess because of potentially adverse long-term health effects. Nevertheless, it was experimentally verified for the prototype IPT system, that at maximum power transmission, the heating of the living tissue can be maintained within safe limits. In addition, an effective electrical shielding concept was proposed, which allows to significantly reduce the high electrical near field component in the tissue, that is surrounding the energy receiver coil.

The efficiency optimal control of the wireless power transmission requires an adaptive impedance transformation on the primary and secondary side of the IPT system, which is achieved with the use of additional DC-DC converter stages. The comparison of different boost-type DC-DC converter concepts has revealed, that for the low voltage and power levels at hand, the conventional hard-switched DC-DC converter solution outperforms the more complex soft-switched converter solutions, such as the TCM and CL-TCM converter operation. The reason is twofold: on the one hand, the latest GaN semiconductor switches allow for very low switching power losses and on the other hand, the implementation of the soft-switching modulation scheme requires a specialized controller with higher hardware complexity, and hence, with a higher power consumption compared to the simple control of the hard-switched converter type.

For the control of the wireless power transmission and for the monitoring or the high-level control of the LVAD, it is recommended to use two separate wireless communication channels. A near field communication system with TET coil integrated loop antennas allows for the real-time feedback control of the wireless power transmission, and a second long range communication channel allows for a remote monitoring of physiological sensor data, even if the patient removes the external TET controller. Furthermore, the two communication channels allow for redundancy and hence, increase the operational safety of the TET system.

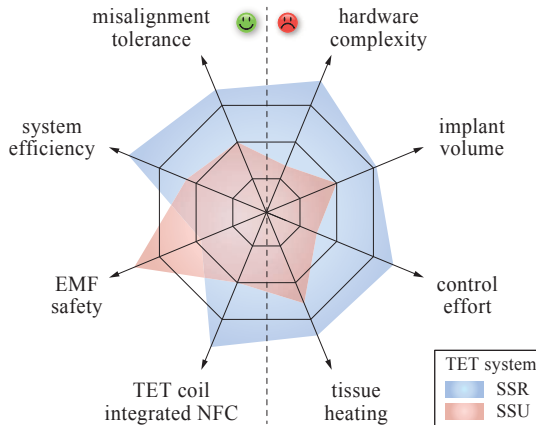


Fig. 10.1: Qualitative evaluation of the advantages and disadvantages of the SSR and SSU TET system with respect to critical performance characteristics.

Throughout this thesis, two distinct operating modes of the series-series compensated IPT system are considered, i.e. the operation at resonance (SSR) and the operation above resonance (SSU). The comparison of the operating characteristics of the SSR and the SSU TET system topology and the power loss distribution at different operating points have indicated several advantages and disadvantages of each system type. A qualitative evaluation and comparison of the two TET system types is visualized in **Fig. 10.1**, with respect to several performance characteristics that are addressed in this work and which must be considered for an effective TET system implementation. In the following, each of the considered properties is individually explained and the associated advantages and disadvantages are outlined for both TET system types.

- **Hardware Complexity:** The SSR TET system has a considerably higher hardware complexity compared to the SSU TET system. The operation of the SSR system requires a buck-boost DC-DC converter on both sides of the IPT system and for the controller implementation, the primary-side and secondary-side resonant tank currents must be measured in addition, in order to estimate the coil coupling. The high operating frequency and

the switching operation of the inverter and the rectifier circuit complicate the current measurement even more.

- ▶ **Implant Volume:** In case of the SSR TET system, each converter stage is cascaded and during the charging of the implanted backup battery, the total power for the LVAD and for the charging process has to be delivered by the internal DC-DC converter stage. Consequently, the inductor of the secondary-side buck-boost converter must be designed for a larger volume, compared to the inductor of the SSU TET system battery charging converter, in order to achieve the same energy efficiency. Furthermore, the buck-boost type DC-DC converter requires two additional semiconductor switches, and as mentioned above, the SSR TET system requires additional current measurement circuits, which further increase the implant volume.
- ▶ **Control Effort:** The SSR IPT system shows the behaviour of a current source and the primary-side and secondary-side DC-link voltages must be tightly controlled, in order to provide the impedance matching needed for an operation of the IPT resonant circuit at the optimum load resistance. The set-point of the DC-link voltages are dependent on the IPT system output power and on the coil coupling factor, which must be estimated based on the IPT coil currents. In contrast, the SSU IPT system behaves more like a voltage source and the primary-side and secondary-side DC-link voltages are adjusted, based on the output power only, which simplifies the controller implementation significantly.
- ▶ **Coil Misalignment Tolerance:** The SSR TET system is actively controlled such that the IPT resonant circuit is operated always with the optimal load resistance, and hence, the TET coil misalignment tolerance is very high. In contrast, in case of the SSU TET system, the input impedance of the IPT resonant circuit shows an increasingly inductive behaviour at large coil separation distances. As a result, the reactive power is increasing substantially on the primary side of the IPT system, which in turn limits the maximum power transfer capability at low coil coupling factors.
- ▶ **System Efficiency:** At the minimum coil separation distance, both TET system types achieve the same DC-DC efficiency. How-

ever, at larger coil separation distances, the SSU TET system efficiency decreases significantly, because of the increased power loss in the extracorporeal part of the TET system. In total, considering a weighted efficiency for multiple operating points, i.e. different coil separation distances and load conditions, the SSR TET system shows a superior performance.

- ▶ **Tissue Heating:** The heating of the subcutaneous tissue is mainly associated with the power loss that is generated in the implanted TET coil. At minimum coil separation distance, the TET coil power loss is similar for both TET system types. In case of the SSR TET system, the primary-side and secondary-side IPT DC-link voltages are decreased simultaneously at increasing coil separation distance. Accordingly, at constant power transmission, the power loss in the implanted TET coil is increasing as well and amplifies the heating of the subcutaneous tissue. In contrast, at constant power transmission, the SSU TET system experiences a constant secondary-side coil power loss, which is independent of the coil coupling factor.
- ▶ **EMF Safety:** It was previously shown, that due to the series-series compensated IPT resonant circuit, the electric field can attain very high values in close proximity to the implanted TET coil. Therefore, an electrical shielding of the IPT coils is advantageous for both TET system types. However, in case of the SSR TET system, the electric field and the induced currents are increasing in the tissue with increasing coil separation distance, which is due to the increased secondary-side coil current at low coil coupling factors, and hence, limits the power transfer capability at large coil misalignment.
- ▶ **TET Coil Integrated NFC:** It is mentioned in **Section 8.1.2** that for the SSU TET system prototype, a near field communication was realized, using TET coil integrated loop antennas. Experiments have shown that this type of communication is effective and is a promising solution for the implementation of the feedback control of the IPT system. However, experience with the hardware prototype has shown, that due to the inductive and capacitive coupling, it is very difficult to electrically separate the NFC antennas from the IPT coils, and hence, a high noise immunity of the NFC link is difficult to achieve. This is aggravated by

the fast switching transitions of the inverter output voltage and the synchronous rectifier input voltage. In this case, the NFC benefits from the SSR TET system operation, since at large coil separation distances, the IPT system DC-link voltages are lowered and accordingly, the amplitudes of the high-frequency harmonic content of the switching transitions are reduced. As a result, the NFC link can be operated more reliably and the communication range is extended.

An improved coil misalignment tolerance is important to maintain the required energy transfer capability despite of the movements of the patient, and therefore, to increase the usability of the TET system. Together with a high energy transfer efficiency, the coil misalignment tolerance is an important and decisive property, which allows to chose the most practical TET system design. Therefore, as a final conclusion, it can be stated, that despite the numerous disadvantages, the SSR TET system outperforms the SSU system in these two particular properties and hence, for the application at hand, allows for a more effective TET system implementation. However, a final assessment can be provided only by an extensive practical study.

10.2 Future Research Areas

The aim of this thesis is to show the energy transfer efficiency limits and the design limitations for IPT systems, which are intended for the use with implantable medical devices, that have an increased power consumption. The focus of the research is on the series-series compensated IPT circuit topology, using two loosely coupled energy transfer coils. But there is room for further improvement and new questions have emerged in the course of this work and are still unresolved. Accordingly, the following topics are proposed for future work:

- It was experimentally verified, that a power of up to 30 W can be transmitted across the skin, without excessive heating of the tissue. The power losses that are temporary generated within the TET implant during the charging process of the backup battery were not considered in the experiments. Therefore, a final thermal safety assessment of the overall TET system in an in-vivo study still needs to be made. The investigation of the feasible power loss density of the implant is of particular interest, as it poses

limitations on the feasible battery charging current and on the size of the internal power electronic circuit components, such as the inductors and the filter capacitors.

- ▶ The series-series compensated IPT system allows for a highly efficient operation at high power transfer levels, which comes at the expense of large coil terminal voltages. The EMF simulations have shown, that without additional shielding, the peak electric field strength in the tissue surrounding the implanted TET coil may reach critical levels which could exceed the safety regulations. An experimental verification is yet required and it is not clear if the high electric field strength has an adverse physiological impact, and hence, requires further investigation.
- ▶ The simulations of the EMF exposure have shown that the maximum permissible current density in the muscle tissue below the implanted IPT coil of the TET system prototype is exceeding the basic restrictions of the ICNIRP guidelines from 1998. Therefore, further research on an effective and energy-efficient shielding of the magnetic field towards the inside of the body is needed.
- ▶ In recent years, a variation of the classical IPT system design has emerged, which is commonly known as wireless energy transfer via *strongly coupled magnetic resonances*. These systems rely usually on a four-coil configuration and are operated at high frequencies in the lower megahertz range. The additional degrees of freedom allow for a further optimization of the IPT system and with the very high quality factors of the resonator coils, an efficient energy transmission is possible over fairly large distances of a multiple of the resonator coil diameter [170,171]. An alternative three-coil energy transfer system, which is explained in [172,173], employs an additional relay resonator coil on the primary side of the IPT system, which allows to shift the current stress from the primary-side inverter and driving coil to the relay coil which has a high quality factor. A direct comparison of the technology with the IPT systems presented in this work, specifically with the SSR IPT system, is of particular interest. The comparison should include application specific aspects, such as the operational safety in terms of the EMF exposure and the heating of the tissue. Specifically for the four-coil IPT system, it is questionable if the restrictions on

the internal electric field and SAR can be met at the increased operating frequencies, and further investigations are required.

- ▶ The efficiency comparison of the hard-switched DC-DC boost converter with the more advanced soft-switched solutions has shown that specifically for low voltage/low power applications, and with the technological improvements of wide-bandgap semiconductor switches, the constant power loss caused by the control circuit is an important limiting factor for the converter efficiency. Hence, further efforts are needed for the design of application-specific control circuits, which are optimized for an ultra-low power consumption.

The improvement of TET system technology will finally contribute to an increased quality of life for patients who rely on mechanical circulatory support systems. It can be hoped that despite the great hurdles of medical approval, further research and developments allow for an integration of the TET system technology into existing MCS systems in the very near future.

Appendices

A

IPT Efficiency Calculation

THIS chapter provides a summary of analytical equations for the calculation of the power transfer efficiency for different IPT resonant circuit topologies, such as the series-series, the series-parallel and the series-series-parallel compensated IPT topology. However, the equations for the energy transfer efficiencies apply also for the primary-side parallel compensated IPT circuit topologies. The equations are derived similar to the calculations given in [48, 51, 174] and are also partly given therein. Note that the efficiency calculation includes the primary-side and secondary-side IPT coil power losses only. The power loss in the compensation capacitors are typically very small and are therefore neglected. As outlined in [43], even if the IPT resonant circuit is supplied by means of a full-bridge class-D inverter with 50% duty-cycle, the high-frequency harmonic content of the primary-side coil current is attenuated substantially, which is due to the band-pass filter characteristic of the IPT resonant circuit. Accordingly, purely sinusoidal primary-side and secondary-side coil currents i_1 and i_2 are assumed for the calculations. The mathematical definition of several important parameters that are used for the efficiency calculation are given in **Tab. A.1**.

Parameter	Equation	Parameter	Equation
Angular frequency	$\omega_0 = 2\pi f_0$	Load factor	$\gamma = R_{L1}/\omega_0 L_2$
Coupling factor	$k = M/\sqrt{L_1 L_2}$	Transmitter quality factor	$Q_1 = \omega_0 L_1/R_{L1}$
Transformer ratio	$v = \frac{1}{k}\sqrt{L_2/L_1}$	Receiver quality factor	$Q_2 = \omega_0 L_2/R_{L2}$

Tab. A.1: Mathematical definition of parameters used for the IPT resonant circuit efficiency calculation.

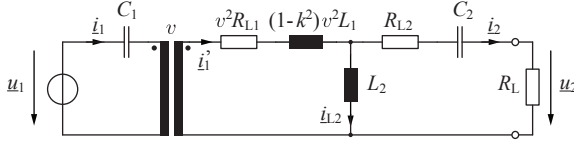


Fig. A.1: Equivalent circuit of the series-series compensated IPT resonant circuit topology.

A.1 Series-Series Compensation

For the series-series compensated IPT circuit topology, it is distinguished between the operation at the natural resonance frequency, denoted as SSR-operation, where the resonant capacitors are designed to fully compensate for the reactance of the primary-side and secondary-side IPT coils, and the operation above resonance, denoted as SSU-operation, where only a part of the IPT coil reactance is cancelled.

A detailed description on the design and the operation of the two compensation methods is provided in **Chapter 2**.

A.1.1 Operation at Resonance

The derivation of the equation for the optimum load factor, i.e. at which the energy transfer efficiency is maximized, is provided in [174] and is summarized in the following. The equations can be derived using the equivalent circuit shown in **Fig. A.1** and using the parameter definitions shown in **Tab. A.1**.

The compensation capacitances are calculated according to

$$C_1 = \frac{1}{\omega_0^2 L_1}, \quad C_2 = \frac{1}{\omega_0^2 L_2}. \quad (\text{A.1})$$

The primary-side and secondary-side loss factors, λ_1 and λ_2 , are defined as the ratio of the primary-side and secondary-side coil power loss $P_{v,Li}$, $i \in [1, 2]$, respectively and the output power P_2 delivered to the load resistor, and are given by

$$\lambda_1 = \frac{P_{v,L1}}{P_2} = \frac{1}{\gamma Q_1 k^2} \left(\gamma + \frac{1}{Q_2} \right)^2 \quad (\text{A.2})$$

$$\lambda_2 = \frac{P_{v,L2}}{P_2} = \frac{1}{\gamma Q_2}. \quad (\text{A.3})$$

The primary-side efficiency can be calculated with

$$\eta_{\text{SSR,prim}} = \frac{1 + \lambda_2}{1 + \lambda_1 + \lambda_2} = \frac{k^2 Q_1 Q_2}{1 + \gamma Q_2 + k^2 Q_1 Q_2}, \quad (\text{A.4})$$

and the secondary-side efficiency results as

$$\eta_{\text{SSR,sec}} = \frac{1}{1 + \lambda_2} = \frac{\gamma Q_2}{1 + \gamma Q_2}. \quad (\text{A.5})$$

The total energy transfer efficiency

$$\eta_{\text{SSR}}(\omega_0, k) = \frac{1}{1 + \lambda_1 + \lambda_2} = \frac{\gamma k^2 Q_1 Q_2^2}{(1 + \gamma Q_2)(1 + \gamma Q_2 + k^2 Q_1 Q_2)} \quad (\text{A.6})$$

is maximized for the optimal load factor given by

$$\gamma_{\text{opt,SSR}}(\omega_0, k) = \frac{R_{\text{L,opt,SSR}}}{\omega_0 L_2} = \frac{1}{Q_2} \sqrt{1 + k^2 Q_1 Q_2}. \quad (\text{A.7})$$

For equal and large coil quality factors, (A.7) is simplified to

$$\gamma_{\text{opt,SSR}}(\omega_0, k)|_{Q_1=Q_2>100} \approx k. \quad (\text{A.8})$$

A.1.2 Operation above Resonance

The equation for the energy transfer efficiency and the optimum load factor provided in [46] for the operation of the series-series compensated IPT circuit topology above resonance are calculated similarly as above, using the same equivalent circuit (cf. **Fig. A.1**). The derivation of the design parameter k_0 , which is used to calculate the resonance capacitances, is explained in detail in **Section 2.1.4**.

The compensation capacitances are calculated according to

$$C_1 = \frac{1}{\omega_0^2 L_1 (1 - k_0)}, \quad C_2 = \frac{1}{\omega_0^2 L_2 (1 - k_0)}. \quad (\text{A.9})$$

The primary-side and secondary-side loss factors, λ_1 and λ_2 , are given by

$$\lambda_1 = \frac{P_{\text{v,L1}}}{P_2} = \frac{1}{\gamma Q_1 k^2} \left[\left(\gamma + \frac{1}{Q_2} \right)^2 + k_0^2 \right] \quad (\text{A.10})$$

$$\lambda_2 = \frac{P_{\text{v,L2}}}{P_2} = \frac{1}{\gamma Q_2}. \quad (\text{A.11})$$

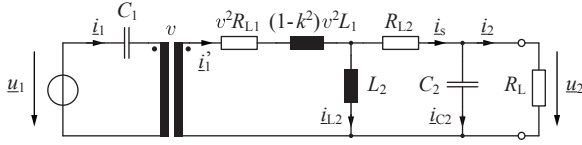


Fig. A.2: Equivalent circuit of the series-parallel compensated IPT resonant circuit topology.

The primary-side efficiency can be calculated with

$$\eta_{SSU, \text{prim}} = \frac{k^2 Q_1 Q_2 (1 + \gamma Q_2)}{1 + Q_2 (2\gamma + k^2 Q_1 + (\gamma^2 + k_0^2 + \gamma k^2 Q_1) Q_2)}, \quad (\text{A.12})$$

and the secondary-side efficiency results as

$$\eta_{SSU, \text{sec}} = \frac{\gamma Q_2}{1 + \gamma Q_2}. \quad (\text{A.13})$$

The total energy transfer efficiency

$$\eta_{SSU}(\omega_0, k) = \frac{\gamma k^2 Q_1 Q_2^2}{1 + Q_2 (2\gamma + k^2 Q_1 + (\gamma^2 + k_0^2 + \gamma k^2 Q_1) Q_2)} \quad (\text{A.14})$$

is maximized for the optimal load factor given by

$$\gamma_{\text{opt}, SSU}(\omega_0, k) = \frac{R_{L, \text{opt}, SSU}}{\omega_0 L_2} = \frac{1}{Q_2} \sqrt{1 + k^2 Q_1 Q_2 + (k_0 Q_2)^2}. \quad (\text{A.15})$$

For equal and large coil quality factors, (A.15) is simplified to

$$\gamma_{\text{opt}, SSU}(\omega_0, k)|_{Q_1=Q_2>100} \approx \sqrt{k^2 + k_0^2}. \quad (\text{A.16})$$

A.2 Series-Parallel Compensation

The equations for the compensation capacitances and the optimum load factor given in [48] can be derived using the equivalent circuit shown in **Fig. A.2**. The choice of the design parameter k_0 in (A.17) is explained in detail in **Section 2.1.1**.

The compensation capacitances are calculated according to

$$C_1 = \frac{1}{\omega_0^2 L_1 (1 - k_0^2)}, \quad C_2 = \frac{1}{\omega_0^2 L_2}. \quad (\text{A.17})$$

The primary-side and secondary-side loss factors, λ_1 and λ_2 , are given by

$$\lambda_1 = \frac{P_{v,L1}}{P_2} = \frac{1}{\gamma Q_1 k^2} \left[\left(\frac{1}{Q_2} \right)^2 + \left(1 + \frac{\gamma}{Q_2} \right)^2 \right] \quad (\text{A.18})$$

$$\lambda_2 = \frac{P_{v,L2}}{P_2} = \frac{1}{\gamma Q_2} (1 + \gamma^2) . \quad (\text{A.19})$$

The primary-side efficiency can be calculated with

$$\eta_{\text{SP,prim}} = \frac{k^2 Q_1 Q_2 (1 + \gamma(\gamma + Q_2))}{1 + k^2 Q_1 Q_2 + Q_2^2 + \gamma^2 (1 + k^2 Q_1 Q_2) + \gamma Q_2 (2 + k^2 Q_1 Q_2)} , \quad (\text{A.20})$$

and the secondary-side efficiency results as

$$\eta_{\text{SP,sec}} = \frac{\gamma Q_2}{1 + \gamma^2 + \gamma Q_2} . \quad (\text{A.21})$$

The total energy transfer efficiency

$$\eta_{\text{SP}}(\omega_0, k) = \frac{\gamma k^2 Q_1 Q_2^2}{1 + k^2 Q_1 Q_2 + Q_2^2 + \gamma^2 (1 + k^2 Q_1 Q_2) + \gamma Q_2 (2 + k^2 Q_1 Q_2)} \quad (\text{A.22})$$

is maximized for the optimal load factor given by

$$\gamma_{\text{opt,SP}}(\omega_0, k) = \frac{R_{L,\text{opt,SP}}}{\omega_0 L_2} = \sqrt{\frac{1 + k^2 Q_1 Q_2 + Q_2^2}{1 + k^2 Q_1 Q_2}} . \quad (\text{A.23})$$

For equal and large coil quality factors, (A.23) is simplified to

$$\gamma_{\text{opt,SP}}(\omega_0, k)|_{Q_1=Q_2>100} \approx \frac{1}{k} \sqrt{1 + k^2} . \quad (\text{A.24})$$

A.3 Series-Series-Parallel Compensation

The equations for the compensation capacitances and the optimum load factor are given in [47] and are derived using the equivalent circuit shown in **Fig. A.3**. The design parameter k_0 in (A.25) is chosen according to **Tab. 2.1**.

The compensation capacitances are calculated according to

$$C_1 = \frac{1}{\omega_0^2 L_1 (1 - k_0)}, \quad C_2 = \frac{1}{\omega_0^2 L_2 (1 - k_0)}, \quad C_3 = \frac{1}{\omega_0^2 L_2 k_0} . \quad (\text{A.25})$$

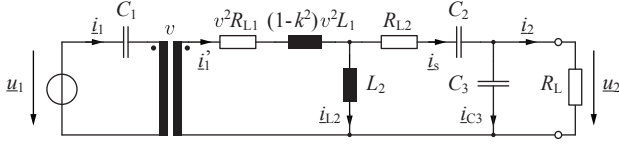


Fig. A.3: Equivalent circuit of the series-series-parallel compensated IPT resonant circuit topology.

The primary-side and secondary-side loss factors, λ_1 and λ_2 , are given by

$$\lambda_1 = \frac{P_{v,L1}}{P_2} = \frac{1}{\gamma k^2 Q_1} \left[\left(k_0 + \frac{\gamma}{k_0 Q_2} \right)^2 + \frac{1}{Q_2^2} \right] \quad (\text{A.26})$$

$$\lambda_2 = \frac{P_{v,L2}}{P_2} = \frac{1}{\gamma Q_2} \left(1 + \frac{\gamma^2}{k_0^2} \right). \quad (\text{A.27})$$

The primary-side efficiency can be calculated with

$$\eta_{\text{SSP,prim}} = \frac{k^2 Q_1 Q_2 (\gamma^2 + k_0^2 + \gamma k_0^2 Q_2)}{\gamma^2 + k_0^2 + (2\gamma k_0^2 + k^2 (\gamma^2 + k_0^2) Q_1) Q_2 + k_0^2 (k_0^2 + \gamma k^2 Q_1) Q_2^2}, \quad (\text{A.28})$$

and the secondary-side efficiency results as

$$\eta_{\text{SSP,sec}} = \frac{\gamma k_0^2 Q_2}{\gamma^2 + k_0^2 + \gamma k_0^2 Q_2}. \quad (\text{A.29})$$

The total energy transfer efficiency

$$\eta_{\text{SSP}}(\omega_0, k) = \frac{\gamma k^2 k_0^2 Q_1 Q_2^2}{\gamma^2 + k_0^2 + (2\gamma k_0^2 + k^2 (\gamma^2 + k_0^2) Q_1) Q_2 + k_0^2 (k_0^2 + \gamma k^2 Q_1) Q_2^2} \quad (\text{A.30})$$

is maximized for the optimal load factor given by

$$\gamma_{\text{opt,SSP}}(\omega_0, k) = \frac{R_{L,\text{opt,SSP}}}{\omega_0 L_2} = k_0 \sqrt{\frac{1 + k^2 Q_1 Q_2 + (k_0 Q_2)^2}{1 + k^2 Q_1 Q_2}}. \quad (\text{A.31})$$

For equal and large coil quality factors, (A.31) is simplified to

$$\gamma_{\text{opt,SSP}}(\omega_0, k)|_{Q_1=Q_2>100} \approx k_0 \sqrt{\frac{k^2 + k_0^2}{k^2}}. \quad (\text{A.32})$$

B

CL-TCM Boost Converter with Reduced Hardware Complexity

IN **Chapter 6**, a sophisticated ZVS modulation scheme referred to as Clamp-Switch TCM (CL-TCM) operation [123, 127] was explained, where the clamp-switch in parallel to the boost inductor is realized with an anti-series connection of two active switches. The modulation scheme allows for ZVS operation for all switches, independent of the output power level and without restrictions on the input-to-output voltage conversion ratio, given the natural boundaries for boost operation.

This chapter essentially presents the results that are published in [124]. Therein, a simplified ZVS modulation scheme [127] is used for the CL-TCM converter which allows to reduce the hardware complexity and which increases the reliability of the converter by replacing the bidirectional clamp-switch used in [123, 126, 127] with an anti-series connection of an active switch and a single diode, as shown in **Fig. B.1(a)**.

The topology was proposed in [175] in a similar form as hard-switched boost converter, which is referred to as tri-state boost converter and which allows to improve the dynamic performance of the converter by eliminating the right-half-plane zero in the small signal control-to-output transfer function. In another more recent application presented in [176], a hard-switched tri-state boost converter was used on the receiver side of a wireless power transfer system, which allows to implement an adaptive resonance frequency tuning and load matching.

In the following, the converter shown in **Fig. B.1(a)** is referred to as 3-switch CL-TCM boost converter and allows for ZVS operation at unidirectional power flow. Furthermore, a unidirectional 2-switch CL-

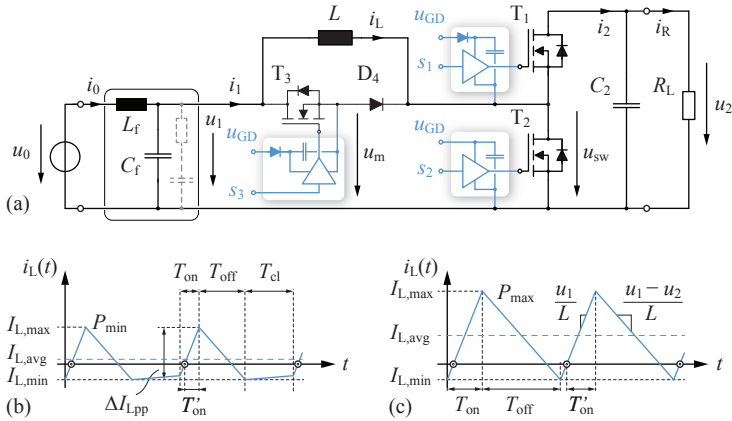


Fig. B.1: (a) Proposed 3-switch Clamp-Switch TCM (CL-TCM) boost converter topology with input filter stage. (b)-(c) typical CL-TCM converter inductor current waveforms at minimum and maximum output power.

TCM converter operation is proposed and explained in detail, which allows for ZVS of all switches as well, but which reduces the complexity of the converter hardware and the modulation scheme to a minimum.

The topological simplification of the converter and the ZVS modulation schemes come at the expense of restrictions on the input-to-output voltage conversion ratio and output power range, as will be explained in detail in **Section B.1**. The design of the boost inductance and the calculation of the timing intervals T_{on} , T_{off} and T_{cl} (cf. **Figs. B.1(b)** and **(c)**) are presented in **Section B.2**. In addition, two converter operating modes, either offering a variable or a constant switching frequency operation are analyzed and compared. In **Section B.3**, the controller implementation is explained for both the 3-switch and the 2-switch CL-TCM converter, and in **Section B.4**, the experimental verification of the ZVS operation and the proposed operating modes is presented. In addition, a DC-DC efficiency comparison for the different CL-TCM converter types is given in the same section. Finally, **Section B.5** addresses the input and output filter design of the converter.

B.1 Modulation Scheme

Typical inductor current waveforms for the considered CL-TCM converter operation at minimum and maximum output power are illustrated in **Figs. B.1(b)** and **(c)**, respectively.

As explained in **Section 6.1**, at maximum output power, the CL-TCM operation corresponds to the TCM operation, i.e. the clamp switch T_3 is unused, wherever at light load conditions, the clamp-switch is used to introduce a free-wheeling state for the inductor current after the turn-off of switch T_1 and hence allows to stretch the switching period as shown in **Fig. B.1(b)**. Consequently, the switching frequency variation can be controlled depending on the output power and depending on the voltage conversion ratio. The maximum switching frequency f_{\max} occurs always at the maximum voltage conversion ratio, whereas the maximum feasible operating frequency is mainly limited by the time delays in the measurement and control circuit, because the switching time intervals need to be calculated and synchronized to the zero-crossings of the inductor current, which will be explained in detail in **Section B.3**.

The ZVS modulation schemes, explained in the following, allow to reduce the number of active switches in the circuit topology. However, as already mentioned, the reduced hardware complexity comes at the expense of a limitation of the input-to-output voltage conversion ratio in order to achieve ZVS for all the switches, and when neglecting the forward voltage drop of the diodes, can be expressed by

$$u_2 \geq \frac{C_{T3} + C_{D4}}{C_{D4}} u_1, \quad (\text{B.1})$$

which reduces to $u_2 \geq 2u_1$, if $C_{T3} = C_{D4}$ applies. C_{T3} and C_{D4} denote the parasitic output capacitance of switch T_3 and the junction capacitance of diode D_4 , respectively. Nevertheless, a unidirectional operation and voltage step-up ratios according to (B.1) are common in numerous applications, such as in module-integrated converters for photovoltaic systems [177–179], fuel-cell based backup energy systems and uninterruptible power supplies [180, 181] as well as in automotive applications [182, 183].

The main focus of this chapter is on the operation of the 3-switch CL-TCM converter topology depicted in **Fig. B.1(a)**. However, the ZVS modulation scheme can be extended as well to a 2-switch CL-TCM operation, where the high-side switch T_1 is replaced by a diode.

Appendix B. CL-TCM Boost Converter with Reduced Hardware Complexity

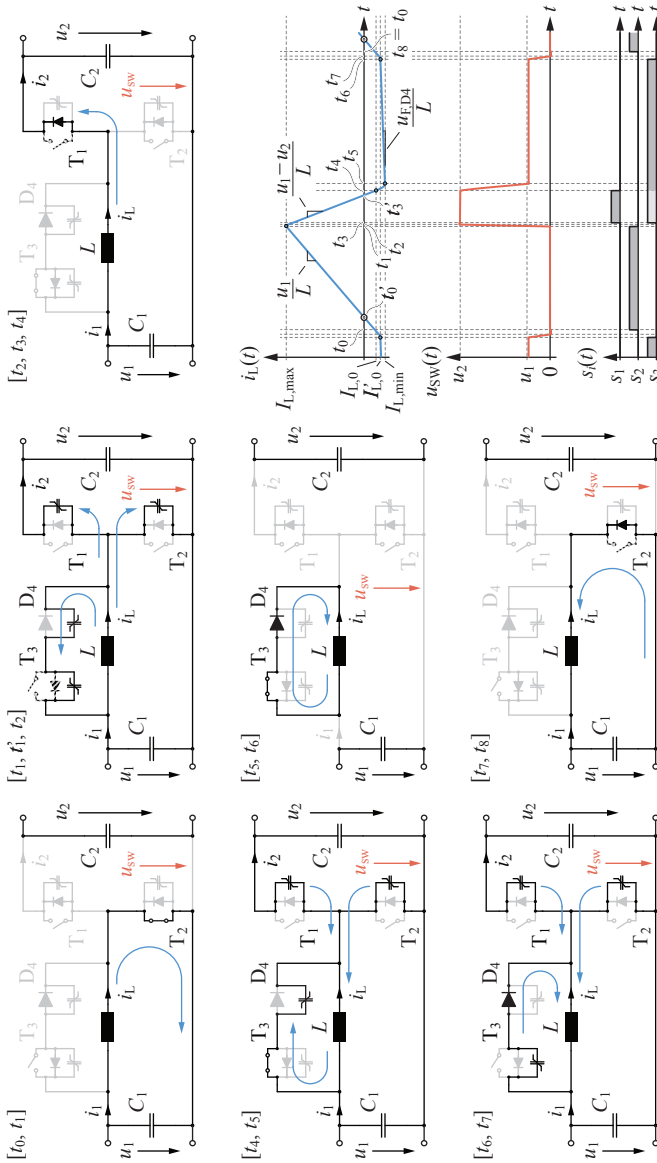


Fig. B.2: Operating states of the 3-switch CL-TCM modulation scheme for a full switching cycle $[t_0, t_8]$ and typical waveforms of the inductor current i_L and the switch-node voltage u_{sw} , belonging to the switch control signals s_i .

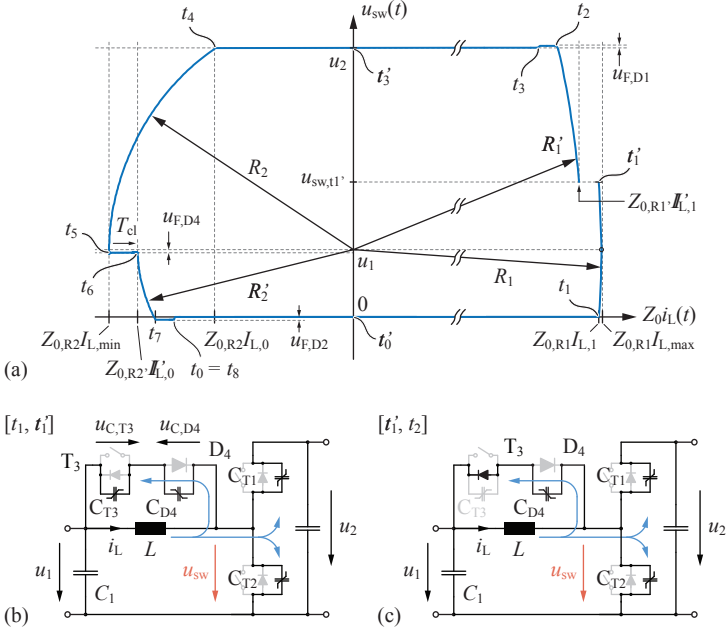


Fig. B.3: (a) State-plane diagram, showing the scaled inductor current $Z_0 i_L(t)$ with respect to the switch-node voltage $u_{sw}(t)$ for the 3-switch CL-TCM converter operation. (b)-(c) Operating states of the converter during the time interval $[t_1, t_1']$ and $[t_1', t_2]$, respectively.

This type of operation and the ZVS conditions are explained later in this section.

Note that both converter topologies allow to use a boot-strap gate drive power supply for the clamp-switch T_3 (cf. **Fig. B.1(a)**), which simplifies the hardware complexity significantly.

B.1.1 3-Switch CL-TCM Operation

First, the detailed principle of operation and ZVS modulation scheme is explained for the 3-switch CL-TCM converter, based on the operating states and the corresponding inductor current i_L and switch-node voltage u_{sw} waveforms shown in **Fig. B.2**. A useful representation for the analysis of the ZVS operation of the converter is provided by the state-plane diagram shown in **Fig. B.3(a)**, which displays the switch-node

voltage u_{sw} with respect to the inductor current i_L that is scaled by the characteristic impedance of the resonant circuit formed by the inductor and the parasitic output capacitances of the switches and diodes.

Despite of the non-linearity of the parasitic capacitance of the diodes and switches, the analysis that is provided in the following sections considers constant capacitances only, in order to simplify the formalism and to give a meaningful insight into the operation of the converter. The analysis however could be extended to non-linear capacitances as well, as it is shown in **Section 6.2.1**. Further it is assumed, that the steady-state input and output voltage u_1 and u_2 are constant throughout a switching cycle, which is ensured by the input and output filter stage. The diode forward voltage drops are denoted with $u_{F,Dx}$ and $x \in [1, 4]$ and the turn-off process of each switch is considered to be free of power losses.

Starting with the first time interval $[t_0, t_1]$, switch T_2 is turned on and the body diode of switch T_3 is blocking the input voltage and prevents a short circuit of the input capacitor C_1 . Hence, the inductor current rises linearly and its zero crossing is detected at t'_0 in switch T_2 and is used to synchronize the switching times and the gate drive control signals s_i to the actual inductor current waveform as described in **Section B.3**. Accordingly, the remaining inductor current rise time interval T'_{on} (cf. **Fig. B.1(a)**) and the time interval T_{off} are calculated such that the required average inductor current and the current $I_{L,0}$ needed at t_4 to allow for ZVS of the switches in the following time intervals, are achieved.

When the inductor current reaches the value $I_{L,1}$ at time t_1 (cf. **Fig. B.3(a)**), switch T_2 is turned off and the inductor current starts to charge the parasitic output capacitance of switch T_2 , while discharging the output capacitance of T_1 . Initially, the voltage across the parasitic capacitance C_{T3} is $(u_1 - u_{F,D4})$ and the voltage across diode D_4 is $-u_{F,D4}$. Hence, the parasitic output capacitance of switch T_3 is discharged and the junction capacitance of D_4 is charged, as shown in **Fig. B.3(b)**. Due to the series connection of C_{T3} and C_{D4} , the total capacitance that needs to be charged by the inductor current is $C_{\text{tot,R1}} = C_{T1} + C_{T2} + C_{T3}C_{D4}/(C_{T3} + C_{D4})$. The resonant transition is described in the state-plane diagram with a circle with the center located at $u_{\text{sw}} = u_1$ and $i_L = 0$, and with a radius

$$R_1 = \sqrt{u_1^2 + (Z_{0,R1}I_{L,1})^2}, \text{ and } Z_{0,R1} = \sqrt{\frac{L}{C_{\text{tot,R1}}}}. \quad (\text{B.2})$$

The maximum inductor $I_{L,\max} = R_1/Z_{0,R1}$ is reached as soon as the switch-node voltage u_{sw} is equal to the input voltage u_1 . At time t'_1 , the switch-node voltage at which the voltage across T_3 approaches zero volts and its body diode D_3 starts to conduct, can be calculated according to

$$u_{\text{sw},t'1} = \frac{C_{T3} + C_{D4}}{C_{D4}} (u_1 + u_{F,D3} - u_{F,D4}) \approx \frac{C_{T3} + C_{D4}}{C_{D4}} u_1, \quad (\text{B.3})$$

if $u_{F,D3} \approx u_{F,D4}$ applies. Note that if $C_{D4} \gg C_{T3}$, the body diode of T_3 will start to conduct as soon as u_{sw} approaches u_1 , where the inductor current reaches its maximum current $I_{L,\max}$. In contrast, if $C_{T3} > C_{D4}$, the capacitance C_{T3} can be discharged to zero only if $(u_2 + u_{F,D1}) \geq u_{\text{sw},t'1}$, which is equal to the condition (B.1), if the forward voltage drop of the diodes are neglected. Therefore, if condition (B.1) is not met, soft-switching of switch T_3 cannot be achieved in the subsequent operating states.

As soon as the body diode of T_3 starts to conduct, the total capacitance of the resonant circuit changes to $C_{\text{tot},R1'} = C_{T1} + C_{T2} + C_{D4}$, as shown in **Fig. B.3(c)**. Hence, the characteristic impedance of the resonant circuit decreases, which appears as a discontinuity in the state-space trajectory (cf. **Fig. B.3(a)**). The inductor current at time t'_1 is given by

$$I'_{L,1} = \frac{1}{Z_{0,R1}} \sqrt{R_1^2 - (u_{\text{sw},t'1} - u_1)^2}, \quad (\text{B.4})$$

and hence, using $Z_{0,R1'} = \sqrt{L/C_{\text{tot},R1'}}$, the radius R'_1 can be calculated according to

$$R'_1 = \sqrt{(u_{\text{sw},t'1} - u_1)^2 + (Z_{0,R1'} I'_{L,1})^2}. \quad (\text{B.5})$$

If it is assumed that $u_{F,D3} \approx u_{F,D4}$ and $C_{T3} = C_{D4}$, the switch-node voltage at time t'_1 is $u_{\text{sw},t'1} = 2u_1$ and the inductor current is $I_{L,1} = I'_{L,1}$, and hence, equation (B.5) is reduced to

$$R'_1 \approx \sqrt{u_1^2 + (Z_{0,R1'} I_{L,1})^2}. \quad (\text{B.6})$$

In this case, if the initial inductor current $I_{L,1}$ is large enough, C_{D4} is charged up to the voltage $(u_2 - u_1)$, assuming that the diode D_4 and the body diode of switch T_1 have the same forward voltage drop. At time t_2 , the body diode of switch T_1 starts to conduct and clamps the voltage across T_1 to the diode forward voltage drop $u_{F,D1}$. If the diode

voltage drop $u_{F,D1}$ is neglected, the condition for ZVS operation of switch T_1 follows from $R'_1 \geq (u_2 - u_1)$, and using (B.6), the condition can be expressed with

$$I_{L,1} \geq \frac{1}{Z_{0,R1'}} \sqrt{u_2(u_2 - 2u_1)}, \quad \text{for } (u_2 > 2u_1). \quad (\text{B.7})$$

If conditions (B.1) and (B.7) are met, switch T_1 can be turned on at t_3 at nearly zero voltage and since the parasitic output capacitance of T_3 was discharged completely during $[t_1, t'_1]$, switch T_3 can be turned on at any time between t_3 and t_4 without causing power losses. The critical operating point, where ZVS of switch T_1 could be lost, is at minimum output power and maximum output voltage.

During time interval $[t_3, t_4]$ switch T_1 is in ON-state and the inductor current is supplied to the output and is decreasing linearly and reverses its flow direction at time t'_3 .

At t_4 , switch T_1 is turned off and the negative inductor current $I_{L,0}$ starts to discharge the parasitic capacitances of switch T_2 and diode D_4 , while charging the output capacitance of switch T_1 . Hence, during $[t_4, t_5]$, the total equivalent resonant capacitance is $C_{\text{tot},R2} = C_{\text{tot},R1'} = C_{T1} + C_{T2} + C_{D4}$ and the resonant transition is described in **Fig. B.3(a)** with a circle with the radius

$$R_2 = \sqrt{(u_2 - u_1)^2 + (Z_{0,R1'} I_{L,0})^2}. \quad (\text{B.8})$$

As soon as the voltage u_{sw} reaches a value of $(u_1 - u_{F,D4})$ at t_5 , diode D_4 starts to conduct and the inductor clamping time interval $[t_5, t_6]$ is initiated. During this time interval, the inductor current is free-wheeling in the clamp-switch and no energy is delivered from the input to the output of the converter. Therefore, the clamping time interval can be used as a degree of freedom to control the switching period and the amount of power that is delivered to the load.

Due to the forward voltage drop of diode D_4 , and if the ohmic losses in the inductor current loop are neglected, the inductor current is increasing with a slope of $di_L/dt = u_{F,D4}/L$. This must be taken into account, specifically if the clamping time interval T_{cl} is large, because the inductor current amplitude at t_6 , denoted with $I'_{L,0}$, could increase (decreasing absolute value) to a value where ZVS of switch T_2 could not be achieved anymore at time t_8 . The negative inductor current $I'_{L,0}$ at the turn-off of switch T_3 at t_6 can be calculated with good

approximation according to

$$I'_{L,0} \approx I_{L,\min} + \frac{u_{F,D4}}{L} T_{cl} \quad \text{and} \quad I_{L,\min} = -\frac{R_2}{Z_{0,R1'}}. \quad (\text{B.9})$$

During $[t_6, t_7]$, the inductor current continues discharging the parasitic output capacitance of switch T_2 and charges the parasitic output capacitance of T_1 . The output capacitance of switch T_3 is charged as well by a part of the inductor current flowing through diode D_4 . Hence, the total equivalent resonant capacitance changes to $C_{\text{tot},R2'} = C_{T1} + C_{T2} + C_{T3}$ and the radius R'_2 in **Fig. B.3(a)** is given by

$$R'_2 = \sqrt{u_{F,D4}^2 + (Z_{0,R2'} I'_{L,0})^2}, \quad \text{and} \quad Z_{0,R2'} = \sqrt{\frac{L}{C_{\text{tot},R2'}}}. \quad (\text{B.10})$$

As soon as the switch-node voltage u_{sw} reaches a voltage of $-u_{F,D2}$ at t_7 , the parasitic output capacitance of switch T_3 is charged up to the input voltage u_1 and the diode D_4 stops conducting. At the same time, the body diode of switch T_2 starts to conduct and the inductor current starts to rise linearly again, as shown in **Fig. B.2** for the time interval $[t_7, t_8]$. The switch T_2 can then be turned on at nearly zero voltage as long as the inductor current is negative. As soon as the inductor current gets positive, the body diode of T_2 would prevent a current flow in the reverse direction and the parasitic output capacitance of T_2 would be charged again.

The condition for ZVS operation of switch T_2 follows directly from condition $R'_2 \geq u_1$ and is given by

$$I'_{L,0} \leq -\frac{1}{Z_{0,R2'}} \sqrt{u_1^2 - u_{F,D4}^2} \approx -\frac{u_1}{Z_{0,R2'}}, \quad (\text{B.11})$$

which is mainly dependent on the inductor current $I_{L,0}$ and the duration of the clamping time interval T_{cl} , assuming constant input and output voltages.

Note that if $u_2 \geq 2u_1$ applies, and considering traditional TCM operation only, i.e. $T_{cl} = 0$, a zero voltage transition of the switch-node voltage u_{sw} in the time interval $[t'_3, t_7]$ can always be achieved, even when starting with an inductor current $I_{L,0} = 0$. This allows to reduce the converter hardware complexity further, i.e. by replacing the switch T_1 by a single diode D_1 as shown in **Fig. B.4(a)**. This modification allows to increase the converter reliability as the number of active components in the circuit is reduced. However, the conduction

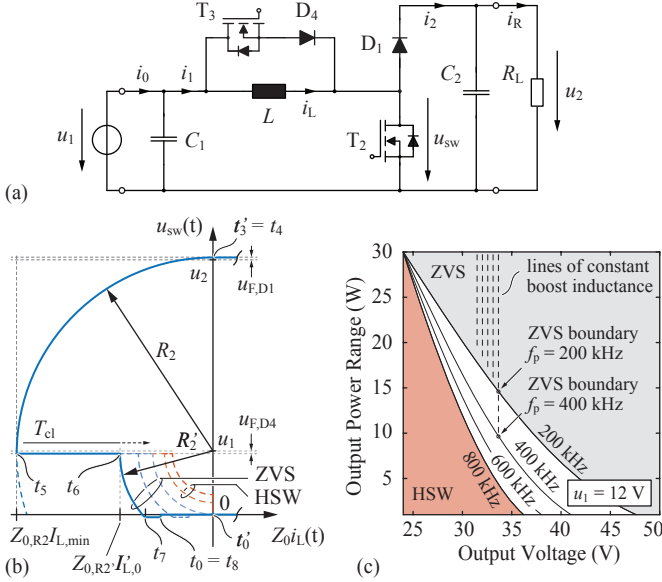


Fig. B.4: (a) 2-switch CL-TCM converter topology. (b) Associated state-plane diagram illustrating the resonant transition during the time intervals with negative inductor current. (c) Operating range for Zero Voltage Switching (ZVS) and for hard-switching (HSW) operation for the 2-switch CL-TCM converter with respect to output power, designed for different output voltages and switching frequencies f_p in a range of 200 kHz to 800 kHz.

losses are increased as well, and hence, the energy efficiency of the converter is reduced.

The operation principle, the limitations and the conditions for ZVS operation of the 2-switch CL-TCM converter are explained in the following, based on the state-plane diagram shown in **Fig. B.4(b)**, which depicts the resonant current and voltage transition during the time intervals with negative inductor current.

B.1.2 2-Switch CL-TCM Operation

The operating states during $[t_0, t_2]$ are the same as for the 3-switch CL-TCM converter. If condition (B.7) is met, diode D_1 starts to conduct at t_2 and the inductor current starts to decrease linearly. Switch T_3 can

be turned on at any time between t_2 and t'_3 , without causing switching losses. At $t'_3 = t_4$, when the inductor current reverses its flow direction, D_1 stops to conduct naturally and the resonant transition is initiated. The inductor current starts to charge the junction capacitance of D_1 and as soon as the switch-node voltage u_{sw} reaches a value of $(u_1 - u_{F,D4})$, close to the minimum inductor current $I_{L,\min}$, the clamping time interval is started. The decrease of the switch-node voltage, as a result of D_1 blocking a current flow in the reverse direction, can be detected easily. Hence, the start of the clamping time interval at t_5 can be detected without the need for an additional inductor current zero crossing detection and allows to simplify the controller implementation, as explained in detail in **Section B.3**.

After the clamping time interval T_{cl} , switch T_3 is turned off and the inductor current further discharges the parasitic output capacitance of switch T_2 . If the negative inductor current $I'_{L,0}$ at t_6 is large enough, the voltage across T_2 is reduced to zero and at t_7 its body diode starts to conduct. Hence, switch T_2 can be turned on at nearly zero voltage at time t_8 .

Since the inductor current $I_{L,0}$ at the beginning of the resonant voltage transition at t_4 is zero and cannot be controlled, the ZVS operation of switch T_2 at t_7 depends on the input-to-output voltage ratio, the characteristic impedance of the resonant circuit and on the duration of the clamping time interval T_{cl} , and hence also on the output power of the converter. The radius R_2 of the circle describing the resonant transition in the state-plane diagram in **Fig. B.4(b)** is given by $R_2 = (u_2 + u_{F,D1} - u_1)$ and the minimum inductor current $I_{L,\min}$ can be expressed with

$$I_{L,\min} = -\frac{R_2}{Z_{0,R2}}, \text{ and } Z_{0,R2} = \sqrt{\frac{L}{C_{D1} + C_{T2} + C_{D4}}}. \quad (\text{B.12})$$

The radius R'_2 of the circle describing the resonant transition after the clamping time interval (cf. **Fig. B.4(b)**) is given in (B.10), using $C_{\text{tot},R2'} = C_{D1} + C_{T2} + C_{T3}$. In order to allow for ZVS for switch T_2 at time t_8 , the condition $R'_2 \geq u_1$ must be fulfilled. By taking (B.9) for the inductor current $I'_{L,0}$ and assuming that $u_{F,D4}^2 \ll (Z_{0,R2'} I'_{L,0})^2$ applies in (B.10), the ZVS condition for T_2 can be expressed with

$$\frac{1}{Z_{0,R2}} (u_2 + u_{F,D1} - u_1) - \frac{u_{F,D4}}{L} T_{cl} \geq \frac{u_1}{Z_{0,R2'}}. \quad (\text{B.13})$$

If it is further assumed that $(u_2 + u_{F,D1} - u_1) \approx (u_2 - u_1)$ and $Z_{0,R2} = Z_{0,R2'} = Z_0$, i.e. if $C_{T3} = C_{D4}$, condition (B.13) is simplified to

$$u_2 \geq 2u_1 + Z_0 \frac{u_{F,D4}}{L} T_{cl}. \quad (\text{B.14})$$

Note that if the clamping-time interval $T_{cl} = 0$, i.e. at maximum output power, expression (B.14) is reduced to $u_2 \geq 2u_1$, which is equal to the ZVS condition of the traditional TCM operation [129] with $i_{L,0} = 0$.

As an example, **Fig. B.4(c)** shows the ZVS boundary according to (B.14), where the 2-switch CL-TCM converter is designed according to (B.15)-(B.20) described in **Section B.2.1**, for a fixed input-to-output voltage conversion ratio, a maximum output power of $P_{\max} = 30$ W and a switching frequency f_p in a range of 200 kHz to 800 kHz. It is evident that at a voltage conversion ratio of $u_2 = 2u_1$, the 2-switch CL-TCM converter allows ZVS operation only at the specified maximum output power, which corresponds to the traditional TCM operation, and as soon as the output power is reduced, the introduction of the clamping time interval leads to hard-switching immediately. This is a main limitation of the 2-switch CL-TCM converter. However, at larger voltage conversion ratios, the output power range that allows for ZVS operation is extended significantly, but is highly dependent on the specified switching frequency and input voltage of the converter, because these parameters also determine the value of the boost inductance.

However, the 3-switch CL-TCM converter allows for ZVS operation even in the hard-switching region of the 2-switch CL-TCM converter, since it allows to adjust the negative inductor current $I_{L,0}$ accordingly in order to achieve zero voltage switching.

B.2 Operating Modes

In this section, two operating modes of either the 2-switch or 3-switch CL-TCM converter are outlined and equations for the calculation of the boost inductance value and the switching time intervals T_{on} , T'_{on} , T_{off} and T_{cl} are provided.

B.2.1 Variable Switching Frequency Operation

The main objectives of the first mode of operation is the minimization of the switching frequency variation and the simultaneous min-

imization of the inductor RMS current for a variable output power $P \in [P_{2,\min}, P_{2,\max}]$ and a variable output voltage $u_2 \in [u_{2,\min}, u_{2,\max}]$, similar to the 4-switch CL-TCM converter operation presented in **Section 6.2.3**. It is assumed that the input voltage u_1 has a constant value, and as explained above, the clamping time interval T_{cl} is used as an additional degree of freedom to control the output power and the switching frequency variation of the converter.

At maximum output power, it is beneficial to emulate TCM operation, by reducing the clamping time interval T_{cl} to zero [126], as shown in **Fig. B.1(a)**. Accordingly, if the negative inductor current $I_{L,\min}$ is fixed, the switching frequency still varies in a certain range, if the input and/or the output voltage are not fixed. In contrast, for constant terminal voltages and variable output power, the switching frequency can be maintained constant, by introducing the clamping time interval.

Similar to (6.16), assuming a lossless operation of the converter, i.e. $P_1 = P_2$, the inductor must be designed according to

$$L = \frac{u_1 (u_{2,\min} - u_1)}{2u_{2,\min} f_{p,\min} (P_{1,\max}/u_1 - I_{L,\min})}, \quad (\text{B.15})$$

in order to achieve TCM operation at maximum output power and such that the converter is always operated above the specified minimum operating frequency $f_{p,\min}$, which is attained at the minimum output voltage $u_{2,\min}$.

In contrast to the 4-switch CL-TCM converter, for an accurate calculation of the switching time intervals T_{on} , T'_{on} , T_{off} and T_{cl} (cf. **Figs. B.1(b)** and **(c)**), the increase of the minimum inductor current $I_{L,\min}$ to

$$I'_{L,0} = I_{L,\min} + \frac{u_{F,D4}}{L} T_{\text{cl}} \quad (\text{B.16})$$

during the clamping time interval, cannot be neglected. This is specifically the case for the operation at low output power and low output voltage when the clamping time interval T_{cl} is large. Assuming that the resonant voltage transition time intervals are much shorter than the switching period, the time interval T_{on} can be calculated for a desired average input current $I_{1,\text{avg}} = P_1/u_1$ using

$$T_{\text{on}} = \frac{L}{u_1} \sqrt{4I_{1,\text{avg}} \left(\frac{P_{1,\max}}{u_1} - I_{L,\min} \right) + I_{L,\min}^2 - \frac{L}{u_1} I_{L,\min} - \frac{u_{F,D4}}{u_1} T_{\text{cl}}}, \quad (\text{B.17})$$

which is independent of the output voltage variation. The switching time intervals labeled with T_{off} and T_{cl} (cf. in **FIGS. B.1(b)** and **(c)**) are calculated according to

$$T_{\text{off}} = \frac{T_{\text{on}}(u_{\text{F,D4}} - u_1) - T_{\text{p,P(max)}}u_{\text{F,D4}}}{u_1 - u_2 - u_{\text{F,D4}}}, \quad (\text{B.18})$$

$$T_{\text{cl}} = T_{\text{p,P(max)}} - T_{\text{on}} - T_{\text{off}}, \quad (\text{B.19})$$

using the switching period T_{p} , evaluated for the nominal input power $P_{1,\text{max}}$, which follows from (B.15) and is given by

$$T_{\text{p,P(max)}} = \frac{2u_2L(P_{1,\text{max}}/u_1 - I_{\text{L,min}})}{u_1(u_2 - u_1)}. \quad (\text{B.20})$$

After the clamping time interval, the inductor current starts rising from $I'_{\text{L},0}$ and at the current zero crossing at t'_0 , the remaining ON-time interval T'_{on} is set by the control circuit, which is calculated with

$$T'_{\text{on}} = T_{\text{on}} + \frac{L}{u_1}I_{\text{L,min}} + \frac{u_{\text{F,D4}}}{u_1}T_{\text{cl}}. \quad (\text{B.21})$$

Note that the switching time intervals are calculated iteratively, since the clamping time interval T_{cl} is not known initially. Hence, starting with $T_{\text{cl}} = 0$ in (B.17), the switching time intervals (B.17)-(B.19) and (B.21) can be calculated within few iterations. In order to further improve the accuracy of the inductance and switching time interval calculations, the DC-DC efficiency $\eta_{\text{P(max)}}$ at maximum output power can be estimated in advance and the predicted maximum input power $P_{1,\text{max}} = P_{2,\text{max}}/\eta_{\text{P(max)}}$ can be used in (B.15) and (B.17)-(B.20).

Using (B.15) and (B.20), the maximum switching frequency can be calculated according to

$$f_{\text{p,max}} = f_{\text{p,min}} \cdot \frac{u_{2,\text{min}}}{u_{2,\text{max}}} \cdot \frac{(u_{2,\text{max}} - u_1)}{(u_{2,\text{min}} - u_1)}, \quad (\text{B.22})$$

which is obtained at maximum output voltage and is independent of the output power. Note that for large input-to-output voltage conversion ratios $u_2 \gg u_1$, the switching frequency variation is very small, i.e. $f_{\text{p,min}} \approx f_{\text{p,max}}$.

B.2.2 Constant Switching Frequency Operation

Generally, a varying switching frequency operation is not desired in EMI sensitive applications as it spreads the noise emissions over a wide spectral range and therefore complicates the filter design. Therefore, the second mode of operation allows to maintain a constant switching frequency by adjusting the clamping time interval and/or the minimum inductor current [126]. Note that this mode of operation cannot be achieved with the 2-switch CL-TCM converter, since the magnitude of the minimum inductor current $I_{L,\min}$ cannot be controlled.

The boost inductance can be calculated according to (B.15) with the desired constant switching frequency $f_{p,\text{const}}$. In order to maintain the switching frequency while the output voltage is allowed to vary with respect to the constant input voltage, the minimum inductor current $I_{L,\min}$ must be adjusted during the converter operation according to

$$I_{L,\min} = \frac{u_1^2 (u_1 - u_2) + 2Lf_{p,\text{const}}P_{1,\text{max}}u_2}{2Lf_{p,\text{const}}u_1u_2}. \quad (\text{B.23})$$

The switching time intervals T_{on} , T'_{on} , T_{off} and T_{cl} can then be calculated by inserting (B.23) into (B.17)-(B.21) and $T_{p,P(\text{max})} = 1/f_{p,\text{const}}$ into (B.18)-(B.19).

In order to outline the differences between the variable and the constant switching frequency operation, the switching frequency variation, the RMS inductor current - which gives an indication for the converter power losses - and the typical inductor current waveforms are illustrated in **Figs. B.5(a)-(f)** for both operating modes. The CL-TCM converter is operated with variable output voltage and variable output power, i.e., $u_2 \in [u_{2,\min}, u_{2,\max}]$ and $P \in [P_{2,\min}, P_{2,\max}]$, and is designed for the same minimum switching frequency. **Fig. B.5(a)** shows the variation of the switching frequency for the first operating mode. The switching frequency is kept constant for a fixed voltage conversion ratio and increases with increasing output voltage. In contrast, the RMS inductor current remains constant for a fixed output power and variable output voltage and is increasing almost linearly with increasing output power and fixed output voltage, as shown in **Fig. B.5(b)**. The typical inductor current waveforms for the converter operating points labeled with (A)-(D) are shown in **Fig. B.5(c)**.

The constant switching frequency operating mode of the CL-TCM converter (cf. **Fig. B.5(d)**) comes at the expense of an increased RMS inductor current at higher voltage conversion ratios, as illustrated in

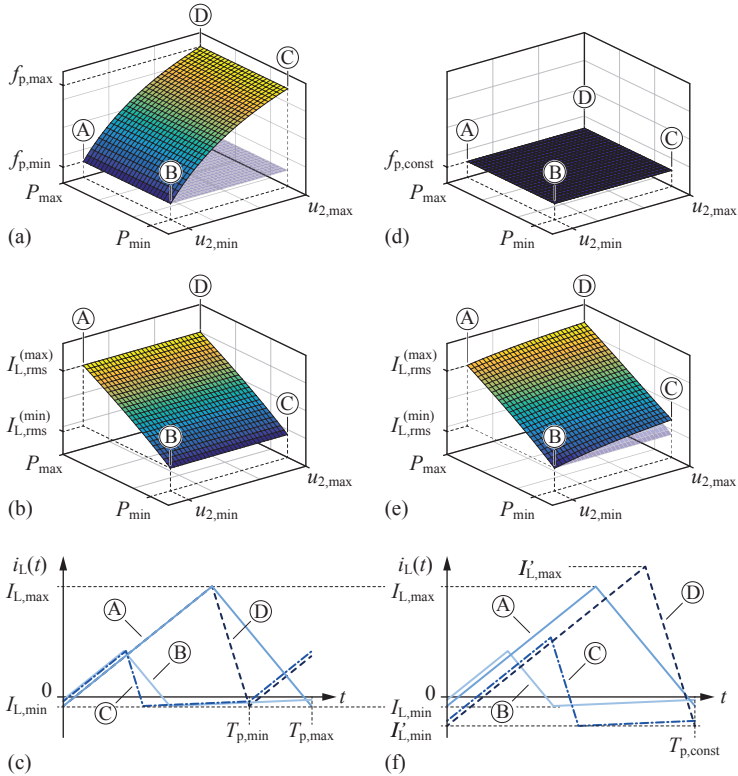


Fig. B.5: Switching frequency variation, inductor RMS current variation and inductor current waveforms for variable switching frequency operation (a)-(c) and for constant switching frequency operation (d)-(f), assuming a constant input voltage.

Fig. B.5(e). Hence, the converter power losses are increased at high output voltage, which is due to the larger peak-to-peak inductor current ripple (cf. **Fig. B.5(f)**), which is necessary to maintain the constant switching frequency. Hence, this mode of operation should be used only for applications which inherently limit the variation of the input and output voltage to a narrow range or which have a large voltage conversion ratio.

In the following section, the controller implementation for the CL-TCM converter operated at variable switching frequency is explained.

B.3 Controller Implementation

First, the implementation of the digital control is explained for the 3-switch CL-TCM converter, which is derived from the 4-switch CL-TCM controller shown in **Section 6.2.3**. Second, the controller implementation is presented for the 2-switch CL-TCM converter.

B.3.1 3-Switch CL-TCM Control

In order to implement the ZVS modulation scheme explained in **Section B.1.1**, the switch control signals must be synchronized to the inductor zero crossing. As described in **Section 6.2.3**, an effective implementation of the current zero crossing detection is shown in **Fig. B.6(a)**, where the low-side switch current i_{T_2} is sensed in order to detect the current zero crossing during the rising edge of the inductor current (cf. **Fig. B.6(b)**). The timing values T'_{on} , T_{off} and T_{cl} are calculated by a DSP and are transmitted to an FPGA, which implements the modulator Finite State Machine (FSM) shown in **Fig. B.6(c)** and which generates the gate control signals s_i , $i \in [1, 3]$. A counter t_c within the FPGA is used to set the duration of the individual switching time intervals. After the time T'_{on} in state 1 has expired, the current zero crossing detector is disabled and the modulator enters state 2, which sets the first dead-time interval $T_{dead,1}$ for the switches. In state 3, switch T_1 and T_3 are enabled and with the expiration of T_{off} , the modulator enters the clamping time-interval in state 4, followed by the second dead-time interval in state 5. After the dead-time, switch T_2 is turned on and the current zero crossing detector is enabled. As explained in **Section 6.2.3**, its output is blanked in the first place in order to prevent the detection of an erroneous current zero crossing, which could be due to the charging of the boot-strap capacitors of the high-side gate drivers or due to a hard-switching event at the turn-on of switch T_2 . After the blanking time interval, the current zero crossing detector output signal is evaluated. If the detector output is indicating that the inductor current is already positive, the state machine continues with state 2 in order to reduce the inductor current until its value is below zero when exiting state 6. If the inductor current is negative at the end of state 6, the modulator enters state 7 and waits for the detection of the current zero crossing, which then triggers the start of the modulation sequence from the beginning.

The output voltage control can be implemented as explained for the

Appendix B. CL-TCM Boost Converter with Reduced Hardware Complexity

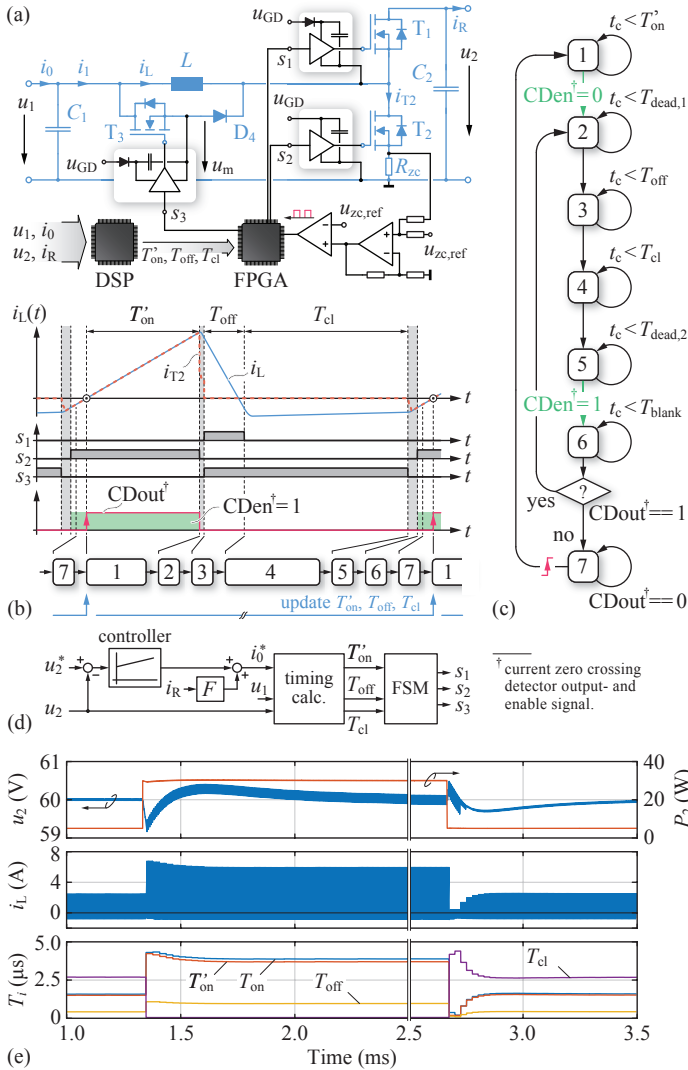


Fig. B.6: (a) Proposed realization of the control circuit and the current zero crossing detection for the 3-switch CL-TCM converter. (b) 3-switch CL-TCM current waveforms, modulator states and (c) modulator Finite State Machine (FSM). (d) 3-switch CL-TCM output voltage control with load current feed-forward. (e) Simulation of the 3-switch CL-TCM output voltage controller performance for a 25 W load step.

4-switch CL-TCM converter (cf. **Section 6.2.3**). In **Fig. B.6(d)**, a PI-controller and a load current feed-forward is used to set the average input current target i_0^* , which together with a measurement of the input and output voltage allows to compute the timing values T'_{on} , T'_{off} and T_{cl} . Since the evaluation of the timing values is computationally expensive, the values may be updated only every n -th cycle, e.g. every 5-th cycle as shown in the transient response simulation in **Fig. B.6(e)**. In case of the 3-switch CL-TCM converter it is not necessary to calculate the timing values iteratively for every update, since the iteration process can be performed directly within the periodic control sequence, using the last clamping time interval T_{cl} as initial condition for the next timing calculation. If the timing values are interpolated online using a look-up table, the iteration process can be omitted completely.

Due to the small inductance value and the tight control of the inductor current, the converter allows for a highly dynamic operation. As an example, **Fig. B.6(e)** shows the simulation of the controller performance for the 3-switch CL-TCM converter prototype discussed in **Section B.4**, for a 25 W load step and an output voltage reference set point u_2^* of 60 V. In this case, the boost inductor has a value of 7.51 μH and the input and output DC-link capacitances are set to 10 μF . It is assumed that five switching cycles are needed to finish the calculation of the timing values, which in this case corresponds to approximately 27 μs computation time. Due to the load current feed-forward, the controller reacts with little delay to the load disturbance and the inductor current is set directly to the desired value. As a result, the voltage drop at the output of the converter is less than 1 V and the voltage settles within less than 1 ms.

B.3.2 2-Switch CL-TCM Control

The realization of the control circuit of the 2-switch CL-TCM converter is shown in **Fig. B.7(a)**. In this case, the synchronization of the modulator state machine and the inductor current can be realized with very little hardware effort. As shown in **Fig. B.7(b)**, if the current in D_1 reaches zero within the falling edge of the inductor current, D_1 stops to conduct and the switch-node voltage u_{sw} starts to decrease. As soon as the switch-node voltage falls below the input voltage u_1 , D_4 starts to conduct and initiates the clamping time interval. As an advantage of the 2-switch topology, the start of the clamp-switch time interval can

Appendix B. CL-TCM Boost Converter with Reduced Hardware Complexity

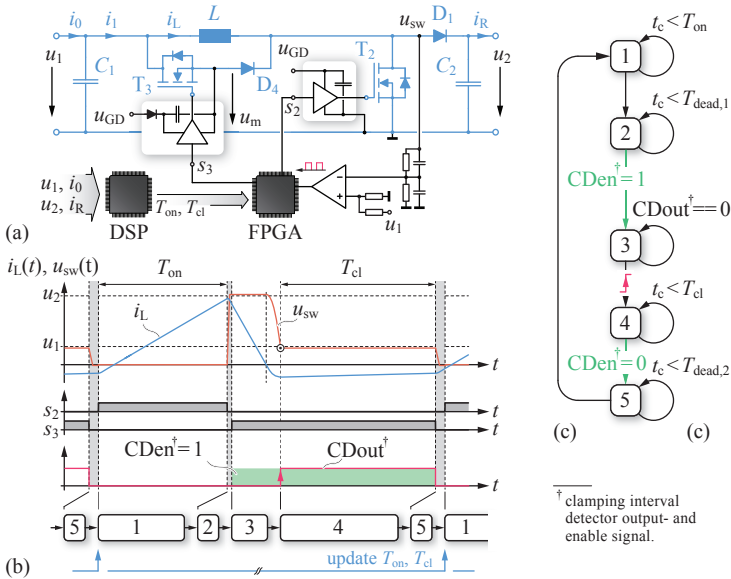


Fig. B.7: (a) Realization of the control circuit of the 2-switch CL-TCM converter. (b) 2-switch CL-TCM current/voltage waveforms and modulator states, and (c) modulator state machine.

be detected easily by comparing the switch-node voltage u_{sw} with the input voltage u_1 , as shown in **Fig. B.7(a)**, using a comparator circuit with a propagation delay as small as 5 ns and a very low hardware effort.

The modulator state machine is shown in **Fig. B.7(c)**. After the pre-calculated ON-time T_{on} and the first dead-time interval have expired, the clamping interval detector is enabled and switch T_3 is enabled. The decreasing inductor current is supplied to the output via diode D_1 and the modulator state machine waits in state 3 for the rising edge of the detector output signal, indicating that the clamping time interval is initiated. After the clamping time interval T_{cl} has expired, T_3 is turned off and after a short dead-time interval, the control sequence starts from the beginning. The output voltage control of the 2-switch CL-TCM converter can be implemented as shown in **Fig. B.6(d)**.

In the following section, the operating modes and the ZVS operation of the 2-switch and the 3-switch CL-TCM converter are verified experimentally using the hardware prototype presented in **Section 6.3.1**.

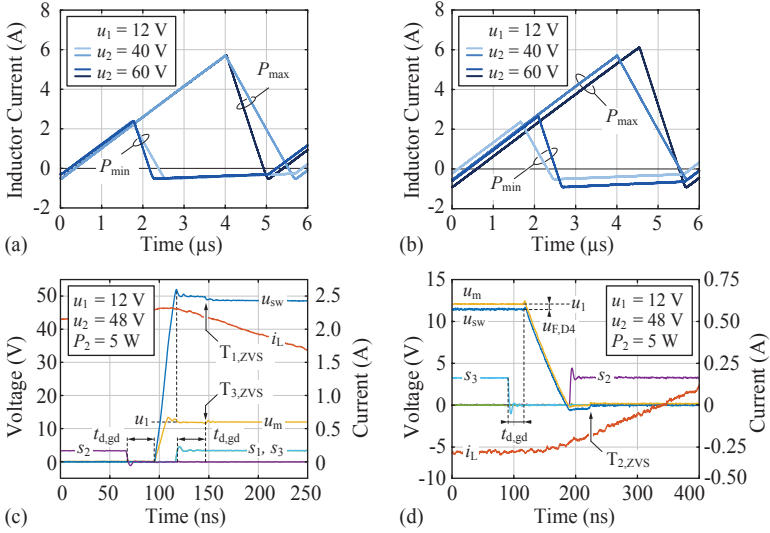


Fig. B.8: Measurement of the inductor current waveform for variable switching frequency operation (a) and constant switching frequency operation (b) of the 3-switch CL-TCM converter. (c)-(d) Verification of the ZVS operation of the switches T_1 , T_3 and T_2 respectively.

B.4 Experimental Verification

The measurements are performed with the CL-TCM hardware prototype depicted in **Fig. 6.7(a)**, which is described in detail in **Section 6.3.1**. Note that the prototype includes a GaN FET in parallel to D_4 as well, in order to allow for the 4-switch CL-TCM operation, which however is turned off permanently for the 2-switch and the 3-switch CL-TCM converter measurements. The specifications and the realization of the boost inductor are shown in **Fig. 6.7(b)**.

During the measurements, the converter was operated in open-loop mode and the timing values for the modulator state machine are calculated offline. The input voltage is set to a constant value of 12 V. The output voltage range is set to 40-60 V, with a nominal output voltage of 48 V, and the output power range is set to 5-30 W. **Fig. B.8(a)** shows the inductor current waveform for the variable switching frequency operating mode of the 3-switch CL-TCM converter. It can be seen that the switching frequency varies only by a factor 1.14 between 175 kHz

and 199 kHz, which is due to the large voltage conversion ratio. In **Fig. B.8(b)**, the inductor current waveforms are shown for constant switching frequency operation and the increased peak-to-peak inductor current ripple at the higher output voltage is clearly evident. In this case however, the RMS inductor current is only a factor of 1.03-1.23 higher compared to the variable frequency operating mode.

The ZVS operation of the switches T_1 - T_3 is shown in **Figs. B.8(c)** and **(d)** for an output voltage of 48 V and minimum output power. In **Fig. B.8(c)** the resonant voltage transition of the switch-node voltage u_{sw} is shown at the maximum inductor current. The voltage transition is initiated with the turn-off of switch T_2 after a gate drive propagation delay $t_{d,gd}$ of approximately 27 ns. The inductor current is large enough to discharge the parasitic output capacitance of switch T_1 well within the dead-time interval of 50 ns. The output capacitance of switch T_3 is discharged even faster as indicated by the clamp-switch midpoint voltage u_m . Hence, the two switches T_1 and T_3 can be turned on simultaneously after the dead-time interval without causing switching losses. At the end of the clamping time interval shown in **Fig. B.8(d)**, the resonant voltage transition is initiated with the turn-off of switch T_3 . The negative inductor current discharges the parasitic output capacitance of switch T_2 until its diode starts to conduct. Accordingly, switch T_2 can be turned on at nearly zero voltage after the dead-time interval of 100 ns.

The measurement results for the 2-switch CL-TCM converter operation are shown in **Fig. B.9** for a fixed input and output voltage of 12 V and 48 V, respectively. **Fig. B.9(a)** shows the measured inductor current waveforms for variable output power and **Fig. B.9(b)** shows the verification of the calculation of the switching time intervals according to (B.12) and (B.17)-(B.20). In order to simplify the calculation, it is assumed that the converter causes no power losses and that the capacitances C_{D1} , C_{T2} and C_{D4} , used in (B.12), have a value of 352 pF, which is the total charge equivalent capacitance [67] of the EPC2016C GaN FET connected in parallel to the Schottky diode, at an output voltage of 48 V. For the diode forward voltages a value of 0.6 V is used, which is the typical forward voltage drop of the Schottky diode MBR1H100SFT3G at 300 mA and 25 °C. The measured waveforms of the switch-node voltage u_{sw} and the inductor current i_L are shown in **Fig. B.9(c)** for minimum and maximum output power.

The measured DC-DC efficiency and the power loss of the proposed

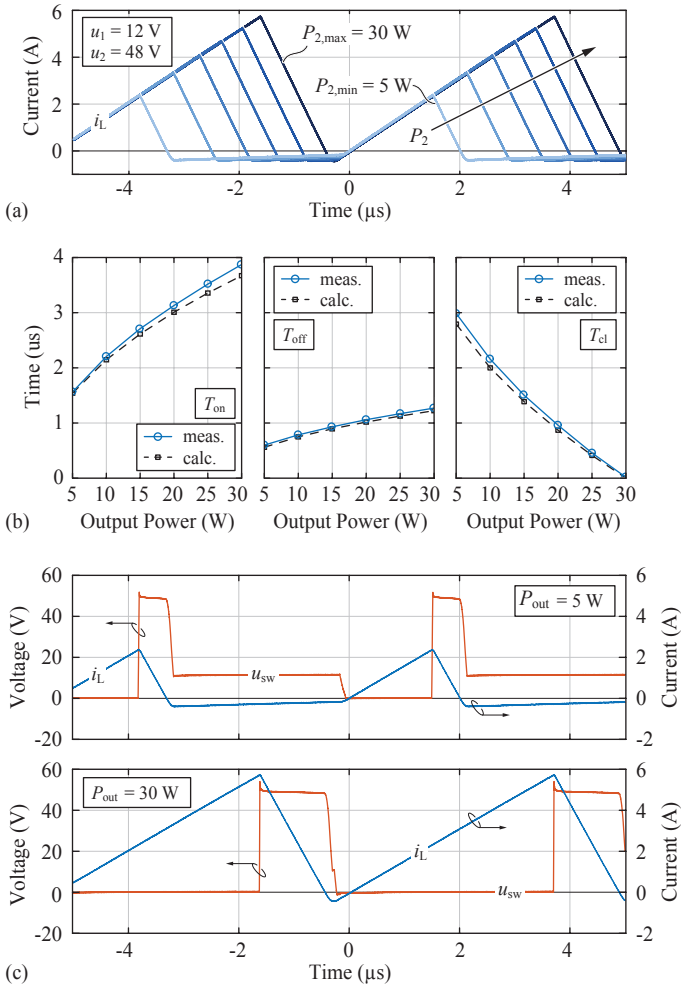


Fig. B.9: (a) Measurement of the inductor current waveforms for the 2-switch CL-TCM converter operation for fixed input/output voltages and variable output power. (b) Measured and calculated switching time intervals T_{on} , T_{off} and T_{cl} . (c) Measured waveforms of the switch-node voltage u_{sw} and the inductor current waveform for minimum and maximum output power.

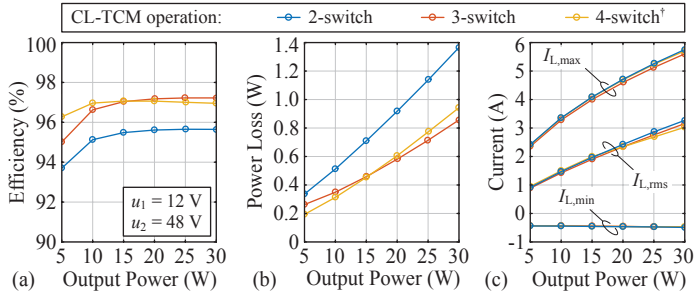


Fig. B.10: (a)-(b) Measured DC-DC efficiency and power loss at variable output power for the proposed 2-switch and 3-switch CL-TCM operation, as well as for the 4-switch CL-TCM operation explained in **Section 6.2**. Note that these measurements do not include the constant power loss of the DSP/FPGA control board. (c) Measured minimum, maximum and RMS inductor current.

converter operations are shown in **Figs. B.10(a)** and **(b)**, respectively. The input and output power is calculated based on the measurement of the terminal voltages and currents using Agilent 34410A multimeters. The 37.2 mW power loss caused by the current and voltage measurement circuits, as well as the gate drive power losses are measured separately and are included in the total power loss and efficiency measurement. However, the measurements do not include the constant power loss of 994 mW, which are caused by the DSP/FPGA control board, since it is not optimized for the hardware prototype at hand and it could be designed with significantly reduced footprint and power loss.

As shown in **Fig. B.10(a)**, a maximum efficiency of 97.2% was obtained for the 3-switch CL-TCM operation at maximum output power. The efficiency of the 2-switch operation is almost 1.5% lower compared to the 3-switch operation, which is due to the conduction losses caused in diode D_1 . It is important to note, that the diodes that are used in the hardware prototype are intended to lower the voltage drop across the GaN switches during the short dead-time interval and are not suited to carry the inductor current for a much longer time. Therefore, a more suitable diode such as the V10PL45-M3 Schottky rectifier diode could be used for D_1 to improve the efficiency of the 2-switch CL-TCM converter.

In order to provide a complete comparison, the DC-DC efficiency is measured as well for the 4-switch CL-TCM converter operation explained in **Section 6.2**. It is shown in **Fig. B.10(a)** that the 4-switch CL-TCM converter achieves a higher efficiency at low output power compared to the 3-switch operation, which is due to the decreased power losses during the clamping time interval. However, at maximum output power, the 4-switch CL-TCM converter shows a lower performance, which is due to the increased diode conduction power loss during the dead-time intervals.

The measurement of the minimum and maximum inductor current, as well as of the RMS inductor current is shown in **Fig. B.10(c)** for each converter operation. The minimum inductor current cannot be controlled for the 2-switch CL-TCM converter operation and therefore, the same negative inductor current value was chosen for the 3-switch and 4-switch CL-TCM converter operation, in order to achieve the same operating frequency, which is in a range of 187-194 kHz. As expected, the maximum and the RMS inductor current do not significantly differ among the different CL-TCM converter operations. Hence, the main differences in the power loss measurement results arise mainly from the different diode conduction losses and also from the different gate drive power losses, as the number of active switches varies for the different CL-TCM converter topologies.

The analysis of the operation of the CL-TCM converter is based on the assumption, that the input and output voltage are approximately constant over a switching cycle. Therefore, due to the large inductor current ripple needed for the ZVS operation, an appropriate filter stage is required at the input and the output of the CL-TCM converter, which is the topic of the following section.

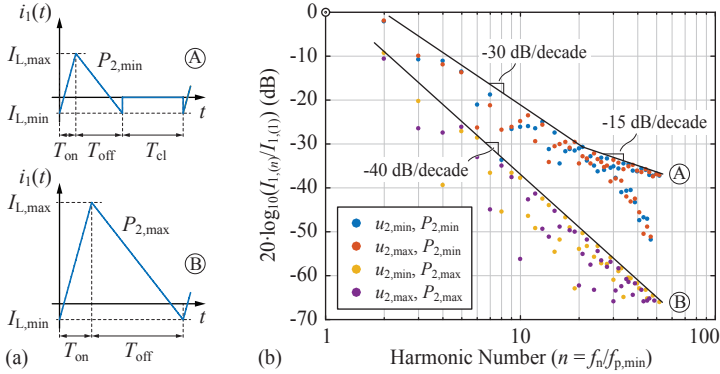


Fig. B.11: (a) CL-TCM converter input current i_1 for minimum and maximum output power. (b) Frequency spectrum of the input current i_1 at minimum (A) and maximum output power (B), normalized to the amplitude of the fundamental frequency component $I_{1,(1)}$.

B.5 Filter Design

Input Filter

The input filter stage protects the main power supply of the converter from the large inductor current ripple and guarantees an approximately constant input voltage u_1 . Typical waveforms of the filter output current i_1 (cf. **Fig. B.1(a)**) at minimum and maximum output power are illustrated in **Fig. B.11(a)**. The corresponding spectrum, normalized to the amplitude of the fundamental frequency component, is shown in **Fig. B.11(b)** for minimum and maximum output power P_2 and minimum and maximum output voltage u_2 , respectively. Compared to the operation at maximum output power, at minimum output power, the magnitude of the harmonic content is larger with respect to the amplitude of the fundamental frequency component, and drops with approximately -30 dB per decade and with an even lower rate at higher frequencies. This is due to the introduction of the clamping time interval, during which the current i_1 is zero, and hence, causes the high harmonic content in the spectrum of i_1 . At maximum output power, the operation of the converter is equivalent to the TCM operation, i.e. the clamping time interval is set to zero and the filter output current i_1 is equal to the inductor current i_L . In this case, the magnitudes of

the harmonic content of i_1 are decreasing with -40 dB per decade. Obviously, at maximum output power, the peak-to-peak inductor current ripple reaches a maximum value and the amplitudes of the harmonic components are much larger compared to the operation at minimum output power.

At maximum output power, the amplitudes of the harmonic content of i_1 can be calculated according to [184]

$$\hat{I}_{1,(n),P_{\max}} = \frac{u_0 T_{\text{on,max}}}{2L} \left| \frac{-2(-1)^n m^2}{n^2(m-1)\pi^2} \sin\left(n\pi\left(1 - \frac{1}{m}\right)\right) \right|, \quad n \in [1, 2, \dots], \quad (\text{B.24})$$

and $m = T_p/T_{\text{on,max}}$, using the approximation $u_1 \approx u_0$ and T_{on} is evaluated for $P_{2,\max}$.

Considering the variable switching frequency operation of the CL-TCM converter, the input filter must be designed for the operating point at maximum output power and minimum switching frequency, which is observed at the minimum output voltage, such that the peak-to-peak voltage ripple $\Delta u_{1,\text{pp}}$ and the peak-to-peak current ripple $\Delta i_{0,\text{pp}}$ comply with the given converter specifications. In this case, the amplitude of the fundamental frequency component of i_1 can be calculated with

$$\hat{I}'_{1,(1)} = \frac{2(P_{2,\max} - I_{L,\min}u_0)u_{2,\min}^2}{\pi^2 u_0^2 (u_{2,\min} - u_0)} \cdot \sin\left(\frac{\pi u_0}{u_{2,\min}}\right), \quad (\text{B.25})$$

assuming a lossless operation of the converter and assuming $u_1 \approx u_0$.

In the simplest case, a single-stage L-C-filter can be used at the input of the converter, as shown in **Fig. B.1(a)**. Accordingly, the filter transfer functions which relate the current i_1 to the voltage u_1 and to the input current i_0 can be calculated with

$$|\underline{G}_v(j\omega)| = \frac{|\hat{U}_1(j\omega)|}{|\hat{I}_1(j\omega)|} = \frac{\omega L_f}{|\omega^2 L_f C_f - 1|} \quad (\text{B.26})$$

and

$$|\underline{G}_i(j\omega)| = \frac{|\hat{I}_0(j\omega)|}{|\hat{I}_1(j\omega)|} = \frac{1}{|\omega^2 L_f C_f - 1|}, \quad (\text{B.27})$$

and are shown in **Fig. B.12(a)**. The filter specifications are given in terms of a limit of the peak-to-peak voltage ripple $\Delta u_{1,\text{pp}}$ and the peak-to-peak input current ripple $\Delta i_{0,\text{pp}}$, with respect to the primary power supply voltage u_0 and the maximum average input current, respectively

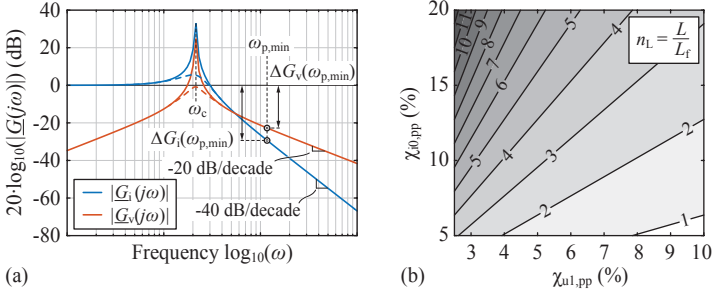


Fig. B.12: (a) Input filter transfer functions $|\underline{G}_i(j\omega)| = |\hat{L}_0(j\omega)/\hat{L}_1(j\omega)|$ and $|\underline{G}_v(j\omega)| = |\hat{U}_1(j\omega)/\hat{I}_1(j\omega)|$. (b) Ratio between the boost inductance L and the required filter inductance L_f according to (B.35), with respect to the current and voltage ripple specifications $\chi_{i0,pp}$ and $\chi_{u1,pp}$, and $u_{2,min} = 2 \cdot u_0$.

(assuming a lossless operation of the converter, i.e. $P_1 = P_2$):

$$\Delta u_{1,pp} \leq \chi_{u1,pp} \cdot u_0 \quad \text{and} \quad \Delta i_{0,pp} \leq \chi_{i0,pp} \cdot \frac{P_{1,max}}{u_0}, \quad (\text{B.28})$$

with $\chi_{u1,pp} \in [0, 1]$ and $\chi_{i0,pp} \in [0, 1]$.

Using (B.25)-(B.27) and $\omega_{p,min} = 2\pi f_{p,min}$, the filter component values C_f and L_f can be calculated with

$$C_f \geq \frac{\chi_{i0,pp} P_{1,max} + 2u_0 \hat{I}'_{1,(1)}}{\chi_{u1,pp} u_0^2 \omega_{p,min}} \quad (\text{B.29})$$

and

$$L_f \geq \frac{\chi_{u1,pp} u_0^2}{\chi_{i0,pp} P_{1,max} \omega_{p,min}}. \quad (\text{B.30})$$

Accordingly, the attenuation of the voltage and current ripple at the minimum switching frequency is

$$\Delta G_v(\omega_{p,min}) = 20 \cdot \log_{10} \left(\frac{\chi_{u1,pp} u_0}{2 \hat{I}'_{1,(1)}} \right) \quad (\text{B.31})$$

and

$$\Delta G_i(\omega_{p,min}) = 20 \cdot \log_{10} \left(\frac{\chi_{i0,pp} P_{1,max}}{2u_0 \hat{I}'_{1,(1)}} \right). \quad (\text{B.32})$$

The resonance frequency of the L-C-filter follows from (B.29) and (B.30), and is given by

$$f_c = \frac{1}{2\pi\sqrt{L_f C_f}} = \left(\frac{P_{1,\max} \omega_{p,\min}^2 \chi_{i0,pp}}{4\pi^2 \left(2\hat{I}'_{1,(1)} u_0 + P_{1,\max} \chi_{i0,pp} \right)} \right)^{\frac{1}{2}}. \quad (\text{B.33})$$

Note that the previous analysis does not consider any power losses within the filter or the converter, which allows for a simplified analytical design of the filter components. However, for the control of the converter, a sufficient damping of the resonant peak of the output impedance of the filter is mandatory in order to guarantee a stable operation of the converter [52]. Preferably, the damping of the filter's resonant peak is achieved by adding a series connected resistor and capacitor in parallel to the filter capacitor C_f as indicated in **Fig. B.1(a)** and is discussed in detail in [52].

In order to get an indication of the size of the filter inductor with respect to the boost inductor, the ratio between the inductances can be calculated using (B.15) and (B.30), assuming that $u_1 \approx u_0$ and $P_{1,\max} = P_{2,\max}$, and is given by

$$n_L = \frac{L}{L_f} = \frac{\chi_{i0,pp}}{\chi_{u1,pp}} \cdot \frac{\pi P_{2,\max} (u_{2,\min} - u_0)}{u_{2,\min} (P_{2,\max} - I_{L,\min} u_0)}, \quad (\text{B.34})$$

which can be further simplified to

$$n_L \approx \frac{\chi_{i0,pp}}{\chi_{u1,pp}} \pi \left(1 - \frac{u_0}{u_{2,\min}} \right), \quad (\text{B.35})$$

if $P_{\max} \gg I_{L,\min} u_0$ applies. The inductance ratio given by (B.35) is shown in **Fig. B.12(b)** for $u_{2,\min} = 2 \cdot u_0$. As expected from (B.34), the filter inductance with respect to the boost inductance depends mainly on the ratio of the ripple specifications $\chi_{i0,pp}$ and $\chi_{u1,pp}$ and is independent of the choice of the minimum switching frequency. The inductance ratio n_L gives already an indication for the filter inductor volume, but since the peak current in the filter inductor is much smaller compared to the peak current in the boost inductor, it can be expected that the volume of the filter inductor is much smaller than the volume of the boost inductor.

Output Filter

At the output of the converter, the filter capacitor C_2 (cf. **Fig. B.1(a)**) is designed such that the peak-to-peak voltage ripple $\Delta u_{2,pp}$ does not exceed a specified fraction of the nominal output voltage, i.e.

$$\Delta u_{2,pp} \leq \chi_{u_{2,pp}} \cdot u_2, \quad (\text{B.36})$$

the output filter capacitance C_2 is then calculated for the worst case operating point, which is at the maximum output power and the minimum output voltage, according to

$$C_2 \geq \frac{\left(\frac{u_0}{L} T_{\text{on,max}} + I_{L,\text{min}} - \frac{P_{2,\text{max}}}{u_{2,\text{min}}} \right)^2 L}{2\chi_{u_{2,pp}} u_{2,\text{min}} (u_{2,\text{min}} - u_1)}. \quad (\text{B.37})$$

B.6 Summary of the Chapter

In this chapter, two CL-TCM boost converter topologies offering a reduced hardware complexity are proposed and the ZVS modulation schemes are explained in detail. In addition, the timing calculations for the switching signals, the controller implementation, as well as the limitations for the ZVS operation are presented for both converter topologies. In addition, two operating modes of the CL-TCM converter are compared and additional design considerations are provided for the input and output filter design.

The main results of this chapter are summarized as follows:

- ▶ Together with the ZVS modulation scheme, the reduction of the hardware complexity of the CL-TCM converter, i.e. by reducing the number of active switches, comes at the expense of an unidirectional power flow and a restriction on the minimum input-to-output voltage conversion ratio, which is needed to ensure ZVS operation for all the switches.
- ▶ Two different operating modes are explained for the CL-TCM converter. The first operating mode allows for minimum switching frequency variation and a minimized RMS inductor current, which is achievable for all considered CL-TCM converter topologies.

- ▶ The second mode of operation allows for constant switching frequency operation and can be achieved with the 3-switch and the 4-switch CL-TCM converter only. However, the constant switching frequency operation has limitations regarding the converter efficiency, since the RMS inductor current increases as the output voltage is increased. Hence, this mode of operation is intended mainly for applications requiring a small input or output voltage operating range or a high voltage conversion ratio.
- ▶ A detailed description of the control schemes of the 2-switch and the 3-switch CL-TCM converter is provided, which allows for a simple and effective implementation of the converter operation.

It is important to note that the modulation schemes and the operating modes presented in this chapter are not limited to the CL-TCM boost converter only, but could be easily adapted for an unidirectional buck-type CL-TCM converter operation as well.

Bibliography

- [1] Eurotransplant, “Annual Report 2016,” Eurotransplant International Foundation, Leiden, The Netherlands, 2017. [PDF]
- [2] T. Puehler, S. Ensminger, M. Schoenbrodt, J. Börgermann, E. Rehn, K. Hakim-Meibodi, M. Morshuis, and J. Gummert, “Mechanical circulatory support devices as destination therapy—current evidence,” *Ann. Cardiothorac. Surg.*, vol. 3, no. 5, pp. 513–524, 2014. DOI: [10.3978/j.issn.2225-319X.2014.08.20](https://doi.org/10.3978/j.issn.2225-319X.2014.08.20) [PDF]
- [3] O. Knecht and J. W. Kolar, “Performance evaluation of series-compensated IPT systems for high power transcutaneous energy transfer,” *IEEE Trans. Power Electron.*, pp. 1–14, published, April 2018. DOI: [10.1109/TPEL.2018.2822722](https://doi.org/10.1109/TPEL.2018.2822722) [PDF]
- [4] E. J. Molina and S. W. Boyce, “Current status of left ventricular assist device technology,” *Semin. Thorac. Cardiovasc. Surg.*, vol. 25, no. 1, pp. 56–63, 2013. [PDF]
- [5] C. A. Milano and A. A. Simeone, “Mechanical circulatory support: Devices, outcomes and complications,” *Heart Fail. Rev.*, vol. 18, no. 1, pp. 35–53, 2013. DOI: [10.1007/s10741-012-9303-5](https://doi.org/10.1007/s10741-012-9303-5) [PDF]
- [6] A. Prinzing, U. Herold, A. Berkefeld, M. Krane, R. Lange, and B. Voss, “Left ventricular assist devices—current state and perspectives,” *Journal of Thoracic Disease*, vol. 8, no. 8, pp. 1–7, 2016. DOI: [10.21037/jtd.2016.07.13](https://doi.org/10.21037/jtd.2016.07.13) [PDF]
- [7] M. E. DeBakey, “Left ventricular bypass pump for cardiac assistance: Clinical experience,” *Am. J. Cardiol.*, vol. 27, no. 1, pp. 3–11, 1971. DOI: [10.1016/0002-9149\(71\)90076-2](https://doi.org/10.1016/0002-9149(71)90076-2) [PDF]
- [8] HeartWare, “Resources - Image Library,” 2017. [Online]. Available: <https://heartware.com/resources>. [Accessed: Aug. 02, 2017].
- [9] Thoratec, “HeartMate 3,” 2017. [Online]. Available: <http://www.thoratec.com/medical-professionals/vad-product-information/heartmate3.aspx>. [Accessed: Aug. 02, 2017]. [PDF]

- [10] J. K. Kirklin, D. C. Naftel, F. D. Pagani, R. L. Kormos, L. W. Stevenson, E. D. Blume, S. L. Myers, M. A. Miller, J. T. Baldwin, and J. B. Young, “Seventh INTERMACS annual report: 15,000 patients and counting,” *J. Heart Lung Transpl.*, vol. 34, no. 12, p. 1495–1504, 2015. DOI: [10.1016/j.healun.2015.10.003](https://doi.org/10.1016/j.healun.2015.10.003) [PDF]
- [11] A. Zierer *et al.*, “Late-onset driveline infections: The achilles’ heel of prolonged left ventricular assist device support,” *Ann. Thorac. Surg.*, vol. 84, no. 2, pp. 515–520, 2007. DOI: [10.1016/j.athoracsur.2007.03.085](https://doi.org/10.1016/j.athoracsur.2007.03.085) [PDF]
- [12] D. J. Goldstein, D. Naftel, W. Holman, L. Bellumkonda, S. V. Pamboukian, F. D. Pagani, and J. Kirklin, “Continuous-flow devices and percutaneous site infections: Clinical outcomes,” *J. Heart Lung Transpl.*, vol. 31, no. 11, pp. 1151 – 1157, 2012. DOI: [10.1016/j.healun.2012.05.004](https://doi.org/10.1016/j.healun.2012.05.004) [PDF]
- [13] B. H. Trachtenberg, A. Cordero-Reyes, B. Elias, and M. Loebe, “A review of infections in patients with left ventricular assist devices: Prevention, diagnosis and management,” *Methodist De-Bakey Cardiovascular Journal*, vol. 11, no. 1, pp. 28–32, 2015. DOI: [10.14797/mdcj-11-1-28](https://doi.org/10.14797/mdcj-11-1-28) [PDF]
- [14] M. S. Slaughter *et al.*, “Advanced heart failure treated with continuous-flow left ventricular assist device,” *N. Engl. J. Med.*, vol. 361, no. 23, pp. 2241–2251, 2009. DOI: [10.1056/NEJMoa0909938](https://doi.org/10.1056/NEJMoa0909938) [PDF]
- [15] M. Rasouli and L. S. J. Phee, “Energy sources and their development for application in medical devices,” *Expert Review of Medical Devices*, vol. 7, no. 5, pp. 693–709, 2010. DOI: [10.1586/erd.10.20](https://doi.org/10.1586/erd.10.20) [PDF]
- [16] T. Pirbodaghi, C. Cotter, and K. Bourque, “Power consumption of rotary blood pumps: Pulsatile versus constant-speed mode,” *Artif. Organs*, vol. 38, no. 12, pp. 1024–1028, 2014. DOI: [10.1111/aor.12323](https://doi.org/10.1111/aor.12323) [PDF]
- [17] M. S. Slaughter and T. J. Myers, “Transcutaneous energy transmission for mechanical circulatory support systems: History, current status, and future prospects,” *J. Card. Surg.*, vol. 25, no. 4, pp. 484–489, 2010. DOI: [10.1111/j.1540-8191.2010.01074.x](https://doi.org/10.1111/j.1540-8191.2010.01074.x) [PDF]

-
- [18] K. Unthan, F. Gräf, M. Laumen, T. Finocchiaro, C. Sommer, H. Lanmüller, and U. Steinseifer, “Design and evaluation of a fully implantable control unit for blood pumps,” *BioMed Research International*, vol. 2015, no. 257848, pp. 1–9, 2015. DOI: [10.1155/2015/257848](https://doi.org/10.1155/2015/257848) [PDF]
- [19] J. C. Schuder, “Powering an artificial heart: Birth of the inductively coupled-radio frequency system in 1960,” *Artif. Organs*, vol. 26, no. 11, pp. 909–915, 2002. [PDF]
- [20] Greatbatch Medical, “Xcellion rechargeable batteries,” 2009. [Online]. Available: <http://greatbatchmedicalstaging.info/assets/products/XcellionRechargeableBatteries.pdf>. [Accessed: May. 18, 2017]. [PDF]
- [21] C. H. Kao, Y. P. Lin, and K. T. Tang, “Wireless data and power transmission circuits in biomedical implantable applications,” in *Proc. of the Int. Symp. on Bioelectronics and Bioinformatics (ISBB)*, 2011, pp. 9–12. DOI: [10.1109/ISBB.2011.6107632](https://doi.org/10.1109/ISBB.2011.6107632) [PDF]
- [22] A. Vilches, A. Sanni, and C. Toumazou, “Single coil pair transcutaneous energy and data transceiver for low power bio-implant use,” *Electron. Lett.*, vol. 45, no. 14, pp. 727–728, 2009. DOI: [10.1049/el.2009.0457](https://doi.org/10.1049/el.2009.0457) [PDF]
- [23] C. Rathge and D. Kuschner, “High efficient inductive energy and data transmission system with special coil geometry,” in *Proc. of the 13th European Conf. on Power Electronics and Applications*, 2009, pp. 1–8. [PDF]
- [24] G. Wang, P. Wang, Y. Tang, and W. Liu, “Analysis of dual band power and data telemetry for biomedical implants,” *IEEE Trans. Biomed. Circuits Syst.*, vol. 6, no. 3, pp. 208–215, 2012. DOI: [10.1109/TBCAS.2011.2171958](https://doi.org/10.1109/TBCAS.2011.2171958) [PDF]
- [25] F. Merli, “Implantable antennas for biomedical applications,” Ph.D. dissertation, Dept. Elect. Eng., Swiss Federal Inst. Technol. Lausanne (EPFL), Switzerland, 2011. [PDF]
- [26] A. Väyrynen and J. Salminen, “Lithium ion battery production,” *J. Chem. Thermodyn.*, vol. 46, pp. 80–85, 2012. DOI: [10.1016/j.jct.2011.09.005](https://doi.org/10.1016/j.jct.2011.09.005) [PDF]

- [27] A. El-Banayosy, L. Arusoglu, L. Kizner, M. Morshuis, G. Tenderich, W. E. Pae, and R. Körfer, “Preliminary experience with the LionHeart left ventricular assist device in patients with end-stage heart failure,” *Ann. Thorac. Surg.*, vol. 75, no. 5, pp. 1469–1475, 2003. DOI: [10.1016/S0003-4975\(02\)04097-3](https://doi.org/10.1016/S0003-4975(02)04097-3) [PDF]
- [28] S. M. Mehta, W. E. Pae, G. Rosenberg, A. J. Snyder, W. J. Weiss, J. P. Lewis, D. J. Frank, J. J. Thompson, and W. S. Pierce, “The LionHeart LVD-2000: A completely implanted left ventricular assist device for chronic circulatory support,” *Ann. Thorac. Surg.*, vol. 71, no. 3, pp. S156–S161, 2001. DOI: [10.1016/S0003-4975\(00\)02641-2](https://doi.org/10.1016/S0003-4975(00)02641-2) [PDF]
- [29] K. M. Zareba, “The artificial heart - past, present, and future,” *Med. Sci. Monit.*, vol. 8, no. 3, pp. 72–77, 2002. [PDF]
- [30] J. A. Miller, G. Bélanger, and T. Mussivand, “Development of an autotuned transcuteaneous energy transfer system,” *ASAIO J.*, vol. 39, no. 3, pp. 706–710, 1993. [PDF]
- [31] T. Mussivand *et al.*, “Transcutaneous energy transfer system performance evaluation,” *Artif. Organs*, vol. 17, no. 11, pp. 940–947, 1993. DOI: [10.1111/j.1525-1594.1993.tb00407.x](https://doi.org/10.1111/j.1525-1594.1993.tb00407.x) [PDF]
- [32] C. C. Tsai, B. S. Chen, and C. M. Tsai, “Design of wireless transcuteaneous energy transmission system for totally artificial hearts,” in *Proc. of the IEEE Asia-Pacific Conf. on Circuits and Systems (APCCAS)*, 2000, pp. 646–649. DOI: [10.1109/APCCAS.2000.913603](https://doi.org/10.1109/APCCAS.2000.913603) [PDF]
- [33] H. Miura, S. Arai, Y. Kakubari, F. Sato, H. Matsuki, and T. Sato, “Improvement of the transcuteaneous energy transmission system utilizing ferrite cored coils for artificial hearts,” *IEEE Trans. Magn.*, vol. 42, no. 10, pp. 3578–3580, 2006. DOI: [10.1109/TMAG.2006.879630](https://doi.org/10.1109/TMAG.2006.879630) [PDF]
- [34] Q. Chen, S.-C. Wong, C. K. Tse, and X. Ruan, “Analysis, design, and control of a transcuteaneous power regulator for artificial hearts,” *IEEE Trans. Biomed. Circuits Syst.*, vol. 3, no. 1, pp. 23–31, 2009. DOI: [10.1109/TBCAS.2008.2006492](https://doi.org/10.1109/TBCAS.2008.2006492) [PDF]
- [35] E. Okamoto, Y. Yamamoto, Y. Akasaka, T. Motomura, Y. Mitamura, and Y. Nosé, “A new transcuteaneous energy transmission

- system with hybrid energy coils for driving an implantable biven-
tricular assist device,” *Artif. Organs*, vol. 33, no. 8, pp. 622–626,
2009. DOI: [10.1111/j.1525-1594.2009.00785.x](https://doi.org/10.1111/j.1525-1594.2009.00785.x) [PDF]
- [36] T. D. Dissanayake, “An effective transcuteaneous energy transfer
(TET) system for artificial hearts,” Ph.D. dissertation, Inst. Bio-
eng., Univ. Auckland, New Zealand, 2010. [PDF]
- [37] H. Y. Leung, D. M. Budgett, D. McCormick, and A. P. Hu, “Wire-
less power system for implantable heart pumps based on energy
injection control,” in *Proc. of the Progress In Electromagnetics
Research Symp. (PIERS)*, 2012, pp. 445–449. [PDF]
- [38] L. Lucke, J. Mondry, S. Scott, and W. Weiss, “A totally implant-
able controller for use with rotary LVADs,” Minnetronix Inc.,
2014. [Online]. Available: [http://www.minnetronix.com/assets/
documents/publications/totally-implantable-controller.pdf](http://www.minnetronix.com/assets/documents/publications/totally-implantable-controller.pdf). [Ac-
cessed: Aug. 08, 2017]. [PDF]
- [39] Y. Fu, L. Hu, X. Ruan, and X. Fu, “A transcuteaneous energy
transmission system for artificial heart adapting to changing im-
pedance,” *Artif. Organs*, vol. 39, no. 4, pp. 378–387, 2015. DOI:
[10.1111/aor.12384](https://doi.org/10.1111/aor.12384) [PDF]
- [40] A. S. Marinčić, “Nikola Tesla and the wireless transmission of
energy,” *IEEE Trans. Power App. Syst.*, vol. PAS-101, no. 10,
pp. 4064–4068, 1982. DOI: [10.1109/TPAS.1982.317084](https://doi.org/10.1109/TPAS.1982.317084) [PDF]
- [41] K. van Schuylenbergh and R. Puers, *Inductive Powering: Ba-
sic Theory and Application to Biomedical Systems*, 1st edition.
Dordrecht, NL: Springer Science+Business Media, 2009. DOI:
[10.1007/978-90-481-2412-1](https://doi.org/10.1007/978-90-481-2412-1) [PDF]
- [42] B. Lenaerts and R. Puers, *Omnidirectional Inductive Powering
for Biomedical Implants*, 1st edition. Dordrecht, NL: Analog
Circuits and Signal Processing, Springer Science+Business Media
B.V., 2009. DOI: [10.1007/978-1-4020-9075-2](https://doi.org/10.1007/978-1-4020-9075-2) [PDF]
- [43] R. Bosshard, “Multi-objective optimization of inductive power
transfer systems for EV charging,” Ph.D. dissertation, Dept.
Elect. Eng., Swiss Federal Inst. Technol. Zurich (ETH Zurich),
Switzerland, 2015. [PDF]

- [44] R. Bosshard, T. Guillod, and J. W. Kolar, “Electromagnetic field patterns and energy flux of efficiency optimal inductive power transfer systems,” *Electrical Engineering*, vol. 99, no. 3, p. 969–977, 2017. DOI: [10.1007/s00202-016-0461-7](https://doi.org/10.1007/s00202-016-0461-7) [PDF]
- [45] O. Knecht, R. Bosshard, J. W. Kolar, and C. T. Starck, “Optimization of transcutaneous energy transfer coils for high power medical applications,” in *Proc. of the 15th IEEE Workshop on Control and Modeling of Power Electronics (COMPEL)*, 2014, pp. 1–10. DOI: [10.1109/COMPEL.2014.6877190](https://doi.org/10.1109/COMPEL.2014.6877190) [PDF]
- [46] O. Knecht, R. Bosshard, and J. W. Kolar, “High-efficiency transcutaneous energy transfer for implantable mechanical heart support systems,” *IEEE Trans. Power Electron.*, vol. 30, no. 11, pp. 6221–6236, 2015. DOI: [10.1109/TPEL.2015.2396194](https://doi.org/10.1109/TPEL.2015.2396194) [PDF]
- [47] O. Knecht and J. W. Kolar, “Comparative evaluation of IPT resonant circuit topologies for wireless power supplies of implantable mechanical circulatory support systems,” in *Proc. of the 32nd IEEE Applied Power Electronics Conf. and Expo. (APEC)*, 2017, pp. 3271–3278. DOI: [10.1109/APEC.2017.7931166](https://doi.org/10.1109/APEC.2017.7931166) [PDF]
- [48] R. Bosshard, J. W. Kolar, J. Mühlethaler, I. Stevanović, B. Wunsch, and F. Canales, “Modeling and η - α -Pareto optimization of inductive power transfer coils for electric vehicles,” *IEEE J. Emerg. Sel. Topics Power Electron.*, vol. 3, no. 1, pp. 50–64, 2015. DOI: [10.1109/JESTPE.2014.2311302](https://doi.org/10.1109/JESTPE.2014.2311302) [PDF]
- [49] I. Nam, R. Dougal, and E. Santi, “Optimal design method to achieve both good robustness and efficiency in loosely-coupled wireless charging system employing series-parallel resonant tank with asymmetrical magnetic coupler,” in *Proc. of the 5th IEEE Energy Conversion Congr. and Expo. (ECCE USA)*, 2013, pp. 3266–3276. DOI: [10.1109/ECCE.2013.6647129](https://doi.org/10.1109/ECCE.2013.6647129) [PDF]
- [50] W. Zhang, S.-C. Wong, C. K. Tse, and Q. Chen, “Analysis and comparison of secondary series- and parallel-compensated inductive power transfer systems operating for optimal efficiency and load-independent voltage-transfer ratio,” *IEEE Trans. Power Electron.*, vol. 29, no. 6, pp. 2979–2990, 2014. DOI: [10.1109/TPEL.2013.2273364](https://doi.org/10.1109/TPEL.2013.2273364) [PDF]

-
- [51] E. Waffenschmidt and T. Staring, “Limitation of inductive power transfer for consumer applications,” in *Proc. of the 13th European Conf. on Power Electronics and Applications (EPE)*, 2009, pp. 1–10. [PDF]
- [52] R. W. Erickson and D. Maksimović, *Fundamentals of Power Electronics*, 2nd edition. New York, USA: Springer Science+Business Media, 2001. DOI: [10.1007/b100747](https://doi.org/10.1007/b100747) [PDF]
- [53] R. Bosshard, U. Badstübner, J. W. Kolar, and I. Stevanović, “Comparative evaluation of control methods for inductive power transfer,” in *Proc. of the 1st Int. Conf. on Renewable Energy Research and Applications (ICRERA)*, 2012, pp. 1–6. DOI: [10.1109/ICRERA.2012.6477400](https://doi.org/10.1109/ICRERA.2012.6477400) [PDF]
- [54] C.-S. Wang, G. A. Covic, and O. H. Stielau, “Power transfer capability and bifurcation phenomena of loosely coupled inductive power transfer systems,” *IEEE Trans. Ind. Electron.*, vol. 51, no. 1, pp. 148–157, 2004. DOI: [10.1109/TIE.2003.822038](https://doi.org/10.1109/TIE.2003.822038) [PDF]
- [55] R. L. Steigerwald, “A comparison of half-bridge resonant converter topologies,” *IEEE Trans. Power Electron.*, vol. 3, no. 2, pp. 174–182, 1988. DOI: [10.1109/63.4347](https://doi.org/10.1109/63.4347) [PDF]
- [56] G. Ivensky, A. Kats, and S. Ben-Yaakov, “An RC load model of parallel and series-parallel resonant DC-DC converters with capacitive output filter,” *IEEE Trans. Power Electron.*, vol. 14, no. 3, pp. 515–521, 1999. DOI: [10.1109/63.761695](https://doi.org/10.1109/63.761695) [PDF]
- [57] I. Nam, R. Dougal, and E. Santi, “Optimal design method for series LCLC resonant converter based on analytical solutions for voltage gain resonant peaks,” in *Proc. of the 28th IEEE Applied Power Electronics Conf. and Expo. (APEC)*, 2013, pp. 1429–1437. DOI: [10.1109/APEC.2013.6520486](https://doi.org/10.1109/APEC.2013.6520486) [PDF]
- [58] W. Zhang, S.-C. Wong, C. K. Tse, and Q. Chen, “Design for efficiency optimization and voltage controllability of series-series compensated inductive power transfer systems,” *IEEE Trans. Power Electron.*, vol. 29, no. 1, pp. 191–200, 2014. DOI: [10.1109/TPEL.2013.2249112](https://doi.org/10.1109/TPEL.2013.2249112) [PDF]
- [59] J. Mühlethaler, “Modeling and multi-objective optimization of inductive power components,” Ph.D. dissertation, Dept. Elect.

- Eng., Swiss Federal Inst. Technol. Zurich (ETH Zurich), Switzerland, 2012. [PDF]
- [60] M. Leibl, G. Ortiz, and J. W. Kolar, “Design and experimental analysis of a medium-frequency transformer for solid-state transformer applications,” *IEEE J. Emerg. Sel. Topics Power Electron.*, vol. 5, no. 1, pp. 110–123, 2017. DOI: [10.1109/JESTPE.2016.2623679](https://doi.org/10.1109/JESTPE.2016.2623679) [PDF]
- [61] T. Guillod, J. Huber, F. Krismer, and J. W. Kolar, “Litz wire losses: Effects of twisting imperfections,” in *Proc. of the 18th IEEE Workshop on Control and Modeling of Power Electronics (COMPEL)*, 2017, pp. 1–8. DOI: [10.1109/COMPEL.2017.8013327](https://doi.org/10.1109/COMPEL.2017.8013327) [PDF]
- [62] W. R. Smythe, *Static and Dynamic Electricity*, 2nd edition. New York, USA: McGraw-Hill Book Company Inc., 1950. [PDF]
- [63] G. Trebbin, “Deriving the expression for the off-axis magnetic field of a circular current loop,” 2012. [Online]. Available: <http://www.grant-trebbin.com/2012/04/off-axis-magnetic-field-of-circular.html>. [Accessed: Apr. 06, 2017]. [PDF]
- [64] D. Meeker, “Finite Element Method Magnetism (FEMM),” 2014. [Online]. Available: <http://www.femm.info/wiki/HomePage>. [Accessed: Jun. 20, 2017].
- [65] Keysight Technologies Inc., “Agilent 4294A precision impedance analyzer datasheet,” 2008. [Online]. Available: <https://literature.cdn.keysight.com/litweb/pdf/5968-3809E.pdf>. [Accessed: Mai. 03, 2017]. [PDF]
- [66] Foundation for Research on Information Technology in Society (IT²IS), “Tissue Properties,” [Online]. Available: www.itis.ethz.ch/virtual-population/tissue-properties/database. [Accessed: Oct. 07, 2016].
- [67] F. Krismer, “Modeling and optimization of bidirectional dual active bridge DC-DC converter topologies,” Ph.D. dissertation, Dept. Elect. Eng., Swiss Federal Inst. Technol. Zurich (ETH Zurich), Switzerland, 2010. [PDF]

-
- [68] EPC - Efficient Power Conversion, “EPC2016 - Enhancement mode power transistor datasheet,” 2013. [Online]. Available: http://epc-co.com/epc/Portals/0/epc/documents/datasheets/EPC2016_datasheet.pdf. [Accessed: Jul. 31, 2014]. [PDF]
- [69] EPC - Efficient Power Conversion, “Dead-time optimization for maximum efficiency (White Paper WP012),” 2013. [Online]. Available: <http://epc-co.com/epc/documents/papers/Dead-TimeOptimizationforMaximumEfficiency.pdf>. [Accessed: Jun. 01, 2014]. [PDF]
- [70] Texas Instruments Inc., “LM5113 half-bridge gate driver datasheet,” 2016. [Online]. Available: <http://www.ti.com/lit/ds/symlink/lm5113.pdf>. [Accessed: Jul. 23, 2017]. [PDF]
- [71] STMicroelectronics, “STSR30 Synchronous Rectifier Smart Driver for Flyback,” 2004. [Online]. Available: <http://www.st.com>. [Accessed: Jul. 23, 2017]. [PDF]
- [72] B. Wang, A. P. Hu, and D. Budgett, “Autonomous synchronous rectifier for heart pump applications,” in *Proc. of the IEEE Int. Conf. on Industrial Technology (ICIT)*, 2013, pp. 481–486. DOI: [10.1109/ICIT.2013.6505719](https://doi.org/10.1109/ICIT.2013.6505719) [PDF]
- [73] International Organization for Standardization (ISO), “Implants for surgery - Active implantable medical devices - Part 1: General requirements for safety, marking and for information to be provided by the manufacturer”. ISO 14708-1:2014, Geneva, Switzerland, Aug. 2014. [PDF]
- [74] D. J. Thrimawithana and U. K. Madawala, “A primary side controller for inductive power transfer systems,” in *Proc. of the IEEE Int. Conf. on Industrial Technology (ICIT)*, 2010, pp. 661–666. DOI: [10.1109/ICIT.2010.5472724](https://doi.org/10.1109/ICIT.2010.5472724) [PDF]
- [75] C. Y. Huang, J. T. Boys, and G. A. Covic, “LCL pickup circulating current controller for inductive power transfer systems,” *IEEE Trans. Power Electron.*, vol. 28, no. 4, pp. 2081–2093, 2013. DOI: [10.1109/TPEL.2012.2199132](https://doi.org/10.1109/TPEL.2012.2199132) [PDF]
- [76] R. Bosshard, J. W. Kolar, and B. Wunsch, “Control method for Inductive Power Transfer with high partial-load efficiency

- and resonance tracking,” in *Proc. of the Int. Power Electronics Conf. (IPEC - ECCE ASIA)*, 2014, pp. 2167–2174. DOI: [10.1109/IPEC.2014.6869889](https://doi.org/10.1109/IPEC.2014.6869889) [PDF]
- [77] Keysight Technologies Inc., “34410A and 34411A multimeters datasheet,” 2015. [Online]. Available: <https://literature.cdn.keysight.com/litweb/pdf/5989-3738EN.pdf>. [Accessed: Nov. 01, 2016]. [PDF]
- [78] Shin-Etsu Chemical Co., Ltd., “Characteristic properties of silicone rubber compounds,” 2016. [Online]. Available: http://www.shinetsusilicone-global.com/catalog/pdf/rubber_e.pdf. [Accessed: Aug 16, 2017]. [PDF]
- [79] Dow Corning Corporation, “Silastic MDX4-4210 biomedical grade elastomer datasheet,” 2005. [Online]. Available: http://www.dowcorning.com/content/healthcare/healthrubber/rtv_elastomer.asp. [Accessed: Jun. 01, 2017]. [PDF]
- [80] O. Knecht and J. W. Kolar, “Impact of transcutaneous energy transfer on the electric field and specific absorption rate in the human tissue,” in *Proc. of the 41th Annu. Conf. of the IEEE Industrial Electronics Society (IECON)*, 2015, pp. 4977–4983. DOI: [10.1109/IECON.2015.7392881](https://doi.org/10.1109/IECON.2015.7392881) [PDF]
- [81] A. Zolfaghari and M. Maerefat, “Bioheat transfer,” in *Developments in heat transfer*, M. A. Dos Santos Bernardes, Ed. InTech, 2011, chapter 9, pp. 153–170. [Online]. Available: <http://www.intechopen.com/books/developments-in-heat-transfer/bioheat-transfer>. DOI: [10.5772/22616](https://doi.org/10.5772/22616) [PDF]
- [82] F. Xu, T. J. Lu, K. A. Seffen, and E. K. Ng, “Mathematical Modeling of Skin Bioheat Transfer,” *ASME. Appl. Mech. Rev.*, vol. 62, no. 5, pp. 1–35, 2009. DOI: [10.1115/1.3124646](https://doi.org/10.1115/1.3124646) [PDF]
- [83] L. M. Jiji, *Heat Conduction*, 3rd edition. Springer Berlin Heidelberg, 2009. DOI: [10.1007/978-3-642-01267-9](https://doi.org/10.1007/978-3-642-01267-9) [PDF]
- [84] H. H. Pennes, “Analysis of tissue and arterial blood temperatures in the resting human forearm,” *J. Appl. Physiol.*, vol. 1, no. 2, pp. 93–122, 1948. [PDF]

- [85] C. T. Minson, L. T. Berry, and M. J. Joyner, “Nitric oxide and neurally mediated regulation of skin blood flow during local heating,” *J. Appl. Physiol.*, vol. 91, no. 4, pp. 1619–1626, 2001. [PDF]
- [86] T. R. Gowrishankar, D. A. Stewart, G. T. Martin, and J. C. Weaver, “Transport lattice models of heat transport in skin with spatially heterogeneous, temperature-dependent perfusion,” *Biomed. Eng. Online*, vol. 3, no. 42, 2004. DOI: [10.1186/1475-925X-3-42](https://doi.org/10.1186/1475-925X-3-42) [PDF]
- [87] A. R. Moritz and F. C. Henriques Jr, “Studies of thermal injury II: The relative importance of time and surface temperature in the causation of cutaneous burns,” *Am. J. Pathol.*, vol. 23, no. 5, p. 695–720, 1947. [PDF]
- [88] F. Grödl, “(in German) Simulationstool zur Auslegung transkutaner Energieübertragungssysteme,” Ph.D. dissertation, Fac. Mech. Eng., Tech. Univ. Munich, Munich, 2013.
- [89] D. L. Kellogg, Y. Liu, I. F. Kosiba, and D. O’Donnell, “Role of nitric oxide in the vascular effects of local warming of the skin in humans,” *J. Appl. Physiol.*, vol. 86, no. 4, pp. 1185–1190, 1999. [PDF]
- [90] A. Yigit, “Combining thermal comfort models,” *ASHRAE Trans.*, vol. 105, pp. 149–157, 1999. [PDF]
- [91] S. B. Stanković, D. Popović, and G. B. Poparić, “Thermal properties of textile fabrics made of natural and regenerated cellulose fibers,” *Polymer Testing*, vol. 27, no. 1, pp. 41–48, 2008. DOI: [10.1016/j.polymertesting.2007.08.003](https://doi.org/10.1016/j.polymertesting.2007.08.003) [PDF]
- [92] R. J. de Dear, E. Arens, Z. Hui, and M. Oguro, “Convective and radiative heat transfer coefficients for individual human body segments,” *Int. J. Biometeorol.*, vol. 40, no. 3, pp. 141–156, 1997. DOI: [10.1007/s004840050035](https://doi.org/10.1007/s004840050035) [PDF]
- [93] Y. Kurazumi, T. Tsuchikawa, J. Ishii, K. Fukagawa, Y. Yamato, and N. Matsubara, “Radiative and convective heat transfer coefficients of the human body in natural convection,” *Build. Environ.*, vol. 43, no. 12, p. 2142–2153, 2008. DOI: [10.1016/j.buildenv.2007.12.012](https://doi.org/10.1016/j.buildenv.2007.12.012) [PDF]

- [94] B. Cain and B. Farnworth, "Two new techniques for determining the thermal radiative properties of thin fabrics," *Journal of Thermal Insulation*, vol. 9, no. 4, pp. 301–322, 1986. DOI: [10.1177/109719638600900403](https://doi.org/10.1177/109719638600900403) [PDF]
- [95] H. Zhang, T. L. Hu, and J. C. Zhang, "Surface emissivity of fabric in the 8–14 μm waveband," *J. Textile Inst.*, vol. 100, no. 1, pp. 90–94, 2009. DOI: [10.1080/00405000701692486](https://doi.org/10.1080/00405000701692486) [PDF]
- [96] M. Oguro, E. Arens, R. J. de Dear, H. Zhang, and T. Katayama, "Evaluation of the effect of air flow on clothing insulation and on dry heat transfer coefficients for each part of the clothed human body," *J. Archit. Plann. Environ. Eng.*, vol. 66, no. 549, pp. 13–21, 2001. DOI: [10.3130/aija.66.13](https://doi.org/10.3130/aija.66.13) [PDF]
- [97] G. Ochsner *et al.*, "In vivo evaluation of physiological control algorithms for LVADs based on left ventricular volume or pressure," *ASAIO J.*, vol. 63, no. 5, p. 568–577, 2017. DOI: [10.1097/MAT.0000000000000533](https://doi.org/10.1097/MAT.0000000000000533) [PDF]
- [98] F. Meurens, A. Summerfield, H. Nauwynck, L. Saif, and V. Gerdts, "The pig: A model for human infectious diseases," *Trends in Microbiology*, vol. 20, no. 1, pp. 50–57, 2012. DOI: [10.1016/j.tim.2011.11.002](https://doi.org/10.1016/j.tim.2011.11.002) [PDF]
- [99] A. Summerfield, F. Meurens, and M. E. Ricklin, "The immunology of the porcine skin and its value as a model for human skin," *Molecular Immunology*, vol. 66, no. 1, pp. 14–21, 2015. DOI: [10.1016/j.molimm.2014.10.023](https://doi.org/10.1016/j.molimm.2014.10.023) [PDF]
- [100] Suter Kunststoffe AG, "Swiss-Composite SCS-RTV 3428 A&B technical datasheet," 2016. [Online]. Available: <http://www.swiss-composite.ch/pdf/t-SCS-RTV-3428-e.pdf>. [Accessed: Jun. 27, 2017]. [PDF]
- [101] A. Kurz, "Effects of anaesthesia on thermoregulation," *Current Anaesthesia and Critical Care*, vol. 12, no. 2, pp. 72 – 78, 2001. DOI: [10.1054/cacc.2001.0328](https://doi.org/10.1054/cacc.2001.0328) [PDF]
- [102] T. D. Dissanayake, D. Budgett, P. Hu, and S. Malpas, "Experimental thermal study of a TET system for implantable biomedical devices," in *Proc. of the IEEE Biomedical Circuits and Sys-*

- tems (BioCAS) Conf.*, 2008, pp. 113–116. DOI: [10.1109/BIO-CAS.2008.4696887](https://doi.org/10.1109/BIO-CAS.2008.4696887) [PDF]
- [103] A. Christ, M. Douglas, J. Nadakuduti, and N. Kuster, “Assessing human exposure to electromagnetic fields from wireless power transmission systems,” *Proc. IEEE*, vol. 101, no. 6, pp. 1482–1493, 2013. DOI: [10.1109/JPROC.2013.2245851](https://doi.org/10.1109/JPROC.2013.2245851) [PDF]
- [104] I. Laakso, T. Shimamoto, A. Hirata, and M. Feliziani, “Applicability of quasistatic approximation for exposure assessment of wireless power transfer,” in *Proc. of the Int. Symp. on Electromagnetic Compatibility, Tokyo*, 2014, pp. 430–433. [PDF]
- [105] X. L. Chen, A. E. Umenei, D. W. Baarman, N. Chavannes, V. De Santis, J. R. Mosig, and N. Kuster, “Human exposure to close-range resonant wireless power transfer systems as a function of design parameters,” *IEEE Trans. Electromagn. Compat.*, vol. 56, no. 5, pp. 1027–1034, 2014. DOI: [10.1109/TEMC.2014.2308013](https://doi.org/10.1109/TEMC.2014.2308013) [PDF]
- [106] T. Sunohara, A. Hirata, I. Laakso, and T. Onishi, “Analysis of in situ electric field and specific absorption rate in human models for wireless power transfer system with induction coupling,” *Phys. Med. Biol.*, vol. 59, no. 14, pp. 3721–3735, 2014. DOI: [10.1088/0031-9155/59/14/3721](https://doi.org/10.1088/0031-9155/59/14/3721) [PDF]
- [107] K. Shiba and N. Higaki, “Analysis of SAR and current density in human tissue surrounding an energy transmitting coil for a wireless capsule endoscope,” in *Proc. of the 20th Int. Zurich Symp. on Electromagnetic Compatibility*, 2009, pp. 321–324. DOI: [10.1109/EMCZUR.2009.4783455](https://doi.org/10.1109/EMCZUR.2009.4783455) [PDF]
- [108] L. Lucke and V. Bluvshstein, “Safety considerations for wireless delivery of continuous power to implanted medical devices,” in *Proc. of the 36th Annu. Int. Conf. of the IEEE Engineering in Medicine and Biology Society (EMBC)*, 2014, pp. 286–289. DOI: [10.1109/EMBC.2014.6943585](https://doi.org/10.1109/EMBC.2014.6943585) [PDF]
- [109] K. Shiba, M. Nukaya, T. Tsuji, and K. Koshiji, “Analysis of current density and specific absorption rate in biological tissue surrounding transcutaneous transformer for an artificial heart,” *IEEE Trans. Biomed. Eng.*, vol. 55, no. 1, pp. 205–213, 2008. DOI: [10.1109/TBME.2007.900550](https://doi.org/10.1109/TBME.2007.900550) [PDF]

- [110] International Commission on Non-Ionizing Radiation Protection (ICNIRP), “Guidelines for limiting exposure to time-varying electric and magnetic fields (1 Hz - 100 kHz),” *Health Phys.*, vol. 99, no. 6, pp. 818–836, 2010. DOI: [10.1097/HP.0b013e3181f06c86](https://doi.org/10.1097/HP.0b013e3181f06c86) [PDF]
- [111] C. Gabriel, “The dielectric properties of tissues,” in *Radio frequency radiation dosimetry and its relationship to the biological effects of electromagnetic fields*, B. J. Klauenberg and D. Miklavčič, Eds. Dordrecht: Springer Netherlands, 2000, chapter 10, pp. 75–84. DOI: [10.1007/978-94-011-4191-8_10](https://doi.org/10.1007/978-94-011-4191-8_10) [PDF]
- [112] Keysight Technologies Inc., “Basics of measuring the dielectric properties of materials,” 2017. [Online]. Available: <https://literature.cdn.keysight.com/litweb/pdf/5989-2589EN.pdf>. [Accessed: Mai. 09, 2017]. [PDF]
- [113] C. Gabriel, “Compilation of the dielectric properties of body tissues at RF and microwave frequencies,” Occupational and environmental health directorate, Radiofrequency Radiation Division, Brooks Air Force Base, Texas (USA), 1996. [PDF]
- [114] U. Birgersson, “Electrical impedance of human skin and tissue alterations: Mathematical modeling and measurements,” Ph.D. dissertation, Dept. of Clinical Science, Intervention and Technology, Karolinska Institute, Stockholm, Sweden, 2012. [PDF]
- [115] Federal Communications Commission (FCC), ”Guidelines for evaluating the environmental effects of radiofrequency radiation”. FCC 96-326, Washington, D.C., USA, Aug. 1996. [PDF]
- [116] Institute of Electrical and Electronics Engineers (IEEE), ”IEEE standard for safety levels with respect to human exposure to radio frequency electromagnetic fields, 3 kHz to 300 GHz”. IEEE Std C95.1-2005, New York, NY, USA, Apr. 2006. DOI: [10.1109/IEEESTD.2006.99501](https://doi.org/10.1109/IEEESTD.2006.99501) [PDF]
- [117] International Commission on Non-Ionizing Radiation Protection (ICNIRP), “Guidelines for limiting exposure to time-varying electric, magnetic and electromagnetic fields (up to 300 GHz),” *Health Phys.*, vol. 74, no. 4, pp. 494–522, 1998. [PDF]

-
- [118] J. Larsson, “Electromagnetics from a quasistatic perspective,” *Am. J. Phys.*, vol. 75, no. 3, pp. 230–239, 2007. DOI: [10.1119/1.2397095](https://doi.org/10.1119/1.2397095) [PDF]
- [119] N. Orcutt and O. P. Gandhi, “A 3-D impedance method to calculate power deposition in biological bodies subjected to time varying magnetic fields,” *IEEE Trans. Biomed. Eng.*, vol. 35, no. 8, pp. 577–583, 1988. DOI: [10.1109/10.4590](https://doi.org/10.1109/10.4590) [PDF]
- [120] Shin-Etsu Chemical Co., Ltd., “Electrically conductive silicone rubber products,” 2016. [Online]. Available: http://www.shinetsusilicone-global.com/catalog/pdf/ec_e.pdf. [Accessed: Aug 16, 2017]. [PDF]
- [121] Silicone Solutions, “Electrically and thermally conductive products,” 2017. [Online]. Available: <http://siliconesolutions.com/electrically-and-thermally-conductive.html>. [Accessed: May 31, 2017].
- [122] S. J. Han, A. M. Mendelsohn, and R. Ramachandran, “Overview of semiconductive shield technology in power distribution cables,” in *Proc. of the 2005/2006 IEEE/PES Transmission and Distribution Conf. and Exhibition*, 2006, pp. 641–646. DOI: [10.1109/TDC.2006.1668572](https://doi.org/10.1109/TDC.2006.1668572) [PDF]
- [123] O. Knecht, D. Bortis, and J. W. Kolar, “Comparative evaluation of a triangular current mode (TCM) and clamp-switch TCM DC-DC boost converter,” in *Proc. of the 8th IEEE Energy Conversion Congr. and Expo. (ECCE USA)*, 2016, pp. 1–8. DOI: [10.1109/ECCE.2016.7854934](https://doi.org/10.1109/ECCE.2016.7854934) [PDF]
- [124] O. Knecht, D. Bortis, and J. W. Kolar, “ZVS modulation scheme for reduced complexity clamp-switch TCM DC-DC boost converter,” *IEEE Trans. Power Electron.*, vol. 33, no. 5, pp. 4204–4214, 2018. DOI: [10.1109/TPEL.2017.2720729](https://doi.org/10.1109/TPEL.2017.2720729) [PDF]
- [125] S. Waffler, “(in German) Hochkompakter bidirektionaler DC-DC-Wandler für Hybridfahrzeuge,” Ph.D. dissertation, Dept. Elect. Eng., Swiss Federal Inst. Technol. Zurich (ETH Zurich), Switzerland, 2013. [PDF]
- [126] L. Meier, “Design, optimization and implementation of a bidirectional 1-3kW DC/DC converter,” Master’s thesis, Power Electron.

- Syst. Lab., Dept. Elect. Eng., Swiss Federal Inst. Technol. Zurich (ETH Zurich), Switzerland, 2014.
- [127] D. Bortis and J. W. Kolar, “(in German) DC/DC Konverter und Verfahren zur Steuerung eines weich schaltenden bidirektionalen DC/DC Konverters,” Swiss Patent Application No. CH710661 (A2), Filed Jan. 29, 2015, Published Jul. 29, 2016.
- [128] X. Huang, F. C. Lee, Q. Li, and W. Du, “High-frequency high-efficiency GaN-based interleaved CRM bidirectional buck/boost converter with inverse coupled inductor,” *IEEE Trans. Power Electron.*, vol. 31, no. 6, pp. 4343–4352, 2016. DOI: [10.1109/TPEL.2015.2476482](https://doi.org/10.1109/TPEL.2015.2476482) [PDF]
- [129] C. Marxgut, F. Krismer, D. Bortis, and J. W. Kolar, “Ultraflat interleaved triangular current mode (TCM) single-phase PFC rectifier,” *IEEE Trans. Power Electron.*, vol. 29, no. 2, pp. 873–882, 2014. DOI: [10.1109/TPEL.2013.2258941](https://doi.org/10.1109/TPEL.2013.2258941) [PDF]
- [130] D. Gerber and J. Biela, “Interleaving of a soft-switching boost converter operated in boundary conduction mode,” *IEEE Trans. Plasma Sci.*, vol. 43, no. 10, pp. 3374–3380, 2015. DOI: [10.1109/TPS.2015.2422476](https://doi.org/10.1109/TPS.2015.2422476) [PDF]
- [131] S. G. Yoon, J. M. Lee, J. H. Park, I. K. Lee, and B. H. Cho, “A frequency controlled bidirectional synchronous rectifier converter for HEV using super-capacitor,” in *Proc. of the 35th IEEE Annu. Power Electronics Specialists Conf. (PESC)*, 2004, pp. 135–140. DOI: [10.1109/PESC.2004.1355729](https://doi.org/10.1109/PESC.2004.1355729) [PDF]
- [132] J. S. Lai, B. York, A. Koran, Y. Cho, B. Whitaker, and H. Miwa, “High-efficiency design of multiphase synchronous mode soft-switching converter for wide input and load range,” in *Proc. of the Int. Power Electronics Conf. (IPEC)*, 2010, pp. 1849–1855. DOI: [10.1109/IPEC.2010.5542155](https://doi.org/10.1109/IPEC.2010.5542155) [PDF]
- [133] D. M. Sable, F. C. Lee, and B. H. Cho, “A zero-voltage-switching bidirectional battery charger/discharger for the NASA EOS satellite,” in *Proc. of the 17th IEEE Applied Power Electronics Conf. and Expo. (APEC)*, 1992, pp. 614–621. DOI: [10.1109/APEC.1992.228354](https://doi.org/10.1109/APEC.1992.228354) [PDF]

-
- [134] C. P. Henze, H. C. Martin, and D. W. Parsley, “Zero-voltage switching in high frequency power converters using pulse width modulation,” in *Proc. of the 3rd IEEE Applied Power Electronics Conf. and Expo. (APEC)*, 1988, pp. 33–40. DOI: [10.1109/APEC.1988.10548](https://doi.org/10.1109/APEC.1988.10548) [PDF]
- [135] C. R. Swartz, “High performance ZVS buck regulator removes barriers to increased power throughput in wide input range point-of-load applications,” Vicor Corporation, 2012. [Online]. Available: http://www.vicorpower.com/documents/whitepapers/Picor/wp_HighPerformanceZVS.pdf. [Accessed: Feb. 17, 2017]. [PDF]
- [136] Vicor Corporation, “Cool-power ZVS buck switching regulators,” 2017. [Online]. Available: <http://www.vicorpower.com/dc-dc-converters-board-mount/cool-power-pi33xx-and-pi34xx>. [Accessed: Jun. 14, 2017].
- [137] R. Oruganti and F. C. Lee, “State-plane analysis of parallel resonant converter,” in *Proc. of the 16th IEEE Power Electronics Specialists Conf. (PESC)*, 1985, pp. 56–73. DOI: [10.1109/PESC.1985.7070930](https://doi.org/10.1109/PESC.1985.7070930) [PDF]
- [138] J. P. Gegner and C. Q. Lee, “Zero-voltage-transition converters using a simple magnetic feedback technique,” in *Proc. of the 25th IEEE Annu. Power Electronics Specialists Conf. (PESC)*, 1994, pp. 590–596. DOI: [10.1109/PESC.1994.349676](https://doi.org/10.1109/PESC.1994.349676) [PDF]
- [139] EPC - Efficient Power Conversion, “EPC2016C - Enhancement mode power transistor datasheet,” 2015. [Online]. Available: http://epc-co.com/epc/Portals/0/epc/documents/datasheets/EPC2016C_datasheet.pdf. [Accessed: May 12, 2016]. [PDF]
- [140] ON Semiconductor, “MBR1H100SFT3G - Surface mount schotky power rectifier datasheet,” 2014. [Online]. Available: <https://www.onsemi.com/pub/Collateral/MBR1H100SF-D.PDF>. [Accessed: Jan. 04, 2016]. [PDF]
- [141] R. M. Burkart, “Advanced modeling and multi-objective optimization of power electronic converter systems,” Ph.D. dissertation, Dept. Elect. Eng., Swiss Federal Inst. Technol. Zurich (ETH Zurich), Switzerland, 2016. [PDF]

- [142] D. Bortis, O. Knecht, D. Neumayr, and J. W. Kolar, “Comprehensive evaluation of GaN GIT in low- and high-frequency bridge leg applications,” in *Proc. of the 8th IEEE Int. Power Electronics and Motion Control Conf. (IPEMC-ECCE Asia)*, 2016, pp. 21–30. DOI: [10.1109/IPEMC.2016.7512256](https://doi.org/10.1109/IPEMC.2016.7512256) [PDF]
- [143] A. Tüysüz, R. Bosshard, and J. W. Kolar, “Performance comparison of a GaN GIT and a Si IGBT for high-speed drive applications,” in *Proc. of the Int. Power Electronics Conf. (IPEC-Hiroshima 2014 - ECCE ASIA)*, 2014, pp. 1904–1911. DOI: [10.1109/IPEC.2014.6869845](https://doi.org/10.1109/IPEC.2014.6869845) [PDF]
- [144] G. Yilmaz and C. Dehollain, “Capacitive detuning optimization for wireless uplink communication in neural implants,” in *Proc. of the 5th IEEE Int. Workshop on Advances in Sensors and Interfaces (IWASI)*, 2013, pp. 45–50. DOI: [10.1109/IWASI.2013.6576069](https://doi.org/10.1109/IWASI.2013.6576069) [PDF]
- [145] X. Shi, A. N. Parks, B. H. Waters, and J. R. Smith, “Co-optimization of efficiency and load modulation data rate in a wireless power transfer system,” in *Proc. of the IEEE Int. Symp. on Circuits and Systems (ISCAS)*, 2015, pp. 698–701. DOI: [10.1109/ISCAS.2015.7168729](https://doi.org/10.1109/ISCAS.2015.7168729) [PDF]
- [146] S. Mandal and R. Sarpeshkar, “Power-efficient impedance-modulation wireless data links for biomedical implants,” *IEEE Trans. Biomed. Circuits Syst.*, vol. 2, no. 4, pp. 301–315, 2008. DOI: [10.1109/TBCAS.2008.2005295](https://doi.org/10.1109/TBCAS.2008.2005295) [PDF]
- [147] O. Knecht, Y. Jundt, and J. W. Kolar, “Planar inverted-F antenna design for a fully implantable mechanical circulatory support system,” in *Proc. of the 18th IEEE Int. Conf. on Industrial Technology (ICIT)*, 2017, pp. 1366–1371. DOI: [10.1109/ICIT.2017.7915563](https://doi.org/10.1109/ICIT.2017.7915563) [PDF]
- [148] Federal Communications Commission (FCC), “Medical Device Radiocommunications Service (MedRadio),” 2016. [Online]. Available: www.fcc.gov/general/medical-device-radiocommunications-service-medradio. [Accessed: Sept. 28, 2016].

-
- [149] Federal Communications Commission (FCC), "Amendment of Parts 2 and 95 of the Commission's Rules to Provide Additional Spectrum for the Medical Device Radiocommunication Service in the 413-457 MHz band". FCC 11-176, Washington, D.C., USA, Nov. 2011. [PDF]
- [150] Silicon Laboratories Inc., "Si4464/63/61/60 high-performance, low-current transceiver datasheet," 2016. [Online]. Available: <http://www.silabs.com/documents/public/data-sheets/Si4464-63-61-60.pdf>. [Accessed: Jun. 09, 2017]. [PDF]
- [151] Silicon Laboratories Inc., "Si4x6x and EZR32 high-power PA matching (Application Note AN648)," 2016. [Online]. Available: <http://www.silabs.com/documents/public/application-notes/AN648.pdf>. [Accessed: Jun. 09, 2017]. [PDF]
- [152] A. Karlsson, "Physical limitations of antennas in a lossy medium," *IEEE Trans. Antennas Propag.*, vol. 52, no. 8, pp. 2027–2033, 2004. DOI: [10.1109/TAP.2004.832335](https://doi.org/10.1109/TAP.2004.832335) [PDF]
- [153] J. Kim and Y. Rahmat-Samii, "Implanted antennas inside a human body: Simulations, designs, and characterizations," *IEEE Trans. Microw. Theory Techn.*, vol. 52, no. 8, pp. 1934–1943, 2004. DOI: [10.1109/TMTT.2004.832018](https://doi.org/10.1109/TMTT.2004.832018) [PDF]
- [154] M. C. Huynh and W. Stutzman, "Ground plane effects on planar inverted-F antenna (PIFA) performance," *IEE Proc. - Microw. Antennas and Propag.*, vol. 150, no. 4, pp. 209–213, 2003. DOI: [10.1049/ip-map:20030551](https://doi.org/10.1049/ip-map:20030551) [PDF]
- [155] H. T. Chattha, Y. Huang, M. K. Ishfaq, and S. J. Boyes, "A comprehensive parametric study of planar inverted-F antenna," *Wireless Engineering and Technology*, vol. 3, no. 1, pp. 1–11, 2012. DOI: [10.4236/wet.2012.31001](https://doi.org/10.4236/wet.2012.31001) [PDF]
- [156] Y. T. Jean-Charles, V. Ungvichian, and J. A. Barbosa, "Effects of substrate permittivity on planar inverted-F antenna performances," *Journal of Computers*, vol. 4, no. 7, pp. 610–614, 2009. [PDF]
- [157] P. Soontornpipit, C. M. Furse, and Y. C. Chung, "Design of implantable microstrip antenna for communication with medical im-

- plants,” *IEEE Trans. Microw. Theory Techn.*, vol. 52, no. 8, pp. 1944–1951, 2004. DOI: [10.1109/TMTT.2004.831976](https://doi.org/10.1109/TMTT.2004.831976) [PDF]
- [158] A. Mahanfar, S. Bila, M. Aubourg, and S. Verdeyme, “Design considerations for the implanted antennas,” in *Proc. of the IEEE/MTT-S Int. Microwave Symp.*, 2007, pp. 1353–1356. DOI: [10.1109/MWSYM.2007.380463](https://doi.org/10.1109/MWSYM.2007.380463) [PDF]
- [159] V. T. Nguyen and C. W. Jung, “Impact of dielectric constant on embedded antenna efficiency,” *Int. J. Antennas Propag.*, vol. 2014, pp. 1–6, 2014, art. ID 758139. DOI: [10.1155/2014/758139](https://doi.org/10.1155/2014/758139) [PDF]
- [160] M. Pelosi, O. Franek, M. B. Knudsen, and G. F. Pedersen, “Influence of dielectric loading on PIFA antennas in close proximity to user’s body,” *Electronics Letters*, vol. 45, no. 5, pp. 246–247, 2009. DOI: [10.1049/el:20093559](https://doi.org/10.1049/el:20093559) [PDF]
- [161] Victrex, “VICTREX PEEK properties brochure,” 2016. [Online]. Available: www.victrex.com/~media/literature/en/victrex_properties-guide_en_metric.pdf. [Accessed: 21.2.2017]. [PDF]
- [162] S. M. Kurtz and J. N. Devine, “PEEK biomaterials in trauma, orthopedic, and spinal implants,” *Biomaterials*, vol. 28, no. 32, pp. 4845–4869, 2007. DOI: [10.1016/j.biomaterials.2007.07.013](https://doi.org/10.1016/j.biomaterials.2007.07.013) [PDF]
- [163] Keysight Technologies Inc., “User’s manual: HP 85070B dielectric probe kit,” 1997. [Online]. Available: <https://literature.cdn.keysight.com/litweb/pdf/85070-90009.pdf>. [Accessed: Feb. 20, 2017]. [PDF]
- [164] E. S. Takeuchi, R. A. Leising, D. M. Spillman, R. Rubino, H. Gan, K. J. Takeuchi, and A. C. Marschilok, “Lithium Batteries for Medical Applications,” in *Lithium Batteries: Science and Technology*, G.-A. Nazri and G. Pistoia, Eds. Boston, MA: Springer US, 2003, chapter 22, pp. 686–700. DOI: [10.1007/978-0-387-92675-9_22](https://doi.org/10.1007/978-0-387-92675-9_22) [PDF]
- [165] D. C. Bock, A. C. Marschilok, K. J. Takeuchi, and E. S. Takeuchi, “Batteries used to power implantable biomedical devices,” *Electrochim Acta.*, vol. 84, no. 1, pp. 1–31, 2012. DOI: [10.1016/j.electacta.2012.03.057](https://doi.org/10.1016/j.electacta.2012.03.057) [PDF]

-
- [166] M. R. Palacin, “Recent advances in rechargeable battery materials: A chemist’s perspective,” *Chem. Soc. Rev.*, vol. 38, no. 9, pp. 2565–2575, 2009. DOI: [10.1039/B820555H](https://doi.org/10.1039/B820555H) [PDF]
- [167] LiPol Battery Company, Ltd., “Lithium Polymer Battery List 2015,” 2015. [Online]. Available: <http://www.lipolbattery.com/lipoly-battery.html>. [Accessed: Nov. 4, 2016].
- [168] STMicroelectronics, “STM32F407VG High-performance foundation line, ARM Cortex-M4 MCU - datasheet,” 2016. [Online]. Available: <http://www.st.com>. [Accessed: Sept. 16, 2017]. [PDF]
- [169] STMicroelectronics, “STM32L471VG Ultra-low-power, ARM Cortex-M4 MCU - datasheet,” 2016. [Online]. Available: <http://www.st.com>. [Accessed: Sept. 16, 2017]. [PDF]
- [170] X. Wei, Z. Wang, and H. Dai, “A critical review of wireless power transfer via strongly coupled magnetic resonances,” *Energies*, vol. 7, no. 7, pp. 4316–4341, 2014. DOI: [10.3390/en7074316](https://doi.org/10.3390/en7074316) [PDF]
- [171] B. H. Waters, J. R. Smith, and P. Bonde, “Innovative free-range resonant electrical energy delivery system (FREE-D system) for a ventricular assist device using wireless power,” *ASAIO J.*, vol. 60, no. 1, pp. 31–37, 2014. DOI: [10.1097/MAT.000000000000029](https://doi.org/10.1097/MAT.000000000000029) [PDF]
- [172] W. X. Zhong, C. Zhang, X. Liu, and S. Y. R. Hui, “A methodology for making a three-coil wireless power transfer system more energy efficient than a two-coil counterpart for extended transfer distance,” *IEEE Trans. Power Electron.*, vol. 30, no. 2, pp. 933–942, 2015. DOI: [10.1109/TPEL.2014.2312020](https://doi.org/10.1109/TPEL.2014.2312020) [PDF]
- [173] A. K. RamRakhyani and G. Lazzi, “On the design of efficient multi-coil telemetry system for biomedical implants,” *IEEE Trans. Biomed. Circuits Syst.*, vol. 7, no. 1, pp. 11–23, 2013. DOI: [10.1109/TBCAS.2012.2192115](https://doi.org/10.1109/TBCAS.2012.2192115) [PDF]
- [174] R. Bosshard, J. Mühlethaler, J. W. Kolar, and I. Stevanović, “The η - α -Pareto front of inductive power transfer coils,” in *Proc. of the 38th Annu. Conf. of the IEEE Industrial Electronics Society (IECON)*, 2012, pp. 4270–4277. DOI: [10.1109/IECON.2012.6389203](https://doi.org/10.1109/IECON.2012.6389203) [PDF]

- [175] K. Viswanathan, R. Oruganti, and D. Srinivasan, "A novel tri-state boost converter with fast dynamics," *IEEE Trans. Power Electron.*, vol. 17, no. 5, pp. 677–683, 2002. DOI: [10.1109/TPEL.2002.802197](https://doi.org/10.1109/TPEL.2002.802197) [PDF]
- [176] Z. Pantic and S. M. Lukic, "Framework and topology for active tuning of parallel compensated receivers in power transfer systems," *IEEE Trans. Power Electron.*, vol. 27, no. 11, pp. 4503–4513, 2012. DOI: [10.1109/TPEL.2012.2196055](https://doi.org/10.1109/TPEL.2012.2196055) [PDF]
- [177] A. I. Bratcu and I. Munteanu, "Cascaded DC–DC converter photovoltaic systems: Power optimization issues," *IEEE Trans. Ind. Electron.*, vol. 58, no. 2, pp. 403–411, 2011. DOI: [10.1109/TIE.2010.2043041](https://doi.org/10.1109/TIE.2010.2043041) [PDF]
- [178] Q. Li and P. Wolfs, "A review of the single phase photovoltaic module integrated converter topologies with three different DC link configurations," *IEEE Trans. Power Electron.*, vol. 23, no. 3, pp. 1320–1333, 2008. DOI: [10.1109/TPEL.2008.920883](https://doi.org/10.1109/TPEL.2008.920883) [PDF]
- [179] G. R. Walker and P. C. Sernia, "Cascaded DC–DC converter connection of photovoltaic modules," *IEEE Trans. Power Electron.*, vol. 19, no. 4, pp. 1130–1139, 2004. DOI: [10.1109/TPEL.2004.830090](https://doi.org/10.1109/TPEL.2004.830090) [PDF]
- [180] R. S. Maciel, L. C. de Freitas, E. A. A. Coelho, J. B. Vieira, and L. C. G. de Freitas, "Front-end converter with integrated PFC and DC-DC functions for a fuel cell UPS with DSP-based control," *IEEE Trans. Power Electron.*, vol. 30, no. 8, pp. 4175–4188, 2015. DOI: [10.1109/TPEL.2014.2359891](https://doi.org/10.1109/TPEL.2014.2359891) [PDF]
- [181] A. Shahin, M. Hinaje, J. P. Martin, S. Pierfederici, S. Rael, and B. Davat, "High voltage ratio DC-DC converter for fuel-cell applications," *IEEE Trans. Ind. Electron.*, vol. 57, no. 12, pp. 3944–3955, 2010. DOI: [10.1109/TIE.2010.2045996](https://doi.org/10.1109/TIE.2010.2045996) [PDF]
- [182] P. M. Roschatt, R. A. McMahon, and S. Pickering, "A gallium nitride FET based DC-DC converter for the new 48 V automotive system," in *Proc. of the 7th IET Int. Conf. on Power Electronics, Machines and Drives (PEMD)*, 2014, pp. 1–6. DOI: [10.1049/cp.2014.0507](https://doi.org/10.1049/cp.2014.0507) [PDF]

- [183] S. R. Lee, B. Y. Choi, J. Y. Lee, and C. Y. Won, “48 V to 12 V soft-switching interleaved buck and boost converter for mild-hybrid vehicle application,” in *Proc. of the 19th Int. Conf. on Electrical Machines and Systems (ICEMS)*, 2016, pp. 1–6. [\[PDF\]](#)
- [184] E. W. Weisstein, “Fourier Series - Triangle Wave,” MathWorld - A Wolfram Web Resource, 2016. [Online]. Available: <http://mathworld.wolfram.com/FourierSeriesTriangleWave.html>. [Accessed: Dec. 28, 2016].

Curriculum Vitae

Personal Information



Name	Oliver Marco KNECHT
Date of birth	July 09, 1986
Nationality	Switzerland
Citizen of	Uster ZH, Switzerland
Contact	oknecht@swissonline.ch +41 (0)79 769 55 32

Education

2013 – 2017	Doctorate at the Power Electronic Systems Laboratory (PES), ETH Zurich
2013	Master Thesis at the Power Electronic Systems Laboratory (PES), ETH Zurich
2011 – 2013	MSc studies in Information Technology and Electrical Engineering, ETH Zurich
2006 – 2011	BSc studies in Information Technology and Electrical Engineering, ETH Zurich
2002 – 2006	Kantonsschule Limmattal, Urdorf ZH
1998 – 2002	Bezirksschule Bremgarten, Bremgarten AG
1993 – 1998	Primary school, Arni AG

Work Experience

2013 – 2017	Research assistant at the Power Electronic Systems Laboratory (PES), ETH Zurich
2008 – 2012	Part-time employment and full-time, five month internship (in 2011) at Onefive GmbH